UNIVERSITÀ
DEGLI STUDI
DI PADOVA

Head Office: Università degli Studi di Padova

Department of Biology

Ph.D. COURSE IN: Biosciences
CURRICULUM: Cell Biology and Physiology
SERIES XXXII

DOPAL-induced impairment of αSynuclein and cellular proteostasis as molecular mechanism to enhance neuronal vulnerability in Parkinson's disease.

Coordinator: Prof. Ildikò Szabò
Supervisor: Prof. Luigi Bubacco
Co-Supervisor: Dr. Daniela Boassa

Ph.D. student: Anna Masato

Acknowledgements.

First, I would like to express my sincere gratitude to my mentor Prof. Luigi Bubacco, for making me grow as a scientist and as a person. He has been constantly challenging me to come up with my own ideas, never settle and think outside (my) box. That is one of the most import lessons I am thankful for.

Besides my supervisor, I would like to thank all the people from the Biophysics and Molecular Physiology Unit for their help and contribution to this project. To my colleagues and friends Federica, Susanna and Michele with whom I shared goals and difficult moments, always supporting each other. To Nicoletta, for guiding me since I was only a bachelor student.

A special thanks to the members of the National Center for Microscopy and Imaging Research for their help during the period spent as visiting student at the University of California San Diego. Among them, to Dr. Daniela Boassa, for giving me the great opportunity to work with her, for inspiring me and teaching me with passion, for making me feel at home.

I would like to mention my advisors Prof. Ildiko Szabò and Prof. Marisa Brini for the valuable discussions we shared during the three years of my PhD. Also, the reviewers of this dissertation, Prof. Simone Engelender (Technion, Israele) and Dr. Jennifer Morgan (University of Chicago, USA), for providing insightful comments that improved this manuscript.

I am also grateful to the Italian and American Institutions that financially supported my research, the Branfman Family Foundation and the Ing. Aldo Gini Foundation that supported my stay in San Diego.

Finally, I would like to thank my family and my friends for all their support during these years. Above all, my husband Pietro, for always being there for me and never letting me to give up.

"There are more things in heaven and earth, Horatio,
than are dreamt of in your philosophy."
Hamlet (1.5.167-8)

Index

Abstract.

Parkinson's Disease (PD) is pathologically characterized by the progressive loss of nigrostriatal dopaminergic neurons and aberrant accumulation of the pre-synaptic protein αSynuclein (αSyn). Several factors have been proposed to trigger αSyn aggregation, resulting αSyn-induced neurotoxicity. Here, the working hypothesis is to assess how the interplay between αSyn and an altered dopamine metabolism may contribute to the pathogenesis of PD. A relevant role has been assigned to the dopamine metabolite 3,4-dihydroxyphenylacetaldehyde (DOPAL), whose neurotoxic action has been supported by several experimental models. Being an aldehyde, DOPAL covalently modifies lysine residues of proteins, thus αSyn is considered a preferential target due to the high percentage of lysines in its sequence, its unfolded state and abundance at synapses. *In vitro* and cellular studies demonstrated that DOPAL triggers αSyn oligomerization, prevents αSyn association to synaptic vesicle membranes and affects synapse physiology. Of note, some lysines on αSyn sequence that were identified as DOPAL-modified, are also reported as target of functional post-translational modifications that regulate αSyn proteostasis.

On this ground, we aimed to investigate the consequences of DOPAL build-up in neurons on both αSyn and cellular proteostasis, in a wider perspective. To address these issues, cellular biology and biochemical studies were coupled with advanced imaging techniques, like the correlated light and electron microscopy (CLEM), which allows to map the αSyn localization, both at cellular and supra-molecular level. As cellular models, we worked on both rat primary cortical neurons and the catecholaminergic BE(2)-M17 cells.

Here, we provided evidence of a DOPAL-dependent αSyn redistribution in the neuronal compartments, from the peripheral terminals to its axonal trafficking to the soma. These observations were also linked to the assessment of αSyn affected clearance in the presence of DOPAL. Interestingly, DOPAL appeared to promote the αSyn loading in the multi-vesicular bodies (MVBs) of the endosomal

pathway and the αSyn accumulation within perinuclear lysosomes, both in its monomeric and oligomeric forms.

Since αSyn oligomers are known to affect protein degradation systems functionality, we aimed to unravel the hypothesis of a synergistic effect of αSyn and DOPAL on a general impairment of cellular proteostasis. Indeed, increasing concentrations of DOPAL treatment in BE(2)-M17 cells led to a dose-dependent accumulation of ubiquitinated proteins and the autophagic marker p62, suggesting a potential impairment of the proteasome and the autophagic flux, respectively.

Finally, we recently started to explore a translational approach to control DOPAL-associated toxicity. Specifically, we used biguanidine molecules as aldehyde scavengers, i.e. aminoguanidine and metformin, that are already in clinical practice. So far, preliminary experiments confirmed the ability of aminoguanidine to slow-down DOPAL-induced αSyn *in vitro* oligomerization. Also, both aminoguanidine and metformin treatments reduced the accumulation of p62 caused by DOPAL in BE(2)-M17. Given these promising results, the beneficial effect of these compounds against the DOPAL-associated neurotoxicity will be further investigated.

In conclusion, DOPAL build-up in the cellular environment causes impaired αSyn trafficking, αSyn aggregation and decreased clearance. At the same time, DOPAL appears to affect protein degradation systems functionality, which would result in overall impaired neuronal proteostasis. Finally, the DOPAL-induced overload in MVBs together with the blockage of autophagy might promote the secretion of DOPAL-modified αSyn through exosomes, spreading these toxic species in the surrounding environment. On this ground, a therapeutic approach to target DOPAL neurotoxicity on site and to promote protein turnover might be of interest.

List of abbreviations.

αSyn: αSynuclein
αSyn-OVX: αSynuclein-overexpressing
AADC: Aromatic L-Amino acid decarboxylase
AD: Alzheimer's Disease
AEP: Asparagine Endopeptidase
AG: Aminoguanidine
ALDH: Aldehyde Dehydrogenase
ALP: Autophagy-Lysosomal Pathway
ALR/AR: Aldehyde/Aldose Reductase
ALS: Amyotrophic Lateral Sclerosis
CHX: Cycloheximide
CLEM: Correlated Light and Electron Microscopy
CMA: Chaperone-Mediated Autophagy
DA: Dopamine
DAB: 3-3'-diaminobendizine
DAT: Dopamine Transporter
DIV: Day *In Vitro*
DLB: Dementia with Lewy Bodies
DOPAC: 3,4-Dihydroxyphenylacetic acid
DOPAL: 3,4-Dihydroxyphenylacetaldehyde
DOPET: 3,4-Dihydroxyphenylethanol
ER: Endoplasmic Reticulum
GWAS: Genome-Wide Association Study
HBSS: Hank's Balanced Salt Solution
HD: Huntington's Disease
HSC70: Heat-Shock Cognate protein of 70 kDa
HVA: Homovanilic Acid
ICC: Immunocytochemistry
ILVs: Intra-Luminal Vesicles
LAMP2A: Lysosomes-Associated Membrane Protein Type 2A
LBs: Lewy Bodies

LRRK2: Leucine-Reach Repeat Kinase 2

MAO: Monoamine Oxidase

miniSOG: mini Singlet Oxygen Generator

MPTP: 1-methyl-4-phenyl-1,2,3,6-tetrahydropyridine

MSA: Multiple System Atrophy

MVBs: Multi-Vesicular Bodies

nIRF: near InfraRed Fluorescence

Nnd: Nearest neighbor distance

PBS: Phosphate Buffer Saline

PD: Parkinson's Disease

PFA: Paraformaldehyde

PK: Proteinase K

pSer129: phosphorylated Serine 129

PTMs: Post-Translational Modifications

PVDF: polyvinylidenedifluoride

RA: Retinoic Acid

ROS: Reactive Oxygen Species

RP-HPLC: Reverse Phase- High Pressure Liquid Chromatography

SNARE: Soluble N-ethylmaleimide-sensitive factor activating protein receptor

SNpc: *Substantia Nigra pars compacta*

SOD1: Superoxide Dismutase 1

Syn-TKO: Synuclein Triple Knock-Out

TBS-T: Tris Buffer Saline -Tween

TimeSTAMP: Time-Specific Tag for the Measurement of the Age of Proteins

TEM: Transmission Electron Microscopy

TH: Tyrosine Hydroxilase

T2DM: Type 2 Diabetes Mellitus

UPS: Ubiquitin-Proteasome System

VMAT2: Vesicular Monoamino Transporter type-2

VTA: Ventral-Tegmental Area

WT: Wild-Type

4-HNE: 4-Hydroxynonenal

6-OHDA: 6-Hydroxydopamine

1. INTRODUCTION.

1.1 Protein dyshomeostasis as common theme in neurodegenerative diseases.

The sustained amelioration in the quality of life due to the advancement of medicine and science is leading to a remarkable increase in the life expectancy of the population, that has overcome 80 years in industrialized countries. The improvements in people life style and the quality of the health care systems highly reduced the risk of pandemic infections, which have been replaced by cancer and cardiovascular diseases as the main causes of death. Besides them, neurodegenerative diseases are rising in their incidence among the population globally, with a great impact in our society.

The most common neurodegenerative diseases are Alzheimer's Disease (AD) that affects around 5-8% of people over 60 years old (source: World Health Organization), followed by Parkinson's Disease (PD), Amyotrophic Lateral Sclerosis (ALS), Dementia with Lewy Bodies (DLB) and Huntington's Disease (HD). In most cases, these pathologies present a late onset at around 60 years of age and are associated with a slow and long prognosis. They are characterized by a plethora of phenotypes, including dementia and cognitive dysfunctions, psychological breakdown and motor impairments. Despicably, several unresolved questions on their pathogenesis are still challenging the identification of specific biomarkers for early diagnosis and the development of effective disease-modifying treatments to ameliorate the quality of life and expectations of the patients and their families.

At pathological level, neuronal loss is observed in diverse brain regions, with different severity and clinical implications according to the disease (**Table 1.1**). Interestingly, these pathologies are defined proteinopathies, as a common theme is represented by the impaired regulation of protein homeostasis in neurons, with consequent accumulation and aggregation of proteins and neurotoxic outcomes (Ciechanover and Kwon, 2015).

Disease	Etiology	Regions most affected	Characteristic pathology	Disease proteins deposited
Huntington's disease	Huntingtin (dominant)	Striatum, other basal ganglia, cortex, other regions	Intranuclear inclusions and cytoplasmic aggregates	Huntingtin with polyglutamine expansion
Other polyglutamine diseases (DRPLA, SCA1–3, etc., SBMA)	Atrophin-1, ataxin-1–3, etc.; androgen receptor (AR) (dominant)	Basal ganglia, brain stem cerebellum, and spinal cord	Intranuclear inclusions	Atrophin-1, ataxins or AR
Alzheimer's disease (AD)	Sporadic (ApoE risk factor)	Cortex, hippocampus, basal forebrain, brain stem	Neuritic plaques and neurofibrillary tangles	Aβ peptide (from APP) and hyperphosphorylated tau
	Amyloid precursor protein (APP) (dominant)	Same as sporadic	Same as sporadic	Same as sporadic
	Presenilin 1, 2 (dominant)	Same as sporadic	Same as sporadic	Same as sporadic
Fronto-temporal dementia with Parkinsonism	Tau mutations (dominant)	Frontal and temporal cortex, hippocampus	Pick bodies	Hyperphosphorylated tau protein
Parkinson's disease (PD)	Sporadic	Substantia nigra, cortex, locus ceruleus, raphe, etc.	Lewy bodies and Lewy neurites	α-Synuclein
	α-Synuclein (dominant)	Similar to sporadic, but more widespread	Similar to sporadic	α-Synuclein
	Parkin (also DJ-1, PINK1) recessive (some dominant)	Substantia nigra	Lewy bodies absent (or much less frequent)	α-Synuclein (when present)
Amyotrophic lateral sclerosis (ALS)	Sporadic	Spinal motor neurons and motor cortex	Bonina bodies and axonal spheroids	Unknown (neurofilaments)
	Superoxide dismutase-1 (dominant)	Same as sporadic	Same	Unknown
Prion diseases (kuru, CJD, GSS disease, fatal familial insomnia, new variant CJD)	Sporadic, genetic and infectious	Cortex, thalamus, brain stem, cerebellum, other areas	Spongiform degeneration, amyloid, other aggregates	Prion protein

ApoE, apolipoprotein E; APP, amyloid precursor protein; CJD, Creutzfeldt–Jakob disease; DRPLA, dentato-rubral and pallido-Luysian atrophy; GSS, Gerstmann–Straussler–Scheinker; SBMA, spinal and bulbar muscular atrophy; SCA, spino-cerebellar ataxia.

Table 1.1 Neurodegenerative diseases: proteins and pathology.
Ross and Poirier, Nat Med 2004.

1.1.1 Protein quality control in neurons.

Neurons are post-mitotic cells, which implies that they are more sensitive to accumulation of aberrant proteins, as they cannot dilute the toxic components during cell division. Hence, neurodegeneration becomes an irreversible process: whatever insult that cannot be handled and controlled would lead to irreparable damage and cell death. To overcome this issue, neurons are equipped with highly specialized protein quality control machineries, that are tightly regulated to avoid the aberrant accumulation of misfolded and aggregated proteins and to maintain the proper homeostasis during the life-time of the individual.

The proteome homeostasis, or proteostasis, refers to a complex network of pathways that ensure the equilibrium among synthesis, folding, post-translational modifications, specific subcellular localization, protein-protein interactions and protein clearance.

In physiological conditions, misfolded proteins are recognized by chaperone molecules that take care of the protein refolding, assembly and disassembly or targeting for degradation (Feldman and Frydman, 2000). When chaperones fail to restore their physiological conformation, aberrant and aggregated proteins are rapidly and efficiently disposed by the protein degradation systems (**Fig. 1.1**).

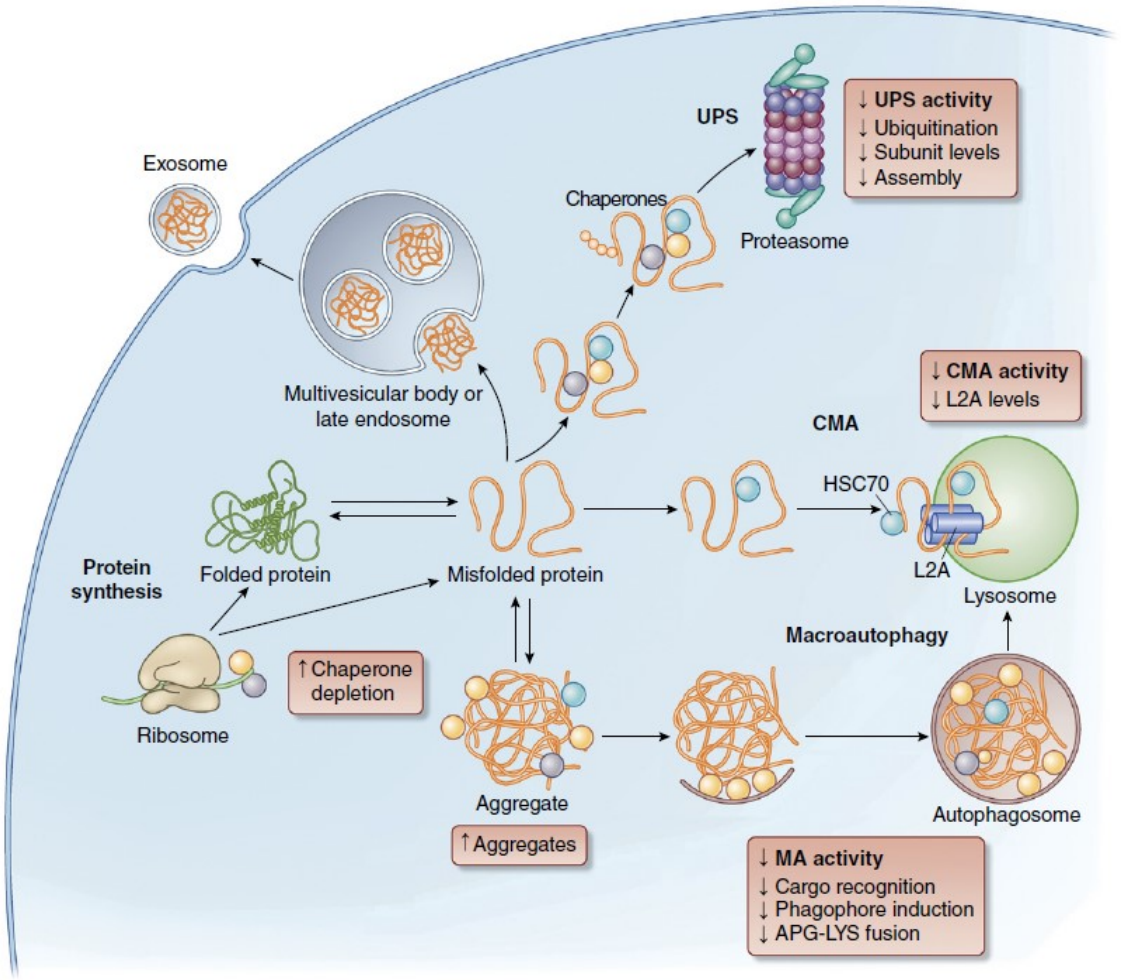

Figure 1.1 The regulation of neuronal proteostasis by different pathways. Chaperone proteins assist in the proper folding of the newly synthetized or handling misfolded proteins. In case the correct conformation is not acquired, the misfolded proteins are targeted to the proteasomal degradation by specific ubiquitin modifications or to the lysosomes by the chaperone-mediated autophagy. Large aggregates are engulfed by the autophagosomes and sent to the lysosomes in the macroautophagy or sorted into the vesicles of the MVBs that further release the exosomes in the extra-cellular space. In the orange boxes, the age-induced alterations on the different steps and components of the protein quality systems are indicated. UPS, ubiquitin-proteasome system, APG-LYS, autophagosome-lysosome; HSC70, heat-shock cognate protein of 70kDa; L2A, lysosome-associated membrane protein type 2A. *Kaushik and Cuervo, Nat Med 2015.*

Briefly, misfolded proteins can be targeted to the proteasomal degradation by specific ubiquitination patterns on their lysines residues (mono-ubiquitination, poly-ubiquitination mediated by K11 and K48 linkages). Alternatively, the degradation is mediated by the autophagic machinery through different pathways. In the macroautophagy, poly-ubiquitination by K63 linkages mediate the recognition of the substrate by the adaptor protein p62, which vehicles the ubiquitinated protein to the auto-phagosomal structures. The mature autophagosome then fuses with the lysosomes, where the acidic pH and the lysosomal proteases digest the content. Otherwise, soluble proteins can be directly sorted into the lumen of the lysosomes by the chaperone-mediated autophagy (CMA). Proteins that contain a specific amino acidic recognition motif KFERQ are identified by the chaperone HSC70, which vehicles the substrate to the LAMP2A receptor on the lysosomal membrane and the translocation in the lysosomal lumen.

Protein aggregates are mainly degraded by the macroautophagy, after being engulfed by the auto-phagosomal structures. Alternatively, they are sorted into intra-luminal vesicles within the multi-vesicular bodies (MVBs), by the invagination of the membrane of late endosomes. The MVBs then either fuse with the lysosomes to degrade their content or with the plasma membrane, releasing the vesicles as exosomes in the extra-cellular space.

A continuous cross-talk among all these pathways, post-translational modifications and involved chaperones and enzymes is essential in maintaining the required protein homeostasis in neurons (Ji and Kwon, 2017). Interestingly, the ubiquitination can be considered a unifying element that links the ubiquitin-proteasome system (UPS) and the selective autophagy. The ubiquitin pathway is extremely complex as it presents various levels of regulation and specificity among the enzymes that conjugate the target proteins with the ubiquitin molecules, in the so called “ubiquitin code” (Rajalingam and Dikic, 2016). Diverse combinations of mono-ubiquitination and poly-ubiquitination can be composed, that correspond to both proteolytic and non-proteolytic functions (Chen and Sun, 2009). Also, high levels (about 60%) of free monomeric ubiquitin are present in neurons, which may serve as a reservoir to mediate rapid responses to cell stimulation, stress and aberrant protein burden (Hallengren et al., 2013).

An additional level of complexity derives from the specialized neuronal compartmentalization among the soma, dendrites, axons and synapses. This also reflects a specific topographic distribution of the protein quality control machineries. In the periphery, the protein clearance is mainly taken care by chaperones, the E3-ubiquitin ligases, the deubiquitinating enzymes (DUBs) and the proteasomes (Wang et al., 2017). Whereas, large protein aggregates and dysfunctional organelles are packaged into autophagic vacuoles and MVBs, to be retrogradely transported to the cell body and degraded by the lysosomes (Hollenbeck, 1993; Larsen and Sulzer, 2002). More recently, the idea of the autophagic process active at the pre-synaptic terminals has been proposed (Vijayan and Verstreken, 2017).

1.1.2 Impaired proteostasis in neurodegenerative diseases.

Ageing represents the greatest challenge for the maintenance of the protein homeostasis in neurons. In **Fig.1.1**, the major age-induced alterations in the different steps and components of the protein quality control pathway are pinpointed. This is reflected by the decreased availability of chaperones and enzymes and the decreased functionality of the protein degradation systems in general (Kaushik and Cuervo, 2015).

Therefore, misfolded proteins progressively build-up, and the aggregation process overcome the degradation capacity in the diseased neurons. Thus, aggregated αSynuclein (αSyn) in PD, Amyloid β and Tau in AD, huntingtin (HTT) in HD, Superoxide Dismutase 1 (SOD1) and TAR DNA-binding protein 43 kDa (TDP-43) in ALS, progressively evolve into β-sheet enriched amyloid structures, that become insoluble and further deposit into intracellular or extracellular inclusions (Ross and Poirier, 2004). Also, these proteins are physiological substrates of both the UPS and the autophagy-lysosomal pathway (ALP) but then acquire a gain-of-toxic function as they affect the proteolytic pathways themselves (Ciechanover and Kwon, 2015). The accumulation of the toxic aggregates triggers a cascade of many other neurotoxic mechanisms, above all mitochondrial dysfunction and oxidative stress, that hinder the neuronal homeostasis at multiple levels.

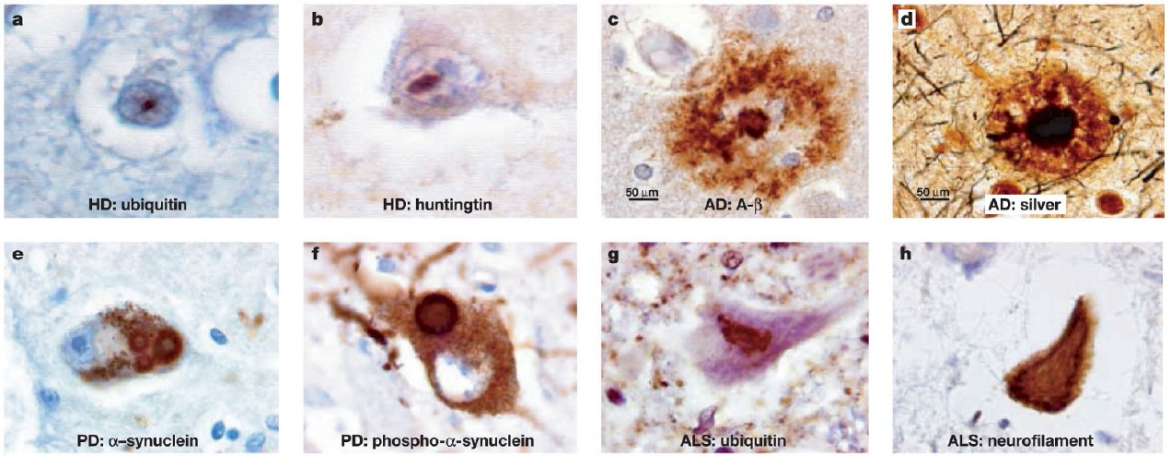

Figure 1.2 Representative images of neuropathological lesions in neurodegenerative diseases. The lesions are characterized by the deposition of abnormal proteins in fibrillar amyloid structures and they can be intranuclear, cytoplasmic or extracellular. In the figures, the lesions were immunolabeled with the indicated antibody, except **d** where the neuritic plaque was silver stained. *Ross and Poirier, Nat Med 2004*.

1.2 The case of Parkinson's Disease.

Among the neurodegenerative disease, PD is known as the most common movement disorder. It currently affects about 1% of the population over 65 years old and more than 4-5% over 80 (Dawson and Dawson, 2002; Tysnes and Storstein, 2017). At present, 6 million people are estimated to be affected by PD, with a higher prevalence in Europe, North America and South America. However, the projections state that this number will double by 2030 (Dorsey et al., 2007).

It was described two centuries ago by the English neurologist James Parkinson in his "*An Essay on the Shaking Palsy*" of 1817, where he characterized a disorder as *paralysis agitans* (later renamed in his honor), with the features and the symptoms that are still used in the diagnosis of PD.

1.2.1 Parkinson's Disease as a complex syndrome.

PD is an age-related and severe neurodegenerative disease with a multi-factorial pathology. Most of the cases are classified as sporadic with an undefined etiology, while only about 15% of cases have genetic causes. Hence, PD is now defined as a syndrome rather than a single distinct disease, due to the high heterogeneity among patients in terms of onset, symptoms, genetics and pathology.

The neurodegeneration process gradually interests different regions of the brain, although it mostly affects the nigrostriatal circuits in the midbrain. This results in the typical motor symptoms, as the nigrostriatal pathway is involved in voluntary movement coordination of the body. Indeed, after the loss of more than 80% of the dopaminergic neurons in the SNpc, parkinsonian syndrome manifests (Sulzer and Surmeier, 2013; Zarow et al., 2003).

The main clinical features are defined as the nigrostriatal T.R.A.P., which stands for:

- Tremor: shaking of the hands while they are at rest;
- Rigidity: muscle stiffness and resistance to movement;
- Akinesia/bradykinesia: difficulty initiating voluntary body movements;
- Postural instability: loss of postural stability that causes falls and a feeling of unsteadiness.

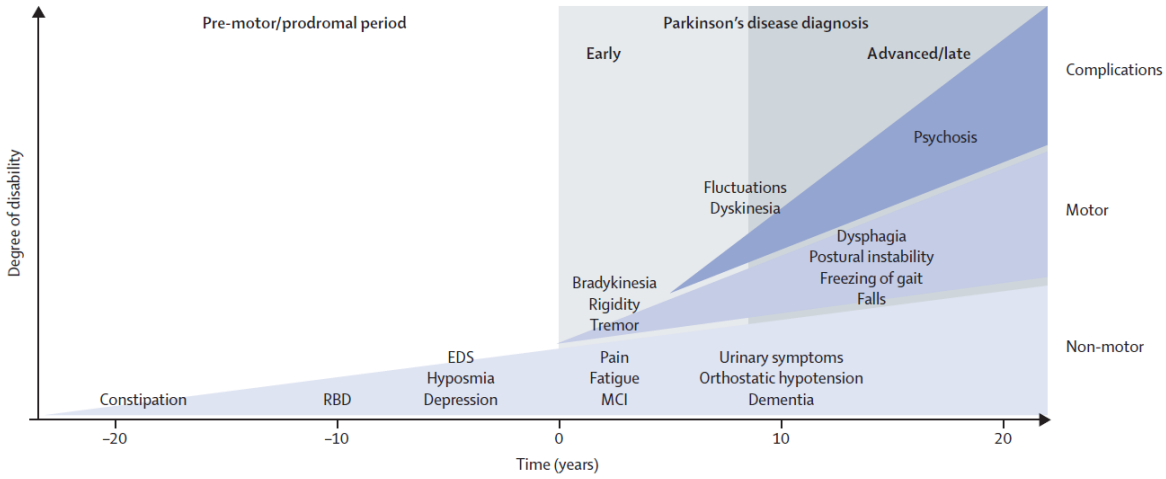

Figure 1.3 Clinical symptoms and time course of Parkinson's Disease progression.
Kalia and Lang, Lancet 2015.

Additional non-motor features are also described in the early stages of the disease, but they are frequently present up to twenty years before the appearance of the motor symptoms and the first diagnosis (**Fig. 1.3**). These include olfactory dysfunction, cognitive impairment, psychiatric symptoms, sleep disorder, autonomic dysfunction (Kalia and Lang, 2015). Along with the disease progression, further complications arise, causing significant disability that cannot be easily managed by the current therapies available.

The diagnosis of PD is usually based on the medical history and evaluation of the patient's symptoms. Several efforts have been made to improve the diagnostic criteria and the identification of specific biomarkers that would allow an early diagnosis. Unfortunately, the currently available therapies, both pharmacological and surgical, are only symptomatic and aim to replace the dopamine (DA) reservoir and action in the nigrostriatal pathway (L-DOPA, DA agonists, inhibitors of DA catabolism). Another line of research is more oriented in finding disease-modifying therapy. The most important is the immunotherapy to target αSyn extra-cellular toxicity by specific antibodies, that are already in clinical trials. Also, the use of compounds that activate the protein degradative pathways to avoid the accumulation of misfolded and aggregated proteins are rising interest in the research community, although they are still in pre-clinical phase.

1.2.2 Etiology and pathogenesis in Parkinson's Disease.

As for the other neurodegenerative diseases, the greatest risk factor for the development of PD is age, followed by gender, ethnicity and environmental factors like pesticide and neurotoxin exposure (i.e. MPTP, rotenone, paraquat), prior head injury and rural living (Kalia and Lang, 2015).

Nevertheless, the contribution from the genetics in the etiology of PD has been widely stated. Since the discovery of mutations in the *SNCA* gene (encoding the αSyn protein) in familial forms of PD (Polymeropoulos et al., 1997), at least 23 loci and 19 disease-causing genes have been identified as cause of monogenic forms of PD with mendelian inheritance (**Table 1.2**), defined as *PARK* loci.

Locus (OMIM)	Location	Full Gene Name Approved by HGNC	HGNC Approved Gene Symbol	Inheritance	Disease onset
PARK1 (168601)	4q22.1	synuclein alpha	*SNCA* (163890)	AD	Early-onset, late-onset*
PARK2 (600116)	6q26	parkin RBR E3 ubiquitin protein ligase	*PRKN* (602544)	AR	Early-onset
PARK3 (602404)	2p13	Parkinson disease 3	*PARK3* (Unclear)	AD	Late-onset
PARK4 (605543)	4q22.1	synuclein alpha	*SNCA* (163890)	AD	Early-onset
PARK5 (613643)	4p13	ubiquitin C-terminal hydrolase L1	*UCHL1* (191342)	AD	Early-onset, late-onset
PARK6 (605909)	1p36	PTEN induced putative kinase 1	*PINK1* (608309)	AR	Early-onset
PARK7 (606324)	1p36.23	parkinsonism associated deglycase	*PARK7* (602533)	AR	Early-onset
PARK8 (607060)	12q12	leucine rich repeat kinase 2	*LRRK2* (609007)	AD	Late-onset
PARK9 (606693)	1p36.13	ATPase 13A2	*ATP13A2* (610513)	AR	Early-onset
PARK10 (606852)	1p32	Parkinson disease 10	*PARK10* (Unclear)	Unclear	Late-onset
PARK11 (607688)	2q37.1	GRB10 interacting GYF protein 2	*GIGYF2* (612003)	AD	Late-onset
PARK12 (300557)	Xq21-q25	Parkinson disease 12	*PARK12* (Unclear)	X-linked inheritance	Late-onset
PARK13 (610297)	2p13.1	HtrA serine peptidase 2	*HTRA2* (606441)	AD	Late-onset, early-onset*
PARK14 (612593)	22q13.1	phospholipase A2 group VI	*PLA2G6* (603604)	AR	Early-onset
PARK15 (260300)	22q12.3	F-box protein 7	*FBXO7* (605648)	AR	Early-onset
PARK16 (613164)	1q32	Parkinson disease 16	*PARK16* (Unclear)	Unclear	Late-onset
PARK17 (614203)	16q11.2	VPS35, retromer complex component	*VPS35* (601501)	AD	Late-onset
PARK18 (614251)	3q27.1	eukaryotic translation initiation factor 4 gamma 1	*EIF4G1* (600495)	AD	Late-onset
PARK19 (615528)	1p31.3	DnaJ heat shock protein family (Hsp40) member C6	*DNAJC6* (608375)	AR	Early-onset
PARK20 (615530)	21q22.1	synaptojanin 1	*SYNJ1* (604297)	AR	Early-onset
PARK21 (616361)	20p13	transmembrane protein 230	*TMEM230* (617019)	AD	Late-onset, early-onset*
PARK22 (616710)	7p11.2	coiled-coil-helix-coiled-coil-helix domain containing 2	*CHCHD2* (616244)	AD	Late-onset, early-onset*
PARK23 (616840)	15q22.2	vacuolar protein sorting 13 homolog C	*VPS13C* (608879)	AR	Early-onset
	11p15.4	RIC3 acetylcholine receptor chaperone	*RIC3* (610509)	AD	Late-onset, early-onset*

HGNC: HUGO Gene Nomenclature Committee, AD: autosomal dominant, AR: autosomal recessive,*: few cases

Table 1.2 Gene locus and disease-causing genes of Parkinson's Disease.
Adapted from *Deng at al., Ageing Res Rev 2018*.

Among them, the genes *SNCA* (point mutations and gene multiplication), Leucine-rich repeat kinase 2 (LRRK2) which encodes for a kinase mainly involved in the regulation of membrane trafficking, *VPS35* which encodes for a protein of the lysosomal pathway, and others mediate autosomal dominant forms of PD; while *Parkin*, *PINK1* and *DJ-1*, all proteins involved in the mitochondria physiology and oxidative stress regulation, are associated with autosomal recessive inheritance. Furthermore, many genetic variants in a high number of loci have been identified as risk factors in sporadic PD. Among them, the most established are variations in *SNCA*, *LRRK2*, *GBA* (β-glucocerebroside) and *MAPT* (Microtubule-associated Protein Tau) genes. Recently, the largest-to-date genome wide association study (GWAS) for PD identified 93 variants in 78 loci as risk factors, which are believed to explain the 26-36% of the heritable risk of PD (Nalls et al., 2019).

A unique aspect of PD is that while the *PARK* loci encode for proteins with diverse physiological functions (sometimes unknown) and different relative abundance in neuronal and non-neuronal cells in the brain, mutations in their sequence have an impact in several molecular pathways that all converge to accumulation of misfolded proteins, mitochondrial dysfunction, oxidative stress (**Fig. 1.4**), frequently observed also in idiopathic PD cases (Schneider and Alcalay, 2017). On this ground, a multiple-hit hypothesis for PD pathogenesis has been put forward, that may explain both similarities and divergences among PD forms (Carvey et al., 2006; Sulzer, 2007). According to this hypothesis, all the risk factors concomitantly affect neuronal homeostasis resulting in progressive degeneration.

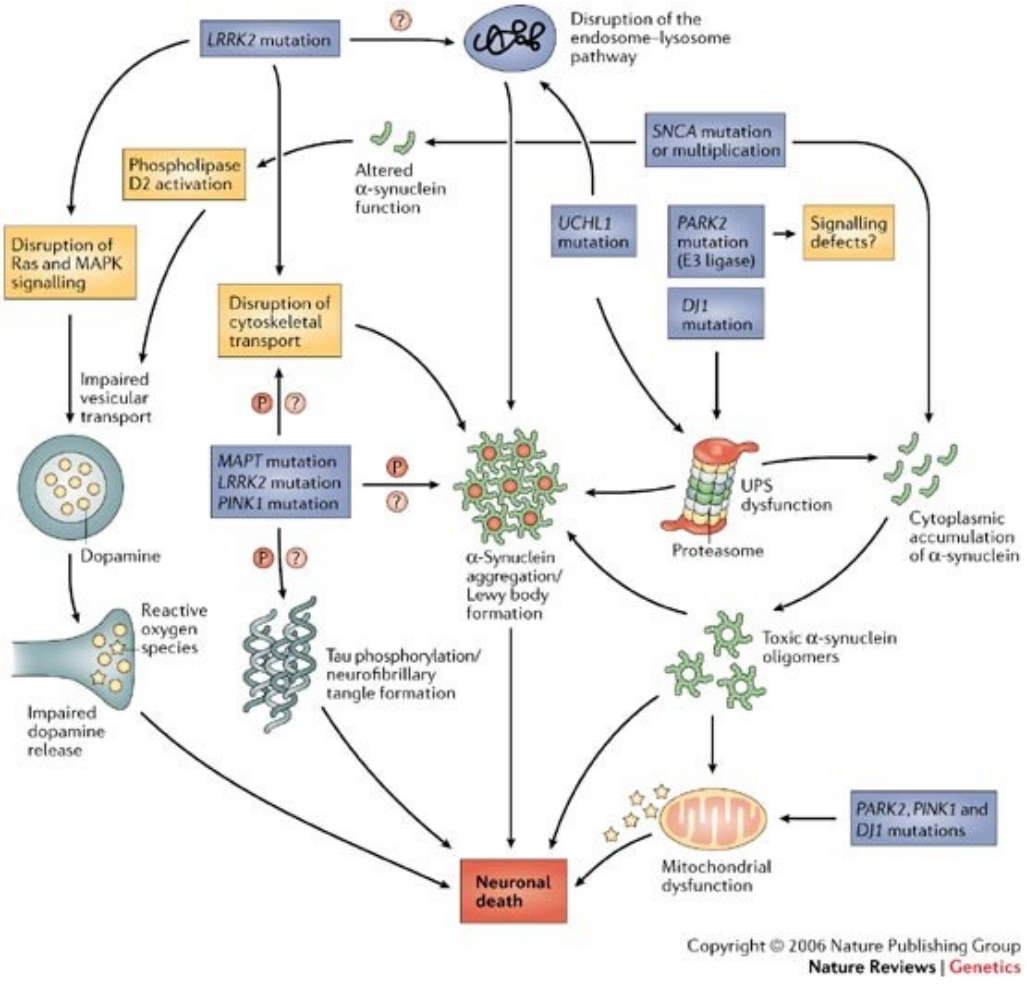

Figure 1.4 Pathways to Parkinson's Disease. The study of the physiological functions and the effects of the mutations on *PARK* loci helps unravelling the cellular pathways that are affected in the pathology. Above all, the accumulation of aggregated αSyn, the impairment of the endo-lysosomal pathway and proteasomal dysfunction; the disruption of the axonal transport; impaired synaptic vesicles trafficking and DA release; oxidative stress and mitochondrial dysfunction. *Farrer, Nat Rev Genet 2006*.

1.2.3 The preferential vulnerability of the nigrostriatal neurons.

One of the main questions that keeps puzzling researchers in the field, is about the identification of the causative factors responsible for the higher susceptibility of the dopaminergic neurons of *Substantia Nigra pars compacta* (SNpc), that leads to the degeneration of their projections to the striatum and further the motor phenotype (**Fig. 1.5**).

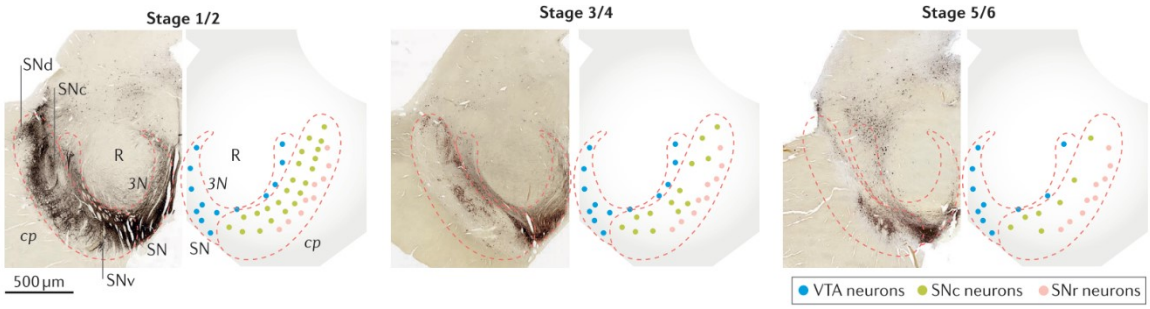

Figure 1.5 Progressive degeneration of SNpc neurons. Transverse sections of the midbrain at different clinical stages of PD. The normal distribution of TH-immunopositive dopaminergic neurons is shown in the left panels, and the pattern is schematized in the right panels. The heavily pigmented neurons of the *Substantia Nigra pars compacta* (SNc, in green) are associated with a greater cell loss compare to the neurons of the ventral-tegmental area (VTA, in blue) and the *Substantia Nigra pars reticulata* (SNr, in pink). Adapted from *Surmeier et al., Nat Rev 2017*.

As Surmeier and colleagues recently reviewed, the analysis of morphological, functional and molecular peculiarities of the SNpc dopaminergic neurons is starting to shed some light on their uniqueness and preferential vulnerability in PD compared to other brain regions, like the neighbor ventral-tegmental area and *Substantia Nigra pars reticulata* (Brichta and Greengard, 2014; Sulzer and Surmeier, 2013; Surmeier et al., 2017a). As main features, SNpc neurons present an intrinsic low calcium buffering capacity and the ability to perform pace-making activity (Surmeier et al., 2017b). This requires a considerable energy demand, which is challenged by the decreased mitochondria supply compared to other neuronal populations (Liang et al., 2007). Interestingly, less anti-oxidant defenses are present in the nigral neurons, resulting in a higher vulnerability oxidative stress caused by mitochondrial dysfunction.

Moreover, the SNpc neurons carry the machinery to metabolize and catabolize DA, the neurotransmitter synthetized and secreted in the nigrostriatal pathway. Indeed, the endotoxicity derived from increasing DA levels, DA oxidation and its reactive catabolites, is recognized as one of the major causes of oxidative stress in PD (Bisaglia et al., 2010, 2013, 2014; Chen et al., 2008; Lotharius and Brundin, 2002).

DA synthesis occurs from tyrosine via a two-steps enzymatic reaction, mediated by the tyrosine hydroxylase (TH) which produces L-DOPA, that is further converted into DA by the aromatic L-amino acid decarboxylase (AADC). Once synthetized, DA is rapidly loaded into synaptic vesicles by the vesicular monoamino transporter type-2 (VMAT2) to store the neurotransmitter into an acidic environment to avoid DA oxidation (Meiser et al., 2013). Hence, DA levels in the cytoplasm are strictly regulated, as an equilibrium among synthesis, synaptic vesicle loading, uptake from the extracellular space and catabolic degradation (Bisaglia et al., 2013).

Recently, an impressive work by Burbulla et al. provided a link between the mitochondrial and lysosomal dysfunctions that underline the degeneration of the SNpc in PD (Burbulla et al., 2017). By using dopaminergic neurons derived from patients with familial and idiopathic PD as model, the authors demonstrated that elevated mitochondrial oxidative stress (i.e. generated by a loss of function in DJ-1, PARK7) induces DA oxidation and relative toxic cascade. Among the consequences, DA oxidation elicits the accumulation of neuromelanin aggregates, impairs the activity of the lysosomal enzyme glucocerebrosidase (GCase), an important PD risk factor, and leads to lysosomal dysfunction. Interestingly, similar observations were found in neurons from patients carrying mutation in other *PARK* loci, specifically mutant parkin, PINK1, LRRK2 and αSyn triplication. Lysosomal dysfunction then results in accumulation of aggregated αSyn, which can in turn affect the functionality of protein degradation systems, leading to defective mitophagy, calcium dyshomeostasis and a noxious feedback loop between mitochondria and lysosomes.

1.3 αSynuclein impaired proteostasis in Parkinson's Disease.

1.3.1 αSynuclein in Lewy Bodies.

αSyn represents a paradigmatic example of misfolded protein accumulation and impaired proteostasis associated with neurodegeneration. The first observation of aggregated αSyn in neurons came out from the analysis of autoptic samples of patients with PD and DLB. In that study by Spillantini et al., the presence of fibrillar aggregates of αSyn were detected by the immunostaining with an antibody against αSyn in structures identified as Lewy Bodies (LB) (Spillantini et al., 1997).

LBs, first described in 1912 by Frederic Lewy in post-mortem PD patients' brains, are defined as spherical eosinophilic cytoplasmic inclusions, with a dense core surrounded by a pale halo 10 nm wide (**Fig. 1.2e-f**). Although αSyn fibrils represent the major constituent of LBs, many other proteins are found, reflecting a general impaired proteostasis in the diseased neurons. The main represented include mediators of protein trafficking, SNARE proteins and pre-synaptic proteins; chaperones i.e. 14-3-3 and HSP70; proteins related to the degradative pathways i.e. p62, proteasome subunits, ubiquitin, ubiquitin-activating enzyme E1; Amyloid β and Tau (Wakabayashi et al., 2013). Also, LBs are highly enriched in lipids, vesicular structures and dysmorphic organelles (Shahmoradian et al., 2019).

The presence of LBs in brain tissues is commonly associated to PD. However, the accumulation and deposition of αSyn amyloid fibrils are observed also in DLB, Multiple System Atrophy (MSA) and Pure Autonomic Failure (PAF), defined collectively as Synucleinopathies. These pathologies differ for both the clinical and pathological points of view, as the LBs lesions are present in different type of cells (i.e. in oligodendrocites in MSA). Also, according to the disease progression, LBs pathology is diffused in various regions of the central nervous system (basal ganglia nuclei, hypothalamus, cortex, cerebellum, olfactory bulb, spinal cord), which led to the formulation of the Braak's hypothesis for staging of the disease (Braak et al., 2003).

1.3.2 αSynuclein physiology.

αSyn is a small protein of 140 amino acids, encoded by the *SNCA* single gene of seven exons, located in chromosome 4q22.1 (Shibasaki et al., 1995). It was first described by Maroteaux in 1988 as a neuron-specific protein localized in the synapses and the nucleus (Maroteaux et al., 1988). Specifically, αSyn accounts for 0.5-1% of the total soluble brain proteins (Iwai et al., 1995) and it is highly concentrated (~40 μM) in pre-synaptic terminals of neurons (Wilhelm et al., 2014).

Structure and conformational states. According to its amino acidic sequence, αSyn primary structure can be divided into three domains (**Fig. 1.6**). The N-terminal domain (residues 1-60) contains five imperfect repeats of eleven amino acids, containing the consensus motif KTKEGV, that confers a propensity to an α-helical folding of this region. The central domain (residues 61-95) was defined the non-amyloid beta component (NAC) as it drives the folding in β-sheet-enriched and aggregation of αSyn in the fibrillar structures that are found in LBs. This segment includes two additional KTKEGV repeats and assists the N-terminus in the αSyn membrane-binding. The C-terminus (residues 96-140) is highly enriched in acidic residues and prolines, providing flexibility to the peptide. This portion is also thought to be the principal protein-protein and protein-small molecules interaction site and modification site by metal ions.

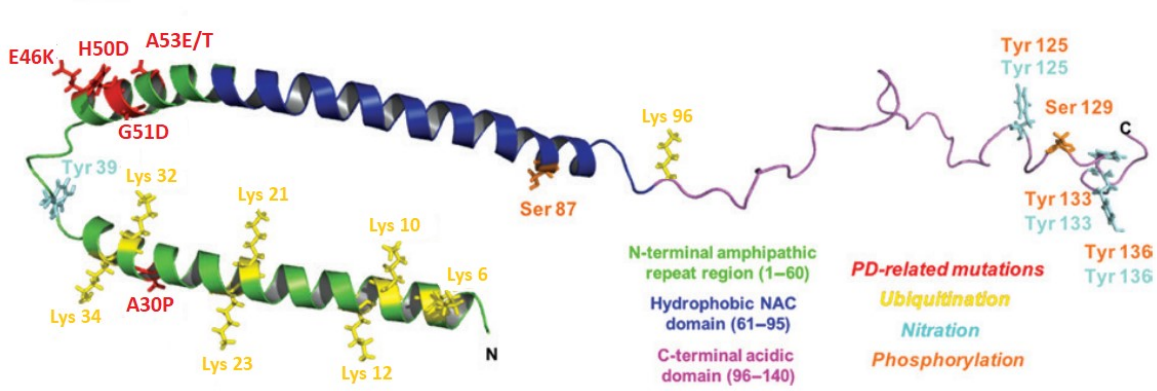

Figure 1.6 αSyn structure, when associated to micelle membrane (PDB: 1XQ8). The N-terminal domain (green) contains KTKEGV repeats where human missense mutations (indicated in red) are associated. The central hydrophobic domain (NAC) is in blue and the C-terminal acidic domain is in purple. Ubiquitination (lys), nitration (tyr) and phosphorylation (ser and tyr) sites are indicated in yellow, pale blue and orange, respectively. Adapted from *Ottolini et al., Biol Chem 2017.*

αSyn is a dynamic protein, in constant equilibrium among different conformers. It is considered a natively unfolded protein when it exists as soluble monomer in the cytoplasm (Breydo et al., 2012). Instead, the N-terminus domain can acquire a partial helical folded state, that is thought to mediate the association of αSyn with negatively-curved membranes like synaptic vesicles, modulating their curvature (Fusco et al., 2018; Middleton and Rhoades, 2010). This is mediated by the many positive-charged lysine residues that drive the interaction with the acidic headgroup of the phospholipids on the membranes. Interestingly, the mutations that are associated with genetic forms of PD (A30P, E46K, H50D, G51D, A53T, A53E) are not randomly distributed, as they map in this specific region (**Fig. 1.6**) and hinder the membrane-binding of αSyn due to their different biochemical properties (Dettmer, 2018). In addition, Burrè and colleagues proposed that αSyn assembles into tetrameric structures when bound to the synaptic vesicles (Burré et al., 2014), even though the exitance of this functional conformation is still under debate (Fauvet et al., 2012).

Function at the synapse. The definition of αSyn physiological function at the pre-synaptic level keeps challenging researchers in the field. αSyn localization on the pre-synaptic vesicles membrane (Boassa et al., 2013) underscores its role in the regulation of the vesicles trafficking and clustering in synaptic vesicle pools (Burre' et al., 2010; Janezic et al., 2013; Vargas et al., 2017). In addition, αSyn was showed to promote the SNARE complex assembly and vesicles docking to the active zone (Burre et al., 2010); more recently, a specific role in promoting the dilation of the exocytotic fusion pore has been demonstrated (Logan et al., 2017). To understand the physiological role of αSyn on synapse architecture, αSyn knock-out and αSyn-overexpressing mouse models have been used. Importantly, both the triple knock-out mouse lacking all three synuclein isoforms (alpha, beta and gamma, to exclude any compensation by the other two isoforms – Syn-TKO) and the αSyn-overexpressing mouse model (αSyn-OVX) display alterations in synapse architecture (Vargas et al., 2017) and in neurotransmitter release (**Fig. 1.7**). In particular, αSyn overexpression results in impaired vesicles clustering with reduced vesicles density at the active zone; fast and incomplete exocytotic fusion

pore dilation and pore closure; consequent decreased DA release in the striatum, weakening the nigrostriatal pathway (Janezic et al., 2013; Logan et al., 2017; Nemani et al., 2010). Conversely, in the Syn-TKO mouse, more pronounced DA release was detected, potentially due to an accumulation of synaptic vesicles in the ready-releasable pool, prolonged exocytotic fusion pore dilation, faster neurotransmitter release and pore closure (Anwar et al., 2011; Logan et al., 2017; Senior et al., 2008). In addition, PD-related mutations affect the tethering among synaptic vesicles and the active zone (Vargas et al., 2017) and negatively modulate the activity of αSyn in the exocytotic events (Logan et al., 2017). Taken together, these observations lead to the concept that although αSyn is not a limiting factor in the synaptic activity, it is essential for maintaining the proper balance in neurotransmitter release and synaptic vesicles distribution.

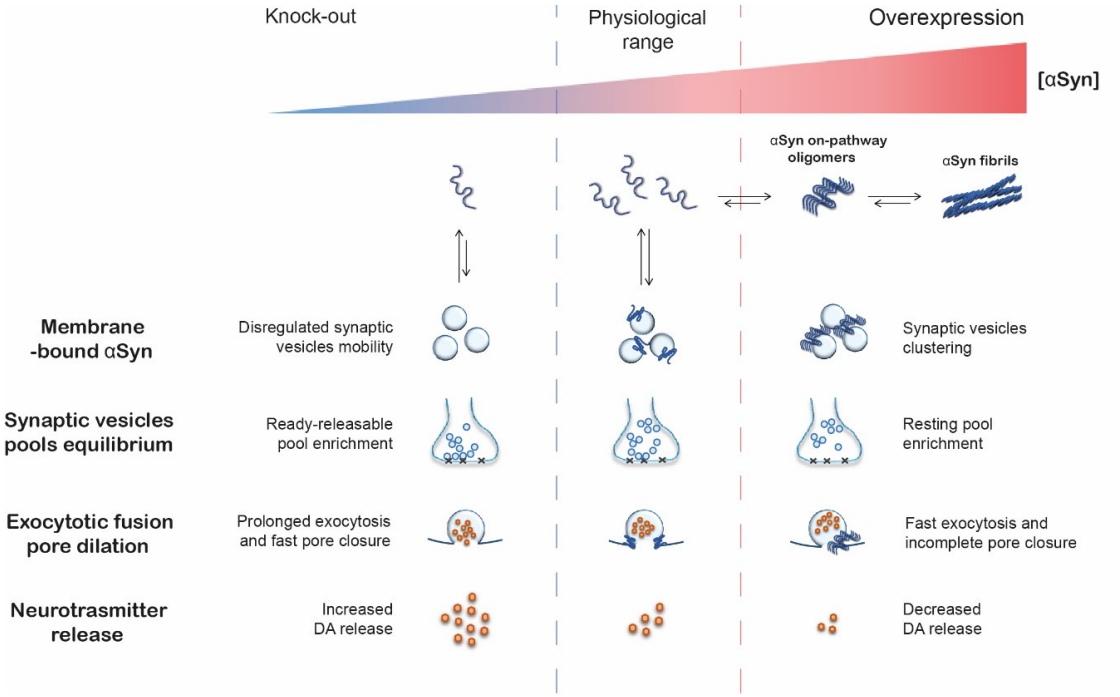

Figure 1.7 Effects of αSyn on synapse functionality. Under physiological conditions, αSyn ensures the correct balance of DA release in the striatum by binding to synaptic vesicles membrane, regulating vesicles mobility and the exocytotic events. However, upon αSyn dyshomeostasis, which includes both αSyn accumulation or its absence, the synaptic vesicles distribution among the different pools and the neurotransmitter release are altered. Adapted from *Masato et al., Mol Neurodegen 2019*.

Clearance. Different proteolytic pathways are involved in αSyn clearance, both intracellular and extracellular (Stefanis et al., 2019). Aside cytosolic proteases i.e. calpain and neurosin (**Fig. 1.8e-f**), intracellular monomeric αSyn is primary degraded by the proteasome by multi-mono-ubiquitination by the E3-ubiquitin ligase SIAH (Rott et al., 2017), by poly-ubiquitination mediated by K48 linkages or though ubiquitin-independent mechanisms (**Fig. 1.8a-b**). Alternatively, monomeric αSyn can be recognized by the chaperone HSC70 on its CMA-recognition motif $_{95}$VKKDQ$_{99}$, that vehicles αSyn to the LAMP2A receptor on the lysosomal membrane (Cuervo et al., 2004) (**Fig. 1.8c**).

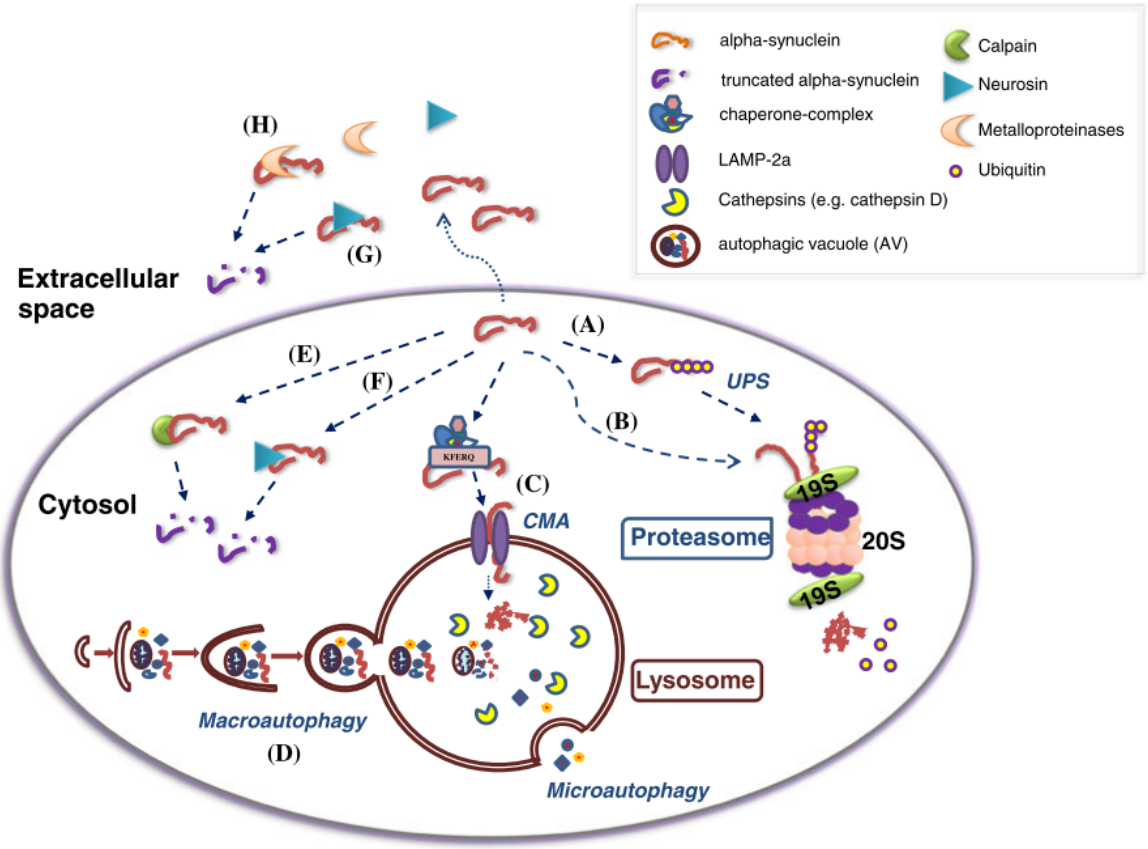

Figure 1.8 Proteolytic pathways implicated in αSyn degradation. Intracellular αSyn can be targeted to the proteasomal degradation by ubiquitin-dependent **(A)** and ubiquitin-independent **(B)** mechanisms or conveyed to the lysosomes by CMA **(C)**. Whereas, aggregated αSyn is mainly disposed by the macroautophagy **(D)**. Alternatively, αSyn can be directly digested by the cytoplasmic proteases i.e. calpain and neurosin **(E,F)**. Finally, αSyn ca be secreted outside the cell where can be degraded by extracellular proteases i.e. neurosin and metalloproteinases **(G, H)**. *Xilouri et al., Mol Neurobiol 2013*.

In the periphery, a fraction of αSyn is likely to be degraded by the proteasome or local proteases. Furthermore, αSyn was also detected within the endo-lysosomal pathway in MVBs (Boassa et al., 2013), that probably mediate the retrograde transport of αSyn to the cell body to be degraded by the lysosomes (**Fig. 1.8d**). Tofaris and colleagues identified the ubiquitin ligase Nedd4 as the most relevant for αSyn ubiquitination, promoting αSyn degradation by the endosomal-lysosomal pathway (Tofaris et al., 2011). Nedd4 recognizes C-terminus of αSyn that contains the required proline-rich motif and synthesized K63-linkages on lysines-21 and -96 of αSyn. This process enhances the degradation of membrane-bound αSyn by the lysosomal pathway, through the recruitment of the endosomal-sorting complex required for transport (ESCRT) that mediates the loading of ubiquitinated proteins into endosomes. Interestingly, K63-linked ubiquitin conjugates are found in LBs, suggesting a PD-related impairment of this pathway (Alexopoulou et al., 2016). Although small soluble oligomers can be digested by the UPS, large oligomeric forms are likely to be degraded by the ALP. Lysosomal cathepsins B, C and L together contribute to the degradation of αSyn within the lysosomes, however their efficiency was found decreased towards αSyn fibrils (McGlinchey and Lee, 2015).

αSyn clearance from neurons also includes the secretion to the extracellular space. This could happen through various proposed mechanisms: by secretory vesicles; by loading into early endosomes with direct secretion to the extracellular space once the recycling endosome fuses with the plasma membrane; finally by incorporation of αSyn into intraluminal vesicles of the MVBs that can be released as exosomal vesicles (Danzer et al., 2012; Fonseca et al., 2015). SUMOylation on lysine 96 and lysine 102 is thought to mediate the sorting of αSyn into extra-cellular vesicles (Kunadt et al., 2015). Once αSyn is released in the extracellular space, it can be digested by extracellular proteases i.e. the neurosin KLK6 o metalloproteinases MMP9 and MMP3 (**Fig. 1.8g-h**). Alternatively, αSyn can be internalized by the surrounding cells by endocytosis, trans-synaptic dissemination and membrane-receptor-mediated access (Lashuel et al., 2013). Notably, this process represents a detrimental pathway of αSyn toxic species transmission from diseased neurons to healthy ones, spreading and accelerating the progression of the pathology and triggering neuroinflammatory responses.

1.3.3 αSynuclein aggregation and neurotoxicity.

αSyn concentration in neurons is strictly regulated as a balance of synthesis, degradation and secretion. However, in Synucleinopathies, several factors can hinder αSyn proteostasis, leading to αSyn accumulation and further aggregation (Lashuel et al., 2013). At the level of expression, duplication and triplication of the *SNCA* gene (associated with hereditary forms of PD), some *SNCA* variations and DNA methylation state result in increased rate of synthesis. On the other hand, failure of protein degradation systems and dysfunctional chaperones decrease the αSyn turnover and the degradation of small oligomers. Finally, additional factors promote αSyn aggregation i.e. *SNCA* mutations, oxidative stress, certain post-translational modifications (PTMs), toxins exposure i.e. 1-methyl-4-phenyl-1,2,3,6-tetrahydropyridine (MPTP) or rotenone, and association with lipids or metal ions. In other words, αSyn concentration and sequence drive the aggregation process: whatever element modulates the two aspects, it can be considered a causative factor of αSyn aggregation.

The unique property of αSyn is that, while highly dynamic in its natively unfolded monomeric state, it can acquire various conformational states (Alam et al., 2019). Under certain conditions, αSyn monomers can assemble in dimer, trimer, tetramer and small oligomers (**Fig. 1.9**). These can serve as nucleating seeds for the evolution into on-pathway oligomers, proto-fibrillar structures and finally mature amyloid fibrils that are found in LBs. Interestingly, diverse types of αSyn fibrils were identified, with different biochemical and structural features, levels of toxicity and propagation properties. These observations were translated into the idea of different strains of αSyn fibrils that might reflect the differences in the progression and cell types affected in the various Synucleinopathies (Bousset et al., 2013; Peelaerts et al., 2018). Otherwise, the small oligomers can follow an off-fibrillar pathway generating aggregates with heterogenous structure, dimension and stability. The real issue is that the study of the αSyn aggregation process in test tubes can be easily modeled, while the detection and identification of specific oligomeric and fibrillar structure *in vivo* in tissues are a totally different game, that urge for the development of innovative experimental tools to shed some light into the topic.

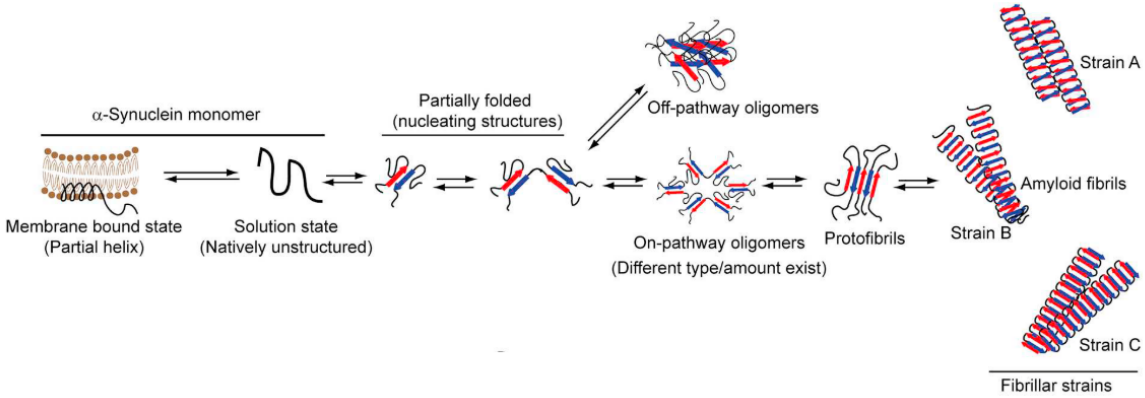

Figure 1.9 Aggregation pathways of αSyn. αSyn monomer exists in two states, i.e., solution (natively unstructured) and membrane-bound state (partially helical conformation). In pathological conditions, the monomeric αSyn converts into oligomers (on-pathway or off-pathway) via partially folded nucleating structures. The on-pathway oligomers eventually convert into highly ordered cross-β-sheet amyloid fibrils whereas the fate of the off-pathway oligomers is unclear. Under different assembly/solution conditions, native proteins can form different types of amyloid fibrils, i.e., fibrillar strains. Adapted from *Mehra et al., BBA 2019*.

It is reasonable to think that a fraction of αSyn monomers constantly assemble into oligomers, that are rapidly degraded by the proteolytic machineries. Until the oligomer concentration increases up to a threshold above which the cell cannot deal with them. Thus, the accumulation of αSyn aggregates in the cells results in the gain-of-toxicity feature we mentioned before, affecting several cellular pathways prior to cell death (Wong and Krainc, 2017).

The main important neurotoxic effects are related to alterations in the structural components of the cells, i.e. disruption of cytoskeleton network, alterations of the plasma membrane integrity and pore formation on membrane of organelles, that might induce calcium dyshomeostasis, releasing of lysosomal enzymes and dysregulation of synaptic transmission. Second, accumulation of αSyn toxic species results in endoplasmic reticulum (ER) stress and impairment of the protein degradation pathways at different levels (Xilouri et al., 2013). Finally, complex I inhibition and mitochondria dysfunction appear to be strongly correlated with αSyn-induced toxicity. In **Fig. 1.10** additional details on the cellular pathways that are affected by αSyn toxicity are reported.

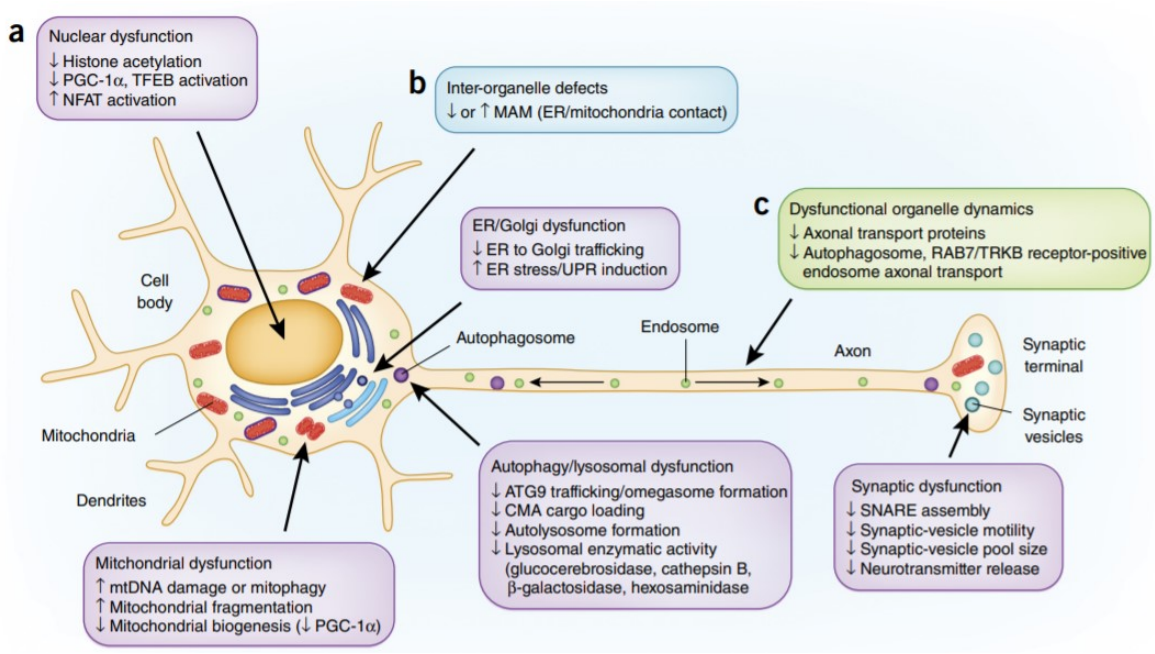

Figure 1.10 Pathways implicated in α-synuclein toxicity: Organelle dysfunction (**a**, purple boxes), defects in inter-organelle contacts (**b**, blue box) and dysfunctional organelle dynamics (**c**, green box). Adapted from *Wong and Krainc, Nat Med 2017*.

1.3.4 The synergy between αSynuclein and dopamine.

Taken together, the preferential loss of SNpc dopaminergic neurons and the deleterious accumulation of aggregated αSyn in the surviving ones posed the question whether DA and αSyn could synergistically act to cause the degeneration of these specific neuronal population. Humorously, αSyn and DA were recently defined the “Bonnie and Clyde in Parkinson’s Disease” (Roy, 2017).

This nickname derived from years of studies that pointed out the tight interplay between αSyn and DA at the pre-synaptic terminals of SNpc neurons. Indeed, αSyn has been demonstrated to modulate the DA pathway, in terms of negative regulation and inhibition of TH and AADC enzymes (Perez et al., 2002; Tehranian et al., 2006) and altered distribution of the DA transporter (DAT) on the plasma membrane (Bellucci et al., 2011).

Importantly, increasing levels of oxidized DA at the synapse were demonstrated to generate αSyn spherical oligomers that are not able to evolve into fibrils (Conway et al., 2001; Mazzulli et al., 2006; Norris et al., 2005). These oligomers have a non-covalent nature and result from the interaction of oxidized DA and dopachrome with the peptide sequence $_{125}$YEMPS$_{129}$ at the C-terminus of αSyn (Norris et al., 2005). Of note, the DA-induced αSyn oligomers were showed to impair several cellular processes i.e. disruption of cytoskeletal organization, alteration in membrane permeability, impairment of the synaptic vesicles trafficking and SNARE complex assembly, mitochondrial dysfunction and inhibition of the CMA degradative pathway (Cuervo et al., 2004).

A recently published paper provided *in vivo* evidence of the DA-induced αSyn oligomers formation in the nigrostriatal neurons (Mor et al., 2017). Specifically, the authors injected a viral vector encoding for the mutant TH with enhanced catalytic activity (TH-RREE, which leads to an increase of DA production) into the SNpc of the transgenic mouse αSyn-A53T. After 5 months post-injection, they observed a motor phenotype and significant synapse loss prior to soma degeneration, modelling the dying-back hypothesis of dopaminergic neurons in PD. These observations were correlated with the presence of αSyn soluble and toxic oligomers, potentially induced by the enhanced oxidized catechols in the neurons.

Certainly, DA autooxidation to quinones generates high levels of reactive oxygen species (ROS) that affect many cellular processes and modulate αSyn propensity to aggregation. However, the DA-induced αSyn aggregates present a non-covalent nature, mainly induced by conformational changes in the C-terminus (Mazzulli et al., 2006; Mor et al., 2017). Although *in vitro* incubation of recombinant αSyn results in oligomers generation, the precise chemistry of a DA modification of αSyn *in vivo* has not been defined yet.

1.4 Impaired dopamine metabolism in the pathogenesis of Parkinson's Disease.

In the last decades, the concept that a dyshomeostasis of catechol amines may lead to endotoxicity has been extended to DA catabolites, as many studies revealed altered levels of DA metabolites in PD models and autoptic samples (Goldstein et al., 2014). Among the several metabolites monitored, attention was focused on 3,4-dihydroxyphenylacetaldehyde (DOPAL), a toxic DA catabolite.

1.4.1 The neurotoxic action of 3,4-dihydroxyphanylacetaldehyde (DOPAL).

As showed in **Fig. 1.11**, DA catabolism starts with the oxidative deamination, a reaction mediated by the mitochondrial monoamine oxidase (MAO), which also generates H_2O_2 and ammonia. The resulting product, DOPAL, is further metabolized either to 3,4-dihydroxyphenylacetic acid (DOPAC) and 3,4-dihydroxyphenylethanol (DOPET) by aldehyde dehydrogenase (ALDH) or by aldehyde/aldose reductase (ALR/AR), respectively.

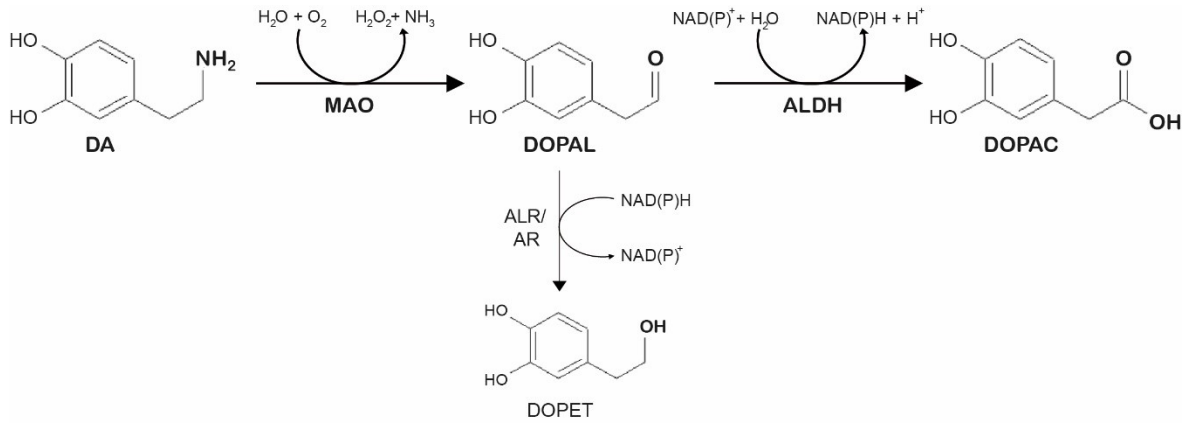

Fig. 1.11 DA catabolism. In dopaminergic neurons, DA catabolism starts with deamination by MAO, resulting in DOPAL production. The aldehyde moiety is then converted into the carboxyl group of DOPAC by ALDHs and, to less extent, into the hydroxyl group of DOPET by ALR/ARs (thinner arrow). *Masato et al. Mol Neurodegen 2019.*

The unique feature of DOPAL is its high reactivity due to the presence of the two mojeties in its molecular structure. These are the aldehyde and catechol, which can both contribute to DOPAL reactivity toward proteins (**Fig. 1.12**). The first one targets mainly primary amines and the second thiols (Follmer et al., 2015; Rees et al., 2009). Of interest, the two moieties do not act independently of each other, being that the oxidation of the catechol ring enhances the Schiff base reaction between the aldehyde moiety of DOPAL and primary amines (Anderson et al., 2016). Also, the oxidation of the catechol is required for the addiction of thiols to the aromatic ring. This implies that DOPAL is prone to covalently modify amino acid residues i.e. lysines and cysteines. Hence, DOPAL reactivity is estimated to be several order of magnitude higher than the other catecholamines (Anderson et al., 2011).

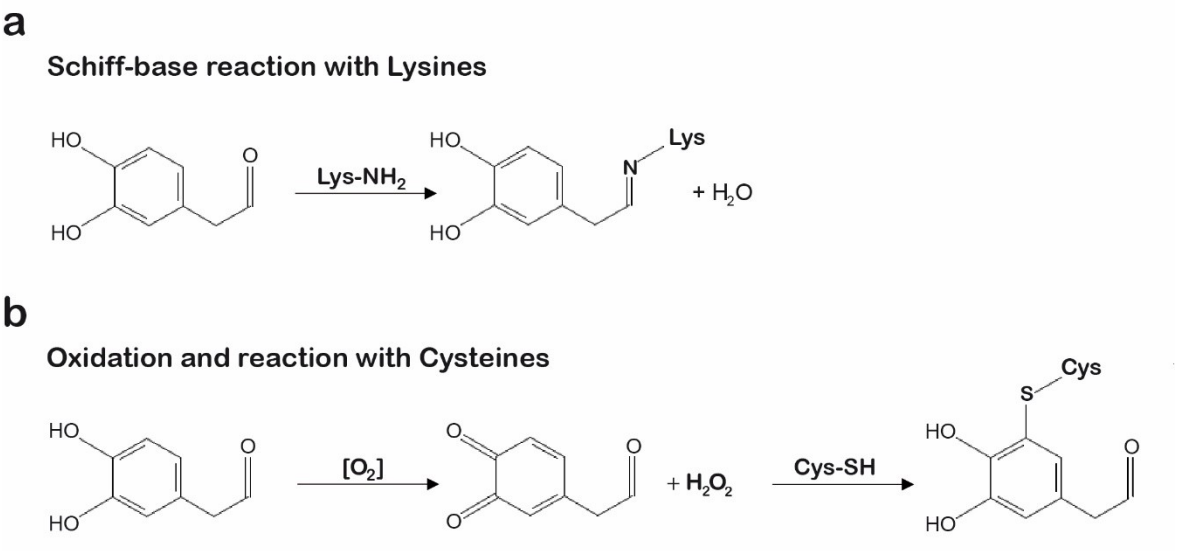

Fig. 1.12 DOPAL reactivity. (a) DOPAL addiction to lysines is the result of a Schiff-base reaction between the aldehyde and the primary amine of the lysine's lateral chain, with the release of a molecule of water. **(b)** In oxidative conditions, the catechol group has the tendency to auto-oxidation, with production of quinones and oxygen radical species. Also, the oxidized catechol is reactive towards the thiols of cysteines. *Masato et al. Mol Neurodegen 2019.*

Although DOPAL is a physiological intermediate in DA catabolism, it resulted to be an endogenous neurotoxin (Mattammal et al., 1995). DOPAL concentration in SNpc dopaminergic neurons has been estimated to be around 2-3 μM but concentrations higher than physiological (>6 μM) have been described as a threshold to elicit cytotoxic effects in various cell lines (Marchitti et al., 2007).

Afterwards, the work of Burke et al. in 2003 provided substantial evidence of DOPAL neurotoxicity *in vivo* (Burke et al., 2003). DOPAL injection in rat nigral dopaminergic neurons resulted in detrimental neuronal loss, more pronounced than that induced by administration of DA or its metabolites (DOPAC, DOPET, HVA). More recently, a *post mortem* study on sporadic PD patients' brains revealed DOPAL build-up relative to DA in the putamen of PD subjects compared to healthy controls (Goldstein et al., 2011).

Based on its high reactivity, DOPAL is believed to trigger several neurotoxic mechanisms. First of all, DOPAL modification of lysines and cysteines leads to protein cross-linking and resulting aggregation, as demonstrated by several *in vitro* and cellular studies (Burke et al., 2008; Follmer et al., 2015; Plotegher et al., 2017; Rees et al., 2007, 2009). Also, lysine residues are often target of functional PTMs (i.e. ubiquitination, SUMOylation, acetylation) that are important in the regulation of protein clearance and subcellular localization. Hence, the DOPAL modification of the same residues might compete with these PTMs, leading to protein burden and impaired signaling pathways.

Second, protein modification by DOPAL has deleterious outcomes in terms of enzyme activity. To generalize, any enzyme with an accessible functional cysteines or lysines in the active site is susceptible to inactivation by DOPAL, with important upshots on the metabolic pathways of interest. For instance, a proteomic study on PC6-3 cells identified TH as target of DOPAL, leading to 80-95% inhibition of TH activity (Mexas et al., 2011).

Finally, additonal down-stream effects have been highlighted, above all oxidative stress, mitochondrial dysfunction and cell death. The direct participation of DOPAL in oxidative stress has been investigated, as DOPAL catechol group has a propensity to auto-oxidase to semiquinone radicals and ortho-quinones similar to DA (Anderson et al., 2011). The resulting ROS production (**Fig. 1.12**) is expected to exacerbate the oxidative stress in neurons, leading to DNA damages, protein cross-linking and lipid peroxidation. Also, DOPAL quinones could covalently modify mitochondrial proteins, possibly affecting mitochondrial physiology (Van Laar et al., 2009).

In this frame, these seminal observations prompted the formulation of the *Catecholaldehyde Hypothesis*, which underscores the key role of DOPAL in the molecular mechanisms responsible for SNpc degeneration in PD (Burke et al., 2003; Lamensdorf et al., 2000; Li et al., 2001; Mattammal et al., 1995; Panneton et al., 2010; Rees et al., 2007).

1.4.2 Evidence of DOPAL build-up in Parkinson's Disease.

Several evidence in the literature support the hypothesis of DOPAL anomalous accumulation and consequent neurotoxicity. The primary site of DOPAL build-up is the pre-synaptic terminals, where the critical hubs are the dysfunction of DA storage in synaptic vesicles, as it would result in cytosolic DA build-up, raised DOPAL production and increased risk of catechol oxidation. Moreover, DOPAL accumulation might be due to an increased rate of DA deamination by MAO and decreased DOPAL catabolism.

DA leakage in the cytoplasm. Some PD-related conditions are thought to compromise a proper DA storage in pre-synaptic vesicles. A key player is the DA transporter VMAT2, whose activity was found to be reduced of about 90% when assessed in DA storage vesicles isolated from post mortem PD patients' SNpc compared to healthy subjects (Pifl et al., 2014). Also, two polymorphisms in the promoter of the *Vmat2* gene (rs363371 and rs363324) were recently associated to PD in a case-control study in an Italian subpopulation (Brighina et al., 2013). Consistently, a mouse model expressing only 5% of the functional VMAT2 displayed nigrostriatal degeneration and increased αSyn immunoreactivity in SNpc (Caudle et al., 2007). Similar results were obtained in rodent models of PD after administration of reserpine, a drug used against high blood pressure and a well-known VMAT2 inhibitor (Fernandez et al., 2006; Leão et al., 2015; Santos et al., 2013). On the other hand, a PD-linked mutant form of LRRK2-G2019S has been shown to affect synaptic vesicles endocytosis in patient-derived dopaminergic neurons, leading to cytoplasmic accumulation of DA and related oxidized catechols, as well as increasing levels of αSyn (Nguyen and Krainc, 2018).

Increased DA catabolism. Being such a reactive molecule, cytoplasmic excess of DA has to be rapidly metabolized by MAO-A and MAO-B. According to different studies, MAOs expression exponentially increases with age and it can be upregulated, for instance, in neuroinflammation (Camell et al., 2017; Chamoli et al., 2018; Nicotra et al., 2004). In PD, MAO-B activity was shown to be enhanced (Damier et al., 1996). In addition, some variants of *Mao-B* gene encode for an hyperactive form of the enzyme and are associated to PD cases (Kurth et al., 1993; Sampaio et al., 2018; Sun et al., 2014). Coherently, a mouse model with an inducible overexpression of MAO-B in astrocytes recapitulates many features of parkinsonian phenotype i.e. dopaminergic neuronal loss, oxidative stress, motor phenotype, αSyn aggregation and neuroinflammation (Mallajosyula et al., 2008).

Decreased DOPAL detoxification. In SNpc dopaminergic neurons, DOPAL degradation primary occurs by oxidation of the aldehyde into a carboxyl group by ALDH (**Fig. 1.11**) (Marchitti et al., 2007). In dopaminergic neurons of SNpc, only two ALDH isoenzymes are expressed: the cytosolic ALDH1A1 and the mitochondrial ALDH2. In **Table 1.3**, the main features of both enzymes are summarized, in terms of expression and preferential substrates. In addition, the main evidence that suggests their role as downstream target as well as contributors in PD pathogenesis are listed (Masato et al., 2019).

Briefly, studies on post-mortem PD patients' brains revealed a marked decreased of the ALDH1A1 enzymes in the SNpc, both at the transcriptomic and protein expression levels (Galter et al., 2003; Grünblatt and Riederer, 2016; Mandel et al., 2007; Werner et al., 2008). These observations were also supported by the study on transgenic mouse models carrying the PD-related mutations A53T on αSyn and the G2019S on LRRK2, where an age-dependent decline of ALDH1A1 expression and the transcription factor Nurr1, which regulates the *Aldh* gene expression, were detected (Lin et al., 2012; Liu et al., 2015). Also, ALDH1A1 activity is thought to be hindered in PD-related conditions. For example, aldehydes like 4-hydroxynonenal (4-HNE) and malondialdehyde (MDA) that derive from lipid peroxidation induced by oxidative stress, strongly bind to the catalytic site of ALDHs and inhibit their activity (Florang et al., 2007; Jinsmaa et al., 2009; Rees et al., 2007).

		ALDH1A1	ALDH2
	Tissue expression	Brain, eye lens, retina, lung, liver, kidney, testis *(Marchitti et al., 2008)*	Liver, kidney, heart, lung, brain *(Marchitti et al., 2008)*
	Subcellular localization	Cytosol *(Cai et al., 2014; Liu et al., 2014; McCaffery and Dräger, 1994)*	Mitochondrial matrix *(Marchitti et al., 2008)*
	Substrates	- Retinaldehyde (k_m <0.1µM) *(Yoshida et al., 1992)* - DOPAL (k_m 0.4µM) *(Ambroziak and Pietruszko, 1991; MacKerell et al., 1986; Marchitti et al., 2007)* - 4-HNE (k_m 4.8µM *(Xiao et al., 2009)*; 17.9µM *(King and Holmes, 1997)*) - MDA (k_m 3.5 µM *(Xiao et al., 2009);* 114.4µM *(Manzer et al., 2003)*) - Y-aminobutyraldehyde (800µM) *(Ambroziak and Pietruszko, 1987)*	- Acetaldehyde (k_m <1µM) *(Klyosov et al., 1996)* - DOPAL (k_m 1µM) *(MacKerell and Pietruszko, 1987)* - 4-HNE and MDA *(Mitchell and Petersen, 1987; Reichard et al., 2000; Vasiliou et al., 2004)* - Y-aminobutyraldehyde (500µM) *(Ambroziak and Pietruszko, 1987)*
PD-related	**Genetic variants**	N.A.	- Haplotype: rs737280; rs968529; rs16941667; rs16941669; rs9971942 (California) *(Fitzmaurice et al., 2014)* - Haplotype: rs4767944; rs441; rs671 (China) *(Zhang et al., 2015)* - rs671 SNP (China) *(Zhao et al., 2016)*
	Expression levels	**Reduced mRNA levels:** - TH-positive neurons in PD patients' brain *(Galter et al., 2003; Grünblatt and Riederer, 2016)* - transgenic A53T mouse striatum *(Lin et al., 2012)* **Decreased protein levels:** - PD patients' brain *(Mandel et al., 2007; Werner et al., 2008)* -LRRK2-G2019S knock-in mouse DA neurons *(Liu et al., 2015)*	N.A.
	Enzyme inhibition	**Epidemiological studies:** - traces of *Dieldrin* in tissues of exposed PD patients *(Corrigan et al., 1998)* - *Benomyl* exposure correlates with PD risk *(Fitzmaurice et al., 2013)* ***In vitro*:** - 4-HNE and MDA *(Florang et al., 2007; Jinsmaa et al., 2009)* - DOPAL (>5µM) *(Florang et al., 2007; MacKerell and Pietruszko, 1987)* - *Benomyl (Fitzmaurice et al., 2013)* **Cellular models of ALDH inhibition:** - rat purified synaptosomes treated with 4-HNE and MDA *(Rees et al., 2007)* - SH-SY5Y cells treated with *Disulfiram (Legros et al., 2004)* - Neurons from *Daidzin* administered hamster *(Rooke et al., 2000)* - PC6-3 cells treated with *Dieldrin* (*Doorn et al., 2014)* - primary neurons and SK-N-MC cells treated with *Benomyl (Fitzmaurice et al., 2013)*	
	***In vivo* models**	**Genetic models:** - A53T/*Aldh1a1*$^{-/-}$mouse *(Liu et al., 2014)* - *Aldh1a1*$^{-/-}$/*Aldh2*$^{-/-}$ mouse *(Wey et al., 2012)* - *Aldh1a1*$^{-/-}$/*Gpx*$^{-/-}$ mouse *(Bai et al., 2017)* **Toxin-based models:** - *Benomyl* intraperitoneally administered mouse *(Casida et al., 2014)* - *Benomyl* exposed zebrafish embryos *(Fitzmaurice et al., 2013)* - *Ziram* exposed zebrafish embryos *(Lulla et al., 2016)*	

Table 1.3 Comparison between ALDH1A1 and ALDH2, in terms of expression, biochemistry and PD-related aspects. Adapted from *Masato et al., Mol Neurodegen 2019*.

Also, many *in vitro* and cellular studies highlighted how the exposure to certain drugs like the anti-alcohol abuse Disulfiram and pesticides i.e. Benomyl, Dieldrin, Ziram results in ALDHs inhibition. This mechanism was confirmed by an epidemiological study in California, which associated the exposure to the pesticide Benomyl with increased risk to develop PD (Fitzmaurice et al., 2013). Moreover, some variants and haplotypes on the ALDH2 gene were associated with PD (Fitzmaurice et al., 2014; Zhang et al., 2015; Zhao et al., 2016), although the *Aldh* genes have not been reported to date in GWAS of PD (Nalls et al., 2019). Finally, the development of both genetic mouse models and toxin-based mouse and zebrafish models contributed in modelling the role of DOPAL in driving the degeneration of dopaminergic neurons of SNpc in PD. Among them, the double-knock out mouse for both ALDHs (*Aldh1a1*$^{-/-}$/*Aldh2*$^{-/-}$) displays an age-dependent motor phenotype, correlated by a significant increase in striatal DOPAL and 4-HNE (Wey et al., 2012).

1.4.3 αSynuclein as a preferential target of DOPAL reactivity.

Starting from the observed reactivity of DOPAL aldehyde against primary amines of lysine residues, some groups proposed that the catechol-induced αSyn oligomerization was effectively triggered by DOPAL modification on αSyn lysines. A pivotal study by Burke et al. in 2008 demonstrated that *in vitro* DOPAL incubation with αSyn monomers triggers a dose-dependent protein aggregation. Similarly, SDS-resistant aggregates of αSyn were detected in lysates from SH-SY5Y cells after administration of DOPAL in the medium. The process was observed also *in vivo* upon direct DOPAL injection into rat SNpc, which resulted in dopaminergic neuron loss and accumulation of αSyn high molecular weight species (Burke et al., 2008).

It is reasonable to think that αSyn represents a preferential target of DOPAL reactivity for at least three reasons. First, lysine accounts for 10.7% of αSyn sequence, which is higher than the average value (around 5%) of the lysine fraction in synaptic proteins (Plotegher and Bubacco, 2016). Second, αSyn is highly abundant at pre-synaptic terminals where also DOPAL is produced by MAO

enzymes on the outer mitochondrial membrane (Meiser et al., 2013). Third, when in the soluble monomeric state, αSyn is a natural unfolded protein with good accessibility to all its lysine residues, making any potential chemical modification more likely.

Since the results showed by Burke and co-workers, other groups provided further insights in DOPAL-dependent αSyn aggregation process. Inhibition of DA uptake into synaptic vesicles by reserpine administration to dopaminergic PC-12 cells, induced DA cytosolic build-up with consequent cytotoxic accumulation of DOPAL and induction of αSyn oligomerization (Goldstein et al., 2012). Furthermore, redox active metal ions i.e. Cu, Fe, Mn, whose levels are increased in parkinsonian SNpc (Dexter et al., 1989), were shown to accelerate DOPAL-induced αSyn oligomerization in PC12 cells (Jinsmaa et al., 2014). On the same ground, *in vitro* assays revealed a modulating effect of N-terminal acetylation and familial mutations on DOPAL-induced αSyn oligomerization (Lima et al., 2018). Also, a transgenic mouse model for the A53T pathogenic form of αSyn and knock-out for the cytosolic ALDH1A1 revealed a significant increase in accumulation of αSyn aggregates modified by catechols, isolated by the amino-phenylboronic acid resin (Liu et al., 2014).

Interestingly, very recent publications pinpointed how DOPAL, rather than DA, covalently modifies αSyn and exacerbates its oligomerization. This is supported by the chemical properties of the molecules involved: in oxidative conditions, the quinone form of DA is covalently modify cysteine residues of proteins (Van Laar et al., 2009; LaVoie et al., 2005), except αSyn doesn’t have any cysteine in its sequence. For instance, the incubation of BSA with 6-OHDA (6-hydroxydopamine) which contains several cysteines resulted in protein aggregation, whereas αSyn was showed not to be modified by quinones in SH-SY5Y (Farzam et al., 2019). Also, in the last paper by Jinsmaa et al., a nIRF assay demonstrated that αSyn monomers and oligomers are modified only by DOPAL, which eventually oxidizes in its quinone form (Jinsmaa et al., 2019).

Interestingly, the study by Follmer and colleagues in 2015 identified by mass spectrometry the lysine residues of αSyn that seem to be preferentially modified

by DOPAL upon in vitro incubation, mainly located at the lysine-enriched N-terminus of αSyn (Follmer et al., 2015). Coherently, independent experiments from our group revealed overlapping results *in vitro*, but with the observation of additional modification sites involving lysine residues in the C-terminal domain upon formation of the αSyn-DOPAL adduct within cells. Moreover, *in vitro* analysis revealed that DOPAL triggers αSyn aggregation leading to annular-shaped off-pathway aggregates, which do not convert to fibrils (Plotegher et al., 2017).

Hence, in the review article we recently published, we proposed a mechanism accounting for the degeneration of the dopaminergic synapse, which is based on the observed functional effects of the αSyn-DOPAL interplay (**Fig. 1.13**). An increased level of DOPAL at presynaptic sites promotes the covalent modification of αSyn and DOPAL-αSyn monomers exhibit reduced affinity for membrane binding (Follmer et al., 2015). Indeed, most of the lysines in the αSyn sequence are within the amino acid repeats containing the consensus motif KTKEGV, which drives the transition to the alpha-helical conformation of αSyn N-terminus and the association to synaptic vesicles membranes (Fusco et al., 2018). DOPAL modification of these residues dramatically alters αSyn biochemical and biophysical properties, increasing its hydrophobicity at the expense of the positive charges. Thus, reducing the membrane-bound fraction of αSyn, DOPAL shifts the equilibrium toward an increased fraction of cytoplasmic αSyn-DOPAL, thus exacerbating αSyn aggregation.

This has also a functional implication in the synapse physiology, as DOPAL induces a redistribution of the synaptic vesicles among the vesicles pools, with more vesicles clustered in the resting pool at the expense of the ready-releasable pool (Plotegher et al., 2017). In addition, we proposed that DOPAL-modified αSyn oligomers might be able to form aggregated oligomers that permeabilize the membrane of synaptic vesicles, thus inducing the release of DA in the cytoplasm, that will be in turn metabolized by MAO into more DOPAL (Plotegher et al., 2017). Taken together, all these events would establish a self-amplifying toxicity loop, which leads to synaptic degeneration. In addition, a very recent study highlighted a potential role for the activity of asparagine endopeptidase (AEP). AEP is reported to be highly activated in PD patients' brain where it can generate a truncated form

of αSyn (Zhang et al., 2017). Interestingly, the resulting N103-truncated αSyn was shown to stimulate MAO-B activity, leading to increased rate of DOPAL production. Not only, DOPAL itself was observed to interact with and stimulate AEP, establishing an additional trail in the vicious cycle described above (Kang et al., 2018).

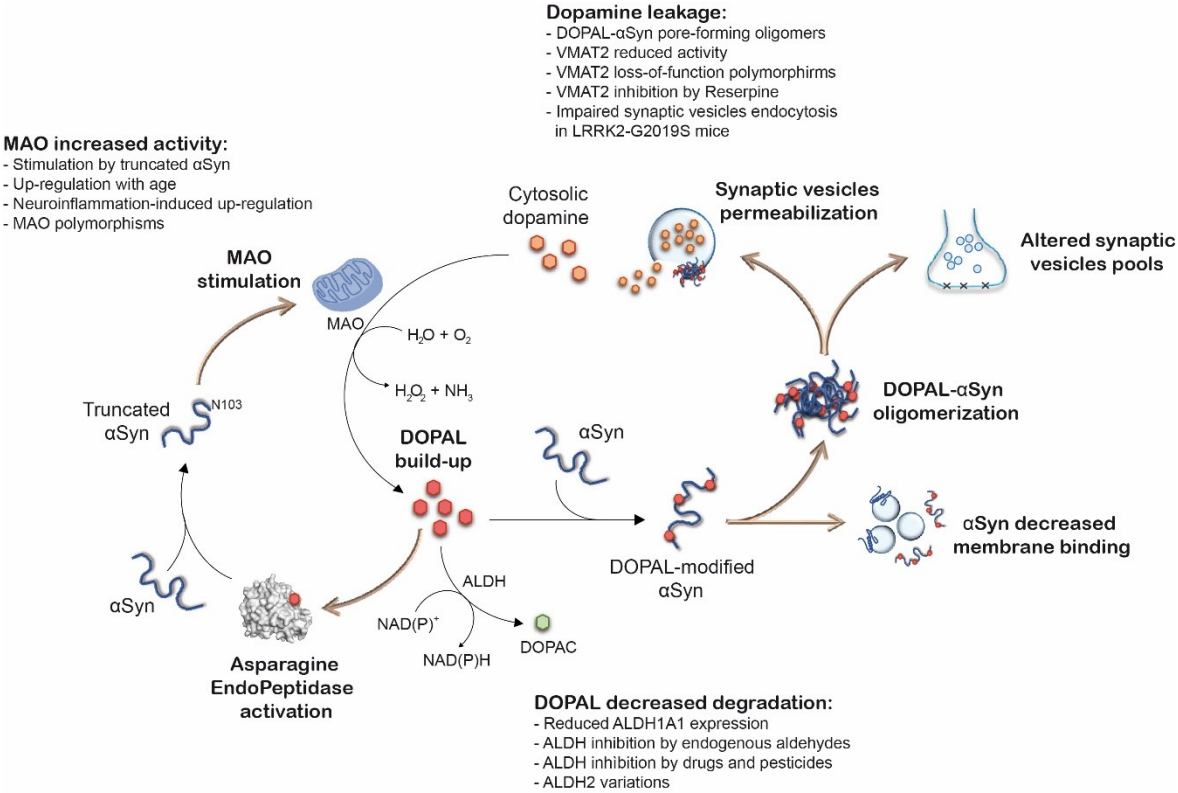

Figure 1.13. Potential interplay between DOPAL and αSynuclein at pre-synaptic terminals and determinants of DOPAL accumulation. DOPAL accumulation at the pre-synaptic terminals covalently modifies αSyn lysines, reducing αSyn affinity for membrane binding and resulting in synaptic vesicles pools redistribution. αSyn-DOPAL oligomers accumulate and permeabilize synaptic vesicles membrane, leading to cytosolic DA release, which is further metabolized into DOPAL by MAO. Also, DOPAL activates AEP (PDB: 4aw9, in the figure), which cleaves αSyn at N103. Truncated αSyn is more prone to aggregation and stimulates MAO activity. Hence, the result is a positive loop that self amplifies, leading to αSyn aggregation and synapse degeneration. In the figure, the black thin arrows indicate the chemical reactions, while the thicker ones highlight the cellular processes. Among the factors that could lead to DOPAL build-up, the critical hubs are the dysfunction of DA storage in synaptic vesicles, increased rate of DA degradation by MAO and decreased DOPAL detoxification by ALDHs. For each point, the evidences are listed in the figure. *Masato et al., Mol Neurodegen 2019*.

2. AIM OF THE PROJECT.

2.1 Investigating the DOPAL-induced impairment of αSynuclein and cellular proteostasis as molecular mechanism to enhance neuronal vulnerability in Parkinson's disease.

Several studies outlined a precise connection among the neurotoxicity induced by DA oxidation, mitochondrial and lysosomal dysfunction and αSyn impaired proteostasis (Burbulla et al., 2017; Mor et al., 2017). However, in the review article we recently published, we proposed the idea that the neurotoxic effects that have been attributed to DA so far, should be reconsidered to include the even more reactive DOPAL. In which, the synergy between the catechol and the aldehyde moieties of DOPAL is likely to increase exponentially the detrimental consequences of an impaired DA regulation.

In a previous paper, we demonstrated a functional consequence of DOPAL build-up at the pre-synaptic region (Plotegher et al., 2017). Specifically, DOPAL was showed to affect the synaptic vesicles pools in primary neuronal cultures, increasing the number of vesicles in the resting pool at the expense of the ready-releasable pool. DOPAL treatment in both primary neurons and neuroblastoma-derived BE(2)-M17 cells induced αSyn aggregation to form SDS-resistant oligomers. Also, DOPAL-αSyn oligomers generate larger annular-shaped species that can act as pore on vesicles, resulting in DA leakage into the cytoplasm.

Aiming to the molecular details of the DOPAL action on αSyn, our LC-MS data on αSyn purified from cells treated with DOPAL, revealed the lysine residues that are preferentially modified by DOPAL (**Table 2.1**), in a Schiff-base reaction between the primary amine and the aldehyde of DOPAL. These data underscore the specific chemistry between DOPAL and αSyn, which is unique compared to other catechols. Furthermore, when compared to other aldehydes i.e. 4-HNE and methylglyoxal (Almandoz-Gil et al., 2017; Vicente Miranda et al., 2017) that were showed to modify αSyn lysines, DOPAL acquires higher significance due to its

confinement within SNpc dopaminergic neurons. Interestingly, most of the lysines that are modified by these aldehydes are also ubiquitination, SUMOylation and acetylation sites (**Table 2.1**), suggesting a potential competition of DOPAL with functional PTMs that regulate αSyn subcellular localization, degradation and secretion (Plotegher and Bubacco, 2016).

αSyn lysines	K6	K10	K12	K21	K23	K32	K34	K43	K45	K58	K60	K80	K96	K97	K102	
Plotegher et al., 2017	D	D	D		D	D	D	D		D	D		D	D		*In vivo* cells
Follmer et al., 2015		D	D	D	D	D	D	D								*In vitro*
Vicente-Miranda et al., 2017	M	M	M	M	M	M	M	M	M							Thy1 mouse brain
Almandoz-Gil et al., 2017	H		H				H		H		H					*In vitro*
Schmid et al., 2013	U	U				U	U	U					U			*In vitro*
Schmid et al., 2013			U	U	U											In LBs
Popovic et al., 2014	U	U	U	U	U	U	U		U				U			In LBs
Kunadt et al., 2015													S		S	*In vivo* cells
Lundbay et al., 2012	A						A		A				A			Rat brain

Table 2.1 αSyn lysines modification by aldehydes and functional PTMs. For each lysines, the modification identified in the cited papers are mapped, together with the relative source of αSyn. In the table, the aldehydes are indicated as D: DOPAL, M: methylglyoxal, H: 4-HNE; the functional PTMs are U: ubiquitination, S: SUMOylation, A: acetylation.

Here, one central issue we aimed to evaluate is the impact of DOPAL on αSyn proteostasis in a wider perspective, aside from its ability to trigger αSyn oligomerization. By coupling imaging data with biochemical studies, we are providing evidence of the DOPAL-dependent αSyn redistribution in the neuronal compartments, from the peripheral terminals, to the axonal trafficking and the soma. These observations were also correlated to the assessment of αSyn affected clearance in the presence of DOPAL.

On the other hand, the accumulation of aggregated αSyn is known to affect protein degradation systems functionality. At the same time, the general DOPAL reactivity against accessible primary amines and thiols might affect the clearance of a broader range of proteins. Thus, we investigated the consequences of DOPAL build-up in whole cellular homeostasis, discussing the possibility of a synergistic action of αSyn and DOPAL in neurotoxic events.

Finally, while looking for a strategy to rescue the DOPAL effects in cells as a proof-of-concept of our paradigm, we started to explore the use of biguanidine molecules as DOPAL scavengers. Interestingly, compounds as aminoguanidine and metformin, that are already in the clinical practice, potentially represent a translational approach in the light of the *Catecholaldehyde hypothesis.*

3. MATERIALS AND METHODS.

3.1 Cell cultures, transfection and treatments.

3.1.1 Rat primary cortical neurons.

Cortical neurons were dissociated by papain from postnatal day 2 (P2) Sprague-Dawley rats, as previously reported (Boassa et al., 2013). At day-*in-vitro* 0 (DIV0), 5 million of isolated primary neurons were transfected with 5 µg of DNA by electroporation using an Amaxa Nucleofection Device (Lonza). The transfected neurons were plated on imaging dishes (P35G-0-14-C, MatTek Corporation) that were coated on the same day with poly-D-lysine (Sigma-Aldrich). Neurons were cultured in Neurobasal A medium (Life Technologies) supplemented with 1X B27 Supplements (Life Technologies), 2 mM GlutaMAX (Life Technologies), 20 U/mL penicillin, and 50mg/mL streptomycin (Life Technologies) for 10-15 days prior to imaging, refreshing half medium every couple of days. All animal procedures were approved by the Institutional Animal Care and Use Committee of UC San Diego.

3.1.2 BE(2)-M17 cell line.

Neuroblastoma-derived BE(2)-M17 cells (ATCC CRL-2267) were cultured in 50% of Dulbecco's modified Eagle's medium (DMEM, Life Technologies) and 50% of F-12 Nutrient Mix (Life Technologies), supplemented with 10% v/v FBS and 1% Penicillin/Streptomycin (Life technologies). Cells were maintained at 37°C, 90% humidity and 5% CO_2 and cultured in T-75 or T-175 flasks (Sarstedt). For cell culture maintenance and cell plating for experiments, cells were washed with Dulbecco's Phosphate Buffer Saline (DPBS, Life technologies) and detached with 1:25 dilution of trypsin 2.5% v/v (Life technologies). For experiments, cells were plated in 6-wells or 12-wells for western blot analysis and protein pull-down assays; for immunocytochemistry experiments, cells were plated on 12 mm-glass coverslips previously coated with poly-L-lysine (Sigma-Aldrich) in 24-wells plates (Sarstedt); for cell viability assays, in 96-wells plates. Before transfection and treatments, cells were maintained in complete medium supplemented with 10 µM retinoic acid (RA, Sigma-Aldrich) over weekend. When at 80% of confluency, cells

were transiently transfected using Lipofectamine 2000 (Invitrogen) with a DNA(µg): Lipofectamine(µl) ratio of 1:2. Cells were transfected with 3 µg of DNA/well when plated in 6-wells plates, 1.5 µg of DNA/well in 12-wells plates and 0.75 µg of DNA/well in 24-wells plates. Transfection mix was prepared in OptiMEM (Reduced serum medium, Life technologies) and added to cell medium; after 4 hrs, half medium was replaced with fresh growth medium. Cells were then treated and processed 24-to-72 hrs post transfection.

3.1.3 Constructs for neuron and cell transfection.

The following constructs for primary neuronal culture and stable cell line transfection were kindly provided by Dr. Daniela Boassa (UCSD): pCAGGS.αSyn-miniSOG full-length; pCAGGS.αSyn-TimeSTAMP-YFP-miniSOG; pCAGGS.Tau-TimeSTAMP-YFP-miniSOG; pCAGGS.αSyn-mKeima. In the αSyn-split-miniSOG experiments, primary rat cortical neurons were co-transduced at DIV 7 with the pCAGGS.αSyn-miniSOG$_{1-94}$(Fragment A) and pCAGGS.αSyn-miniSOG-Jα$_{95-140}$(Fragment B) constructs, expressed in lentiviral vectors HIV1.

The pHT2.αSyn(WT)-HaloTag was generated by cloning the αSyn-encoding sequence into the pHT2 vector previously described (Wang et al., 2008). The K96R and S129A variants were generated using the Quick-Change II site-directed mutagenesis kit (Stratagene) according to manufacturer's instructions, using the following primers:

αSyn(K96R) FOR: 5' CATTGGCTTTGTCAGAAAGGACCAGTTGG 3'
αSyn(K96R) REV: 5' CCAACTGGTCCTTTCTGACAAAGCCAGTG 3'

αSyn(S129A) FOR: 5' GCTTATGAAATGCCTGCAGAGGAAGGGTATC 3'
αSyn(S129A) REV: 5' GATACCCTTCCTCTGCAGGCATTTCATAAGC 3'

The DNA plasmids were amplified and purified from *E. coli* DH5α, previously transformed. Plasmids were extracted using the NucleoBond® Xtra Maxi Plus kit (Macherey-Nagel), following the manufacturer's instructions for high copy plasmids. Once DNA plasmids were eluted, absorbance at 260 nm was measured at the spectrophotometer and their concentration was determined in µg/µl.

3.1.4 Cell treatments.

The compounds that were used for the pharmacological treatments are listed in **Table 3.1**, with relative source, identifier (catalog number) and details of use, i.e. vehicle in which each compound was dissolved and final concentration of use.

Compound	Source	Catalog #	Vehicle	Final concentration
DOPAL	Bisaglia's laboratory	N.A.	H_2O	100 µM*
BILN-2061	ACME Synthetic Chemical	Custom made	DMSO	1 µM
Nocodazole	Millipore	487928	DMSO	5 µg/ml
Retinoic acid	Sigma-Aldrich	R2625	DMSO	10 µM
HaloTag® biotin ligand	Promega	G8281	DMSO	5 µM
HaloTag JF570 ligand	Lavis's laboratory (HHMI Janelia Labs)	N.A.	DMSO	3 µM
Cycloheximide	Santa Cruz Biotech.	Sc-3508	DMSO	50 µg/ml
MG132	Santa Cruz Biotech.	Sc-201270	DMSO	20 µM
Chloroquine	Sigma-Aldrich	C6628	H_2O	10 µM
Bafilomycin A1	Millipore	196000	DMSO	20 nM
Aminoguanidine hydrochloride	Sigma-Aldrich	396494	PBS	100 µM*
Metformin hydrochloride	Sigma-Aldrich	PHR1084	PBS	50 mM*

Table 3.1 List of compounds used for cell treatments. (* unless indicated otherwise)

Treatments in rat primary cortical neurons were performed in complete medium at DIV10-15 for the time frame specified for each experiment in the Result section. In most cases, in BE(2)-M17 cells the chemicals were administrated in OptiMEM. The time frame of each treatment is specified in the Result section.

Starvation was induced by an overnight incubation with a serum-free medium, followed by 2 hrs in Hank's Balanced Salt Solution (HBSS, Life Technologies).

3.2 DOPAL synthesis and quality control.

DOPAL was produced in collaboration with Prof. Bisaglia's laboratory (UNIPD), following the method by Fellman (Fellman, 1958) (**Fig. 3.1**), with slight modification. Briefly, 6 ml 85% ortho-phosphoric acid preheated to 125 °C in an oil bath were added to 400 mg of (±)-epinephrine hydrochloride (E4642, Sigma-Aldrich) in a 2-dram glass scintillation vial. The epinephrine-acid mixture was then vortexed until dissolved, re-submerged in the oil bath until it changes from yellow to a dark orange color and then added to 60 ml of H_2O in a separating funnel. The water mixture was then extracted with 20 ml of ethyl acetate twice, followed by three washes with 10 ml of H_2O of the combined organic layers. Finally, the de-acidified organic layer was evaporated with a stream of N_2 directly into 1 ml of H_2O.

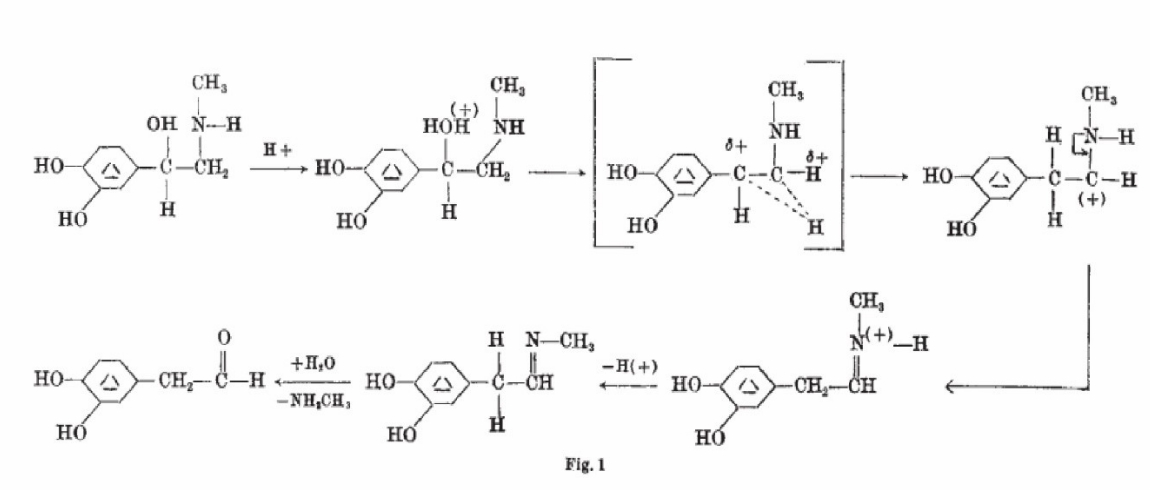

Figure 3.1 DOPAL synthesis. Schematic representation of the chemical reactions that drive the conversion of epinephrine to DOPAL (Fellman, 1958).

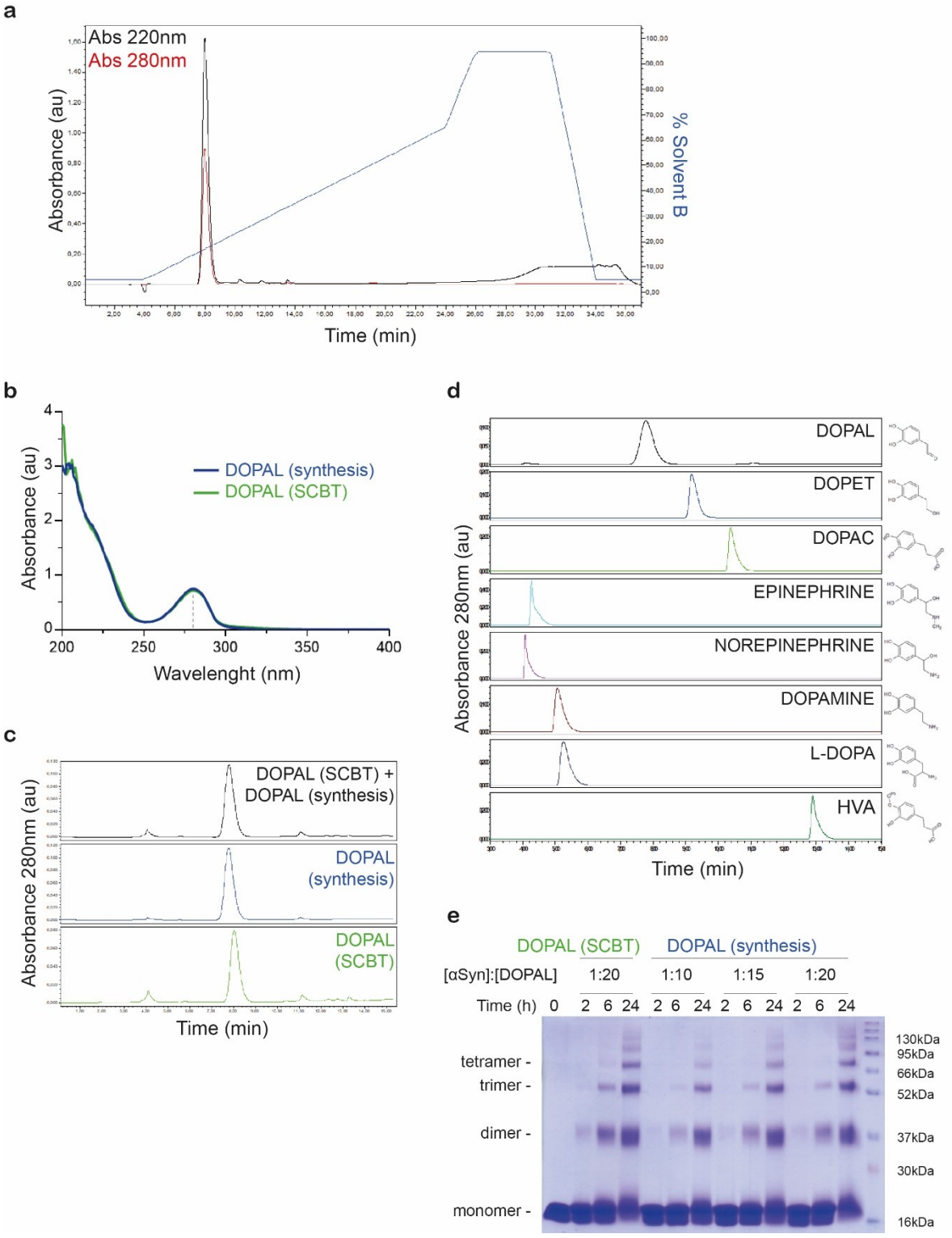

Figure 3.2 DOPAL quality control. (a) RP-HPLC of the synthetized DOPAL with the absorbance profile at 220 nm in black, the absorbance profile at 280 nm in red and the solvent B gradient in blue. The details of the experimental conditions for the RP-HPLC are listed in the main text. **(b)** Overlap between the absorbance spectra of the synthetized DOPAL (in blue) and the DOPAL purchased from SCBT (in green). The dotted line indicates the absorbance peak at 280 nm. **(c)** Comparison of the RP-HPLC retention time and profile of same amount among the synthetized DOPAL (in blue), the DOPAL by SCBT (in green) and the combination of the two (in black). *continues*

Figure 3.2 *continues* **(d)** Comparison of the RP-HPLC retention time and profile among the synthetized DOPAL and other catechols. The chemical structures of the different molecules are indicated on the right side of the corresponding RP-HPLC profile. **(e)** SDS-Page of recombinant αSyn oligomers stained with Comassie blue after *in vitro* incubation for increasing time period (2-6-24 h) with DOPAL by SCBT or synthetized DOPAL, in increasing molar ratio with αSyn (1:10, 1:15, 1:20).

The resulting DOPAL solution was then analyzed for identity, concentration and purity. DOPAL quality was analyzed by reverse-phase HPLC (RP-HPLC) on a Phenomenex Jupiter column (300 Å/5 µm, 250 mm × 4.6 mm), using linear gradients of solvent B in eluent A (A: 0.1% TFA in H_2O, B: 0.08% TFA in acetonitrile; gradient: 5% B to 65% B in 20 minutes) (**Fig. 3.2a**). Purity was calculated about 95%, based on the absorbance measured at 280 nm. As showed in **Fig. 3.2b**, the absorbance spectrum of the synthetized DOPAL perfectly overlaps with the spectrum of DOPAL purchased from Santa Cruz Biotechnology (SCBT; sc-391117) that was used as a reference, with an absorbance peak at 280 nm due to the aromatic ring of the catechol group. DOPAL concentration was determined by assuming the same extinction molar coefficient of DA and L-DOPA (ε_{280nm} = 2.63 cm^{-1} mM^{-1}), resulting in about 20 mg of synthetized DOPAL from 400 mg of epinephrine (yield ~5%). Consistently, the retention time of the synthetized DOPAL (8 mins) corresponds to the peak of the DOPAL by SCBT. Also, the HPLC analysis of a mixture of the two DOPAL preparations, co-eluted in a single peak at the very same retention time (**Fig. 3.2c**). Moreover, DOPAL has a unique retention time and profile in RP-HPLC compared to other catechols (DOPET, DOPAC, epinephrine, norepinephrine, DA, L-DOPA, HVA), confirming the efficacy of the synthesis protocol in converting the epinephrine into DOPAL and in removing the reaction sub-products (**Fig. 3.2d**). Finally, the reactivity of the synthetized DOPAL was assessed by analyzing its ability to trigger the recombinant αSyn oligomerization *in vitro* (see "3.3 *In vitro* DOPAL-induced αSynuclein oligomerization.") compared to the DOPAL by SCBT (**Fig. 3.2e**).

All chemicals and reagents used during the synthesis and the chromatographic analysis were purchased at Sigma-Aldrich.

3.3 *In vitro* DOPAL-induced αSynuclein oligomerization.

3.3.1 Recombinant αSynuclein purification.

Recombinant human αSyn was purified as previously described (Tessari et al., 2008). Briefly, the αSyn gene was cloned in pET-28a plasmid (Novagen) and expressed in *Escherichia coli* BL21(DE3) strain. Bacteria were grown to an OD600nm of 0.3–0.4 and induced with 0.1 mM isopropyl b-D-1-thiogalactopyranoside (IPTG). After 5 hrs, cells were collected by centrifugation and recombinant proteins recovered from the periplasm by osmotic shock. Subsequently, the periplasmic homogenate was boiled for 15 min and the soluble αSyn-containing fraction was subjected to a two-step (35 and 55%) ammonium sulfate precipitation. The pellet was then resuspended, extensively dialyzed against 20 mM Tris–HCl, pH 8.0, loaded into a 6 ml Resource Q column (Amersham Biosciences) and eluted with a 0–500 mM gradient of NaCl. Proteins were then dialyzed against water, lyophilized and stored at -20°C.

3.3.2 DOPAL-induced αSynuclein oligomerization.

Recombinant αSyn was resuspended in PBS and concentration was quantified by measuring the absorbance at 276 nm and using the ε_{276nm} = 5800 cm^{-1} $mM^{-1.}$ DOPAL-αSyn oligomers were produced by incubating 20 μM of recombinant αSyn (dissolved in PBS) with 600 μM of DOPAL (1:20 of molar ratio, unless indicated otherwise) in PBS. The solution was incubated overnight (or for the time indicated in the specific experiment) in agitation at 160 rpm at 25°C. Alternatively, to test the activity of biguanidine molecules as aldehyde scavengers, αSyn and DOPAL were incubated overnight with increasing amounts of Aminoguanidine (AG) in DOPAL : AG ratios of 1:0.5, 1:1, 1:2, 1:5 or 1:10 in PBS. Proteins were then separated by SDS-Page into a gradient 4-20% SDS-Page gel (BioRad) together with a molecular weight ladder (Prestained Protein SHARPMASS VII 6,5-270kDa, EuroClone). Proteins were stained with Comassie brilliant blue, followed destaining with10% isopropanol, 10%acetic acid.

For the limited proteolysis by Proteinase K (PK), monomeric αSyn and DOPAL-αSyn oligomers were incubated with 50 nM PK in PBS. Sample aliquots were collected at different time-points (0-10-20-30 minutes), followed by SDS-Page.

3.4 Imaging techniques.

3.4.1 Immunocytochemistry and confocal microscopy.

For immunocytochemistry (ICC), both rat primary cortical neurons and BE(2)-M17 cells were fixed using 4% paraformaldehyde (PFA, Electron Microscopy Science) in PBS pH 7.4 for 20 minutes at room temperature. Cells were permeabilized in PBS-0.3% Triton-X for 5 minutes, followed by a 1 hr saturation step in blocking buffer (1% Bovine serum Albumin (BSA) Fraction V, 2% Normal Donkey serum (for ICC in neurons) or FBS (for ICC in BE(2)-M17 cells), 0.1% Triton-X and 50 mM Glycine in PBS). Incubations with primary and secondary antibodies (listed in **Table 3.2**) were performed in working solution (1:5 dilution of the blocking buffer) for 1 hr at room temperature, following both incubations with three washing steps in working solution.

Primary Antibody	Source	Catalog #	Dilution
Mouse anti-Bassoon	Abcam	ab82958	1:500
Rabbit anti-p62	Abcam	ab109012	1:200
Mouse anti-pSer129 81/A	Biolegend	825702	1:500

Secondary Antibody	Source	Catalog #	Dilution
Goat anti mouse-Alexa Fluor 568	Invitrogen	A11004	1:200
Goat anti rabbit-Alexa Fluor 488	Invitrogen	A11034	1:200
Goat anti rabbit-Alexa Fluor 633	Invitrogen	A21071	1:200

Table 3.2 List of antibodies used in immunocytochemistry experiments.

For the immunolabeling with the anti-pSer129 antibody in BE(2)-M17 cells, an antigen retrieval step was introduced before saturation. Specifically, fixed cells were incubated with a citrate buffer (10 mM sodium citrate, 0.05% Tween-20, pH 6) at 90°C for 5 minutes or at 70°C for 10 minutes. For the nuclei staining, BE(2)-M17 cells were incubated with Hoechst 33258 (Invitrogen, 1:2000 dilution in PBS) for 5 minutes. Before coverslips mounting on glass slides, cells were washed three times in PBS and rinsed in distilled water. Confocal immunofluorescence images were acquired on the Olympus Fluoview 1000 laser scanning confocal microscope using a 60X oil immersion objective and the Zeiss LSM700 laser scanning confocal microscope using a 63X oil immersion objective.

3.4.2 Live Cell Time-Lapse imaging.

For live time-lapse recordings, neurons overexpressing the αSyn-TimeSTAMP-YFP-miniSOG or the Tau-TimeSTAMP-YFP-miniSOG constructs received a pulse with 1 μM BILN-2061 inhibitor for 4 hrs in complete medium at 37°C. After three washes in HBSS, neurons were incubated with imaging medium (HBSS containing 1X B27 Supplements, 25 mM glucose, 1 mM pyruvate, and 20 mM HEPES) in control conditions or with the addition of DOPAL and/or Nocodazole administration at the indicated concentrations in **Table 3.1**. Neurons were imaged at the inverted Olympus Fluoview 1000 laser scanning confocal microscope using a 40X oil immersion objective lens with numerical aperture 1.3 at 0.2% laser power to avoid photo-toxicity. During the time-lapse recordings, cells were maintained at 37°C in controlled atmosphere. Z-stack images were acquired with 200 μm of confocal aperture and 1 μm step size (17-24 steps in average) every 30 minutes for 18 hrs. Nine different areas were imaged for each independent experiment, adjusting the acquisition parameters for each field of view.

3.4.3 Correlated light and electron microscopy.

Three different experiments of correlated light and electron microscopy (CLEM) were performed, according to the experimental setup described in this section. In the next paragraphs, the common experimental procedures of the confocal fluorescence imaging, the protein photo-oxidation, the sample processing, and the imaging at the transmission electron microscope (TEM) are explained in detail.

CLEM of αSyn-TimeSTAMP-YFP-miniSOG in primary rat cortical neurons. Neurons transfected with the αSyn-TimeSTAMP-YFP-miniSOG construct received a pulse with 1 μM BILN-2061 inhibitor for 4 hrs in complete medium. After three washes in HBSS, neurons were kept in the incubator at 37°C in fresh complete medium with or without 100 μM DOPAL. After 24 hrs from the BILN-2061 pulse-chase, neurons were fixed and processed as follows in section **3.4.4** and **3.4.5**.

CLEM of αSyn-split miniSOG in primary rat cortical neurons. Neurons that were previously transduced with the two fragments of the αSyn-split-miniSOG were treated with 100 μM DOPAL in complete medium for 24 hrs in the incubator at 37°C. At the end of the treatment, the growth medium was replaced with imaging medium in both the treated and untreated samples and live images of the reconstituted split-miniSOG complex were acquired at the Leica SPE II inverted confocal microscope. Position coordinates were saved. Cells were then fixed in place, followed by the photo-oxidation protocol.

CLEM of JF570-labeled αSyn-HaloTag in BE(2)-M17 cells. BE(2)-M17 transfected with the αSyn(WT)-HaloTag and the αSyn(K96R)-HaloTag received a pulse with 3 μM JF570 HaloTag fluorescent ligand for 30 minutes in growth medium. After three washes in HBSS, cells were maintained in fresh growth medium with or without 100 μM DOPAL in the incubator. After 48 hrs from the JF570 HaloTag pulse-chase, cells were fixed and processed as follows in section **3.4.4** and **3.4.5**.

3.4.4 Confocal fluorescence imaging and photo-oxidation.

For the CLEM experiments, cells were fixed using pre-warmed (37°C) 2.5% (w/v) glutaraldehyde (Electron Microscopy Sciences) in 0.1 M sodium cacodylate buffer, pH 7.4 (Ted Pella Incorporated) for 5 mins at room temperature and then transferred on ice for 1 hr. Subsequently, cells were rinsed on ice 3-5 times using chilled cacodylate buffer and treated for 30 minutes on ice in a blocking solution (50 mM glycine, 10 mM KCN, and 5 mM aminotriazole in 0.1 M sodium cacodylate buffer, pH 7.4) to reduce nonspecific background precipitation of DAB. Cells were imaged and photo-oxidized using a Leica SPE II inverted confocal microscope outfitted with a stage chilled to 4°C. Confocal fluorescence and transmitted light images were acquired with minimum exposure to identify transfected cells, with care to avoid sample photo-bleaching. For photo-oxidation, oxygenated DAB (3-3'-diaminobenzidine, Sigma-Aldrich) was dissolved in 0.1 N HCl at a concentration of 5.4 mg/ml and subsequently diluted ten-fold into sodium cacodylate buffer (pH 7.4, with a final buffer concentration of 0.1 M), mixed, and passed through a 0.22 mm syringe filter before use. DAB solutions were freshly prepared on the day of photo-oxidation and placed on ice and protected from light before being added to cells. The cells were then illuminated through a standard FITC filter set (EX470/40, DM510, BA520) for miniSOG photo-oxidation or a ReAsH filter set (P/N:mCherry-A-L01-ZERO, Ex:FF01-562/40(542-582), DM:FF593-Di02, Em:FF01-641/75 (604-679)) for JF570 HaloTag ligand photo-oxidation, with 100% intense light from a 150 W xenon lamp. Illumination was stopped as soon as an optically-dense reaction product began to appear in place of the fluorescence, as monitored by transmitted light (typically 3–8 min, depending on the initial fluorescence intensity, the brightness of the illumination, and the optics used).

3.4.5 Electron microscopy

Multiple areas on a single dish were photo-oxidized as described in the previous section. Subsequently, plates with cells were placed on a bed of ice and washed using ice-cold cacodylate buffer to remove unpolymerized DAB. After washing, cells were post-fixed with 1% osmium tetroxide (Electron Microscopy Sciences) in 0.1 M sodium cacodylate buffer for 30 mins on ice, then washed with ice-cold cacodylate buffer (5 times, 1 min each) and rinsed once in ice-cold distilled water. An additional staining step with filtered 2% uranyl acetate (UA) in distilled water was performed by overnight incubation at 4°C. The day after, the UA was removed and washed-out with ice-cold distilled water (3 times, 3 mins each). The samples were then dehydrated with an ice-cold graded ethanol series (20%, 50%, 70%, 90%, 100%, 100%) for 3 mins each step and washed once in room temperature anhydrous ethanol. Samples were then infiltrated with Durcupan ACM resin (Electron Microscopy Sciences) using a 1:1 solution of anhydrous ethanol:resin for 30 minutes on a platform with gentle rocking, then with 100% resin overnight with rocking. The next day, the resin was removed from dishes (by decanting and gentle scraping with care to avoid touching cells), replaced with freshly prepared resin (3 times, 30 minutes each with rocking), and polymerized in a vacuum oven at 60°C for 48 hrs. Subsequently, photo-oxidized areas of interest were identified by transmitted light, sawed out using a jeweler's saw, and mounted on dummy acrylic blocks with cyanoacrylic adhesive. The coverslip was carefully removed and ultrathin sections (80 nm thick) were cut using a diamond knife (Diatome). Electron micrographs were acquired using a FEI Technai 12 (Spirit) transmission electron microscope operated at 80 kV; micrographs were produced using a Tietz 2k by 2k CCD camera and collected using the SerialEM package.

3.5 Pulse-chase experiments with HaloTag labeling technology.

3.5.1 Pulse-chase experiment with HaloTag JF570-ligand: imaging approach.

BE(2)-M17 cells plated on ICC coverslips, were transfected with the αSyn(WT)-HaloTag or the αSyn(K96R)-HaloTag constructs. 24 hrs post-transfection, cells were subjected to a pulse with 3 μM JF570 HaloTag ligand (Synthetized by Dr. Stephen Adams, UCSD) diluted in complete medium for 30 minutes. After extensive washes in HBSS to remove the excess of ligand, cells were incubated with 100 μM DOPAL in OptiMEM (or without any treatment). At different time-points (t=0-8-24-48 hrs), cell medium was washed out and cells were fixed with 4% PFA for 20 minutes at RT. Samples were then washed with PBS and mounted on glass slides with Gelvatol mounting medium (in-house reagent). Z-stacks of JF570-positive cells were acquired at the Olympus Fluoview 1000 laser scanning confocal microscope using either a 40X or 60X oil immersion objective lens.

3.5.2 Pulse-chase experiment with HaloTag biotin-ligand: biochemical approach.

BE(2)-M17 cells plated on 6-wells plates, were transfected with the αSyn(WT)-HaloTag or the αSyn(K96R)-HaloTag constructs. 36 hrs post-transfection, cells were treated overnight with 100 μM DOPAL in OptiMEM (or without any treatment for the control). At the end of the treatment, cells were subjected to a pulse with 5 μM HaloTag biotin-ligand (Promega) diluted in complete medium for 3 hrs. After three washes in HBSS to remove the excess of ligand, cells were incubated with complete growth medium. At different time-points (t=0-4-8-12-24-30 hrs), cells were collected, spinned down and the cell pellets were stored at -80°C. At the end of the time course, all samples were thawed, and cell were harvested in lysis buffer (20mM Tris-HCl pH7.5, 150mM NaCl, 1 mM EDTA, 2.5mM sodium pyrophosphate, 1mM β-glycerophosphate, 1mM sodium orthovanadate, 1%

Triton® X-100), supplemented protease inhibitor cocktail (Sigma-Aldrich). After incubation in ice for 30 minutes, cell lysates were cleared by centrifugation at 20000 g at 4°C. Protein concentration in the cleared supernatant was determined with the Pierce® BCA Protein Assay Kit (Thermo Scientific) following the manufacturer's instructions. 150 µg of proteins for each sample were diluted in TBS buffer (Tris-HCl 50mM pH 7.4, NaCl 150mM) to a final volume of 300 µl and incubated with 10 µl of medium slurry of streptavidin-coated magnetic beads (GE Healthcare) for 2hrs at RT under continuous rotation. Then, the unbounded proteins were separated by the isolated biotin-labeled αSyn-HaloTag by a magnetic rack and the flow through was collected separately. The beads were then washed three times with TBS-Urea 2mM, incubated with 10 µl of sample buffer 1X (1:4 dilution of 8% SDS, 400 mM DTT, 200 mM Tris pH 6.8, bromophenol blue, 40% glycerol) and boiled at 100°C for 10 minutes. Samples were loaded in gradient 4-20% Tri-Glycine-SDS gels (BioRad) and western blot was performed as follows using the anti-αSyn MJFR1 antibody for the immunoblot. In parallel, 15 µl of flow through were loaded in a 10% polyacrylamide gel and subjected to an SDS-Page and western blot with the anti-Actin antibody as loading control.

3.6 Western blot.

For western blot analysis, BE(2)-M17 cells were harvested in RIPA Buffer (Cell Signaling Technology) supplemented with protease inhibitors (Roche). After incubation on ice for 30 minutes, cell lysates were clarified by centrifugation at 20000g at 4°C. Protein concentration in the cleared supernatant was determined using the Pierce® BCA Protein Assay Kit (Thermo Scientific) following the manufacturer's instructions. 25 to 30 µg of protein samples were resolved on gradient 4-20% Tris-Glycine-SDS gels (BioRad), gradient 4-20% Tris-MOPS-SDS gels (GenScript), 10% or 13% Tris-Glycine polyacrylamide gels, according to the size resolution required. The resolved proteins were transferred to polyvinylidenedifluoride (PVDF) membranes (BioRad), through a semi-dry Trans-

Blot® Turbo™ Transfer System (BioRad). PVDF membranes were subsequently blocked in Tris-buffered saline plus 0.1% Tween (TBS-T) plus 5% non-fat milk for 1 hr at 4°C and then incubated over-night at 4°C with primary antibodies (**Table 3.3**) in TBS-T plus 5% non-fat milk.

Primary Antibody	Source	Catalog #	Dilution
Mouse anti-beta Actin	Sigma-Aldrich	A1978	1:5000
Rabbit anti-Tau	GeneTex	GTX112981	1:1000
Rabbit anti-αSyn MJFR1	Abcam	ab138501	1:5000
Mouse anti-αSyn 211	Sigma-Aldrich	S5566	1:2000
Mouse anti-pSer129 81/A	Biolegend	825702	1:2000
Mouse anti-alpha Tubulin	Sigma-Aldrich	T6074	1:5000
Mouse anti-beta Tubulin	OriGene technology	TA301569	1:10000
Mouse anti-Ubiquitin (P4D1)	Santa cruz Biotech.	sc-8017	1:500
Rabbit anti-p62	Abcam	ab109012	1:200
Rabbit anti-Calnexin	Abcam	Ab22595	1:15000
Rabbit anti-Calreticulin	StressGen	SPA-600	1:5000

Secondary Antibody	Source	Catalog #	Dilution
Goat anti-rabbit-HRP	Sigma-Aldrich	A9169	1:15000
Goat anti-mouse-HRP	Sigma-Aldrich	A9044	1:80000
Goat anti-mouse-HRP	Jackon ImmunoResearch Lab. Inc	115-035-003	1:25000

Table 3.3 List of primary and secondary antibodies used in western blot analysis.

Membranes were then washed in TBS-T (3x10 minutes) at room temperature (RT) and subsequently incubated for 1 hour at RT with horseradish peroxidase (HRP)-conjugated anti-mouse or anti-rabbit IgG (**Table 3.3**). After three more washes in TBS-T, immunoreactive proteins were visualized using Immobilon® Classico Western HRP Substrate (Millipore) or Immobilon® Forte Western HRP Substrate (Millipore) and images were acquired by Imager CHEMI Premium detector (VWR).

3.7 Flow cytometry.

BE(2)-M17 cells plated in 12-wells plates were transfected with the αSyn-mKeima construct. 36 hrs post-transfection, cells were treated for overnight with starvation medium or with MG132 and Bafilomycin in OptiMEM (at the concentration reported in **Table 3.1**), with or without DOPAL 100 μM. After 16 hrs of treatment, cells were collected, the medium was washed out and cells were resuspended in 200 μl of HBSS supplemented with 10 mM Hepes, 44 mM $NaHCO_3$. Cells were maintained in 15 ml-tubes in ice until the flow cytometric analysis; before the loading in the instrument, each sample was vigorously resuspended to dissolve cell clumps. αSyn-mKeima-positive cells (at least 10000 positive cells each sample) were analyzed at the flow cytofluorimeter (FACSAria™ IIIu Cell Sorting) by a simultaneous excitation at 405 nm and emission detection at 610 nm by a BV605 detector, and the excitation at 561 nm with the emission detection at 610 nm with a PE-CF594 detector. The autofluorescence threshold was set based on the measurement of non-transfected cells. As described in protocol by Um et al., the αSyn-mKeima positive cells were divided into two groups according to the contribution in the fluorescence of the dual excitation. Specifically, the cells with a ratio of emission at PE-CF594/BV605 < 1 were defined “low”, while the “high” cells presented a ratio of emission at PE-CF594/BV605 > 1 (Um et al., 2018). The first group identifies the cells with αSyn-mKeima mainly localized in neutral compartments (the cytoplasm), while the second one identifies the cells with αSyn-mKeima mainly localized in acidic compartments (the lysosomes).

3.8 Cell viability assay.

BE(2)-M17 cells plated in 96-wells plates were treated with increasing doses of aminoguanidine, metformin or PBS as control (12 wells each condition) in growth medium for 24-48 hrs, according to the experiment. After medium washing out with PBS, cells were incubated with 75 µl /well of a 1:6 dilution of MTS reagent (Cell Titer 96® AQueous One Solution Cell Proliferation Assay, Promega) in OptiMEM. Cells were then placed back in the incubator to allow the MTS to be converted into the chromogenic formazan by the mitochondrial enzymes. The reaction was then monitored after 30-60-90 minutes by measuring the absorbance at 490 nm at the multi-wells plate reader (Victor). The signal was subtracted for the background absorbance of the MTS dilution in OptiMEM in the absence of cells, while the mean absorbance of the different treatments was normalized for the mean value of the PBS-treated cells, considered 100% of cell viability.

3.9 Data analysis and Statistics.

The densiometric analysis of the bands of the western blot experiments, as well as the processing and analysis of the images acquired at the confocal microscope and the TEM was performed with the Fiji software. In details, to quantify the fluorescence intensity in the live imaging and the ICC experiments, the Integrated Density parameter was used. To quantify the size of synaptic vesicles, intra-luminal vesicles and the multi-vesicular bodies, the Feret diameter was considered as reference. For the synaptic vesicles clustering analysis, the nearest neighbor distance (Nnd) plugin was employed.

The quantitative and statistical analysis of the collected data, as well as the proper graphical visualization, were performed using GraphPad Prism Software Inc. (version 7). In general, when the sample size allowed it (n>3), mean values among data-sets were analyzed by the non-parametric Mann-Whitney test (two data-sets) or by the non-parametric Kruskall-Wallis test with the Dunn’s multiple

comparisons test (more than two data-sets). Instead, for the synaptic vesicles parameters, mean values were analyzed by the One-way ANOVA with Tukey's multiple comparisons test. Additional details on the data analysis are reported in the legend of each figure.

The figures were created and edited by using Adobe Illustrator CC.

4. RESULTS.

4.1 Correlated light and electron microscopy to study DOPAL-induced alterations of αSynuclein localization and trafficking to different neuronal compartments.

4.1.1 Rationale and experimental approach.

αSyn proteostasis in neurons is the results of a strict regulation of protein synthesis in the soma, the trafficking along the axons to reach the pre-synaptic terminals where αSyn exerts its function and finally of αSyn clearance. This last step occurs both in the periphery via the UPS and in the cell body by the autophagic machinery, after the protein is retrogradely transported through the endo-lysosomal pathway to the cell body (Boassa et al., 2013; Tofaris et al., 2011; Volpicelli-Daley, 2017a). Morover, a certain amount of the protein can be secreted in the extra-cellular space via various pathways like exosomes (Danzer et al., 2012). Therefore, any alterations in these processes, i.e. blockage of the axonal transport, engulfment of protein degradation systems or anomalous signaling due to post-translational modifications on αSyn sequence, would trigger αSyn accumulation and further oligomerization, leading to neurotoxicity.

On this ground, we first studied whether DOPAL build-up in the neuronal environment would impact on αSyn trafficking between the soma to the periphery, by pulse-chase experiments coupled to live imaging recordings. Next, we took advantage of the high resolution of the correlated light and electron microscopy (CLEM) technique to investigate any DOPAL-induced variations on αSyn distribution in the different neuronal compartments. Indeed, CLEM is the ideal approach to pinpoint the localization of a protein of interest at both cellular and supra-molecular level in the same specimen. This is achieved by tagging the protein with genetically encoded proteins that act as probe for both light microscopy (LM) and electron microscopy (EM). In this project, we employed various constructs developed at the National Center for Microscopy and Imaging Research (NCMIR, UCSD), encoding αSyn in fusion with the protein miniSOG (mini Singlet Oxygen Generator), which has already been used to map αSyn localization in neurons (Boassa et al., 2013).

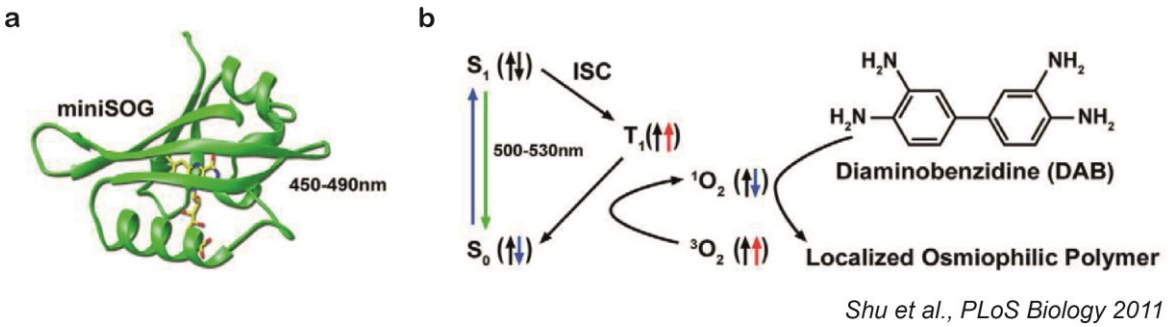

Figure 4.1 miniSOG, a genetically encoded protein as probe for correlated light and electron microscopy. (a) Structure of the miniSOG protein and **(b)** schematic diagram of how miniSOG produces a singlet oxygen upon blue-light illumination, with further DAB polymerization. Spin states are depicted by the arrows. ISC stands for intersystem crossing. Adapted from *Shu et al, PLoS Biology 2011*.

Briefly, miniSOG is an intrinsically fluorescent flavoprotein, which has been engineered from the LOV (light, oxygen and voltage) domain of *Arabidopsis thaliana* phototropin 2 (Shu et al., 2011). It is a small protein (106 amino acids), with a blue light excitation peak (450-490 nm) and a green light emission (500-530 nm), in the presence of the flavin mononucleotide (FMN) cofactor (**Fig. 4.1a**). When illuminated by an intense blue light, the protein photo-oxidizes, generating a singlet oxygen which locally catalyzes the polymerization of DAB into an electron-dense osmiophilic reaction product highly detectable by EM (**Fig. 4.1b**). Importantly, the reaction product has a minimal diffusion, hence the darker signal reflects the specific labeling and localization of miniSOG and, by extension, of αSyn. In **Fig. 4.2a-b**, an example of the photo-oxidation process is showed. After fixation in glutaraldehyde, rat primary cortical neurons overexpressing miniSOG-tagged αSyn are imaged at the confocal microscope, looking for green fluorescent neurons (**Fig. 4.2a**). Once a field of interest is identified, the specimen is incubated with a DAB solution and the area is illuminated by an intense blue light for 3-5 minutes with oxygen blowing on the surface. At the end of the reaction, the miniSOG fluorescence is bleached and replaced by a dark brown signal corresponding to the polymerized DAB (**Fig. 4.2b**), which will be further stained with osmium and processed for the EM imaging.

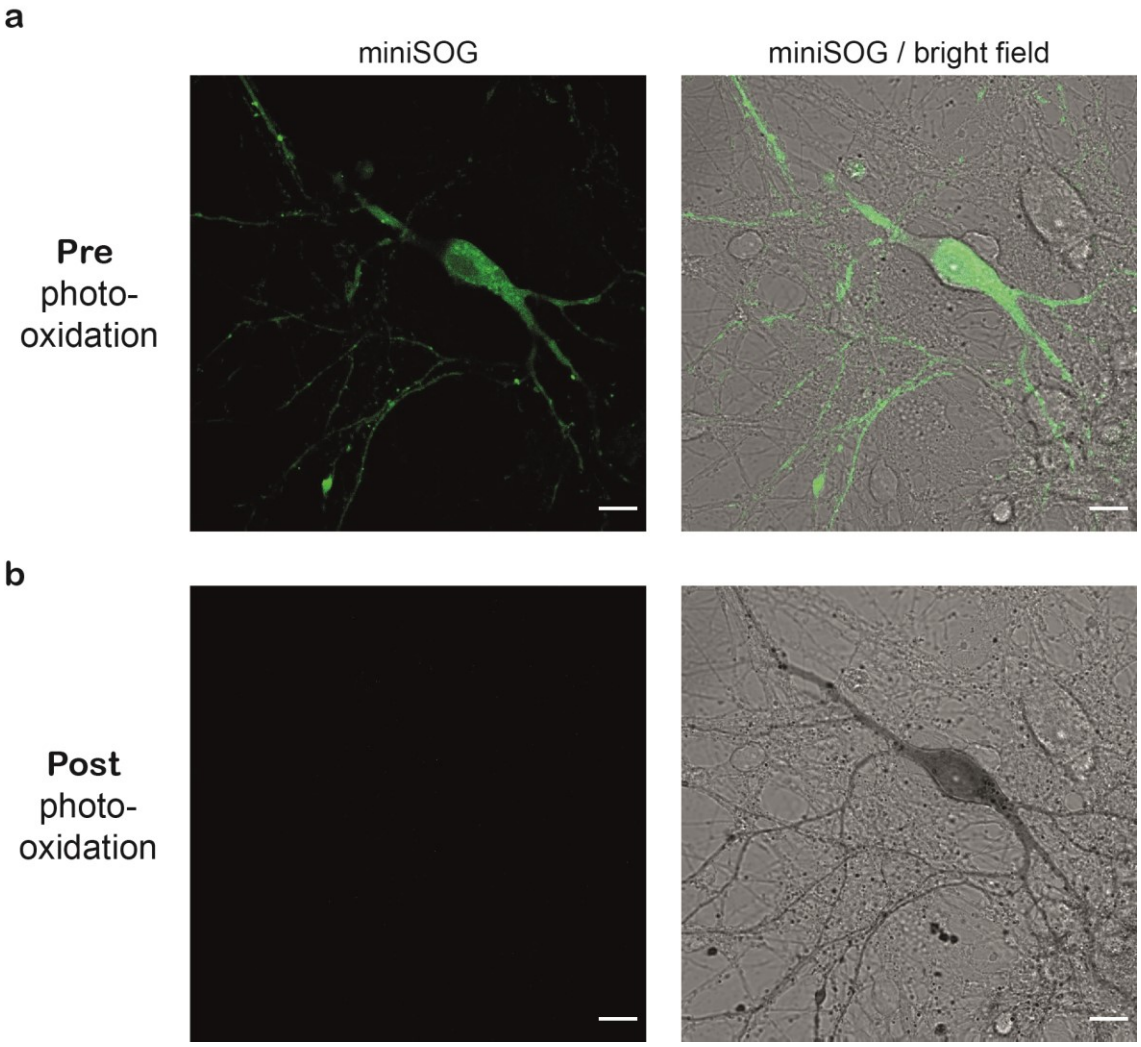

Figure 4.2 miniSOG photo-oxidation process. (a) Rat primary cortical neuron overexpressing the fluorescent αSyn-TimeSTAMP-YFP-miniSOG, imaged at the Leica SPE II confocal microscope before the photo-oxidation. **(b)** After 5 minutes of photo-oxidation, which occurs by illumination with an intense blue light, in the presence of a DAB solution and oxygen blowing on the surface, the miniSOG fluorescence is bleached and it is replaced by the dark signal of the localized DAB polymers. Scale bar: 10 μm.

4.1.2 DOPAL build-up affects αSynuclein trafficking and clearance in rat primary cortical neurons.

First, we investigated whether DOPAL treatment in neurons would affect αSyn localization and trafficking from the soma to the periphery and back. We used the TimeSTAMP tag (Time-Specific Tag for the Measurement of the Age of Proteins) to follow αSyn spatial and temporal organization (Lin et al., 2008).

Briefly, TimeSTAMP is a drug-sensitive on-off switch with a cassette comprising the protease domain of hepatitis C virus (HCV) flanked by protease cleavage sites and followed by a split YFP epitope tag. Upon expression, the protease excises itself and the tag from proteins by default, targeting the two fragments to degradation. However, by applying a cell-permeant protease inhibitor (BILN-2061), the protein of interest is expressed in frame with a reconstituted and active YFP probe, providing the capability to select and image by LM a newly synthetized protein subpopulation. Here, the TimeSTAMP tag was combined with YFP fluorescent protein and miniSOG, providing a powerful tool to analyze αSyn trafficking by both live-imaging and CLEM (**Fig. 4.3**).

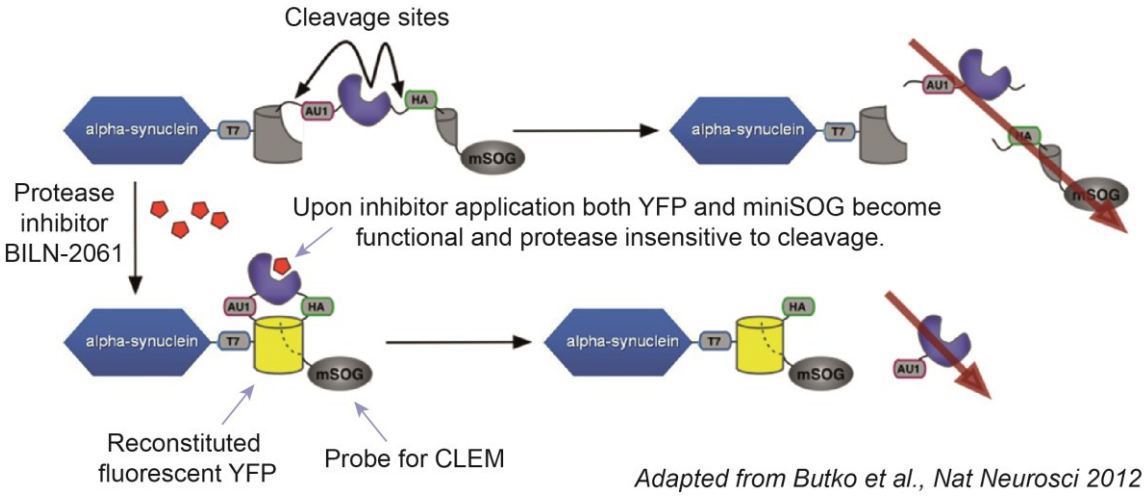

Figure 4.3 αSyn-TimeSTAMP. Schematic diagram of the strategy behind the αSyn-TimeSTAMP-YFP-miniSOG probe. Adapted from *Butko et al., Nat Neurosci 2012*.

As displayed in the diagram in **Fig. 4.4a**, rat primary cortical neurons (DIV11-16) overexpressing αSyn-TimeSTAMP-YFP-miniSOG were subjected to a pulse with 1μM BILN-2061 inhibitor for 4 hrs, switching on the fluorescence of the newly synthetized αSyn during that time-frame. After washing out the excess of BILN, live time-lapse imaging was performed for 18 hrs under control conditions or in the presence of 100 μM DOPAL (each area was imaged every 30 minutes). The representative images in **Fig. 4.4b** show that in both untreated and DOPAL-treated neurons, the fluorescent αSyn-TimeSTAMP-YFP-miniSOG is present in the soma, along the axons and the dendrites, and in the periphery, where it co-localizes with the pre-synaptic scaffold protein Bassoon.

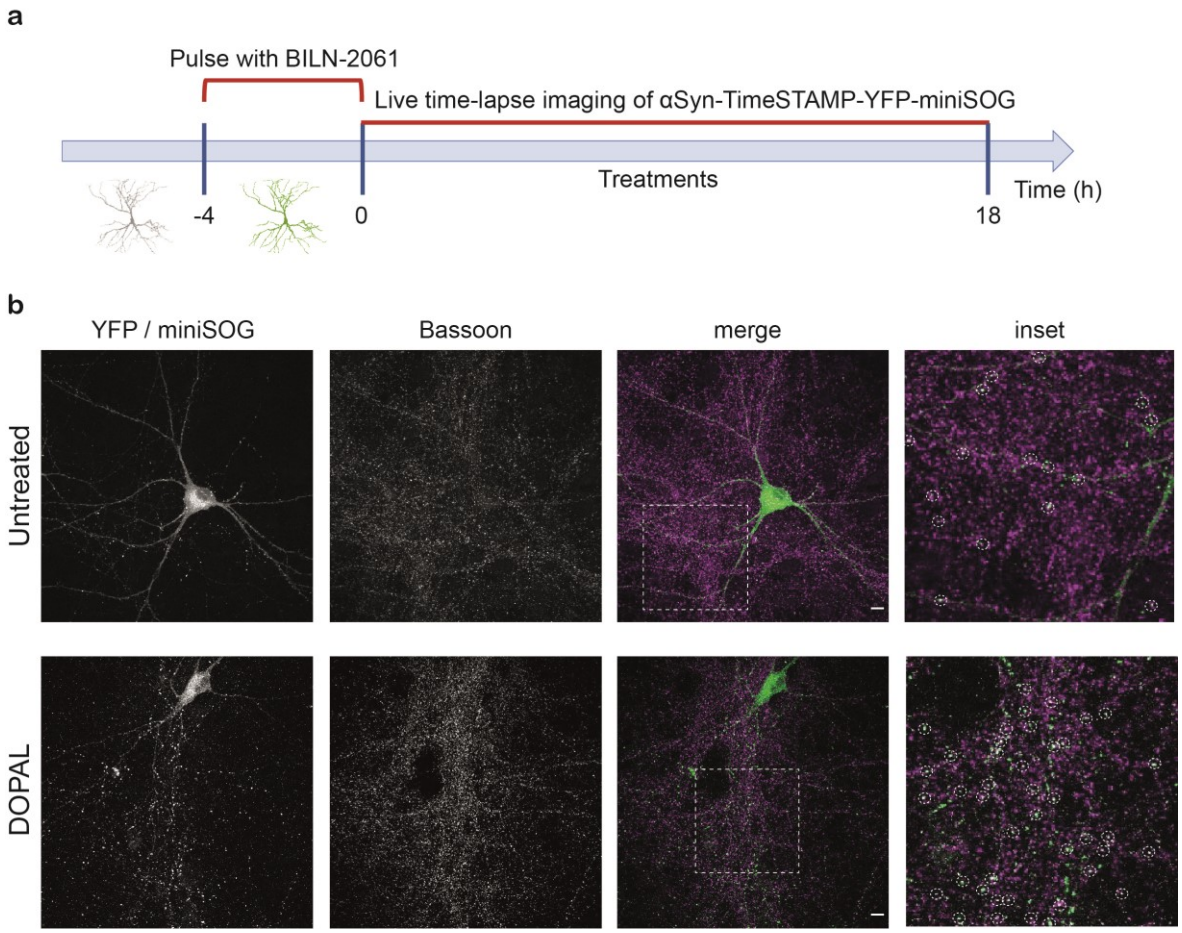

Figure 4.4 Studying αSyn trafficking in neurons by live time-lapse imaging with the TimeSTAMP probe. (a) Schematic representation of the experimental setup of the pulse-chase experiment. During the 4 hrs of BILN-2061 pulse, the transfected rat primary cortical neurons express the fluorescent αSyn-YFP-miniSOG. After the BILN-2061 wash-out, live time-lapse imaging was performed for 18 hrs within the different treatments, acquiring an image every half hour. **(b)** Representative immunocytochemistry images of untreated and DOPAL-treated rat primary cortical neurons over-expressing αSyn-TimeSTAMP-YFP-miniSOG, 24 hrs after BILN-2061 pulse-chase. In the merged images, the green signal stands for the sum of the YFP and miniSOG fluorescence while the magenta signal corresponds to the immunolabeling with the anti-Bassoon antibody. Scale bar: 10 µm. In the inset image, the white circles point out the co-localization between αSyn and Bassoon at the pre-synaptic terminals.

αSyn trafficking was studied by monitoring the YFP fluorescence in the soma and in the synaptic terminals over time. These terminals were identified automatically by a custom-made Matlab script (by Matthew Madany, UCSD), designed to measure the fluorescence intensity of every terminals in the different time-frame. Here, a few statements are due to explain the way the analysis was conducted. As showed in the representative images in **Fig. 4.5a**, bright YFP-positive boutons are

present not only in the inter-neuron space but also along the dendrites. The first ones plausibly indicate the αSyn accumulated at the pre-synaptic terminals where the protein exerts its function and co-localizes with Bassoon, a scaffold protein of the active zone. Whereas, the other boutons might indicate the presence of αSyn at the dendritic spines. Although this event has been already observed, the function of αSyn at the post-synaptic is not clearly stated yet (Teravskis et al., 2018). Also, it could be a consequence of αSyn overexpression in primary neuronal cultures (Blumenstock et al., 2017). Hence, the YFP-positive dots identified in the proximity of the soma were excluded from the analysis. The second observation refers to the fact that each field of view covers just a few cell bodies and the relative proximal processes, while most of the identified pre-synaptic terminals belong to the surrounding αSyn-TimeSTAMP-YFP-miniSOG positive neurons rather than the centered ones, making it challenging to relate the analysis of the YFP fluorescence variations in the soma with the signal in the periphery. Third, some new terminals that are not fluorescent at t0, appear later in the time-lapse. Indeed, even though at the beginning of the live imaging the newly synthetized αSyn has no fluorescent tag, a fraction of the fluorescent protein produced during the BILN-2061 pulse is targeted to terminals that are far away from the soma and it takes a longer time to reach them. Hence, given the complexity of the data analysis, as first approach we considered only the terminals that were identified by the software in the first 3 hrs of the recordings to infer any effect induced by DOPAL build-up on αSyn trafficking and degradation.

Starting from these assumptions, the quantification of the YFP fluorescence intensity variation in the soma indicates that DOPAL treatment significantly induces an impaired αSyn trafficking from the soma to the periphery (**Fig. 4.5, 4.6a**). In untreated neurons, αSyn appears to migrate from the cell body to the periphery, leaving only the 25% of the initial amount in the soma after 8 hrs. In the second phase of the recording, the αSyn progressively comes back in the cell body, reaching up the 50% of the starting fluorescence at t=18 hrs. This behavior can be explained by the combination of the local clearance of the protein both in the soma and at the periphery, together with a retrograde trafficking from the synapses.

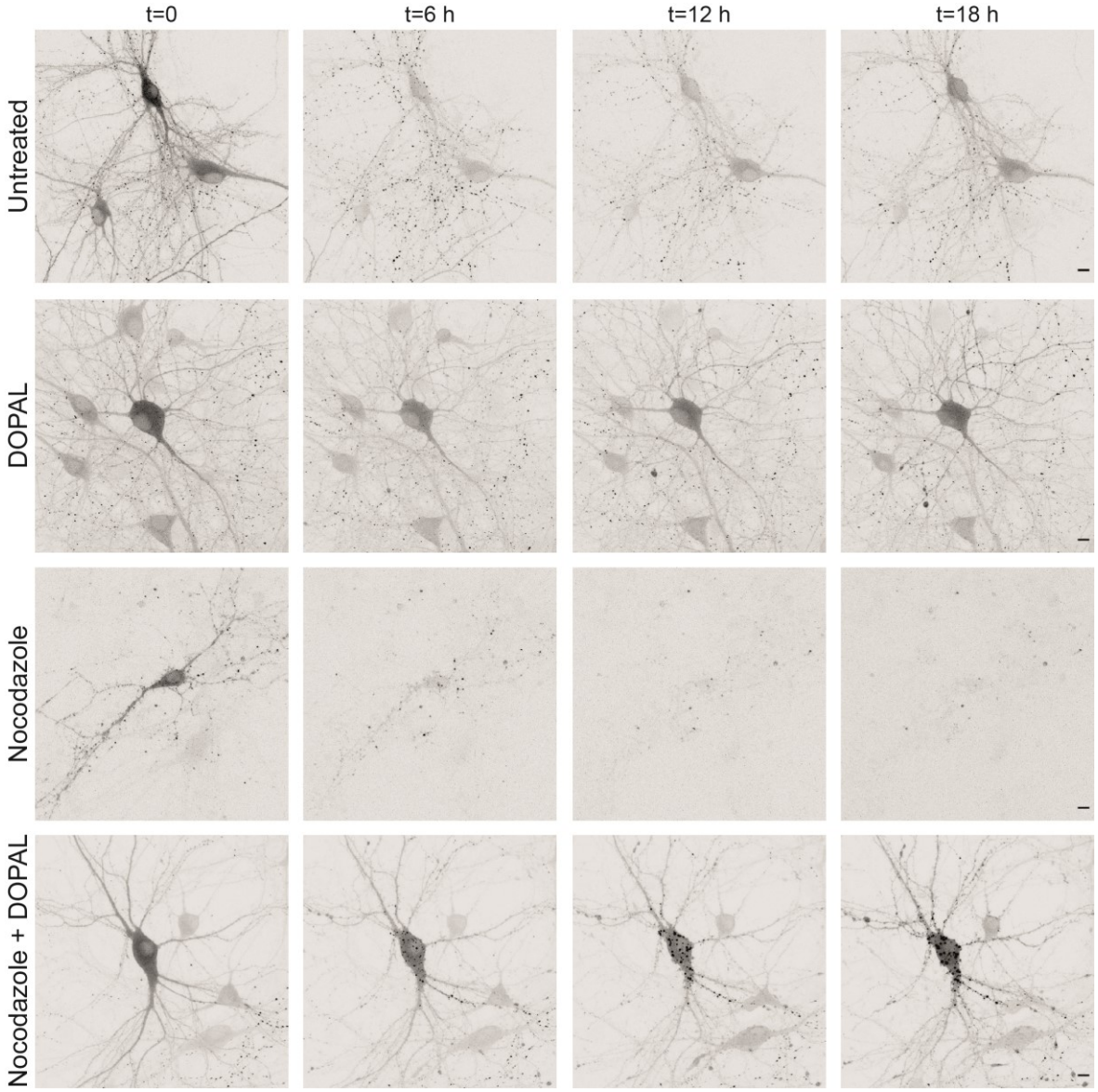

Figure 4.5 Time-lapse imaging of αSyn-TimeSTAMP-YFP-miniSOG overexpressing neurons. Snapshots at different time points (t=0, t=6 hrs, t=12 hrs, t=18 hrs) of representative time-lapse recordings of rat primary cortical neurons overexpressing αSyn-TimeSTAMP-YFP-miniSOG (YFP/miniSOG fluorescence) after the BILN-2061 pulse-chase, in the four conditions tested: Untreated neurons, 100 μM DOPAL, 5 μg/ml Nocodazole and 100 μM DOPAL + 5 μg/ml Nocodazole. Scale bar: 10 μm.

However, in DOPAL-treated neurons, only a slow decrease in the fluorescence is observed in the soma, without any apparent retrograde trafficking, suggesting both an impaired mobility of the protein (the first part of the curve) but also a less efficient degradation rate, as only the 30% of the protein disappears in 18 hrs. Similarly, the YFP variations in the peripheral terminals indicate that in untreated

neurons, the new fluorescent αSyn progressively accumulates at the synapse, followed by a progressive decrease in its concentration once the clearance process occurs. Instead, in DOPAL-treated neurons the level of αSyn remains steady in the first interval of the recording (3 hrs) and then slowly decays over time (**Fig. 4.6b**).

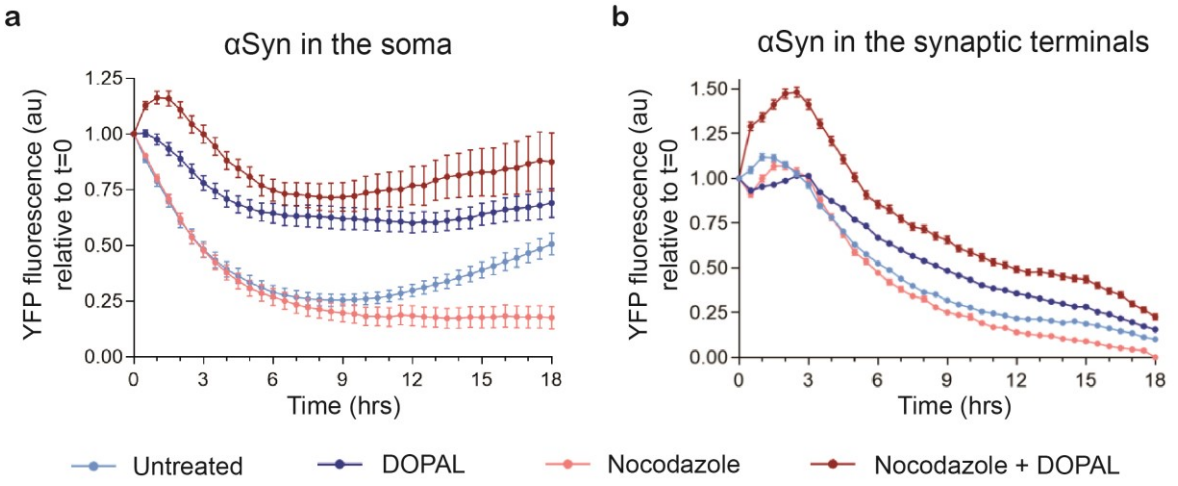

Figure 4.6 DOPAL impairs the trafficking of the newly synthetized αSynuclein from the soma and the mature αSynuclein in the periphery. (a) Quantification of YFP fluorescence in the soma in each time-frame of the live time-lapse imaging. For each cell body, data are normalized to the YFP fluorescence intensity at t=0. **(b)** Quantification of YFP fluorescence in peripheral terminals in each time-frame of the live time-lapse imaging. For each terminal, data are normalized to the YFP fluorescence intensity at t=0. In the graphs, data are presented as Mean ± SEM from n=3 independent experiments pooled together (27 areas imaged in total) for the Untreated (n=3320 terminals), DOPAL (n=3712 terminals) and Nocodazole (n=2154 terminals) treated neurons and from n=2 independent experiments pooled together (16 areas imaged in total) in the Nocodazole + DOPAL (n=2600 terminals) condition.

In addition, to test whether the observed DOPAL-induced αSyn altered mobility is consistent with axonal trafficking inhibition, live time-lapse imaging of αSyn-TimeSTAMP-YFP-miniSOG was performed in the presence of the axonal transport inhibitor Nocodazole or the combined treatment Nocodazole + DOPAL (**Fig. 4.5**, third and fourth rows of confocal images). In the presence of 5μg/ml Nocodazole, which induces microtubule depolymerization (Utton et al., 2005), αSyn disappears from the soma with an exponential trend (25% of the starting level at t=18 hrs), plausibly degraded by the UPS and ALP in the cell body (**Fig. 4.6a**). On the contrary, in the presence of DOPAL within of the axonal trafficking disruption, the protein dramatically accumulates. αSyn cannot exits from the soma

but also its clearance is affected, maintaining approximatively a constant αSyn concentration in the cell body during the considered time-frame of the experiment. Consistently, the rapid and large (1.5-fold) increase in signal in the peripheral terminals (**Fig. 4.6b**) probably reflects an excessive accumulation of αSyn, coupled to an impaired αSyn turn-over caused by DOPAL. Since the protein clearance in the periphery is taken care by the proteasome and other cytoplasmic proteases, this effect appears much greater compared to the cell body where the ALP co-operates in the process.

Furthermore, using the same TimeSTAMP tag approach, we aimed to analyze the trafficking of different proteins, to explore whether the observed DOPAL-induced alteration αSyn mobility is specific or could affect different targets. Thus, we studied the trafficking of Tau, a microtubule-associated protein, that shares with αSyn the axonal transport via microtubules (Utton et al., 2005). Physiologically, Tau participates in the stabilization of the microtubule network and axon integrity, hence it primary localizes along the axons. Tau is also present in the cell body and in the dendrites, where it is known to modulate synaptic plasticity and dendritic spines architecture (Sotiropoulos et al., 2017).

Interestingly, the analysis of the variations of Tau fluorescence in the cell body during the 18 hrs of live time-lapse imaging in untreated primary neurons differs from the behavior in the DOPAL treated neurons (**Fig. 4.7a-b**). In the control, Tau progressively gathers in the soma during the considered time-frame. Instead, within DOPAL treatment, Tau rapidly accumulates up to 2-fold change in the first 3 hrs, maintaining a steady-state level until the end of the recordings.

This result suggests a broader action of DOPAL on protein mobility, which might be explained by general impairment of axonal transport as observed for αSyn. On the other hand, the possibility of a DOPAL modification of Tau lysines (63 lysines residues out of 758 amino acids, about 8% of the sequence), most of which are ubiquitination sites, cannot be ruled out. This would result in decreased Tau clearance by the UPS and the ALP (Lee et al., 2013). Likewise, preliminary data obtained by western blot analysis on BE(2)-M17 cells treated overnight with increasing amount of DOPAL, reveal a dose-dependent accumulation of Tau

oligomeric species (**Fig. 4.7c**), possibly indicating a similar mechanism of DOPAL-induced aggregation and impaired degradation for both αSyn and Tau. In the future, further investigation of the DOPAL impact on Tau proteostasis will be of interest. We also plan to extend our analysis to other proteins with the same cellular localization of αSyn, i.e. synapsin, to unravel the DOPAL action on axonal trafficking of proteins as well as the axonal transport machinery.

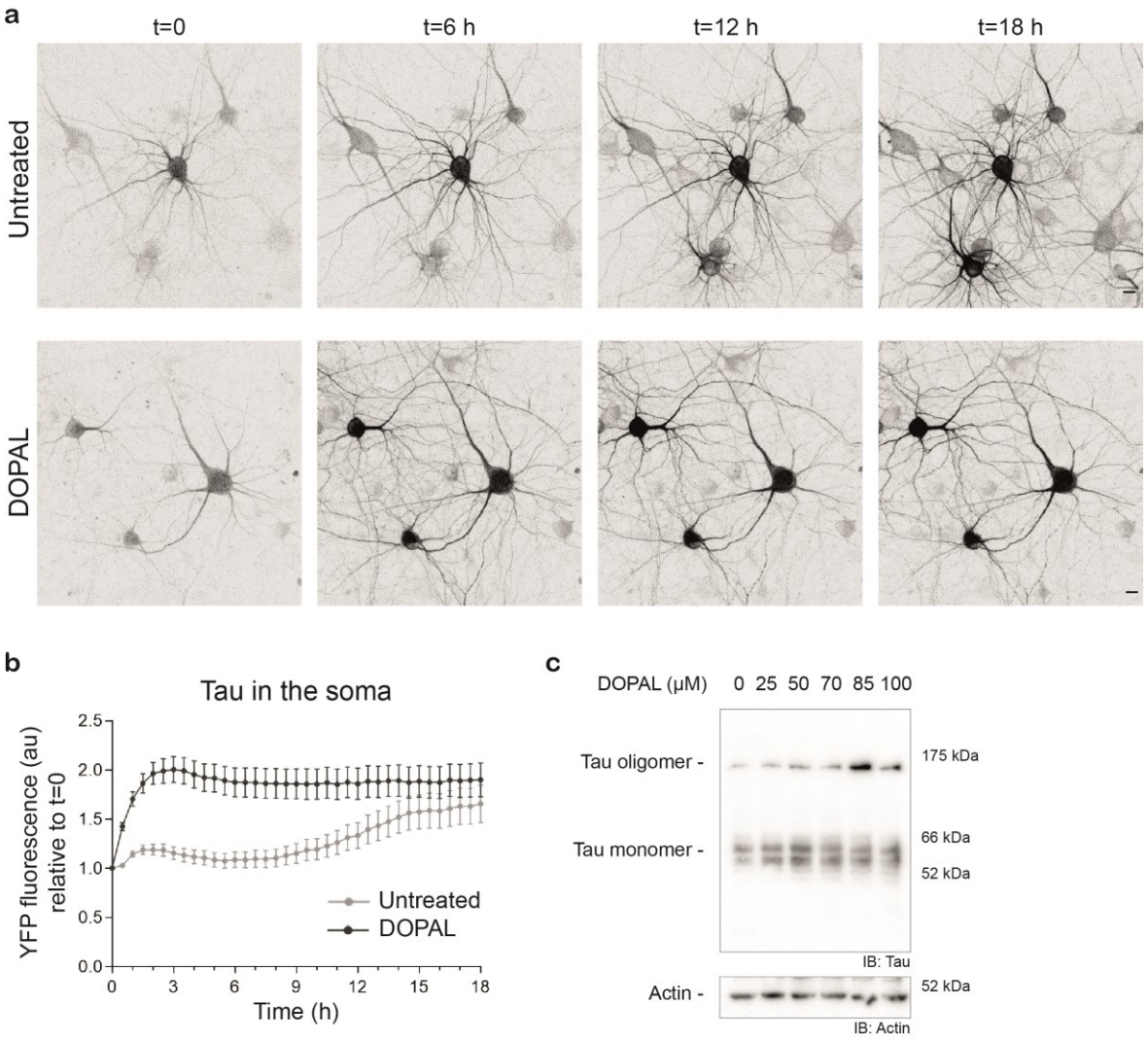

Figure 4.7 DOPAL alters the trafficking of Tau in the soma. (a) Snapshots at different time points (t=0, t=6 hrs, t=12 hrs, t=18 hrs) of representative time-lapse recording of rat primary cortical neurons overexpressing Tau-TimeSTAMP-YFP-miniSOG after the 4 h BILN-2061 pulse-chase, in the two conditions tested: Untreated neurons and DOPAL 100 μM. Scale bar: 10 μm. **(b)** Quantification of YFP fluorescence in the soma in each time-frame of the live time-lapse imaging. For each cell body, data are normalized to the YFP fluorescence intensity at t=0. Data are presented as Mean ± SEM (n=2 independent experiments pooled together, 18 areas imaged in total for the Untreated and DOPAL-treated conditions). **(c)** Western blot of BE(2)-M17 cells after an overnight DOPAL treatment at increasing doses (0-25-50-70-85-100 μM). The immunoblot with the anti-Tau antibody detects both the monomeric and the oligomeric forms of Tau.

4.1.3 Correlated light and electron microscopy of rat primary cortical neurons overexpressing αSyn-TimeSTAMP-YFP-miniSOG.

Based on the presence of miniSOG in the TimeSTAMP cassette, we performed the CLEM in neurons overexpressing the αSyn-TimeSTAMP-YFP-miniSOG construct, to investigate more in depth any redistribution of αSyn subcellular localization due to DOPAL build-up. In **Fig. 4.8a**, representative images of untreated and DOPAL-treated neurons for 22 hrs after the BILN-2061 pulse-chase, are showed. As explained before, the miniSOG fluorescence guides the identification of positive neurons at the confocal microscope. Once an area of interest is identified, the photo-oxidation occurs, with the dark brown signal of the DAB local polymerization in replacement of the miniSOG fluorescence.

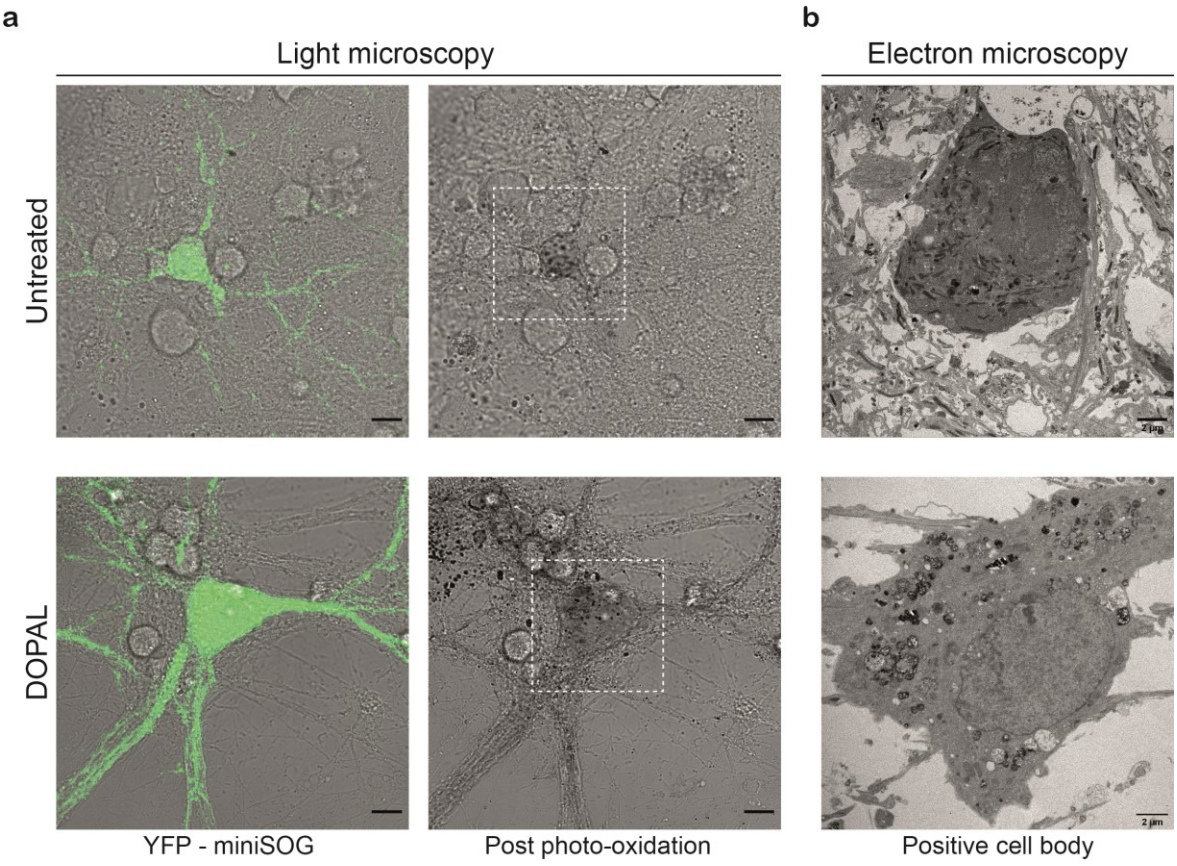

Figure 4.8 CLEM of αSyn-TimeSTAMP-YFP-miniSOG in Untreated and DOPAL-treated neurons, 22 hrs after BILN-2061 pulse-chase. (a) Confocal imaging before and after photo-oxidation, as overlay of YFP/miniSOG fluorescence (green signal) and bright field image. Scale bar: 10 µm. **(b)** Electron micrograph of the cell body of the photo-oxidized neurons, imaged at TEM and identified by the darker contrast compared the surrounding areas, due to the osmium staining of the polymerized DAB. Scale bar: 2 µm.

After sample processing, the osmium-stained DAB that gives a darker contrast compared to the surroundings structures, allows to recall the same neuron at the EM level (**Fig. 4.8b**). We first started to compare the cell body of the αSyn-YFP-miniSOG positive neurons in untreated and DOPAL-treated conditions. As general observations, while in the untreated neurons the darker signal associated to the photo-oxidized αSyn is diffused in the cytoplasm, in the DOPAL-treated soma the greater contrast derives from the lysosomes.

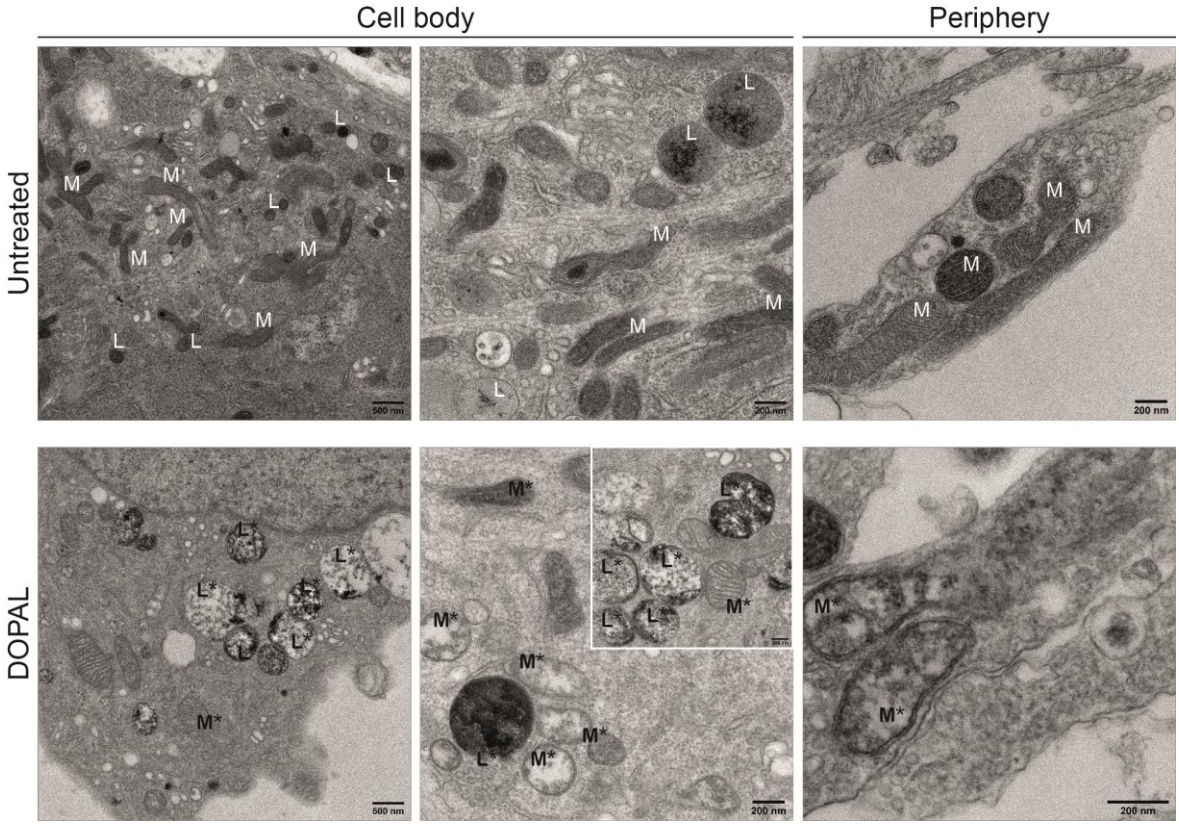

Figure 4.9 CLEM of αSyn-TimeSTAMP-YFP-miniSOG in Untreated and DOPAL-treated neurons, 22 hrs after BILN-2061 pulse-chase, focusing on the lysosomes and mitochondria. Representative EM images at higher magnification of the photo-oxidized αSyn-positive neurons, both the cell body and the periphery. L: lysosome, M: mitochondrion, *: compromised structures. Scale bar: 500 nm (first column), 200 nm (second and third column).

In particular, in the DOPAL-treated sample, the lysosomal-like compartments present higher heterogeneity in shape, dimension and electron-density. Usually, the lysosomal structures appear as electron-dense, rounded and single-membrane organelles, as it is observed in the untreated control samples.

Instead, in the DOPAL-treated cells, these compartments present uneven electron-density, which might derive from an aberrant accumulation of photo-oxidized αSyn in their lumen. Similarly, in untreated neurons, mitochondria are elongated, and well organized cristae are visible when imaged at high magnification, both in the cell body and the peripheral neurites. Instead, in DOPAL-treated neurons, mitochondria appear smaller in size, more fragmented and swollen, which is probably due to an additional outcome of DOPAL toxicity. Hence, these preliminary observations suggest a general impairment of neuronal homeostasis in the presence of high levels of DOPAL.

4.1.4 αSynuclein overexpression affects pre-synaptic terminals organization.

We then specifically looked at the distribution of αSyn at the pre-synaptic terminals, where the protein associates to synaptic vesicles membranes to regulate vesicles clustering and docking to the active zone, as well as the exocytotic events during neurotransmitter release (Burré, 2015; Logan et al., 2017). As showed in **Fig. 4.10a**, the darker signal of photo-oxidized αSyn-YFP-miniSOG confirms the αSyn localization on the membrane of synaptic vesicles, as previously described (Boassa et al., 2013). Specifically, the schematic representation in **Fig. 4.10b** illustrates how the helical-folded N-terminus of αSyn associates to the phospholipids of the outer membrane layer, whereas the C-terminus tagged with the YFP-miniSOG fluorophores (green stars, in the figure) faces the cytosol. Although the YFP-miniSOG size corresponds to 1.5-fold compared to the αSyn molecular weight, we assumed that the tag doesn't interfere with the αSyn localization, association to the vesicles membrane and function. Interestingly, the pre-synaptic terminals deriving from the αSyn-YFP-miniSOG overexpressing neurons are in proximity with non-transfected cells that express the endogenous rat αSyn and represent an internal control. Since the two types of synapses are usually present in the same field of view, the further analysis on the synapse architecture were conducted on both non-transfected and overexpressing neurons, in untreated and DOPAL-treated conditions.

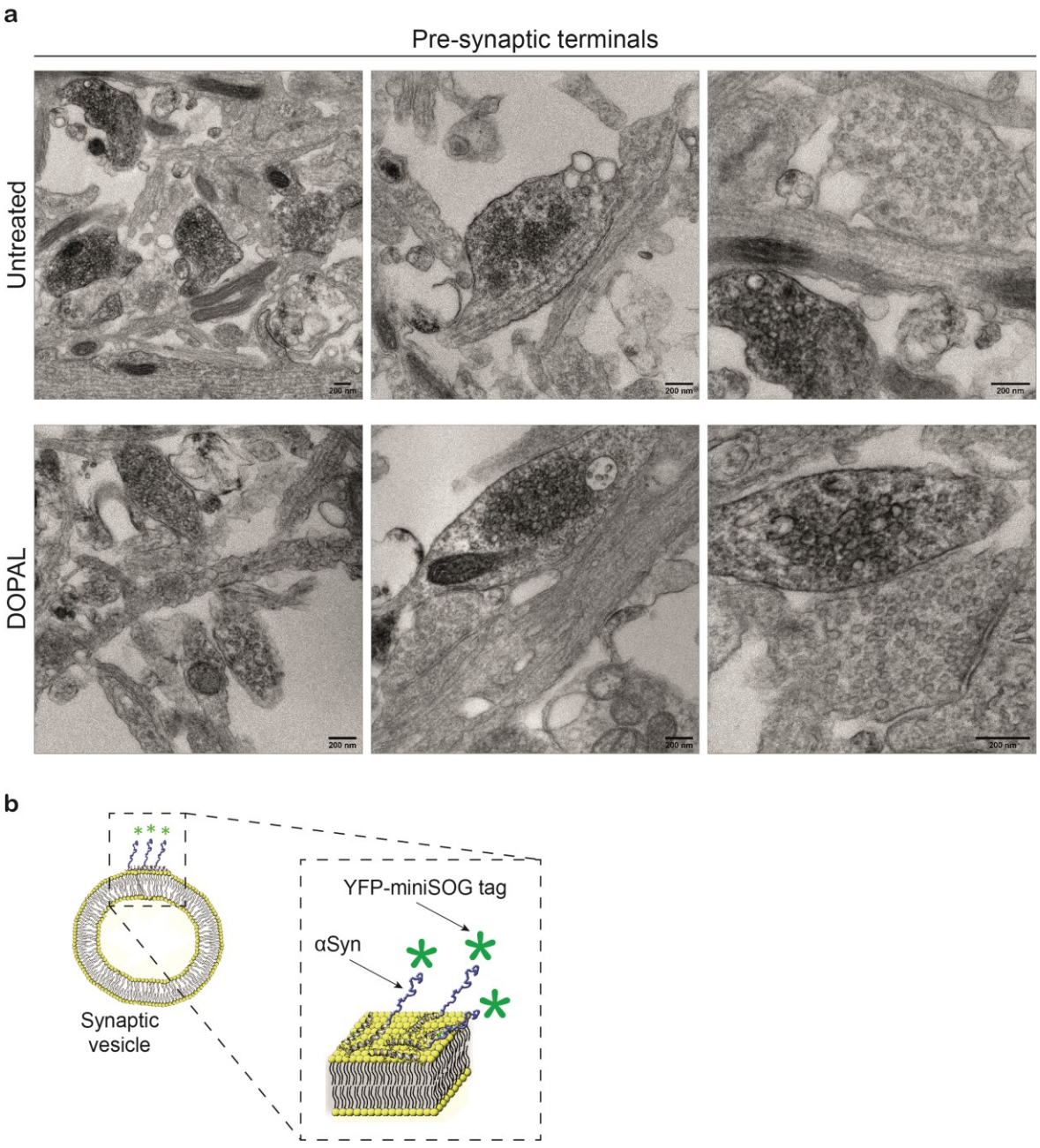

Figure 4.10 CLEM of αSyn-TimeSTAMP-YFP-miniSOG in Untreated and DOPAL-treated neurons, 22 hrs after BILN-2061 pulse-chase, focusing on the pre-synaptic terminals. (a) Representative EM images of pre-synaptic terminals of photo-oxidized neurons (darker staining around the vesicles membrane) in Untreated and DOPAL treated condition, surrounded by non-positive synapses. Scale bar: 200 nm. **(b)** Schematic diagram that illustrates the association of αSyn-TimeSTAMP-YFP-miniSOG to the synaptic vesicles membrane. In the figure, the green stars stand for the YFP-miniSOG fluorescent tag. Adapted from *Boassa et al., J Neurosci 2013*.

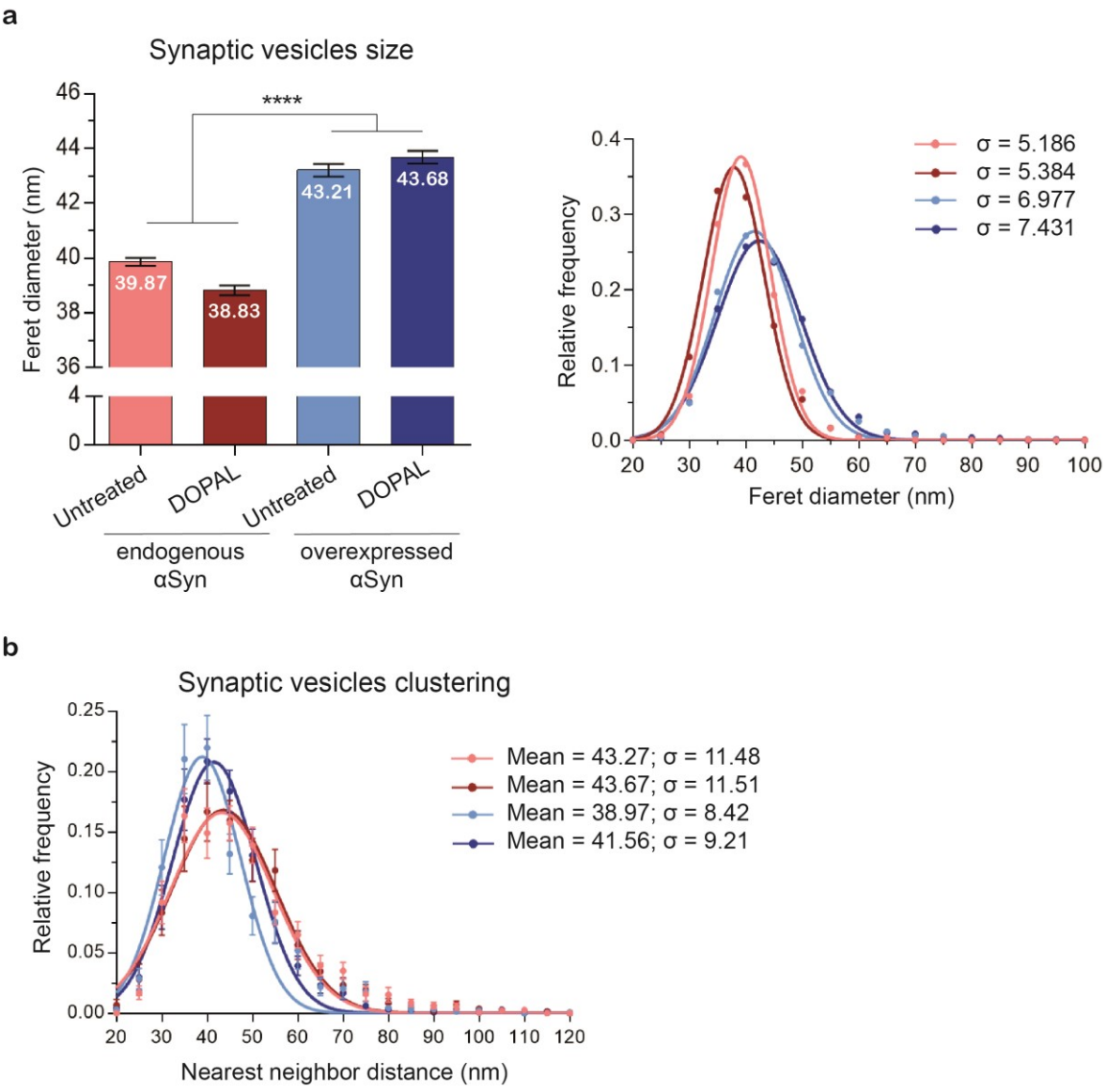

Figure 4.11 αSyn overexpression affects synaptic vesicles size and clustering. CLEM in αSyn-TimeSTAMP-YFP-miniSOG overexpressing neurons, in untreated and DOPAL treated conditions. **(a)** Quantification of the synaptic vesicles' Feret Diameter (nm) in Untreated and DOPAL-treated neurons, from non-transfected (endogenous αSyn) and αSyn overexpressing synapses. Images were collected from two photo-oxidized areas each condition of one independent experiment (non-transfected neurons: Untreated 27 synapses, 1432 vesicles – DOPAL 18 synapses, 1185 vesicles; αSyn overexpressing neurons: 30 synapses, 1398 vesicles – DOPAL 20 synapses, 1234 vesicles). Data are presented as Mean ± SEM (histograms) and frequency distribution (relative frequency), fitted by a Gaussian distribution (the color code is coherent in the two graphs). Mean values of Feret diameter of each single vesicles were analyzed by One-way ANOVA with Tukey's multiple comparisons test (**** $p<0.0001$). **(b)** The same pre-synaptic terminals, were analyzed for the synaptic vesicles clustering, expressed as frequency distribution of the nearest neighbor distance (nm) for each vesicle. The relative frequencies were fitted by a Gaussian curve and the mean value and the standard deviation are reported in the figure.

Since αSyn association to synaptic vesicles membrane is thought to modulate its curvature, hence the vesicle radius (Middleton and Rhoades, 2010), we first measured the synaptic vesicles size using the "Feret diameter" parameter, which is defined as "the longest distance between any two points along the ROI (region of interest) boundary", where in this case the ROI boundary was traced manually along each vesicle membrane. Of note, the overexpression of αSyn significantly increases the dimension of the synaptic vesicles (still in the physiological range of synaptic vesicles size), whereas DOPAL does not induce any obvious contribution (**Fig. 4.11a**). Specifically, in non-transfected neurons, the vesicle Feret diameter results of 39.87 ± 0.15 nm (Untreated), 38.83 ± 0.17 nm (DOPAL-treated); in αSyn-overexpressing neurons, it is estimated equal to 43.21 ± 0.23 nm (Untreated), 43.68 ± 0.23 nm (DOPAL-treated). Also, the frequency distribution of the vesicles' Feret diameter highlights the higher variability of vesicles size in the presence of the overexpressed αSyn (see the σ value for each Gaussian fit in the figure).

We also noticed a differential distribution of the synaptic vesicles in the pre-synaptic terminal area, as the αSyn-overexpressing neurons present more clustered vesicles compared to the non-transfected ones (**Fig. 4.10a**). Hence, to express this observation in quantitative terms, we measured the nearest neighbor distance (Nnd) among pairs of vesicles (**Fig. 4.11b**). In the graph, the gaussian fit of the frequency distribution of the Nnd, confirms the more pronounced vesicles clustering in the αSyn-overexpressing neurons, defined by a shorter Nnd (Untreated: 38.97 nm; DOPAL: 41.56 nm), compared to the higher Nnd in the non-transfected neurons (Untreated: 43.27 nm; DOPAL: 43.67 nm). Of note, in the non-transfected neurons, both the mean value and the standard deviation of the measured Nnd perfectly overlap in the untreated and DOPAL-treated neurons. Instead, in the αSyn-overexpressing terminals, the vesicles clustering is more homogeneous (minor standard deviation), and a slight, non-significant difference is observed in the mean Nnd value in the DOPAL-treated neurons.

So far, the processed pre-synaptic terminals derive from two photo-oxidized areas each condition, out of one single experiment. In the future, more areas from different biological replicates will be analyzed, to confirm these data.

4.1.5 DOPAL promotes αSynuclein loading in intra-luminal vesicles of multi-vesicular bodies.

By observing the specimens at TEM, we noticed some clear variations in the properties of MVBs. These differences triggered our interest in the analysis of MVBs and more precisely on the loading of αSyn in the intra-luminal vesicles (ILVs). Being that MVBs and the endosomal pathway are recruited to vehicle αSyn and other proteins from the periphery to the neuronal cell body to be degraded by the lysosomes. An alternative, that is very relevant for PD, implies that the MVBs fuse with the plasma membrane and release the exosomes in the extra-cellular space (Raposo and Stoorvogel, 2013).

In this frame, we analyzed the αSyn-TimeSTAMP-YFP-miniSOG-positive MVBs (**Fig. 4.12**, yellow arrows) that are present in the soma and the periphery (axons, dendrites and synapses), in terms of MVBs and ILVs size and MVBs filling. Although the dimensions of the MVBs don't differ in untreated versus DOPAL-treated neurons (**Fig. 4.13a**, Feret diameter: Untreated: 230.1 ± 8.7 nm; DOPAL: 235.4 ± 12.4 nm), the ILVs have a significantly increased size in the DOPAL-treated neurons (**Fig. 4.13b**, Feret diameter: Untreated: 43.03 ± 0.38 nm; DOPAL: 47.46 ± 0.60 nm), as well as higher heterogeneity (see the σ of the gaussian fit in the figure).

Furthermore, DOPAL appeared to promote αSyn loading into exosomes, as in treated neurons the MVBs are filled by a higher number of DAB-labeled ILVs (**Fig. 4.13c**). This is extremely relevant, as it possibly implicates the exosomal pathway as spreading mechanism of DOPAL-induced αSyn oligomers to neighboring cells.

Currently, more samples are being analyzed, scrutinizing the DAB-labeled pre-synaptic terminals and MVBs in control and treated conditions. We will also implement these analyses in non-transfected neurons, which represent the internal control condition and will provide indications whether the DOPAL treatment alone affects these neuronal structures.

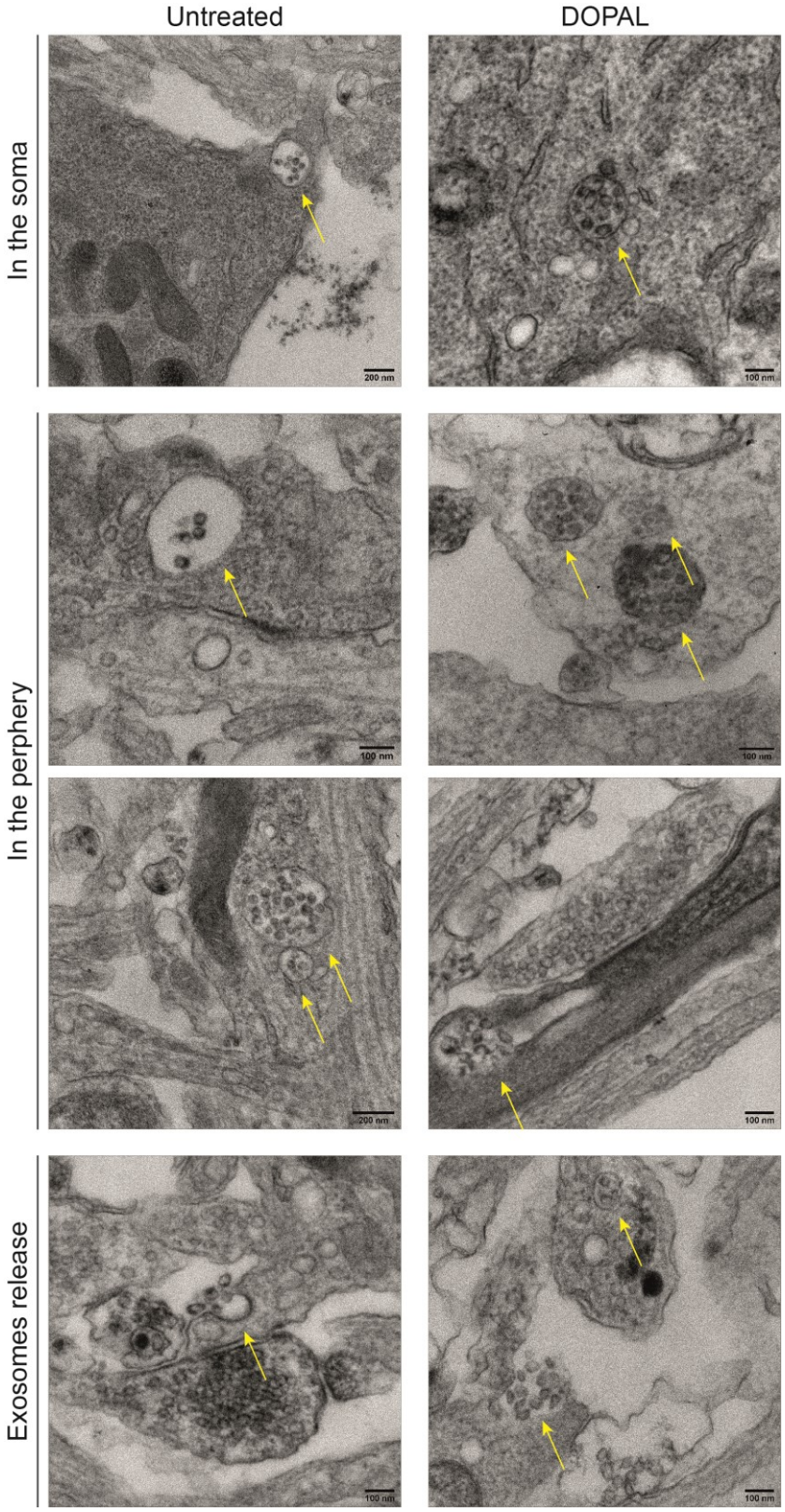

Figure 4.12 CLEM of αSyn-TimeSTAMP-YFP-miniSOG in Untreated and DOPAL-treated neurons, 22 h after BILN-2061 pulse-chase, focusing on the multi-vesicular bodies. Representative EM images of MVBs (yellow arrows), positive for photo-oxidized αSyn-TimeSTAMP-YFP-miniSOG, that are present in the different neuronal compartments of Untreated and DOPAL-treated neurons.

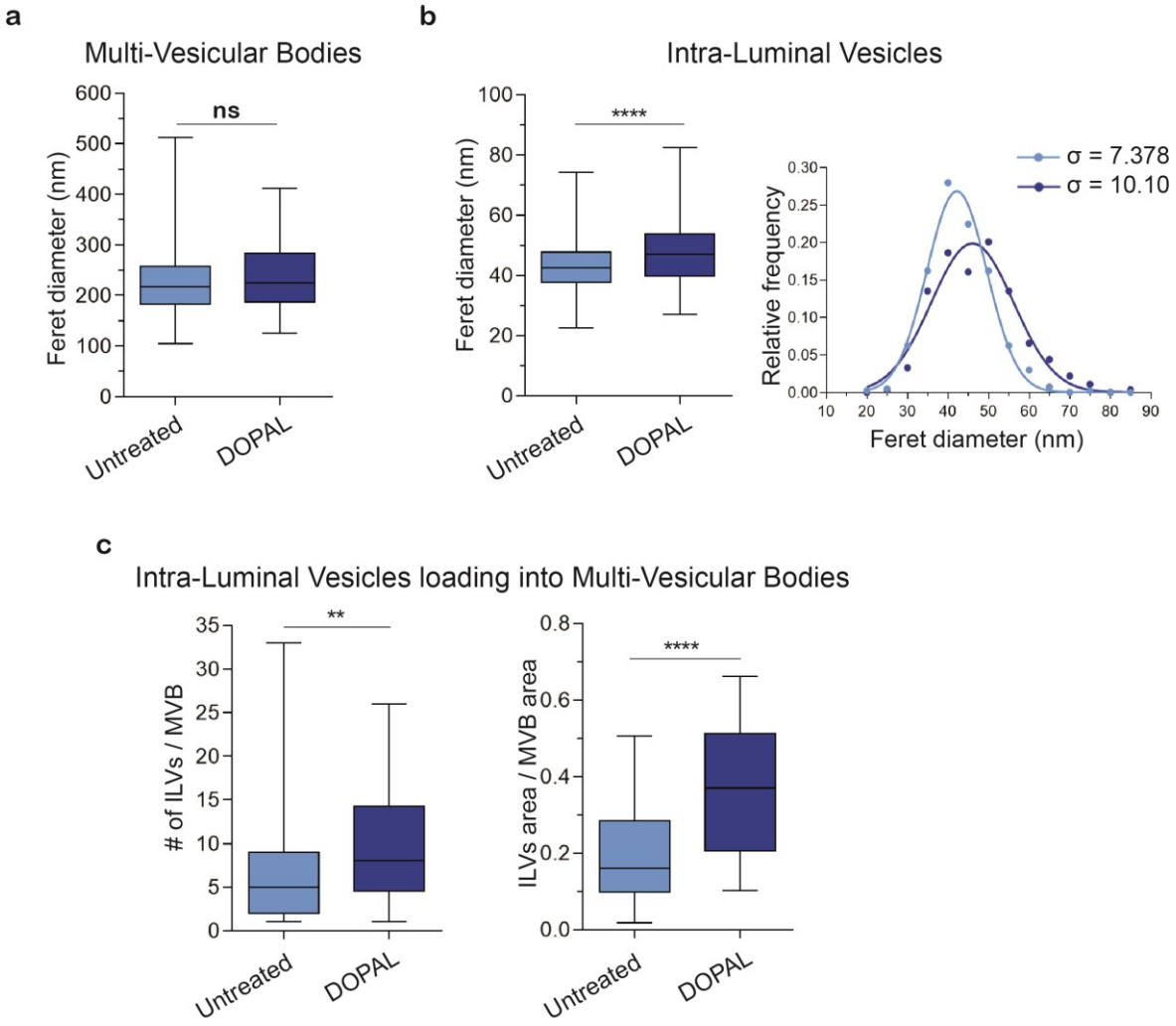

Figure 4.13 DOPAL increases ILVs size and promotes αSyn loading in MVBs. (a-b) Quantification of the Feret Diameter (nm) of MVBs and ILVs in Untreated and DOPAL-treated neurons. **(c)** Quantification of ILVs loading in MVBs, expressed as number of ILVs in each MVB and ratio between the area covered by the ILVs to the MVB area. Images were collected from one independent experiment, two photo-oxidized areas each condition (Untreated 64 MVBs, 401 ILVs – DOPAL 28 MVBs, 278 ILVs). Data are presented as box-plot and, for the ILVs' Feret diameter, as frequency distribution (relative frequency), fitted with the Gaussian distribution (the color code is coherent in the two graphs). Mean values were analyzed by non-parametric Mann-Whitney test (** $p<0.01$, **** $p<0.0001$).

4.1.6 DOPAL exacerbates αSynuclein aggregation in the soma and in the periphery.

As mentioned before, it has already been demonstrated that DOPAL administration triggers αSyn aggregation in different cellular models. However, a precise localization of DOPAL-αSyn oligomers in different neuronal compartments remains poorly investigated. To address this issue, we employed a recently developed probe for CLEM to specifically localize αSyn dimers and oligomers at subcellular level (Boassa et al., 2019). Basically, a split version of the miniSOG protein is used for a protein fragment complementation assay (**Fig. 4.14**).

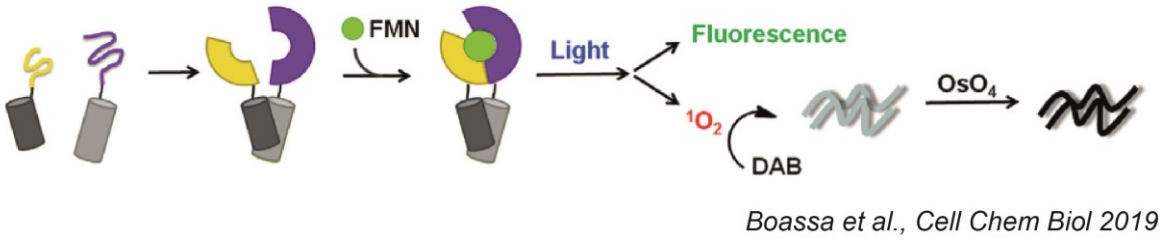

Figure 4.14 CLEM of αSyn-split miniSOG in Untreated neurons and after the treatment with 20 μM DOPAL for 16 hrs. Schematic diagram of the αSyn-split miniSOG protein fragment complementation assay. From *Boassa et al, Cell Chem Biol 2019*.

Here, rat primary cortical neurons were co-infected (DIV8) with lentivirus encoding αSyn fused to the N-terminal fragment of $miniSOG_{1-94}$ (fragmentA) and αSyn fused to the C-terminal fragment of $miniSOG_{95-140}$ (fragmentB), respectively. Once the two miniSOG fragments reconstitute and incorporate the FMN cofactor from the environment, the complex becomes fluorescent as well as it can photo-oxidize for the CLEM approach. Of note, this probe was modified to increase the miniSOG fragments solubility. Also, the complementation of the two miniSOG fragments is reversible and more dynamic compared to other complementation assays, i.e. the split-GFP or split-Venus (Boassa et al., 2019). This implies that the split-miniSOG reconstitution is mainly driven by the interaction between at least two αSyn molecules, hence the darker electron-dense signal reflects the specific labeling of αSyn dimers and oligomers.

As a preliminary experiment, rat primary cortical neurons co-expressing αSyn with the two miniSOG fragments were treated with 20 μM DOPAL for 16 hrs, followed by CLEM analysis (**Fig. 4.15**).

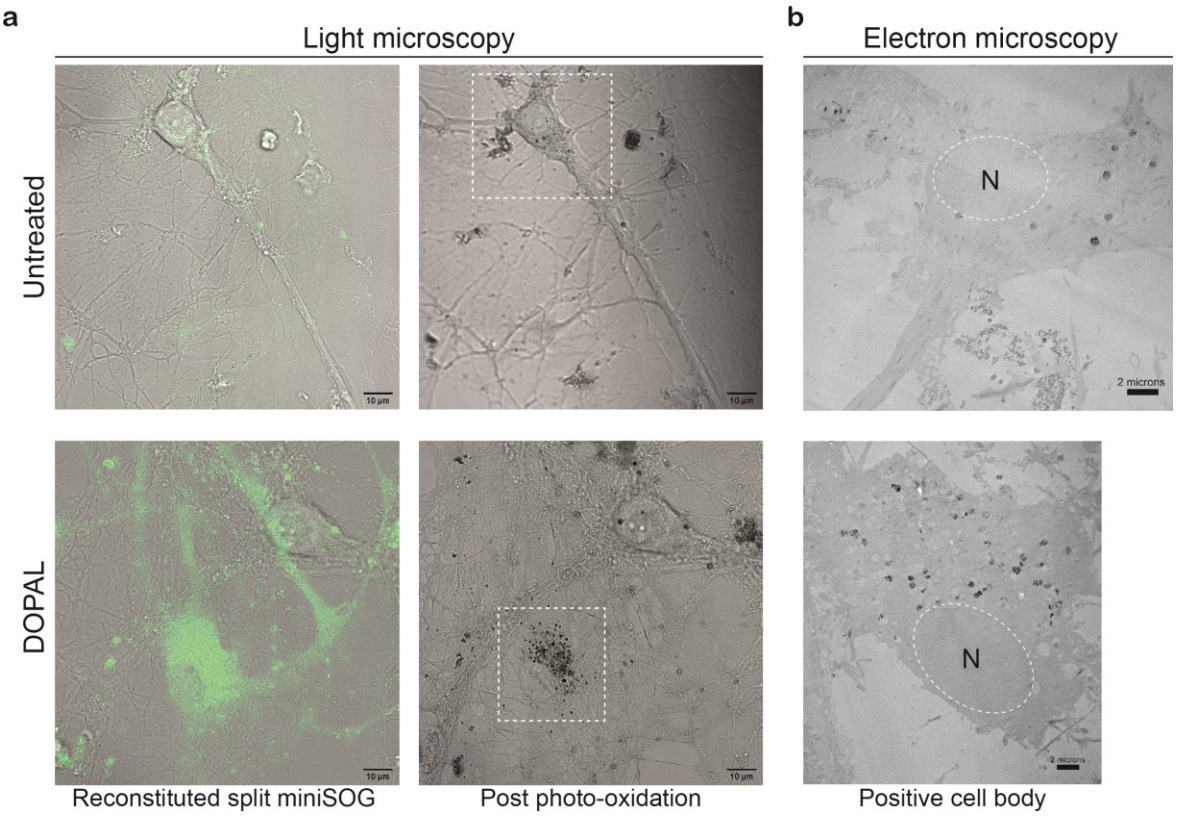

Figure 4.15 CLEM of αSyn-split miniSOG in Untreated neurons and after the treatment with 20 μM DOPAL for 16 hrs. (a) Confocal imaging of live fluorescent neurons and fixed neurons after photo-oxidation, as overlay of reconstituted miniSOG fluorescence (green signal) and bright field image. Scale bar: 10 μm. **(b)** Electron micrograph of the cell body of the photo-oxidized neurons, imaged at TEM. N = nucleus. Scale bar: 2 μm.

Both in treated and untreated neurons, αSyn oligomers are mainly found accumulated as fibrillar and proto-fibrillar structures in lysosomal compartments of the perinuclear region, with increased signal in the DOPAL-treated sample (**Fig. 4.16,** red arrows). The identification of these fibrillar structures can only be done on a morphological base, as we are at the very edge of the resolution capacity of the methodology and it would be difficult to conduct any structural measurement.

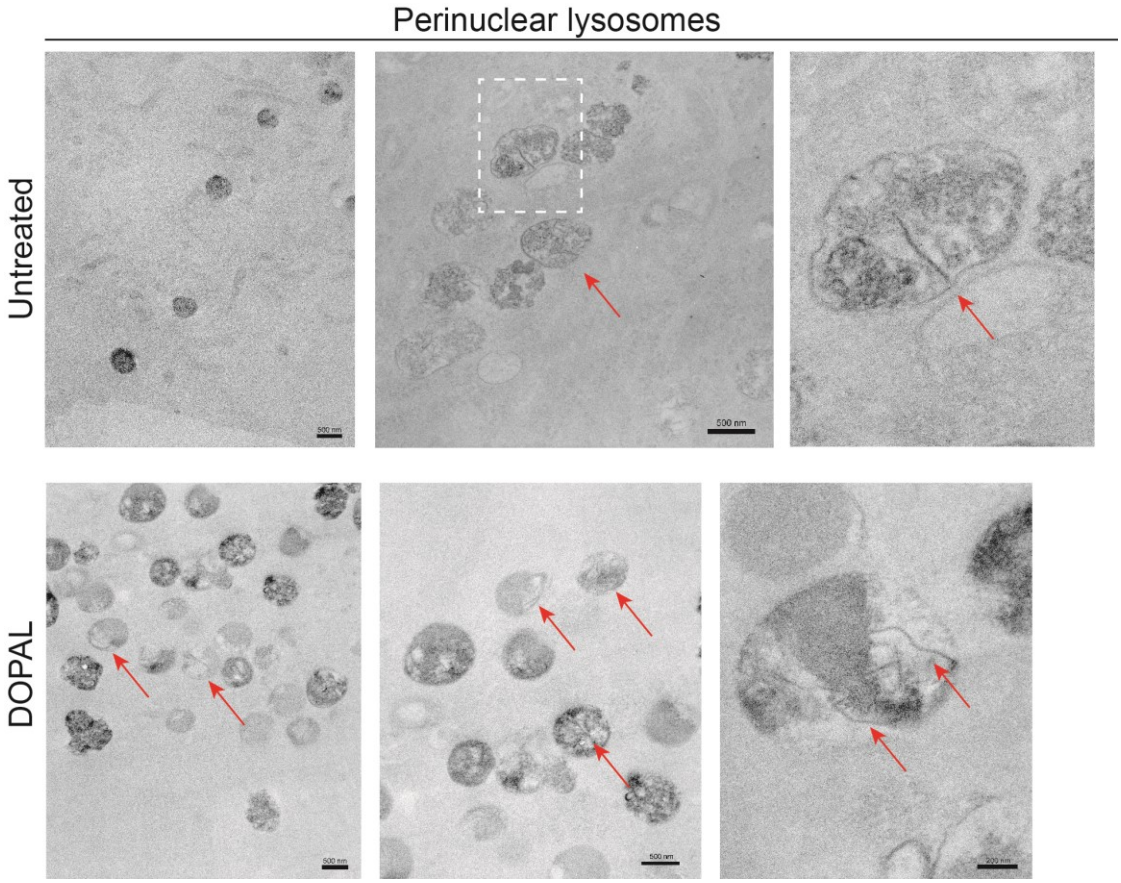

Figure 4.16 CLEM of αSyn-split miniSOG in Untreated neurons and after the treatment with 20 μM DOPAL for 16 hrs, focusing on perinuclear lysososmes. Electron micrograph of the cell body of the photo-oxidized neurons, with higher magnification of the perinuclear lysosomes with αSyn-miniSOG positive proto-fibrillar and fibrillar-like structures (red arrows).

Consequently, a CLEM experiments was performed in rat primary cortical neurons subjected to a longer DOPAL treatment at a higher dose (100 μM DOPAL for 24 hrs), in line with the CLEM experiments with the αSyn-TimeSTAMP-YFP-miniSOG probe (**Fig. 4.17a-b**). Consistently, αSyn oligomers were accumulated in the soma in lysosomal-like compartments (**Fig. 4.18a**, red arrows). As in the previous CLEM experiments, the signal from the photo-oxidized αSyn reveals fibrillar-like structures and the lysosomal compartments present a wider area in the DOPAL-treated neurons.

Of note, in the untreated neurons, we didn't detect any signal of the reconstituted miniSOG at the pre-synaptic level, coherently with the work by Boassa et al. This could be due to the dynamic interaction among αSyn monomers, that don't

stabilize into oligomeric forms at synapses. Instead, in DOPAL-treated neurons a positive DAB signal was detected at pre-synaptic terminals around synaptic vesicles membrane (**Fig. 4.18b**, blue arrows). In the presence of DOPAL, αSyn oligomers are made of covalent and irreversible interactions among modified proteins, enhancing the signal of the reconstituted split-miniSOG even at the synapses. Anyway, the detected oligomers in the periphery are way less compared to the strong signal in the lysosomes of the soma, as well as more images needs to be collected to support this statement. It is also worth to mention that we cannot rule out the possibility of a DOPAL-induced aggregation among overexpressed human αSyn monomers and the endogenous rat monomers, since we are not able to estimate the ratio of the local concentration of the αSyn molecules of the two species.

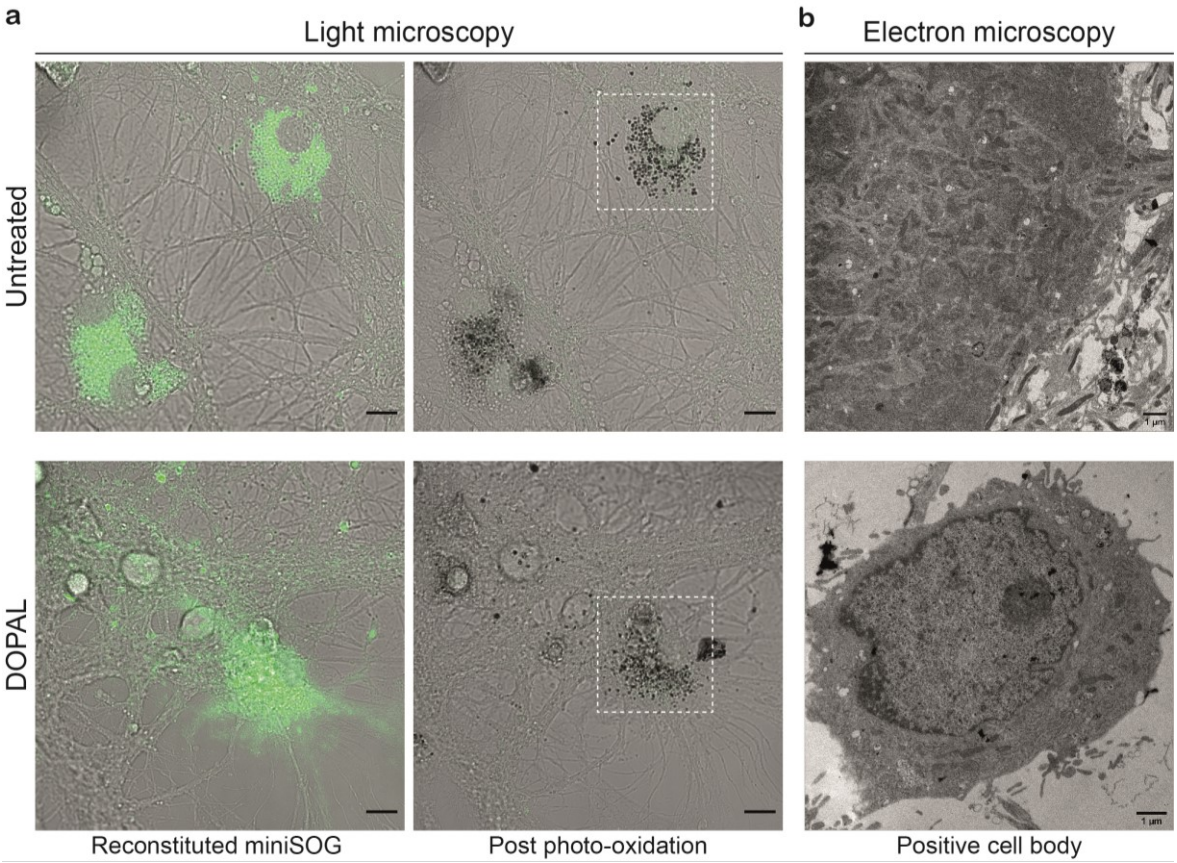

Figure 4.17 CLEM of αSyn-split miniSOG in untreated neurons and in neurons treated with 100 μM DOPAL for 24 hrs. (a) Confocal imaging of live fluorescent neurons and fixed neurons after photo-oxidation, as overlay of reconstituted split miniSOG fluorescence (green signal) and bright field image. Scale bar: 10 μm. **(b)** Electron micrograph of the cell body of the photo-oxidized neurons. Scale bar: 1 μm.

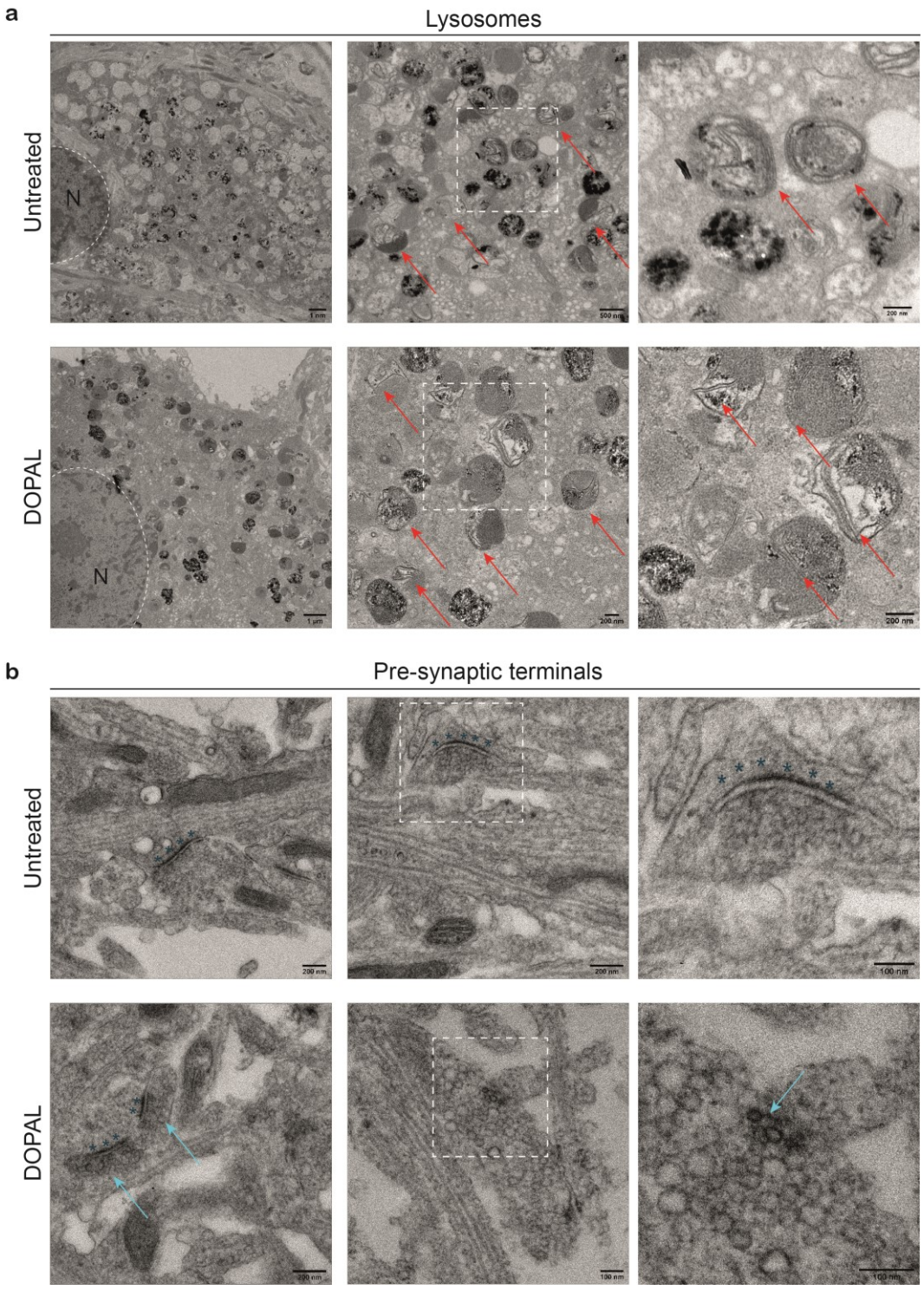

Figure 4.18 CLEM of αSyn-split miniSOG in untreated neurons and in neurons treated with 100 μM DOPAL for 24 hrs, focusing on the lysosomes in the cell bodies and the pre-synaptic terminals. (a) EM images at higher magnification of the neuronal soma and lysosomal-like compartments. The red arrows indicate the αSyn-miniSOG positive proto-fibrillar and fibrillar-like structures. N = nucleus. **(b)** EM images of pre-synaptic terminals in the two conditions tested. The blue stars highlight the post-synaptic density; the light blue arrows indicate the oligomeric αSyn-miniSOG signal around the membrane of a few synaptic vesicle. In all images, the last column shows the inset at higher magnification.

Furthermore, we observed the presence of αSyn oligomeric species in vesicles inside the MVBs, both in untreated and DOPAL-treated samples (**Fig. 4.19**, yellow arrows). Consistently with the CLEM experiments with the αSyn-TimeSTAMP-YFP-miniSOG probe, no difference was observed in the MVBs lumen dimension (**Fig. 4.20a**, Feret diameter: Untreated: 269.6 ± 20.7 nm; DOPAL: 251.3 ± 35.0 nm), while DOPAL induces a significant increase in ILVs size (**Fig. 4.20b**, Feret diameter: Untreated: 41.67 ± 0.54 nm; DOPAL: 49.40 ± 0.76 nm). Also in this experiment, the measured Feret diameter of the ILVs in DOPAL-treated neurons presents more variability among vesicles (see the σ of the gaussian fit in the figure) compared to the untreated condition, potentially due to the different modulation of vesicle curvature by DOPAL-αSyn off-pathway oligomers. Indeed, αSyn-split miniSOG signal was mostly detected on the boundaries of ILVs, suggesting the association of αSyn oligomers on ILVs membrane.

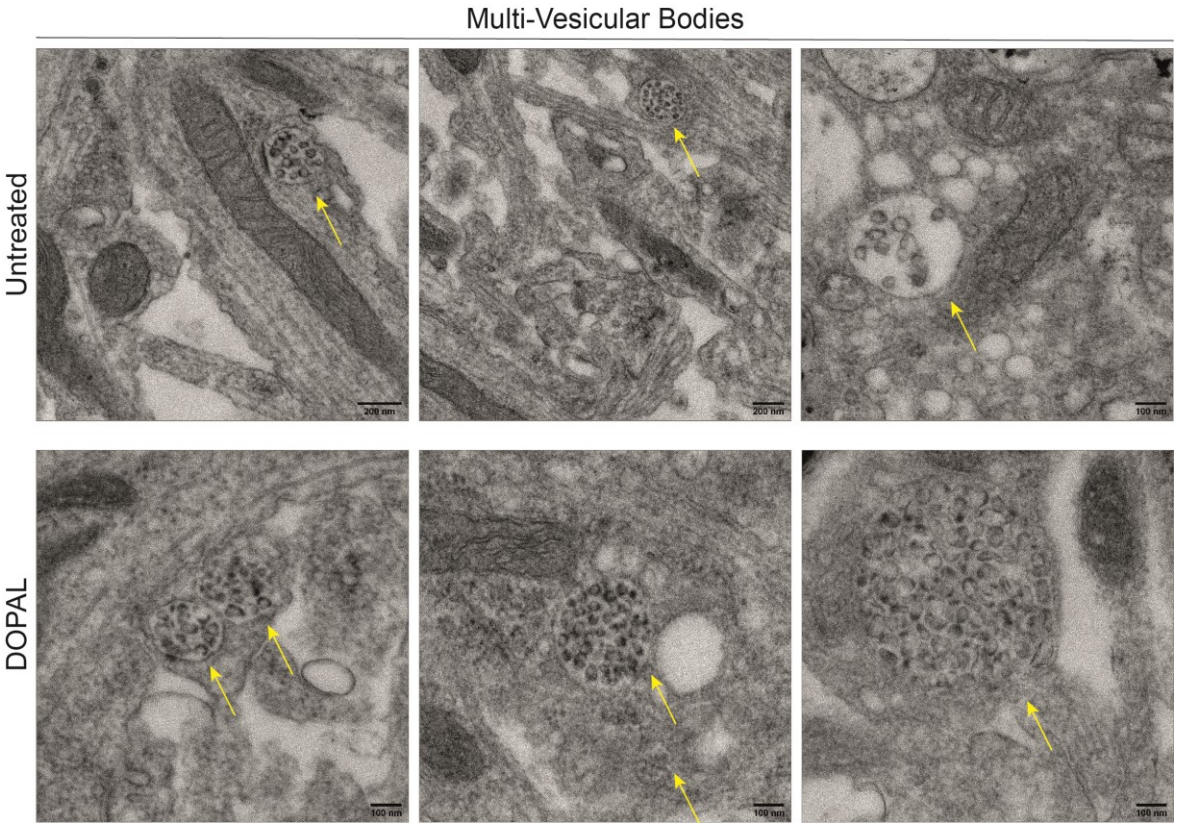

Figure 4.19 CLEM of αSyn-split miniSOG in untreated neurons and in neurons treated with 100 μM DOPAL for 24 hrs, focusing on MVBs. Representative EM images of MVBs (yellow arrows) positive for photo-oxidized αSyn-split miniSOG in Untreated and DOPAL-treated neurons.

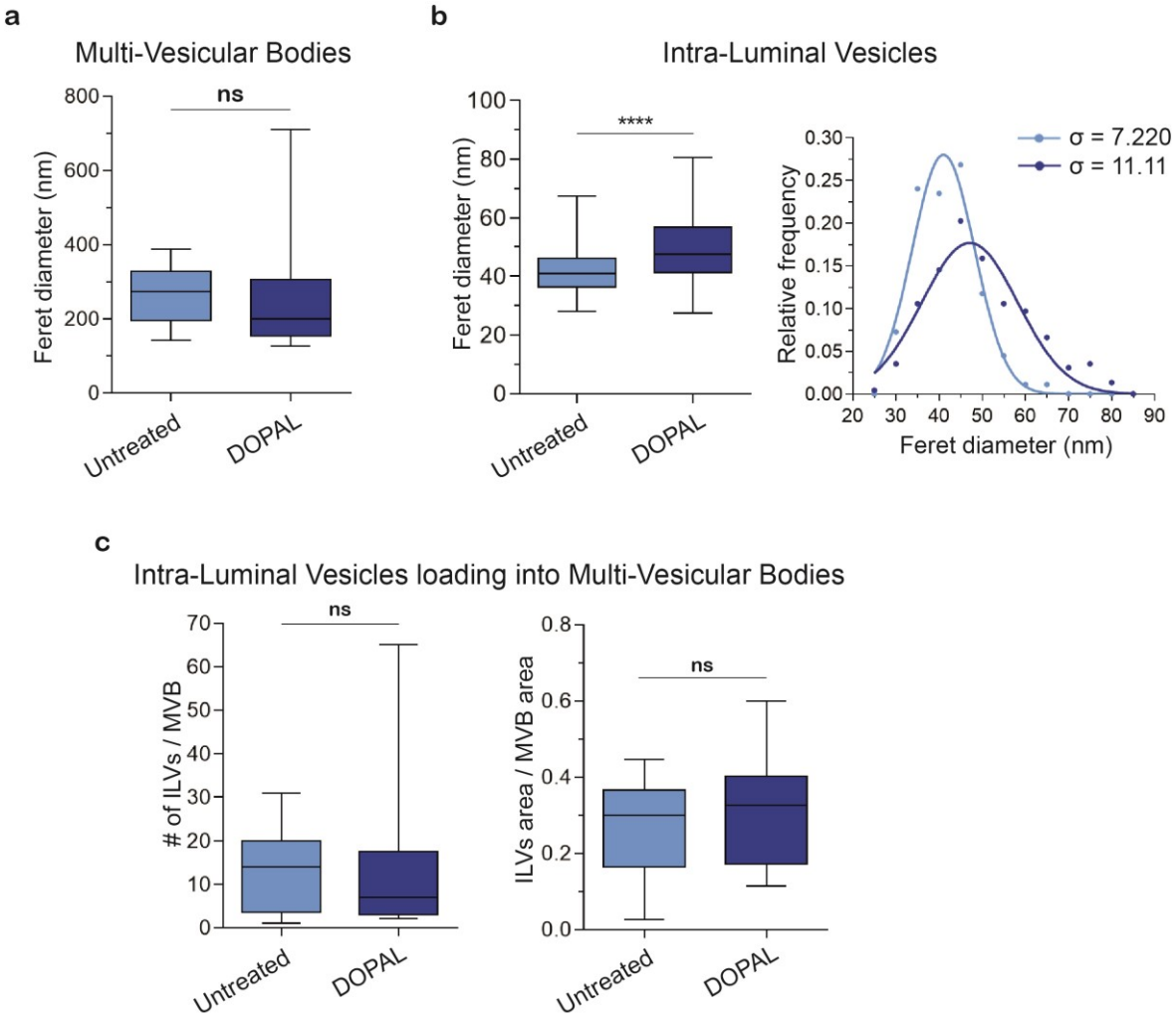

Figure 4.20 DOPAL effect on ILVs and MVBs in the CLEM of αSyn-split miniSOG. (a-b) Quantification of the Feret Diameter (nm) of MVBs and ILVs in Untreated and DOPAL-treated neurons. **(c)** Quantification of ILVs loading in MVBs, expressed as number of ILVs in each MVB and ratio between the area covered by the ILVs to the MVB area. Images were collected from one independent experiment, one photo-oxidized area each condition (Untreated 13 MVBs, 179 ILVs – DOPAL 17 MVBs, 227 ILVs). Data are presented as box-plot and, for the ILVs' Feret diameter, as frequency distribution (relative frequency), fitted with the Gaussian distribution (the color code is coherent in the two graphs). Mean values were analyzed by non-parametric Mann-Whitney test (**** $p<0.0001$).

The correspondence on the analysis of the ILVs size between the two CLEM experiments, underscore the effect of DOPAL on αSyn and the ILVs size without any interference from the two different probes used (αSyn-TimeSTAMP-YFP-miniSOG and αSyn-split-miniSOG). Instead, no significant variation in MVBs loading was observed, even though only few areas from one single experiment were analyzed so far (**Fig. 4.20c**). More sample are currently being analyzed.

4.2 Investigating the DOPAL-induced alteration of αSynuclein clearance.

4.2.1 Rationale and experimental approach.

Under physiological conditions, both the UPS and the ALP contribute in the αSyn clearance, according to the conformational state of the protein (Ebrahimi-Fakhari et al., 2011). Monomeric αSyn is reported to be degraded by the proteasome, the CMA or the endo-lysosomal pathway, whereas multimeric forms of the protein are mainly cleared by lysosomes. Instead, under pathological conditions, mutated αSyn and aberrant aggregates were suggested to impair both the proteasomal and the autophagic functions through different mechanisms (Xilouri et al., 2013).

Here, we aimed to investigate whether the observed DOPAL-induced accumulation and aggregation in the various neuronal compartments was consistent with an altered clearance of DOPAL-modified αSyn and DOPAL-αSyn oligomers. Consistently, an *in vitro* experiment of limited proteolysis by the non-specific proteinase K (PK) of DOPAL-αSyn oligomers highlights a less efficient digestion of DOPAL-modified αSyn species compared to the unmodified αSyn monomer (**Fig. 4.211a-b**). In a cellular contest, this could be translated into a general impaired degradative capacity by the cytoplasmic, proteasomal and lysosomal proteolytic enzymes, inducing an uncontrolled αSyn accumulation.

To test the hypothesis of a DOPAL-dependent impaired degradative capacity, we used diverse experimental approaches (i.e. pulse-chase experiments, imaging, cytofluorimetry) to study αSyn degradation rates and αSyn trafficking through the endo-lysosomal pathway. In this frame, it is worth mentioning that the study of αSyn degradation has an intrinsic level of complexity, as the protein exists both in the monomeric and oligomeric states, especially when overexpressed. Hence, when measuring αSyn turn-over we need to consider the presence of both species and their relative contribution, which cannot be dissected with all approaches.

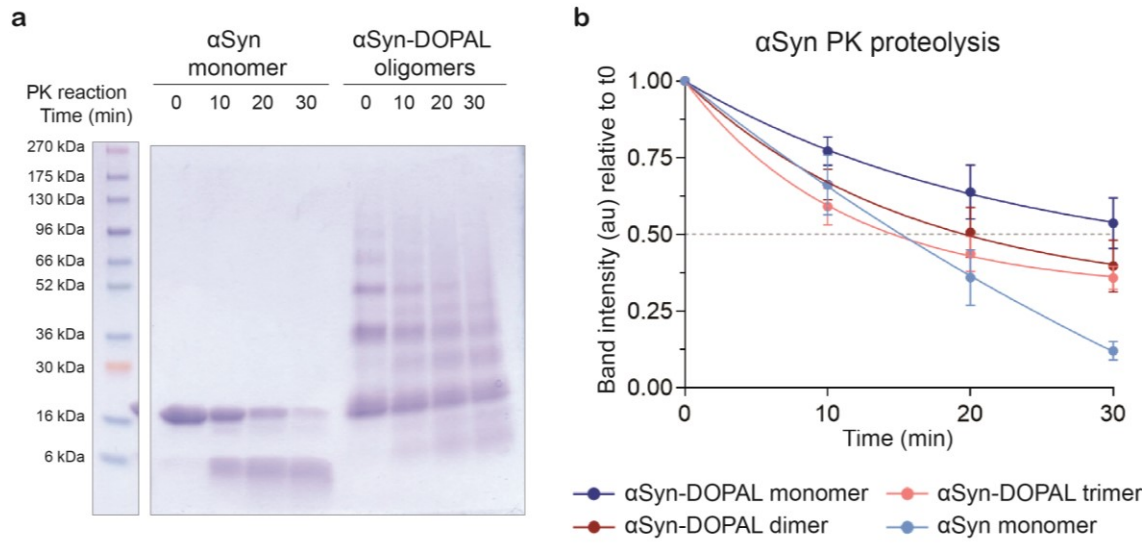

Figure 4.21 ***In vitro*** **Proteinase K digestion of recombinant αSyn monomer and DOPAL-αSyn oligomers. (a)** SDS-Page of the time-course of the PK digestion of recombinant monomeric αSyn and DOPAL-αSyn oligomers. **(b)** Quantification of the unmodified αSyn monomer and DOPAL-αSyn monomer, dimer and trimer band intensity, normalized to the amount present at t0. Data are presented as Mean ± SEM from n=4 independent experiments and fitted by one-phase decay equations.

As cellular model, we chose the catecholaminergic neuroblastoma-derived BE(2)-M17 cell line. Although they are less used than the SH-SY5Y cells in PD-related studies, under the differentiation with retinoic acid, the BE(2)-M17 cells present a neuronal-like phenotype and a higher expression of the enzymes of the dopaminergic pathway, as well as higher concentration of DA and its metabolites (Filograna et al., 2015). Both SH-SY5Y and BE(2)-M17 cells present an endogenous expression of αSyn. However, the endogenous αSyn is hard to detect by conventional western blot, since its concentration is estimated to be in the range of picograms of αSyn per µg of total proteins (**Fig. 4.22a-c**). In our experiments, αSyn was usually overexpressed with various tags cloned in frame at the C-terminus to have congruous amount of protein to work with (i.e. nanograms of αSyn-EGFP per µg of total proteins, **Fig. 4.22b-c**) and to perform all the different presented assays.

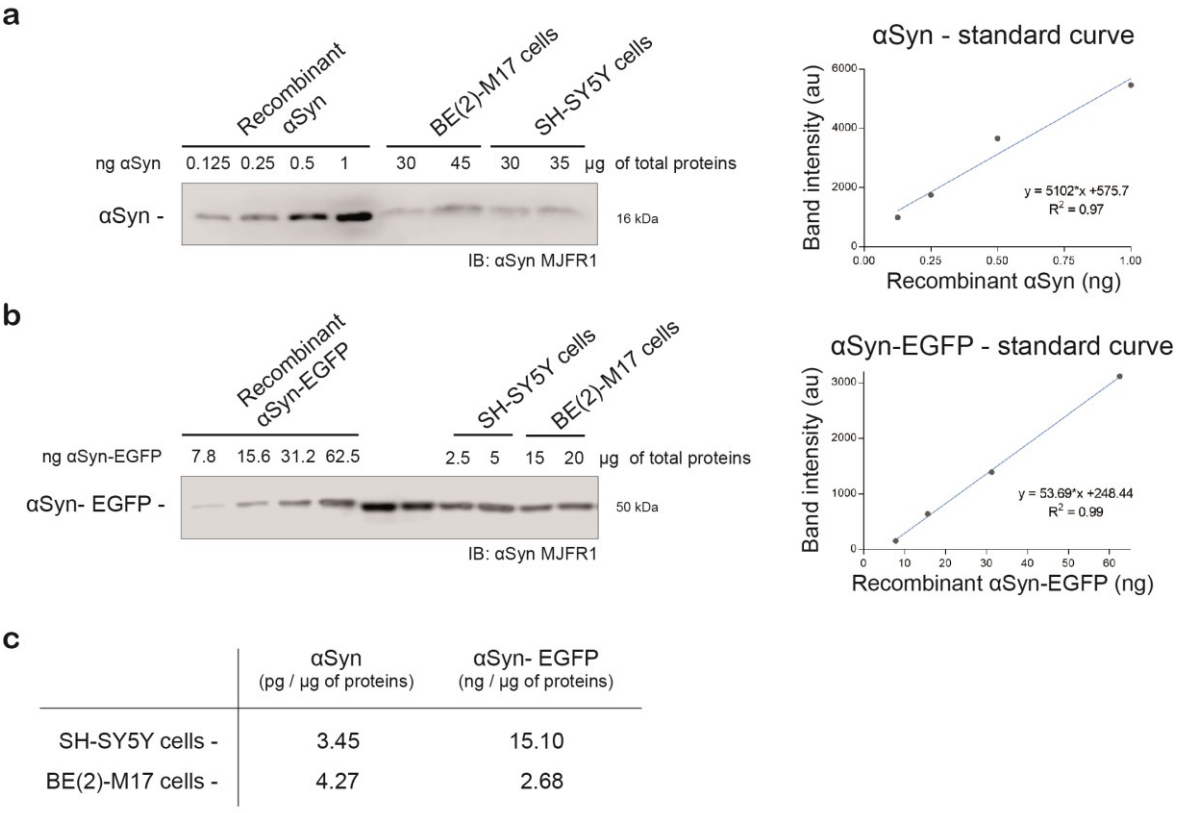

c

	αSyn (pg / µg of proteins)	αSyn- EGFP (ng / µg of proteins)
SH-SY5Y cells -	3.45	15.10
BE(2)-M17 cells -	4.27	2.68

Figure 4.22 αSyn expression levels in SH-SY5Y and BE(2)-M17 cells. (a) Western blot of different amounts of endogenous αSyn in SH-SY5Y and BE(2)-M17 cells compared with a standard curve of recombinant αSyn. **(b)** Western blot of different amounts of over-expressed αSyn-EGFP in SH-SY5Y and BE(2)-M17 cells after transient transfection compared with a standard curve of recombinant αSyn-EGFP. **(c)** Based on the densiometric analysis of the bands in the immunoblots and the standard curves generated with the recombinant αSyn and αSyn-EGFP, the αSyn expression levels of αSyn in the two cells lines were calculated.

4.2.2 DOPAL stabilizes αSynuclein oligomers and affects αSynuclein degradation rates.

To study αSyn degradation rates we performed pulse-chase experiments using the HaloTag labeling technology. The HaloTag protein is a bacterial haloalkane dehalogenase (33 kDa) designed to covalently bind synthetic ligands through an irreversible and specific cloroalkane reaction (Los et al., 2008). HaloTag ligands can be functionalized by different probes i.e. biotin and fluorophores (**Fig. 4.23**).

Hence, the administration of HaloTag ligands allows to specifically label the subpopulation of αSyn-HaloTag constructs that are expressed in the cells during the time-frame of the pulse. After washing-out the excess of unbound ligand, protein degradation can be analyzed by measuring the changes of the labeled αSyn-HaloTag levels over time by a biochemical or an imaging approach, according to the type of ligand used.

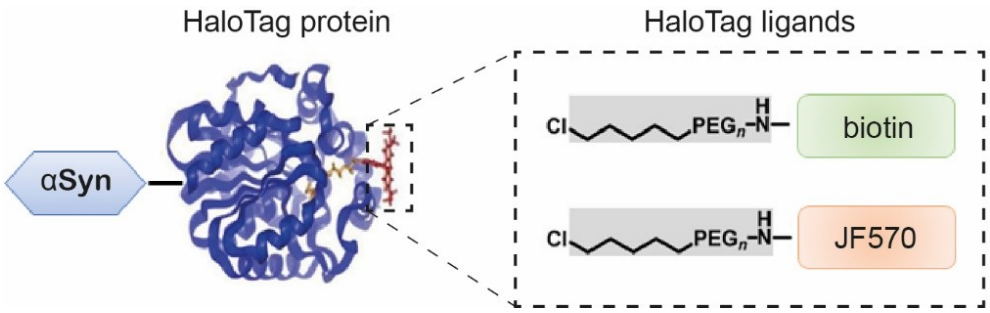

Figure 4.23 HaloTag labeling technology. Schematic representation of the αSyn-HaloTag construct, the HaloTag protein / HaloTag ligand interaction and details of the structures of the HaloTag ligands.

Here, the advantage is to specifically label the protein of interest without perturbing the whole cellular proteome, while in the commonly used approach of *de novo* protein synthesis inhibition by cycloheximide (CHX) the general proteostasis is altered. Hence, this strategy appears more suitable to analyze the effect of DOPAL on αSyn.

In a first set of experiments, we used a biochemical approach by overexpressing the αSyn-HaloTag construct in BE(2)-M17 cells, followed by a pulse-chase with the HaloTag biotin ligand. In **Fig. 4.24a**, the experimental strategy used for the αSyn-HaloTag pulse-chase with biotin ligand is described. After an overnight 100μM DOPAL treatment, cells were pulsed with the 5 μM HaloTag-biotin ligand for 3 hrs. Once the excess of ligand was washed-out, cells were collected at different time-points, lysed, and the biotinylated HaloTagged αSyn was isolated by protein pull-down with streptavidin-coated beads.

Both the wild-type αSyn and the K96R mutant were considered. Indeed, lysine 96 (K96) is believed to be a main ubiquitination site to target αSyn to the lysosomal degradation by the E3-ubiquitn ligase Nedd4 (Tofaris et al., 2011); second, K96 is

within the CMA-recognition motif of αSyn (Cuervo et al., 2004). Interestingly, K96 was one of the lysines modified by DOPAL in our LC-MS experiments on αSyn purified from DOPAL-treated BE(2)-M17 cells (Plotegher et al., 2017).

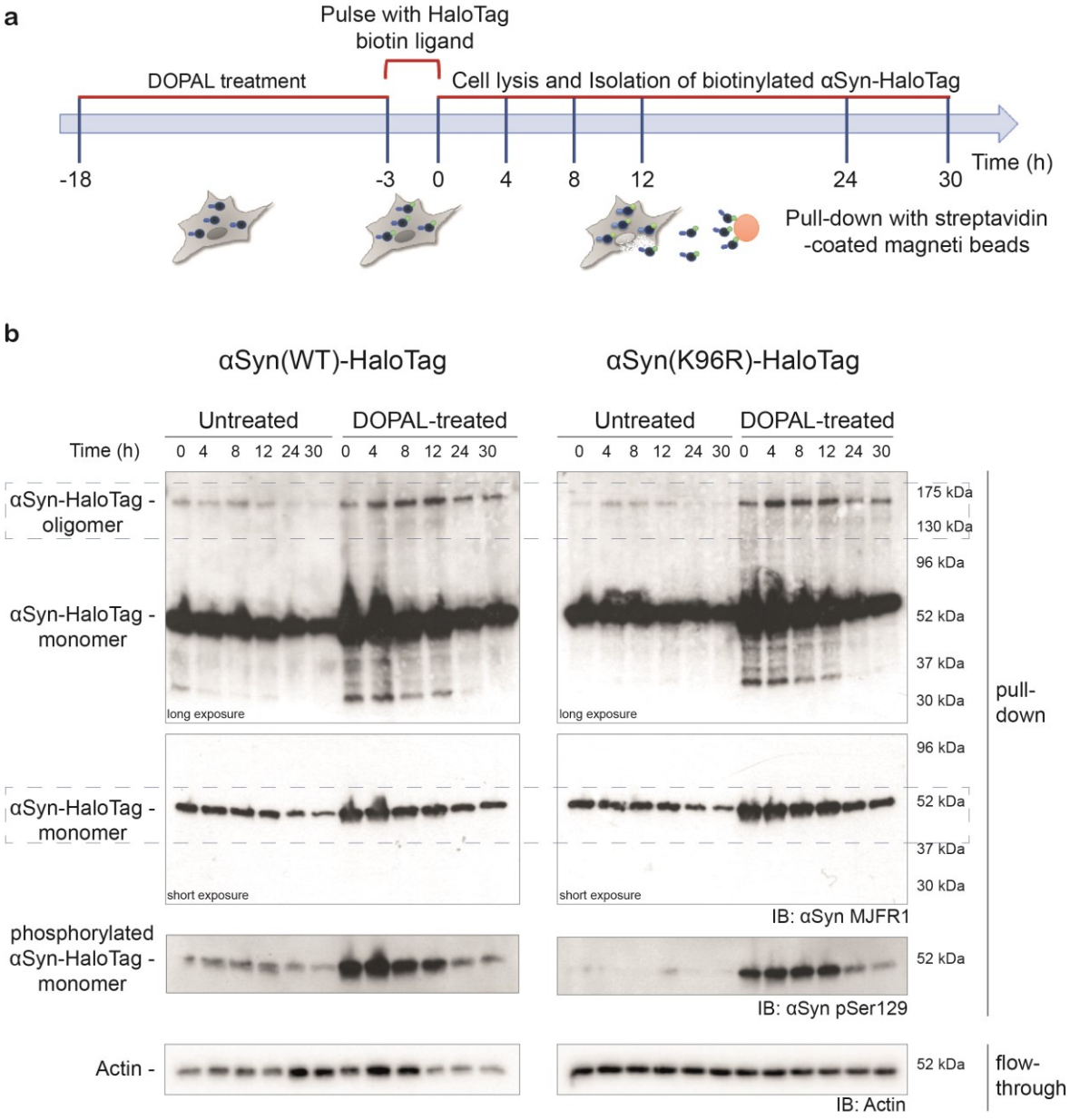

Figure 4.24. Pulse-chase experiment with HaloTag labeling technology in BE(2)-M17 cells – biochemical approach. (a) Schematic representation of the experimental setup of the pulse-chase experiment. **(b)** Western blot of the isolated biotin-labeled αSyn-HaloTag (WT and K96R) over time, in untreated and DOPAL-treated cells. In the figure, a longer (20 mins) and a shorter exposure (15 sec) of the immunoblot with the anti αSyn MJFR1 antibody is showed. Also, the immunoblot with the anti-pSer129 and the anti-Actin antibody of the pull-down flow-through is reported.

The western blot analysis of the isolated proteins in **Fig. 4.24b** reveals two distinct αSyn-positive bands, corresponding to a monomer (~52 kDa) and a covalent SDS-resistant oligomeric form (between 130 kDa and 175 kDa). Each αSyn band intensity was first normalized for the Actin in the flow-through of the pull-down and then expressed as fold-change relative to the αSyn band of t0 of untreated of each αSyn variant.

The quantification of bands corresponding to the monomeric form (**Fig. 4.25a**) show a progressive decrease αSyn levels in the untreated cells, with a similar pattern in both the WT and the K96R αSyn-HaloTag. Instead, in the DOPAL-treated cells, higher levels of the monomeric αSyn in both genotypes are measured, suggesting a progressive accumulation of DOPAL-modified αSyn-HaloTag during the overnight treatment. Also, the level of the monomer is basically constant within the 30 hrs of the experiment. Although αSyn-positive bands at lower molecular weight of the monomer in the DOPAL-treated samples, suggest the presence of degradation products or truncated αSyn-HaloTag. This could imply both an attempt to degrade the DOPAL-modified αSyn monomers but also a cleavage of αSyn in response to DOPAL, that needs further investigations.

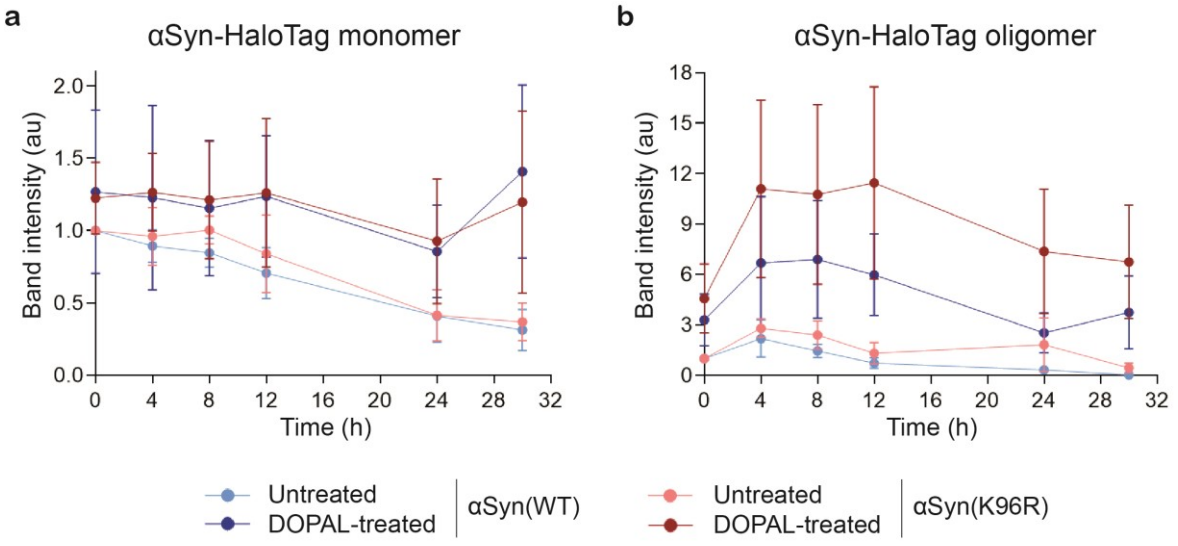

Figure 4.25 Pulse-chase experiment with HaloTag labeling technology in BE(2)-M17 cells – biochemical approach. Quantification of the levels of the αSyn-HaloTag **(a)** monomer and **(b)** oligomer during the time-course. Data are presented as Mean ± SEM from n=4 independent experiments.

Correspondingly, the quantification of the oligomeric αSyn-HaloTag in **Fig. 4.25b**, points out a higher accumulation of DOPAL-induced oligomers at t0 (3-4 fold), followed by a rapid increase in the first 4 hrs and a slow decay during the time-course. Interestingly, the K96R αSyn mutant displays a higher resistance to degradation in DOPAL treated cells, suggesting the implication of the lysosomal pathway in mediating the clearance of pathological forms of αSyn.

Few other considerations are due in the analysis of this result. First, even though the sole αSyn-HaloTag overexpression induces minimal αSyn oligomerization (due to the αSyn propensity to aggregate and / or the effect of the tag), DOPAL shows its greatest action in enhancing and stabilizing the αSyn oligomers. This result confirms the DOPAL action in triggering αSyn oligomerization in covalent detergent-resistant species, which are more difficult to be degraded. Also, as for the previous experiments, we cannot exclude the possibility of aggregation between both the tagged and the endogenous αSyn.

On the other side, it is worth mentioning that the αSyn-positive band at ~52 kDa represents both the unmodified and the DOPAL-modified αSyn-HaloTag monomers. This would lead to an underestimation of the effect of DOPAL-modification in the degradation of the monomer, for example by competing with the ubiquitination that target αSyn monomers to the proteasome.

Taken together, these data highlight the role of DOPAL in triggering αSyn oligomerization, stabilizing these species and decreasing αSyn turn-over. Because of the complexity of the regulation of αSyn degradation, which is mediated by different pathways, additional evaluations were considered to dissect the issue.

4.2.3 DOPAL induces a dose-dependent increase in αSynuclein phosphorylation at serine 129.

In the previous experiment, the immunoblot with the anti-pSer129 antibody on the monomeric αSyn-HaloTag, revealed a DOPAL-dependent increase in the level of monomeric αSyn phosphorylated at serine 129 (pSer129).

Interestingly, the estimated fraction of phosphorylated αSyn under physiological condition is around 4%, whereas in patients with synucleinopathies as well as transgenic animal models of PD, the fraction of pSer129 increases up to 90% (Oueslati, 2016). pSer129 has been reported to modulate αSyn membrane binding, interaction with metal ions, protein-protein interaction, subcellular localization but also to regulate protein turnover, with controversial evidence. Even though the precise role of this PTM on αSyn proteostasis is still unclear, pSer129 is widely recognized as a marker of aberrant αSyn species.

Here, immunocytochemistry and independent western blot analysis confirm a DOPAL dose-dependent hyper-phosphorylation of αSyn, suggesting that the DOPAL modification and induced aggregation of the protein generate αSyn species associated to the pathology (**Fig. 4.26a-c**).

Based on the literature, multiple pathways have been proposed to mediate the clearance of phosphorylated αSyn. According to Machiya et al., the phosphorylated αSyn is targeted to the proteasomal degradation in a ubiquitin-independent manner decreasing the overall αSyn half-life (Machiya et al., 2010), whereas the work by Oueslati suggests that the αSyn phosphorylation at Ser129 by the PLK2 promotes the phosphorylated αSyn clearance via autophagy (Dahmene et al., 2017; Oueslati et al., 2013). Hence, we decided to compare in our model the half-lives of the WT αSyn with the K96R mutant and the non-phosphorylable S129A αSyn form. However, a time-course experiment in the presence of CHX doesn't reveal any significant variation in the kinetics of αSyn degradation in the three different genotypes analyzed **(Fig. 4.27a-b**). Specifically, the calculated half-lives are: αSyn(WT) $t_{1/2}$ = 18.74 ± 2.34 hrs, αSyn(K96R) $t_{1/2}$ = 15.83 ± 3.80 hrs, αSyn(S129A) $t_{1/2}$ = 18.95 ± 1.36 hrs (**Fig. 4.27c**).

In the future, it will be of interest to determine the contribution of the different degradative pathways in mediating the degradation of the three αSyn variants and whether DOPAL modification on the protein when it cannot be phosphorylated has a different behaviour.

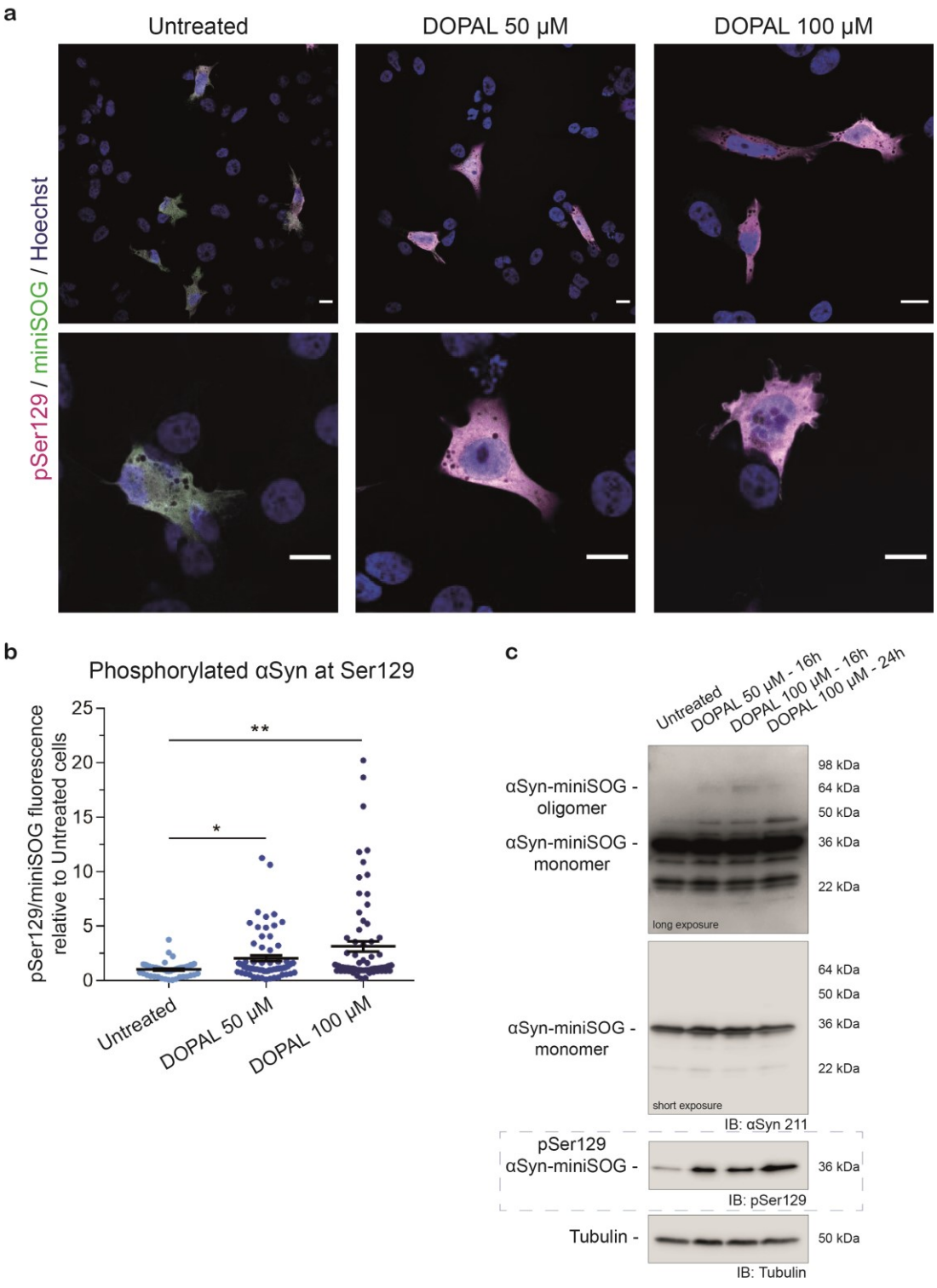

Figure 4.26 DOPAL-induced αSyn phosphorylation at Ser129. (a) Immunocytochemistry of BE(2)-M17 cells over-expressing αSyn-miniSOG after an overnight 0-50-100 µM DOPAL treatment. In the figure, two representative images at different magnification for each condition are showed, as merge of the miniSOG fluorescence (green), the immunolabeling with the anti-pSer129 antibody (magenta) and the Hoechst staining of the nuclei (blue). Scale bar: 10 µm. **(b)** Quantification of the pSer129 signal in each single cell, normalized for the relative miniSOG fluorescence and expressed as fold-change compared to untreated cells. *continues*

Figure 4.26 *continues* Data are presented as Mean ± SEM from n=3 independent experiments pooled together and analyzed by the non-parametric Kruskall-Wallis test with the Dunn's multiple comparisons test (* p<0.05, ** p<0.01). **(c)** Western blot of BE(2)-M17 cells over-expressing αSyn-miniSOG after various DOPAL treatments. In the figure, a longer and a shorter exposure of the immunoblot with the anti αSyn 211 antibody is showed, together with the immunoblot with the anti pSer129 and the anti-Tubulin antibody as loading control.

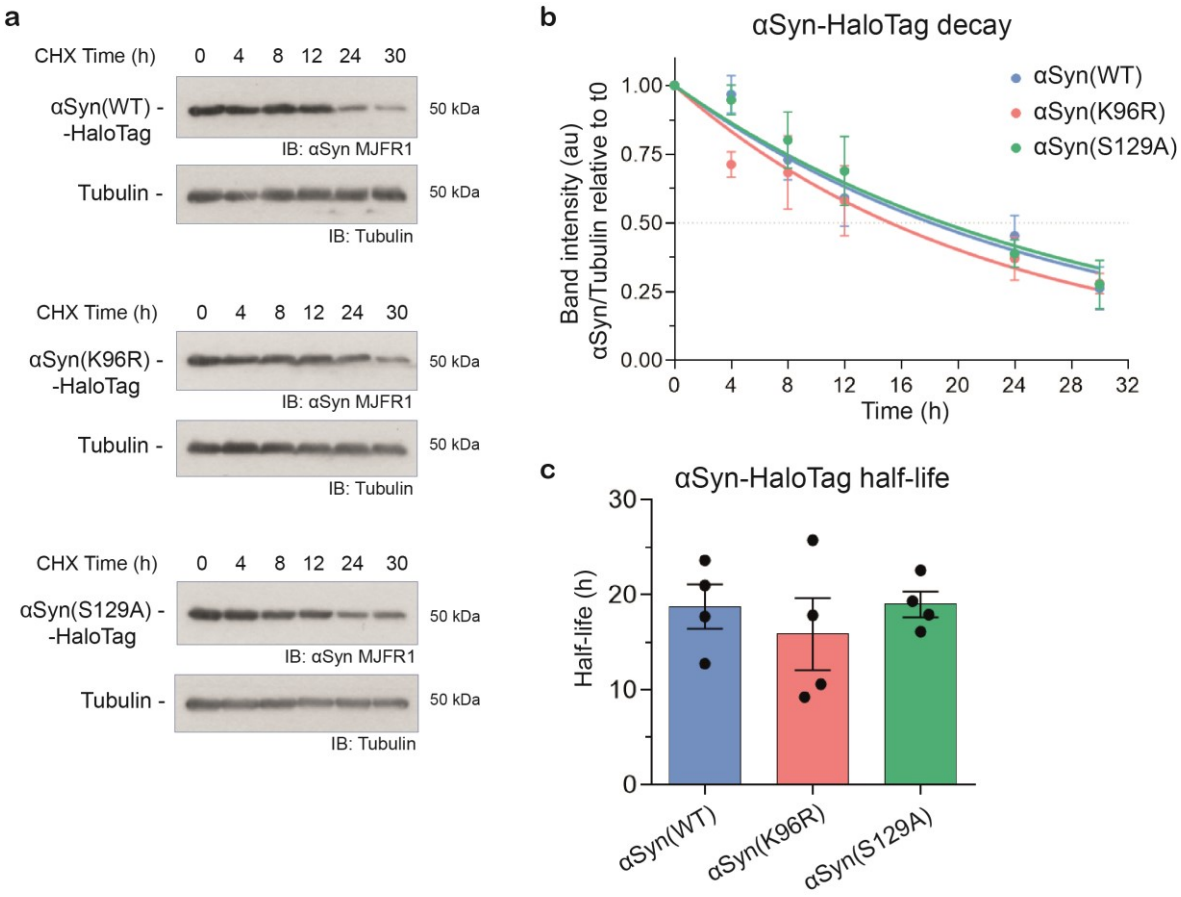

Figure 4.27 Comparison among the αSyn WT, K96R and S129A degradation rates. **(a)** Western blot of BE(2)-M17 cells over-expressing αSyn(WT)-HaloTag, αSyn(K96R)-HaloTag and αSyn(S129A)-HaloTag. For each genotype, time-course experiments were performed within the inhibition of *de novo* protein synthesis by CHX 50 µg/ml. **(b)** Quantification of αSyn-HaloTag levels at the different time-points, normalized for the relative Tubulin band intensity and for the αSyn-HaloTag amount at t0. Data are presented as Mean ± SEM from n=4 independent experiments per genotype and fitted by one-phase decay equations. **(c)** αSyn-HaloTag half-lives calculated in the individual experiments of each genotype. Data are presented as Mean ± SEM and analyzed by the non-parametric Kruskall-Wallis test with the Dunn's multiple comparison test.

4.2.4 DOPAL promotes αSynuclein localization into lysosomal compartments.

Taking advantage of the versatility of the HaloTag labeling technology, we performed a pulse-chase experiment following an imaging approach. In this case, we used the HaloTag JF570 fluorescent ligand (excitation peak at 570 nm) designed by the Lavis lab (HHMI Janelia Labs). As the other commercially available HaloTag ligand, the JF570 ligand easily diffuses in the cells and specifically binds the HaloTag proteins that are expressed in that time-frame. In this case, we aimed to study αSyn redistribution in the cells within the timeframe of DOPAL build-up in the cellular environment. In details, BE(2)-M17 cells overexpressing αSyn(WT)-HaloTag and αSyn(K96R)-HaloTag were administrated with 3 μM JF570 ligand for 30 minutes. After ligand wash out, cells were incubated with DOPAL 100 μM and fixed at different time points. The fluorescence signal of the JF570-labeled αSyn-HaloTag was then acquired with at the laser scanning confocal microscope (**Fig. 4.28**).

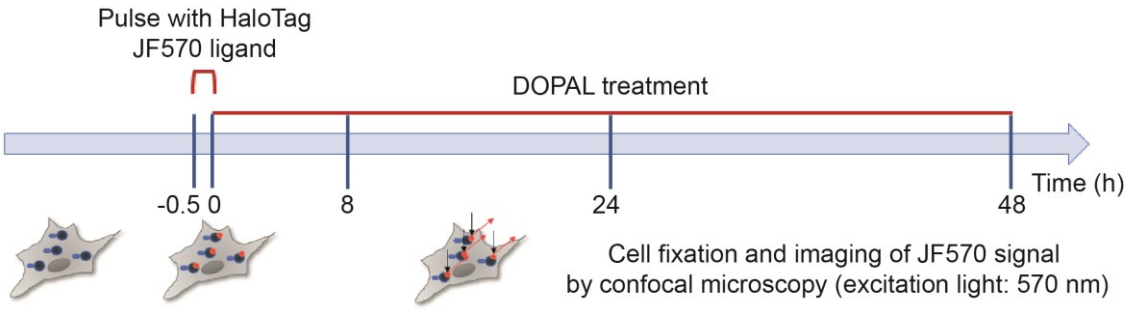

Figure 4.28 Pulse-chase experiment with HaloTag labeling technology in BE(2)-M17 cells – imaging approach. Schematic representation of the experimental setup of the pulse-chase experiment.

Surprisingly, the overall JF570 fluorescence doesn't show a marked decrease over time (**Fig. 4.29**), failing to serve as assay to measure αSyn degradation rates. This is probably due to the high variability in the fluorescence intensity among cells, which limits a rigorous quantitative analysis of the variations in different pools of cells at each time-point, unless the analysis includes a considerable number of cells per sample. Also, the JF570 fluorophore revealed an intrinsic resistance to acidic pH and lysosomal proteases (see later).

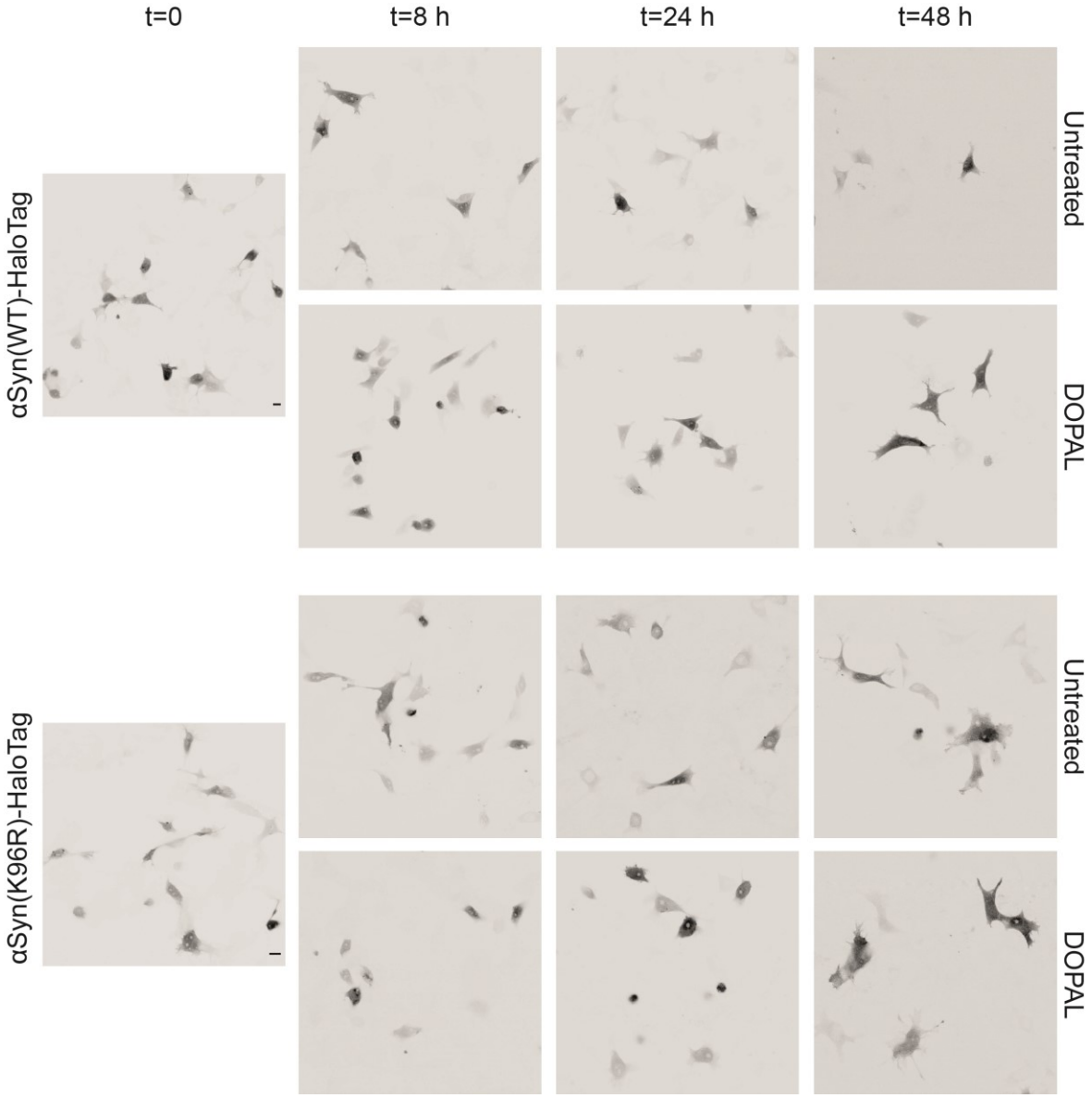

Figure 4.29 Pulse-chase experiment with HaloTag labeling technology in BE(2)-M17 cells – imaging approach. Representative images of labeled αSyn(WT)-HaloTag and αSyn(K96R)-HaloTag at the different time-points in untreated and DOPAL-treated cells. Images were acquired with a 40x objective and acquisition parameters were normalized to t=0 and kept unchanged for all conditions. Scale bar: 10 μm.

Anyway, by observing the cells for both αSyn genotypes at t=48 hrs at a higher magnification, we noticed the presence of JF570-positive inclusions in the cytoplasm, significantly increased in the DOPAL-treated cells (**Fig. 4.30a-b**). Hence, in this experimental setup, a long-term DOPAL treatment leads to rearrangements in the intra-cellular distribution of αSyn, triggering its aggregation.

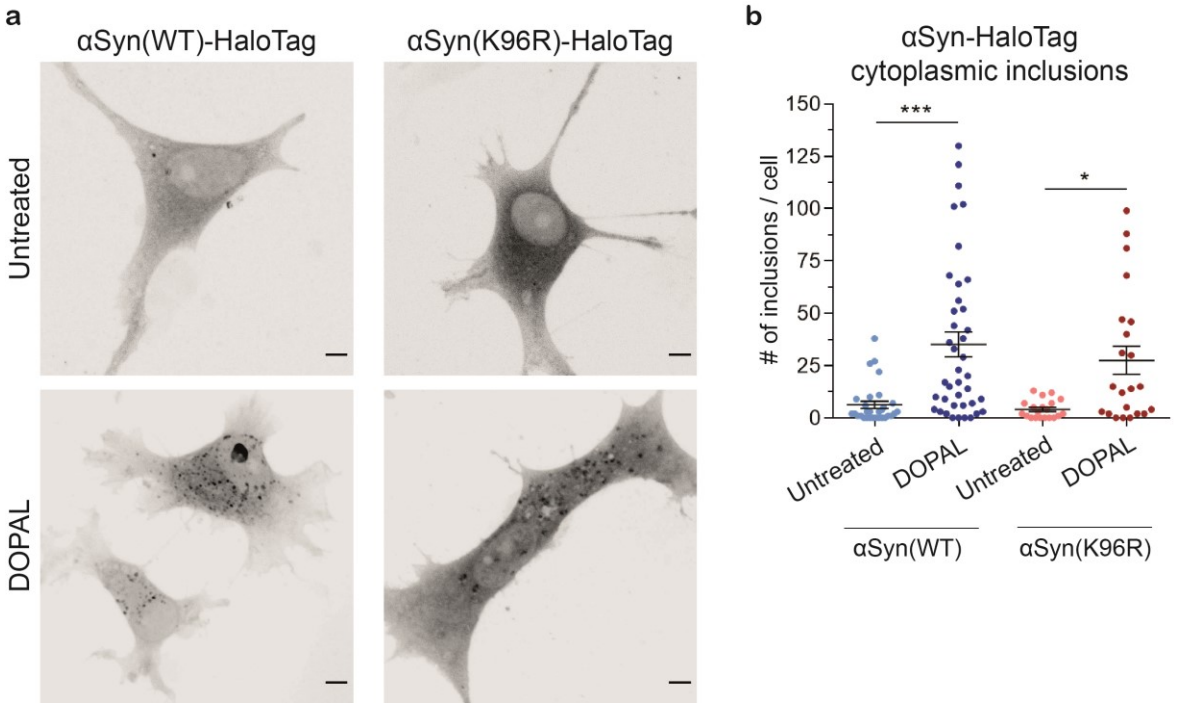

Figure 4.30 High magnification of JF570-labeled αSyn-HaloTag in BE(2)-M17 overexpressing cells, at t=48 hrs after the pulse-chase. (a) Representative images of labeled αSyn(WT)-HaloTag and αSyn(K96R)-HaloTag 48 hrs after the JF570 ligand pulse-chase, in untreated and DOPAL-treated cells. Z-stack images were acquired with a 63x objective. Scale bar: 5 μm. **(b)** Quantification of the number of JF570-positive intra-cytoplasmic inclusions in the four conditions. Data from n=3 independent experiments for αSyn(WT)-HaloTag and n=2 independent experiments for αSyn(K96R)-HaloTag are pooled together; they are presented as Mean ± SEM and analyzed by Kruskal-Wallis non-parametric test with Dunn's multiple comparisons test (* $p<0.05$, *** $p<0.001$).

To better investigate the entity and the subcellular localization of αSyn aggregates induced by DOPAL in BE(2)-M17 cells, we performed a CLEM analysis on both the αSyn(WT)-HaloTag and αSyn(K96R)-HaloTag, as the JF570 HaloTag ligand is designed to catalyze the DAB polymerization under photo-oxidative conditions (**Fig. 4.31a-c**). Notably, in the untreated cells, αSyn is mostly monomeric and cytoplasmatic, as denoted by the darker diffuse staining. Instead, in the DOPAL-treated cells, αSyn is highly accumulated in lysosomal-like compartments, confirming the previous observation at the confocal microscopy (**Fig. 4.31b-d**, indicated by yellow arrows). Indeed, in both experiments the K96R mutant appears to accumulate into the lysosomes to a less extent than the WT, which would be consistent with the impaired targeting to the endo-lysosomal pathway by the amino acidic substitution.

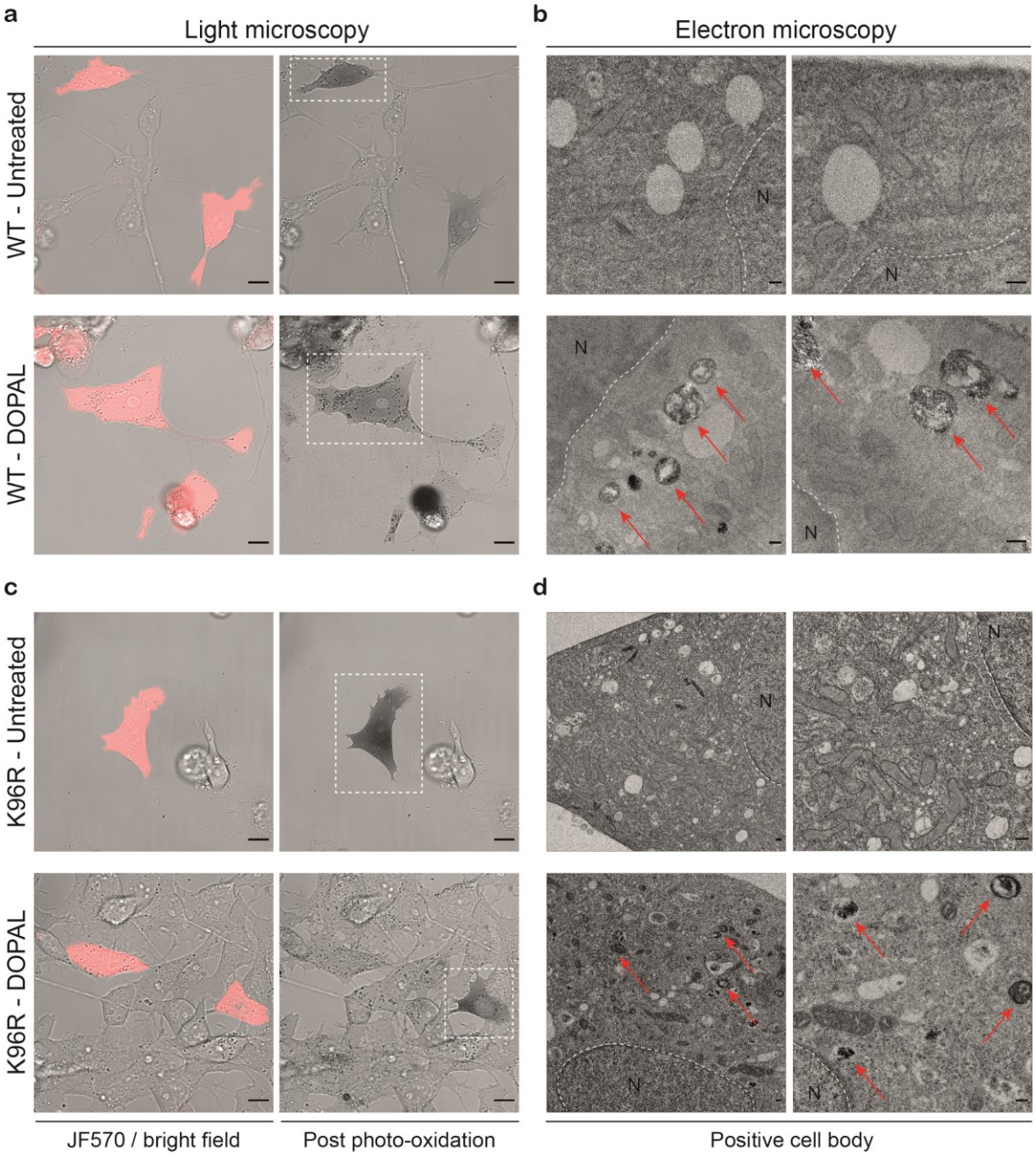

Figure 4.31 CLEM of αSyn(WT)-HaloTag and αSyn(K96R)-HaloTag in Untreated and DOPAL-treated BE(2)-M17 cells, 48 h after the JF570 ligand pulse-chase. (a-c) Confocal imaging before and after photo-oxidation, as overlay of JF570 fluorescence (red signal) and bright field image. In the post photo-oxidation images, the appearance of the optically visible DAB reaction product correlates with the JF570 fluorescence. Scale bar: 10 µm. **(b-d)** Electron micrograph of the photo-oxidized cells indicated by the white squares in the LM images. In the DOPAL-treated cells, the red arrows indicate the accumulated αSyn into the lysosomal-like compartments. N: nucleus. Scale bar: 200 nm.

Finally, to further corroborate the observations that DOPAL is inducing on αSyn trafficking into the endo-lysosomal pathway, we are currently setting up cytofluorimetric assay with αSyn tagged by the pH-sensitive fluorophore mKeima (where “m” stands for monomeric). Briefly, the mKeima probe is a coral GFP-like protein of 25 kDa, resistant to acidic pH and lysosomal proteases (Katayama et al., 2008, 2011). The key feature is the different excitation spectra according to the pH of the surrounding environment. At pH8, the protein has an absorbance peak at 438 nm, which is progressively shifted at higher wavelength values with decreasing pH, with an absorbance peak at 550 nm at pH 4 (**Fig. 4.32a**). By calculating the ratio of the fluorescence emission at 600nm after excitation at both 438 nm and 550 nm, it is possible to infer the pH of the compartment in which the protein is trafficking. Here, we adapted a protocol to measure the mitophagy index using the mito-Keima probe, that was set up by measuring the mito-Keima fluorescence switch in the cells by cytofluorimeter (Um et al., 2018). On the same line, the αSyn-mKeima construct was used to determine the percentage of αSyn trafficking into the lysosomes in response to DOPAL treatment together the modulation of the UPS and ALP. Specifically, αSyn-mKeima overexpressing BE(2)-M17 cells were analyzed at the cytofluorimeter for their dual-excitation ratiometric measurements (405 nm/561 nm; refer to the Materials and Methods section for details) that allows to cluster the positive cells into two groups: the “low” cells with a 561/405 ratio < 1 that represent the cells with more cytoplasmic αSyn; the “high” cells with a 561/405 ration > 1 that indicates the cells with more lysosomal αSyn (in **Fig. 4.32b** the representative results in basal condition are reported). In **Fig. 4.32c** a preliminary result, showing the quantification of the percentage of cell with lysosomal αSyn-mKeima after an overnight 100 μM DOPAL treatment, coupled with modulators of the protein degradation systems, suggests that DOPAL potentially promotes the lysosomal localization of αSyn, that is more emphasized when autophagy is upregulated by starvation. Also, the increasing levels of αSyn-mKeima in acidic compartments within the inhibition of the proteasome by MG132, suggests a contribution of the UPS in the degradation of the protein, even though any different behavior between the monomeric and the oligomeric αSyn cannot be dissected in this experimental setup.

In the future, this experiment will be performed again to confirm these preliminary observations and to explore whether prolonged DOPAL treatments exacerbate the αSyn lysosomal localization.

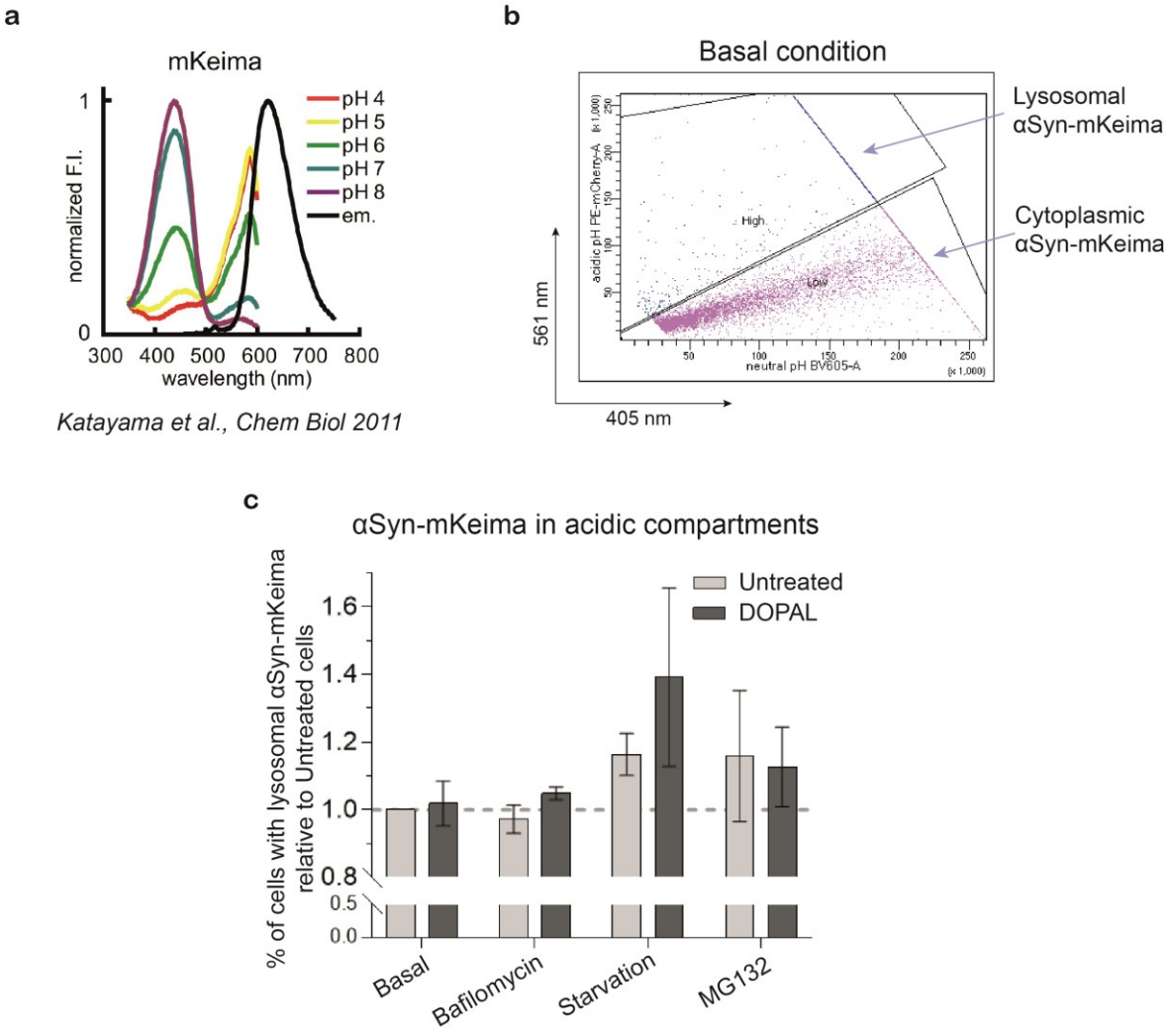

Figure 4.32 Cytofluorimetric assay of αSyn trafficking into lysosomal compartments. (a) Excitation and emission fluorescence spectra of the mKeima probe. Adapted from *Katayama et al., Chem Biol 2011*. **(b)** Representative image of the output from the dual-excitation ratiometric measurement at the cytofluorimeter of αSyn-mKeima over-expressing BE(2)-M17 cells in basal condition. In the x axis, the emission in response to the excitation at 405 nm is plotted, in the y axis the excitation at 561 nm. **(c)** Quantification of the percentage of cells with lysosomal αSyn-mKeima in untreated versus DOPAL-treated cells (100 μM DOPAL for 16 hrs), in basal conditions or in the presence of 20 nM Bafilomycin, 20 μM MG132 and autophagy activation by starvation. Data are presented as Mean ± SEM from n=2 independent experiments.

4.3 Studying the protein clearance capacity of cells in the presence of accumulated DOPAL.

4.3.1 Rationale.

In neurons, the regulation of protein turn-over and clearance is an essential process to ensure the proper cellular homeostasis. This represents a challenge as neurons are post-mitotic cells that must rely on their protein quality control systems to avoid the accumulation of misfolded and aggregated proteins. However, in PD and other neurodegenerative diseases, the failure of protein degradation systems is a well-known feature that leads to protein burden and further deposition in LBs (Ross and Poirier, 2004).

As mentioned before, αSyn turn-over depends on both pathways. However, pathological αSyn species i.e. oligomeric or mutated αSyn, are believed to impair both UPS and ALP functionality. Hence, a similar hindering action could be associated to both DOPAL-modified αSyn and DOPAL-αSyn oligomers.

Starting from the DOPAL-induced decreased αSyn degradation and accumulation in the lysosomal compartments, we aimed to investigate the functionality of the UPS and the autophagic flux, wondering whether the cell can efficiently remove the DOPAL-αSyn species and maintain the appropriate cellular proteostasis.

4.3.2 DOPAL build-up potentially impairs the ubiquitin-proteasome system.

The ubiquitination by poly-ubiquitin chains built on K11- and K48-linkages represent the main post-translational modification that target the proteins to the degradation by the proteasome. Hence, a commonly used read-out of the impaired proteasome activity is the assessment of the ubiquitinated proteins amount of the cells by western blot (Myeku et al., 2011). Interestingly, we detected a dose-dependent accumulation of high-molecular-weight ubiquitinated proteins both in BE(2)-M17 cells and rat primary cortical neurons after treatment with increasing concentrations of DOPAL (**Fig. 4.33a-c**).

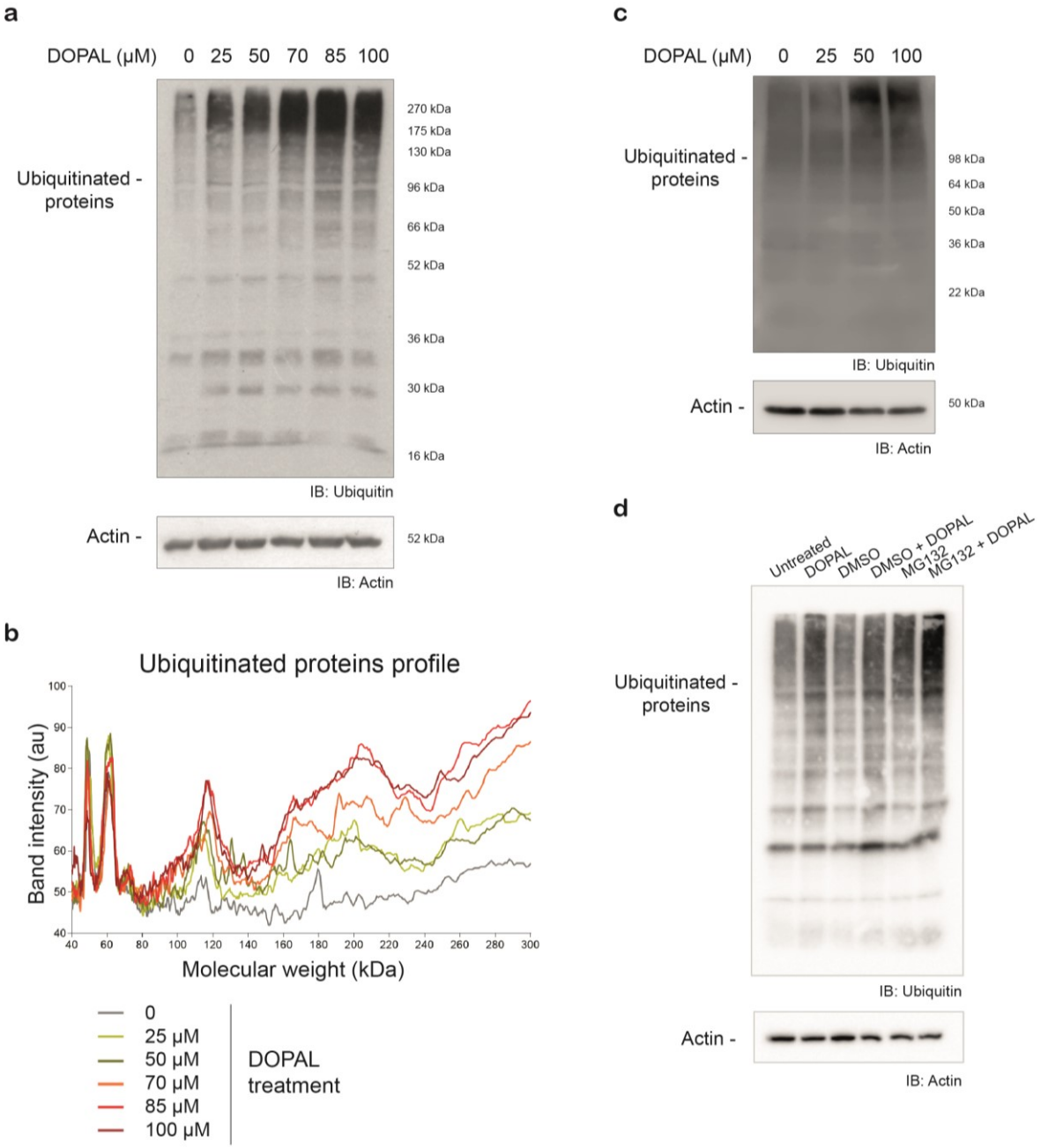

Figure 4.33 Accumulation of ubiquitinated proteins as read-out of DOPAL-induced inhibition of the proteasome. (a) Immunoblot with the anti-Ubiquitin antibody in BE(2)-M17 cells after an overnight treatment with increasing concentrations of DOPAL (0-25-50-70-85-100 μM). The anti-Actin was used as loading control. **(b)** Band intensity profile of the smear detected by the anti-ubiquitin antibody among the different DOPAL treatments. In the graph, the x axis is expressed in kDa, as each pixel along the smear was assigned to a specific molecular weight, based on the standard curve calculated from the distances among the bands of the protein ladder. **(c)** Western blot of BE(2)-M17 cells after an overnight treatment with 100 μM DOPAL, in untreated condition, DMSO or 20 μM MG132 administration. **(d)** Western blot of rat primary cortical neurons after an overnight treatment with increasing concentrations of DOPAL (0-25-50-100 μM).

A similar degree of accumulation of ubiquitinated proteins is observed upon pharmacological proteasome inhibition by MG132, with a cumulative effect after the co-administration of MG132 and DOPAL, suggesting that DOPAL is affecting the ubiquitin signaling and blocking the proteasomal activity (**Fig. 4.33d**).

4.3.3 DOPAL build-up potentially affects the autophagic flux.

In parallel, we investigated any alteration in the functionality of ALP induced by DOPAL treatments. Usually, to monitor the autophagic flux, the levels of the autophagic effectors and substrates LC3b-II and p62/SQSTM1 are quantified, comparing their relative amounts under basal condition with the pharmacological inhibition by small molecules i.e. chloroquine and bafilomycin A1. Chloroquine is a drug used in the prophylaxis of malaria, but it is also known to induce autophagy inhibition by blocking the acidification of lysosomes. Bafilomycin A1 is an antibiotics and specific inhibitor of the V-ATPase pump that regulates the proton influx in the lysosomal lumen. Moreover, bafilomycin A1 inhibits the lysosome fusion with the autophagosomes. In these experimental conditions, a low level of p62 indicates an active autophagic flux, instead the accumulation of both LC3b-II and p62 is a read-out of a blocked autophagy.

Coherently, as showed in **Fig. 4.34a** and the relative quantification in **Fig. 4.34b**, the blockage of the autophagic flux by both chloroquine and bafilomycin A1 induces an increase in the level of p62, whereas the starvation promotes p62 degradation leading to lower protein levels, as expected. Interestingly, the addition of DOPAL results in multiple p62-positive bands, suggesting the presence of SDS-resistant p62 oligomers. Similarly, the immunolabeling with the anti-p62 antibody of BE(2)-M17 cells, reveals the presence of bright dots in the cytoplasm reveling accumulated p62 in DOPAL-treated cells, an effect that was exacerbated by the co-treatment of DOPAL and chloroquine (**Fig. 4.34c**). Indeed, p62 oligomerization is another indication of impaired autophagy. In this frame it is worth to mention that high levels of p62 oligomers are found in PD patients' brains and within LBs (Kuusisto et al., 2003).

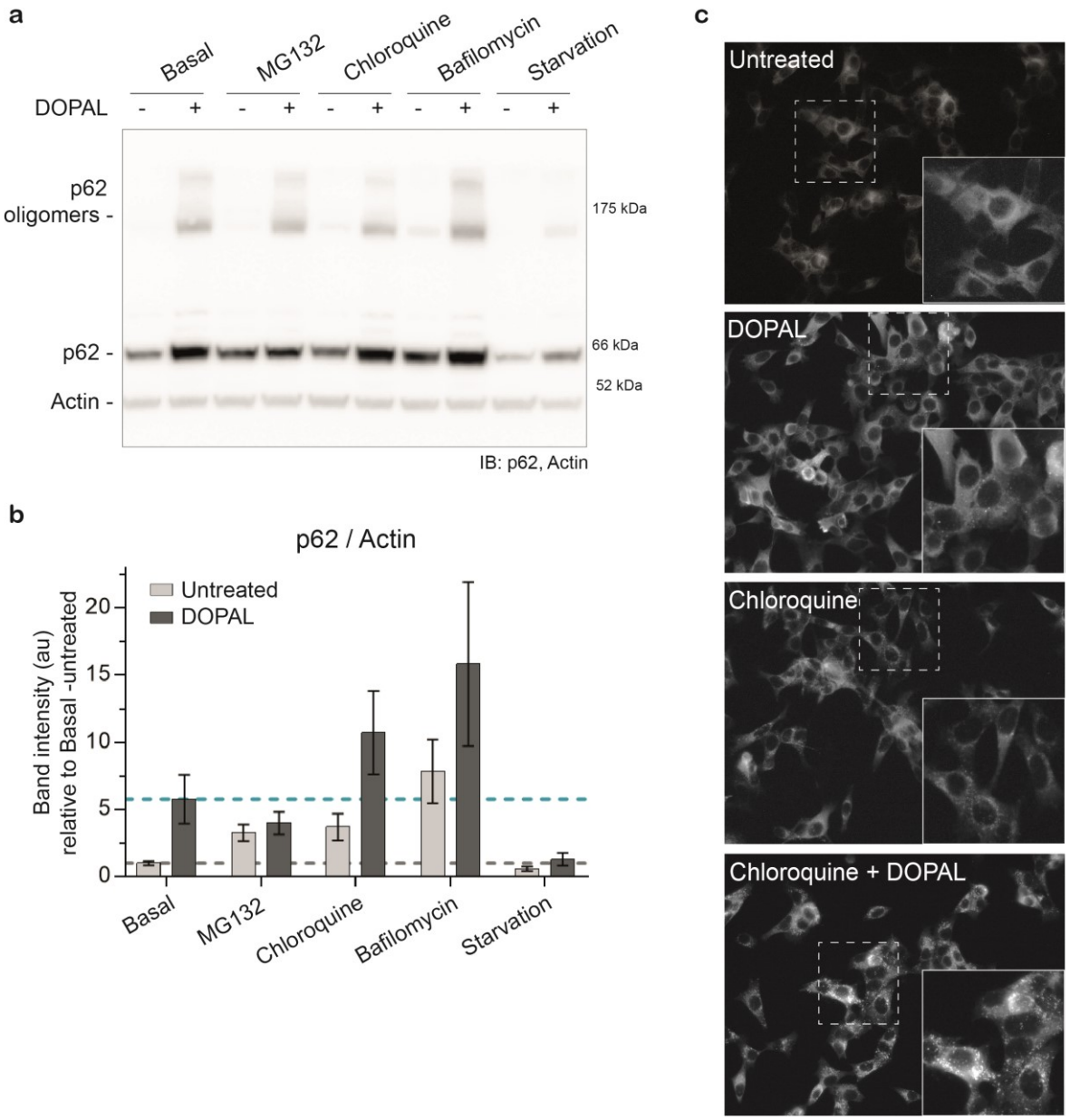

Figure 4.34 Studying the autophagic markers as read-out of the autophagic flux. (a) Western blot of BE(2)-M17 cells after an overnight 100 μM DOPAL treatment versus untreated cells, in basal condition, proteasome inhibition by 20 μM MG132, autophagy blockage by 50 μM chloroquine and 20 nM bafilomycin A1, and autophagy activation by starvation. The immunoblot with the anti-p62 antibody reveals both the p62 monomeric and oligomeric bands. The anti-Actin was used as loading control. **(b)** Quantification of the p62 levels, expressed as fold change compared to the basal untreated condition. Data are presented as Mean ± SEM from n=3 independent experiments with n=2 technical replicates each. In the figures, the grey dotted line is the reference of the level in the untreated basal sample, while the light blue dotted line is the reference of the DOPAL-treated sample. **(c)** Immunocytochemistry with the anti-p62 antibody of BE(2)-M17 cells untreated or treated with 100 μM DOPAL, 50 μM chloroquine and the coupled treatment of chloroquine and DOPAL.

Finally, as an impaired cellular proteostasis due to blockage of the ALP is frequently accompanied by the engulfment of the endoplasmic ER (Kaushik and Cuervo, 2015), we looked for the levels of Calnexin and Calreticulin as read-out of ER-stress. Although increasing DOPAL treatments results in progressive p62 accumulation, no variations are observed in the Calnexin levels (**Fig. 4.35**).

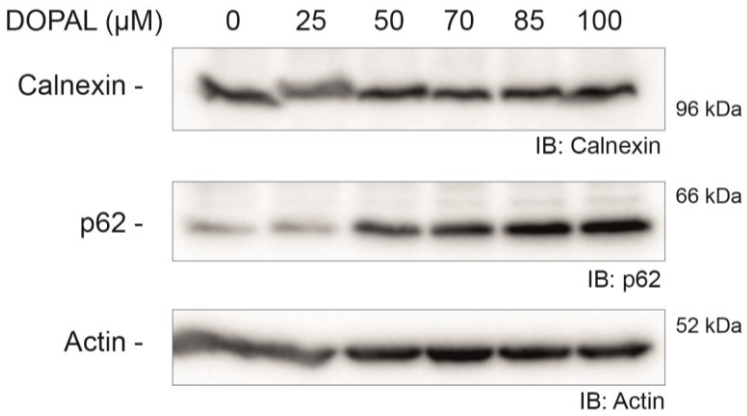

Figure 4.35 DOPAL doesn't affect Calnexin levels. Western blot of BE(2)-M17 cells after an overnight treatment with increasing concentrations of DOPAL (0-25-50-70-85-100 μM). The immunoblot was performed with anti-Calnexin antibody, the anti-p62 antibody as positive control of DOPAL effect and the anti-Actin as loading control.

Coherently, the alteration of the protein degradation systems activity by starvation or administration of MG132, chloroquine and bafilomycin A1, doesn't result in significant differences in neither Calnexin or Calreticulin, except for the Calnexin levels within the proteasome inhibition by MG132 indicating Calnexin as substrate of the UPS (**Fig. 4.36a-c**). Although these results need to be confirmed by studying other markers, they suggest that DOPAL build-up is potentially hindering the protein clearance capacity, without affecting the protein quality regulation at the ER level.

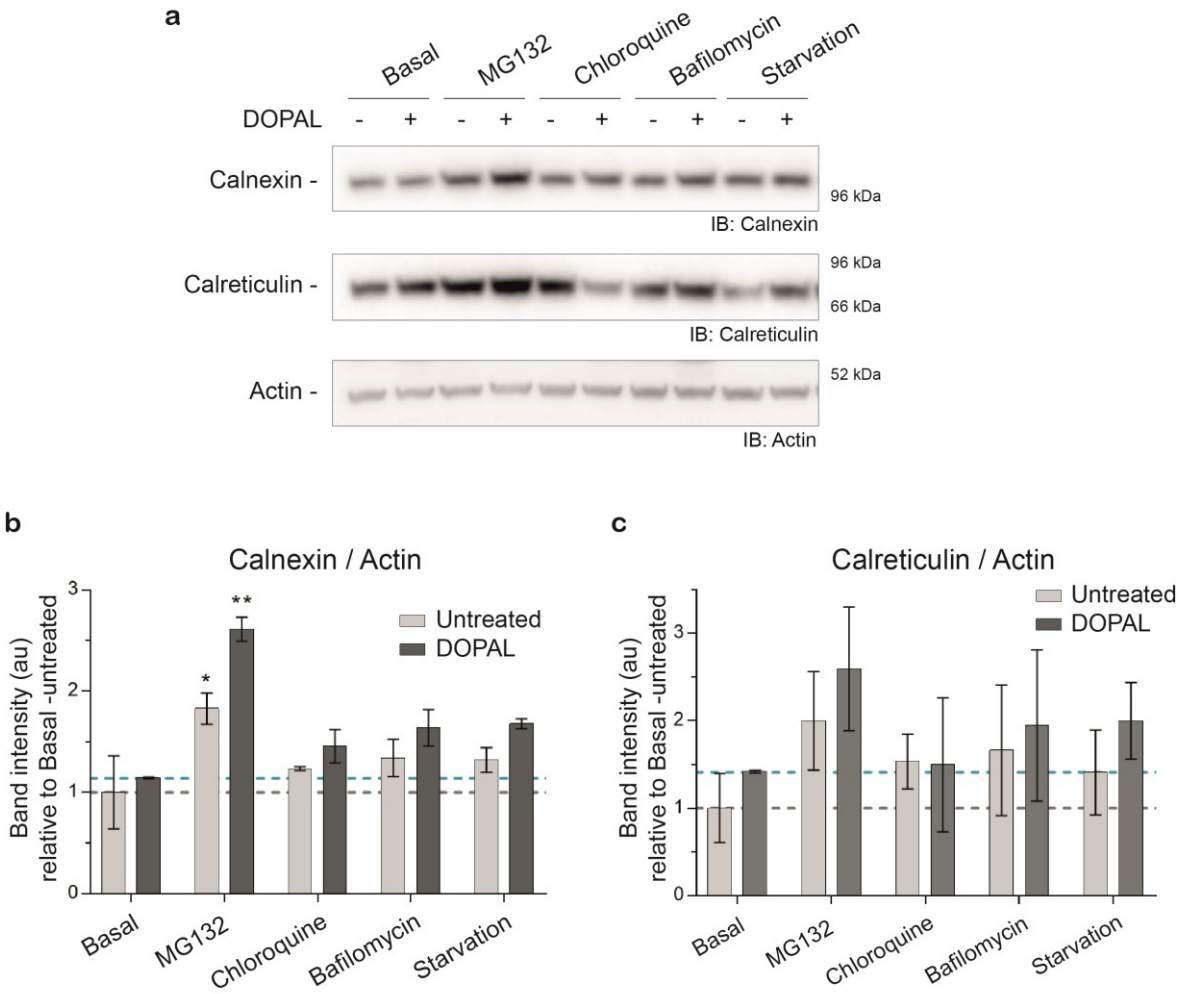

Figure 4.36 Studying the markers of the ER-stress. (a) Immunoblot with the anti-Calnexin and the anti-Calreticulin in of BE(2)-M17 cells after an overnight 100 μM DOPAL treatment versus untreated cells, in basal condition, proteasome inhibition by 20 μM MG132, autophagy blockage by 50 μM chloroquine and 20 nM bafilomycin A1, and autophagy activation by starvation. Quantification of the **(b)** Calnexin and **(c)** Calreticulin levels, expressed as fold change compared to the basal untreated condition. Data are presented as Mean ± SEM from n=3 independent experiments with n=2 technical replicates each and analyzed by non-parametric Kruskal-Wallis test with Dunn's multiple comparison test (* $p<0.05$, ** $p<0.01$). In the figures, the grey dotted line is the reference in the untreated basal sample, while the light blue dotted line is the reference of the basal DOPAL-treated sample.

4.4 Exploring the use of biguanidine molecules as translational approach to control DOPAL-associated toxicity.

4.4.1 Rationale.

Several articles highlighted the beneficial effect of antioxidants i.e. N-acetylcysteine, glutathione and ascorbic acid in preventing the oxidation of the catechol moiety of DOPAL, its modification of cysteines residues of proteins and the general DOPAL-induced oxidative stress (Anderson et al., 2011; Jinsmaa et al., 2018). Here, we started to explore an alternative translational approach to target the aldehyde moiety of DOPAL, which is responsible for the covalent modification of αSyn lysines, triggering αSyn oligomerization.

Specifically, we started to work with the biguanidine class of molecules, as they represent a reservoir of primary amines, the main target of the aldehydic group. Among them, aminoguanidine (AG) and metformin (**Fig. 4.37**) have been already investigated in their action as scavenger of the advanced glycation end products (AGEs), another type of aldehyde molecule whose levels are increased in diabetes-linked pathologies (Biosa et al., 2018).

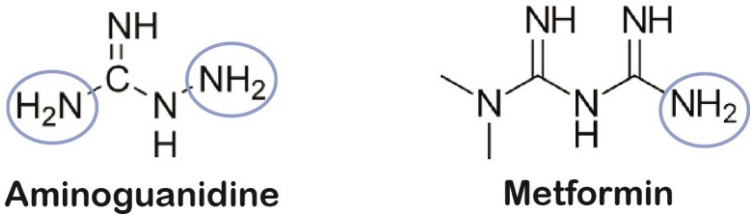

Figure 4.37 Biguanidine molecules as aldehyde scavengers. Molecular structures of Aminoguanidine and Metformin. The light blue circles highlight the primary amine groups.

In details, AG (Pimagedine) was proposed in the prophylaxis of diabetic retinopathy and diabetic nephropathy (Thornalley, 2003). More recently, its beneficial role in reducing the αSyn toxicity and aggregation induced by methylglyoxal has been demonstrated (Vicente Miranda et al., 2017).

Second, it is worth mentioning that metformin is an FDA approved drug since 1994 for the treatment of Type 2 Diabetes (T2DM). Interestingly, T2DM has been recognized as a risk factor for PD (Biosa et al., 2018). Treatments with metformin were showed to have not only antidiabetic but also neuroprotective action (Rotermund et al., 2018). From a molecular point of view, metformin acts on different pathways i.e. controlling mitochondrial physiology, activating the autophagic pathway and modulating neuroinflammation. It has been also demonstrated to reduce the elevation of phosphorylated αSyn by the mTOR-dependent activation of the phosphatase 2A (Katila et al., 2017; Pérez-Revuelta et al., 2014).

Hence, in this last section of the project, we aimed to investigate the beneficial role of aminoguanidine and metformin in rescuing the DOPAL-induced αSyn oligomerization as well as the DOPAL-induced impairment of the protein degradation system.

4.4.2 Aminoguanidine acts as DOPAL scavenger and prevents the DOPAL-induced αSynuclein oligomerization *in vitro.*

The ability of DOPAL to covalently modify αSyn lysines and trigger αSyn oligomerization *in vitro* is well established (Anderson et al., 2016; Burke et al., 2008; Follmer et al., 2015; Jinsmaa et al., 2014, 2019; Lima et al., 2018; Plotegher et al., 2017). Interestingly, the incubation of AG together with DOPAL and recombinant αSyn progressively prevents the DOPAL-αSyn *in vitro* aggregation (**Fig. 4.38a**), hindering the formation of DOPAL-αSyn dimer, trimer and tetramer in a dose-dependent manner (**Fig. 4.38b**). Also, in the Comassie blue stained gel, the DOPAL modification on αSyn monomers can be deduced from the presence of a smeared band, compared to the sharp band of the unmodified recombinant αSyn. However, in the presence of AG, even the monomeric αSyn is less modified by DOPAL, as the band profile progressively resembles the pure αSyn monomer (**Fig. 4.38c**).

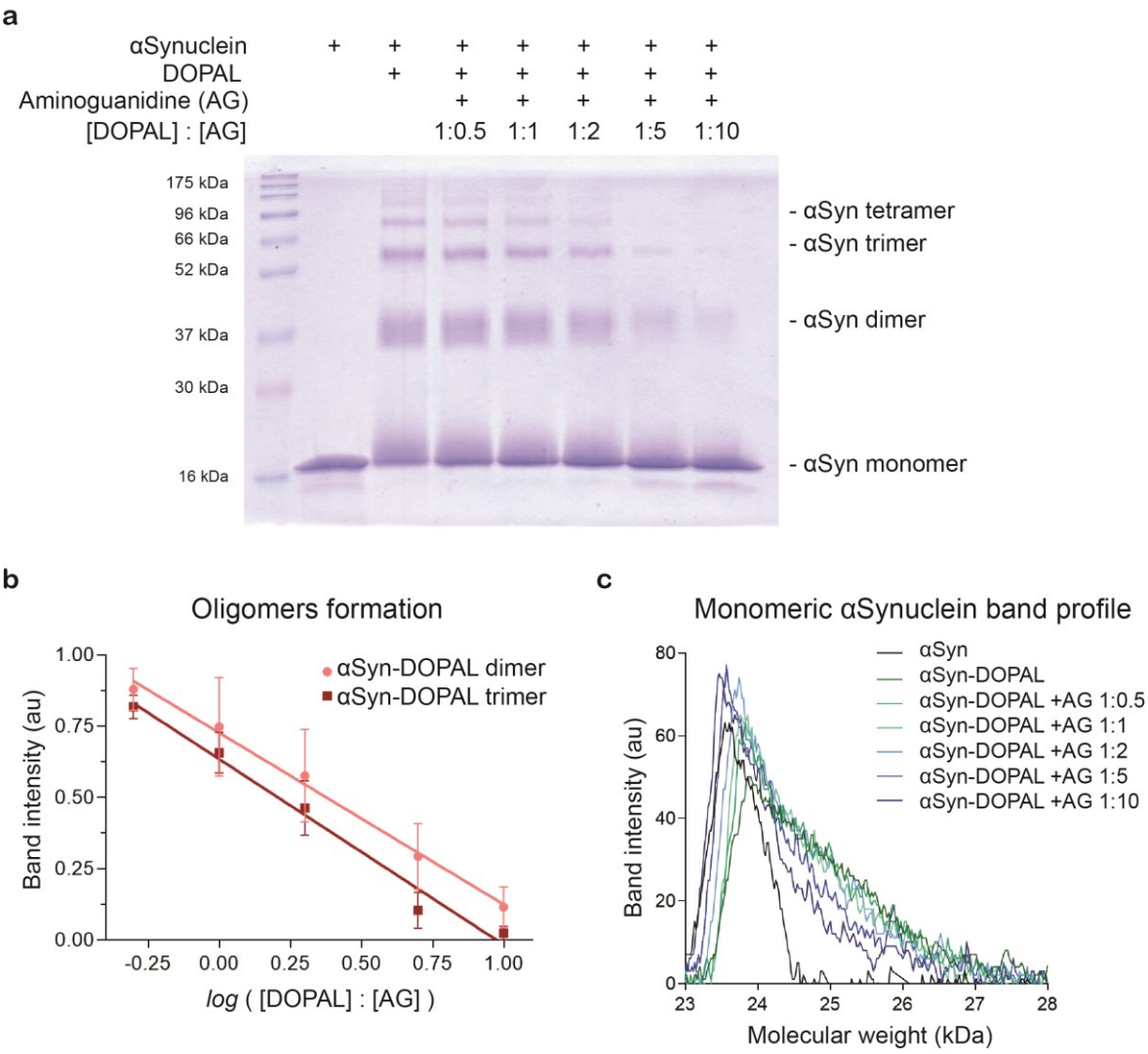

Figure 4.38 Aminoguanidine prevents the DOPAL-induced αSyn oligomerization *in vitro*. (a) SDS-Page stained by Comassie blue of recombinant αSyn and DOPAL-αSyn oligomers in the presence of increasing aminoguanidine concentration. **(b)** Quantification of the band intensity of DOPAL-αSyn dimer and trimer normalized for the different species in the sample without aminoguanidine. Data are presented as Mean ± SEM from n=4 independent experiments. In the x-axis, the ratio between the concentration of DOPAL to AG are converted to a $\log_{10}$ scale; data are fitted by a linear regression (R^2 = 0.99). **(c)** Comparison of the intensity profile of the band corresponding to the monomeric αSyn in the different lanes.

4.4.3 Treatments with biguanidine molecules prevent the DOPAL-induced impairment of protein degradation systems in BE(2)-M17 cells.

We then explored the beneficial role of biguanidine molecules in BE(2)-M17 cells. As starting approach, we investigated whether their administration would succeed in preventing the DOPAL-induced impaired proteostasis. First, we performed cell viability assays, to identify the maximum concentrations that would be tolerated by the cells without inducing any cytotoxicity effects. AG results to be beneficial at concentrations up to 1mM when administrated for 24 hrs (**Fig. 4.39a**), whereas 10mM metformin increases cell viability in the first 24 hrs, leading to a certain degree of toxicity when administrated for 48 hrs, as well as at higher concentration (**Fig. 4.39b**).

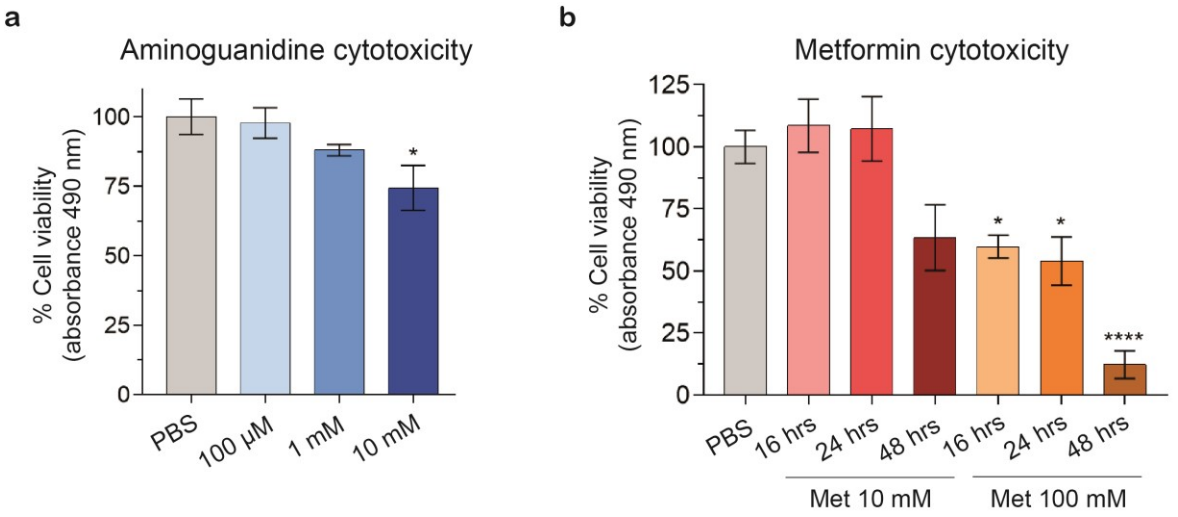

Figure 4.39 Aminoguanidine and metformin cytotoxicity in BE(2)-M17 cells. MTS cell viability assay in BE(2)-M17 cells treated with **(a)** aminoguanidine 100 µM, 1 mM, 10 mM for 24 hrs and **(b)** metformin 10 mM and 100 mM for 16-24-48 hrs. Cell viability was calculated in relation to the PBS-treated control cells, considered 100% of viability.

We then performed some preliminary experiments to study the effects on the p62 levels, as read-out of impaired protein degradation. Indeed, the co-treatment with 100 µM DOPAL and 100 µM AG reduces the level of p62 compared to the sole DOPAL treatment, suggesting that AG is, at least in part, scavenging the DOPAL molecules (**Fig. 4.40a**). More importantly, when 50 mM metformin is administrated 8 hrs before adding the 100 µM DOPAL to the cell medium, the increase of available primary amines reduces the levels of accumulated high-molecular-weight ubiquitinated proteins as well as p62 (**Fig. 4.40b-c**).

Although these experiments show promising results, in the future we plan to confirm these data and to explore the ability of these molecules in restoring the proper αSyn proteostasis.

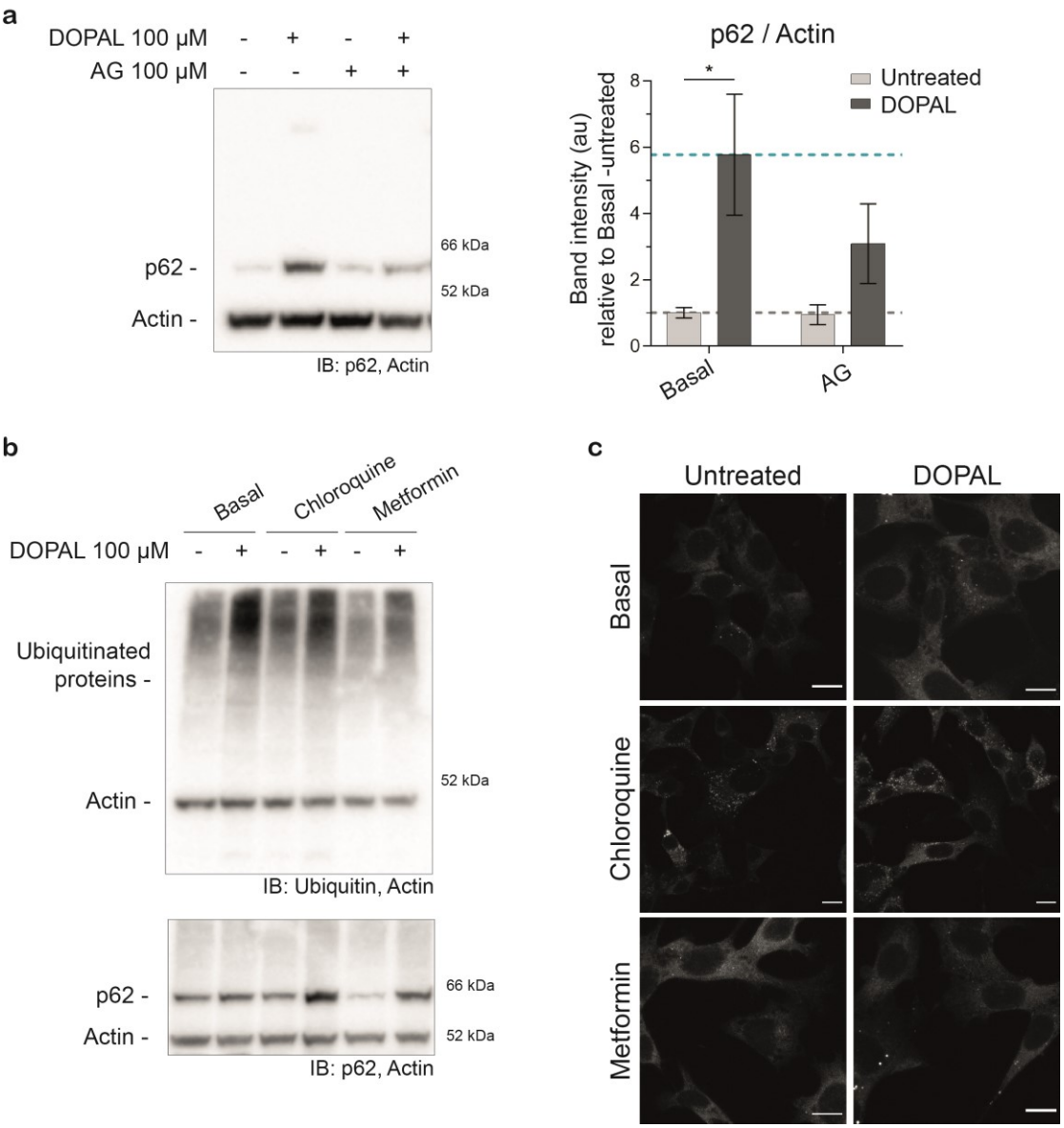

Figure 4.40 Biguanidine molecules potentially rescue the DOPAL-induced impaired proteostasis. (a) Immunoblot with anti-p62 antibody of BE(2)-M17 cells co-treated with 100 µM DOPAL and 100 µM AG and relative quantification of the band intensity, normalized for Actin and the level in the untreated cells. Data are presented as Mean ± SEM from n=3 independent experiments with n=2 technical replicates each and analyzed by non-parametric Kruskal-Wallis test with Dunn's multiple comparison test (* $p<0.05$). **(b)** Immunoblot with the anti-ubiquitin and the anti-p62 antibodies of BE(2)-M17 cells treated with 100 µM DOPAL, 50 µM chloroquine as positive control and the coupled treatment. In the last two samples, cells were pre-treated with 50 mM metformin for 8 hrs before DOPAL addition. **(c)** Immunolabeling of p62 in BE(2)-M17 cells treated with the same conditions of the western blot experiment. Scale bar: 10 µm.

5. DISCUSSION.

5.1 DOPAL affects αSynuclein proteostasis.

In the first part of our project, we aimed to investigate whether increasing DOPAL levels in neurons would affect the physiology of its preferential target αSyn, in terms of mobility, localization and degradation among the different neuronal compartments. In the first instance, we studied αSyn trafficking by a pulse-chase experiment coupled to live time-lapse imaging with αSyn-TimeSTAMP-YFP-miniSOG probe. The variations of the fluorescent αSyn signals in the different conditions tested, suggests that DOPAL affects the relative levels of the protein in the neuronal soma and the periphery, which is exacerbated by microtubules depolymerization induced by Nocodazole. However, an attempt to single out the mechanisms that govern αSyn proteostasis, needs to face with the complexity of its regulation in neurons. The observed DOPAL-induced alterations potentially derive from a combination of an impaired mobility of αSyn along the axons and a decreased degradation efficiency. This is particularly evident in the presence of Nocodazole and DOPAL, when the marked increase of the αSyn amounts both in the soma and the peripheral terminals reflects degradative issues. On this ground, we are currently working on a model that would include the contribution of all variables, to dissect the effect of DOPAL in the mobility and clearance of αSyn.

αSyn axonal transport is reported to occur by both fast and slow components, mainly in association to vesicles rather than axon skeleton proteins (Jensen et al., 1999). According to Utton et al., αSyn traffics in both anterograde and retrograde directions on intact microtubules, as αSyn was showed to interact with both kinesin 1- and dynein-containing complexes (Utton et al., 2005). It is then plausible that a modification of αSyn lysines by DOPAL might impact the αSyn association with these structures and molecular motors, both carrying vesicles and axonal proteins. On the other hand, DOPAL-αSyn aggregates themselves could impair and disrupt the axonal trafficking. Indeed, the work by Volpicelli-Daley extensively explored the effects of αSyn aggregates on the axonal transport. She and other authors suggested that the generation of aggregated αSyn in the periphery, both oligomers and large aggregates, induces the degeneration of the axonal infrastructure, starting from the periphery (Prots et al., 2018; Volpicelli-

Daley, 2017b). This idea also supports the “dying back hypothesis” for PD (Hornykiewicz, 1998), in which the early events of the degeneration process start from the synapse dysfunction and loss, followed by a progressive axonal disruption and degeneration of the soma. Coherently, we noticed a progressive accumulation of fluorescent αSyn in dystrophic terminals in the live imaging of DOPAL-treated neurons. Also, the presence of aggregated αSyn-positive structures in neurites were observed in the CLEM experiment of the αSyn-split-miniSOG in DOPAL-treated neurons, suggesting a similar effect induced by DOPAL-build up in neurons.

Based on the considerations we just made, one important aspect is the DOPAL-induced effect at the pre-synaptic level. We already demonstrated that DOPAL treatment in primary neuronal cultures resulted in a dose-dependent redistribution of the synaptic vesicles pools (Plotegher et al., 2017). Here, the pivotal point is to correlate this observation with a mechanism through which DOPAL elicits this effect on αSyn. Thus, the CLEM approach provides a powerful tool to specifically trace αSyn at the terminals, comparing the αSyn overexpressing neurons with the non-transfected ones, where we assume only the endogenous rat αSyn is present (even if it is not detectable by CLEM). Also, the high resolution of the technique allows to describe morphological differences on the details of synapse architecture, that potentially consents to infer functional implications. For instance, the over-expression of the tagged human αSyn resulted in increased and more heterogeneous dimension of synaptic vesicles, together with a shorten intra-vesicles distance. This would imply an effect due to the presence of αSyn oligomers (generated by the sole αSyn overexpression), in terms of altered vesicles curvature, but also clustering and trafficking, which is consistent with the large body of evidence present in the literature (Janezic et al., 2013; Nemani et al., 2010; Wang et al., 2014). However, the plot of the distribution of the inter-vesicles distances in the DOPAL-treated αSyn-overexpressing neurons, presents a slight shift towards bigger distances that might be explained by a reduced membrane-binding affinity of the DOPAL-modified αSyn, at least in its monomeric form (Follmer et al., 2015). Importantly, the CLEM experiment with the split-miniSOG probe evidenced some signal, that corresponds to the presence of

oligomeric forms, at the pre-synaptic terminals only in the DOPAL-treated neurons. Although only a few vesicles were surrounded by αSyn oligomeric species, this might be sufficient to trigger a synapse dysfunction in the light of the demonstrated pore-forming action of the DOPAL-αSyn large oligomers on the vesicle membranes (Plotegher et al., 2017). It is also worth mentioning that in a previous publication by the group of S. Roy, another bimolecular fluorescence complementation assay (BiFC) revealed the presence of multimerized αSyn at the pre-synaptic boutons in basal conditions (Wang et al., 2014), which appears in contrast with our observations. In this case, the split-Venus probe (VN/VC:αSyn) was used, however the reconstitution of the two Venus fragments is known to be irreversible, hence not only the αSyn oligomers but also the transiently interacting monomers are stabilized and detected by this method. On the contrary, the split-miniSOG complementation has a reversible nature (Boassa et al., 2019), in which the reconstituted complexes derive by the sole stable interactions between the tagged proteins (αSyn monomers). Even though the presence of DOPAL-modified αSyn oligomers at the pre-synaptic terminals needs stronger evidence, the comparison between the experiments with the two different probes (the αSyn-split Venus and the αSyn-split miniSOG) potentially provides relevant hints on the physiology of αSyn. Taken together, the two sets of data suggest that in physiological conditions αSyn exists in a dynamic equilibrium between the monomers and the multimeric forms, whose function has to be clarified. Instead, in pathological conditions, i.e. DOPAL build-up, the generation of stable oligomers occurs, with consequent gain-of-toxicity of αSyn.

To summarize, DOPAL modification of αSyn lysines generates different αSyn conformers that interfere with various neuronal processes (**Fig. 5.1**). DOPAL-modified αSyn has a decreased membrane binding affinity, resulting in synaptic vesicles redistribution. The modified monomers cross-link, leading to covalent oligomers, that further associate into large aggregated. These annular-shaped objects are thought to be very toxic as they affect membranes integrity, i.e. synaptic vesicles. Also, both DOPAL-αSyn oligomers and aggregated might impair the axonal network and the protein degradation systems, just like αSyn on-pathway oligomers and fibrils.

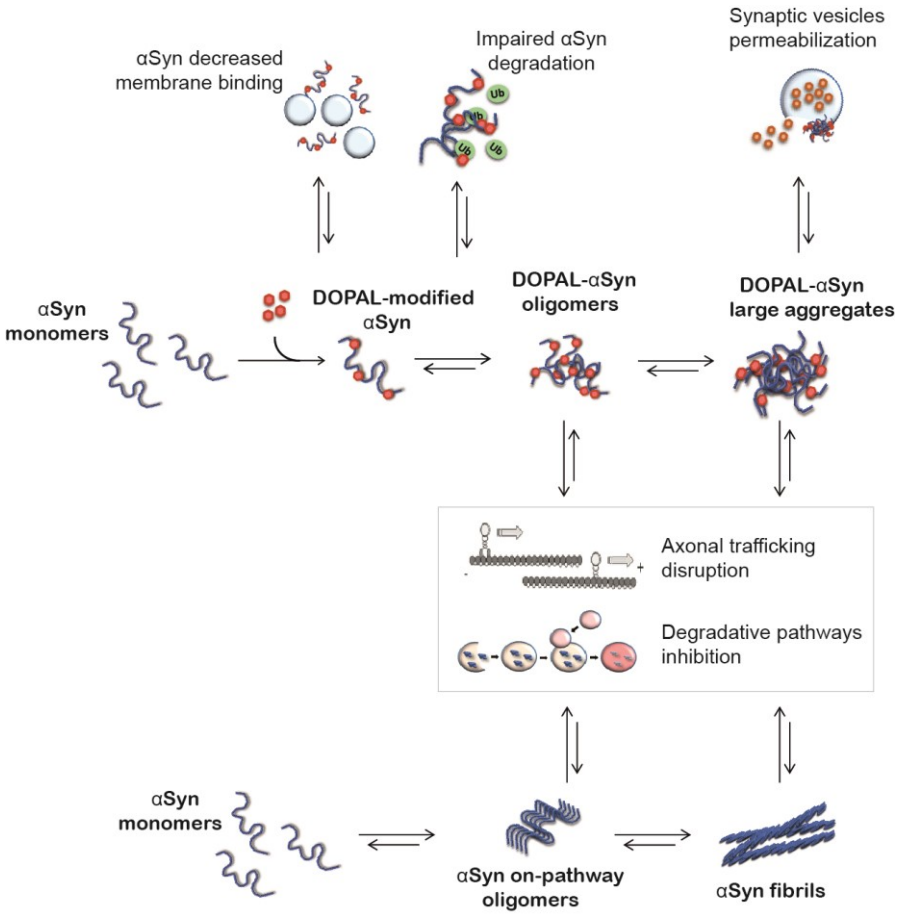

Figure 5.1 DOPAL-induced αSyn aggregation process and functional implications in neurons. DOPAL modification on αSyn generates αSyn covalent oligomers that further associates in large aggregates. All these species lead to functional toxic effects in neurons, like synapse dysfunction and impaired αSyn degradation. These effects are on the top of others that were already addressed to αSyn on-pathway oligomers and fibrils, i.e. disruption of the axonal trafficking and blockage of protein degradation systems.

As mentioned before, the other key issue is αSyn clearance. In the pulse-chase experiment using the HaloTag technology (in the biochemical approach with the biotin ligand) in BE(2)-M17 cells, we demonstrated that DOPAL exacerbates αSyn aggregation, decreases its degradation rates and stabilizes αSyn oligomeric forms. The more pronounced effect of DOPAL in promoting αSyn(K96R) oligomerization compared to the αSyn(WT) suggests that the ubiquitination of αSyn on Lys96 might be helpful in targeting αSyn toxic species to the endosomal pathway to the degradation by the lysosomes (Tofaris et al., 2011). Hence, an interesting issue would be to dissect the ubiquitination pattern on αSyn and whether DOPAL competes with the same modification sites (**Fig. 5.1**).

Also, the other aspect would be to identify the relative contribution and the efficacy of the proteasomal and the endo-lysosomal pathway in disposing DOPAL-αSyn, both monomers, oligomers and large aggregates. We are currently working on a way to model this complex interaction among αSyn, DOPAL, ubiquitin, the E3-ubiqtuitin ligases Nedd4 and SIAH, but also PIAS2 and αSyn SUMOylation (Rott et al., 2017), as presented in **Fig. 5.2**.

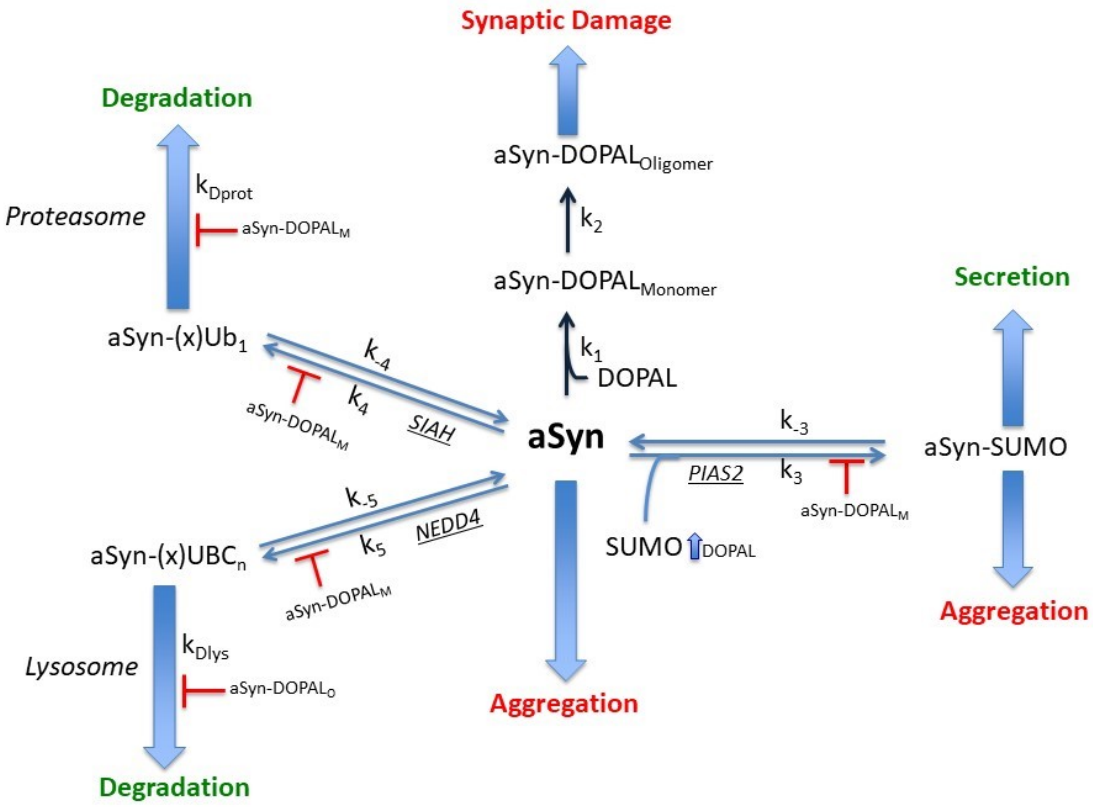

Figure 5.2 Schematic representation of αSyn post-translational modifications kinetics. The variables to consider are the ubiquitination and SUMOylation, mediated by SIAH, Nedd4 and PIAS2 respectively; as down-stream pathway, the degradation by the proteasome and the lysosomes and αSyn secretion. Instead, by competing for the same lysines, DOPAL triggers αSyn aggregation, prevents αSyn degradation and induces synaptic damage. Also, DOPAL-modified αSyn monomer and oligomer might affect the degradative pathways functionality.

In our work, data generated with several independent approaches substantiate the involvement of the ALP in the clearance of DOPAL-αSyn aggregates. More precisely, the CLEM experiments, both in rat primary cortical neurons (with the αSyn-TimeSTAMP-YFP-miniSOG and the αSyn-split-miniSOG probes) and in BE(2)-M17 cells (with the JF570 HaloTag ligand) clearly marked a high accumulation of aggregated αSyn in the perinuclear lysosomes, which is exacerbated by long-term DOPAL treatments. These observations lead us to the conclusion that the proteolytic activity of the lysosomal enzymes might not be able to degrade DOPAL-αSyn oligomers. Indeed, the *in vitro* limited proteolysis by the unspecific PK is coherent with a decreased ability to digest the DOPAL-αSyn oligomers. We also observed a DOPAL dose-dependent increase in αSyn phosphorylation at Ser129. Coherently, both phosphorylated αSyn and DA-incubated αSyn were showed to dramatically inhibit the CMA pathway (Cuervo et al., 2004). Taken together, these evidences suggest a potential impairment of the autophagic pathway, which will be further discussed below.

Finally, another important consideration is related to the upregulation of the endosomal pathway in DOPAL-neurons, where increased oligomeric αSyn-positive ILVs were counted in MVBs, as well as a higher number and bigger vesicles each MVB. Interestingly, the clogging of the lysosomes and the disrupted axonal network are believed to promote the fusion of the MVBs with the plasma membrane, releasing their vesicles in the extra-cellular space (Alvarez-Erviti et al., 2011). This is extremely relevant as the exosomes might represent a Trojan horse to healthy neurons, therefore spreading DOPAL-αSyn toxic oligomers to neighbor neurons and glial cells. In this frame, additional data from our lab demonstrated that DOPAL-αSyn containing exosomes administrated to primary neurons induce synapse dysfunction in terms of number of vesicles per synapse and increased vesicles average distance from the active zone (supplementary **Fig. S1**, Berti et al., unpublished data). Of note, this effect was only detected in wild-type neurons compared with αSyn null-cells, suggesting the importance of the endogenous αSyn to sustain toxicity of the αSyn seed up-taken with the exosomes.

5.1.1 Limitations of the experimental model and future aims.

A few considerations are due on our experimental models. First, in most of the experiments, both in neurons and BE(2)-M17 cells, αSyn was overexpressed with various tags. Although these tags were instrumental for the different strategies we applied to study αSyn trafficking, localization and clearance, we cannot exclude their potential contribution in the αSyn oligomerization and degradation processes.

In primary neurons, being αSyn distribution highly compartmentalized in the cell body and the pre-synaptic terminals, it is not possible to estimate the αSyn overexpression levels by simple western blot of the cell lysate against a calibration curve generated from recombinant αSyn. While in BE(2)-M17 cells, we estimated a 1000-fold overexpression of the EGFP-tagged αSyn compared to the endogenous levels and this data might slightly differ according to the promoter in the plasmid used for the overexpression. To overcome this issue, we generated in our lab monoclonal, stable and inducible BE(2)-M17 cells with the overexpression of untagged wild-type αSyn under the tetracycline promoter (αSyn-encoding DNA was cloned in the pINDUCER20 viral vector, (Meerbrey et al., 2011)). The advantage is a controlled doxycycline dose-dependent αSyn overexpression, that will be used for future investigations.

Also, all our constructs are designed to express the tags in frame with the C-terminus of αSyn. The rationale is to avoid any interference with the aggregation process and the membrane interaction, that occurs primarily at the N-terminal of the protein. However, our experimental strategy exclude the detection of truncated forms of the proteins i.e. αSyn 1-120 that was reported to rapidly self-aggregating and induce high level of neurotoxicity (Michell et al., 2007; Wegrzynowicz et al., 2019). In the future, we plan to consider the use of N-terminal-tagged αSyn, as well as anti-αSyn antibodies that recognize various epitopes along the αSyn sequence to detect the different αSyn subpopulations.

As second important aspect, we are exogenously administrating DOPAL of synthesis in the cell medium, which is believed to diffuse in the cells being a non-polar molecule at physiological pH. Because of its high reactivity, the DOPAL treatment to cells occurs in serum-depleted media. However, the quantification of

the precise DOPAL amount within the cells is hard to measure. At present, the gold-standard technique is the High Pressure Liquid Chromatographic separation coupled to Electro-Chemical Detection (HPLC-ECD) (Filograna et al., 2015; Goldstein et al., 2013; Wey et al., 2012), as it allows singling out DOPAL from other catecholamines, based on its unique electro-chemical properties. In this frame, the next step would be to induce the accumulation of endogenous DOPAL in a pure dopaminergic cellular model by inhibiting the ALDHs enzymes, responsible for DOPAL degradation. Preliminary data in our hands, suggest that the treatment of BE(2)-M17 cells with Benomyl, a very potent irreversible ALDH inhibitor (Fitzmaurice et al., 2013; Koppaka et al., 2012), results in increasing DOPAL and decreasing DOPAC levels. As mentioned before, Benomyl has been identified as a risk factor for PD, and it presents other targets rather than ALDH inhibition, i.e. microtubule disruption and proteasome inhibition (Fitzmaurice et al., 2013; Rathinasamy and Panda, 2006). Thus, we are currently setting up the same strategy by using other more specific ALDHs inhibitors (i.e. Aldi-2 (Khanna et al., 2011), N,N-diethylaminobenzaldehyde (Morgan et al., 2015)), to modulate DOPAL build-up under more controlled and reproducible conditions.

Finally, we still need a tool to selectively detect and quantify the DOPAL-modified αSyn in our experimental models, which is a challenge with the currently available methods. So far, the detection of catechol-modified proteins from cell lysates has been performed by SDS-Page followed by the staining with nitroblue tetrazolium, a redox-cycling dye for the detection of catechol adducts (Rees et al., 2007). Alternatively, the protein pull-down assay with aminophenylboronic acid resin allows the isolation of catechol-modified proteins from cell lysates (Liu et al., 2014; Plotegher et al., 2017), with the caveat that it also binds glycosylated proteins. More recently, the near Infrared Fluorescence scanning was applied to the detection and quantification of o-quinones in cells and tissues, as well as proteins modified by oxidized catechols (Burbulla et al., 2017; Jinsmaa et al., 2018; Mazzulli et al., 2016; Mor et al., 2017). Instead, our group is currently collaborating with Abcam for the development of a monoclonal antibody raised against DOPAL-modified αSyn-derived peptides (**Fig. S2** for details of epitope synthesis strategy) to specifically detect DOPAL-αSyn species in our models and experiments.

5.2 DOPAL impairs the cellular homeostasis: a synergy with αSynuclein?

Starting from the observed DOPAL-dependent accumulation of αSyn aggregates in lysosomal compartment, even more pronounced in the presence of the proteasome inhibitor MG132, we wondered whether the cell is able to get rid of the DOPAL-αSyn toxic species and whether the functionality of the protein quality control systems was still functional. In this frame, we monitored the variations of the levels of the autophagic and proteasomal markers p62 and ubiquitin, respectively, in response to DOPAL. Although, the assessment of the failure of both protein degradation systems needs additional confirmations, the DOPAL-dependent accumulation of high molecular weight ubiquitinated proteins and p62 oligomerization were clearly detected. These observations are fascinating as aggregated αSyn, highly phosphorylated at Ser129, ubiquitin and p62 are the main constituents of LBs (**Fig. 5.3**) (Alafuzoff; et al., 2001; Kuusisto et al., 2003; Spillantini et al., 1998). Thus, a provocative speculation would be to appoint DOPAL as the linker of the phosphorylated and aggregated αSyn, ubiquitin and p62 co-deposition in LBs.

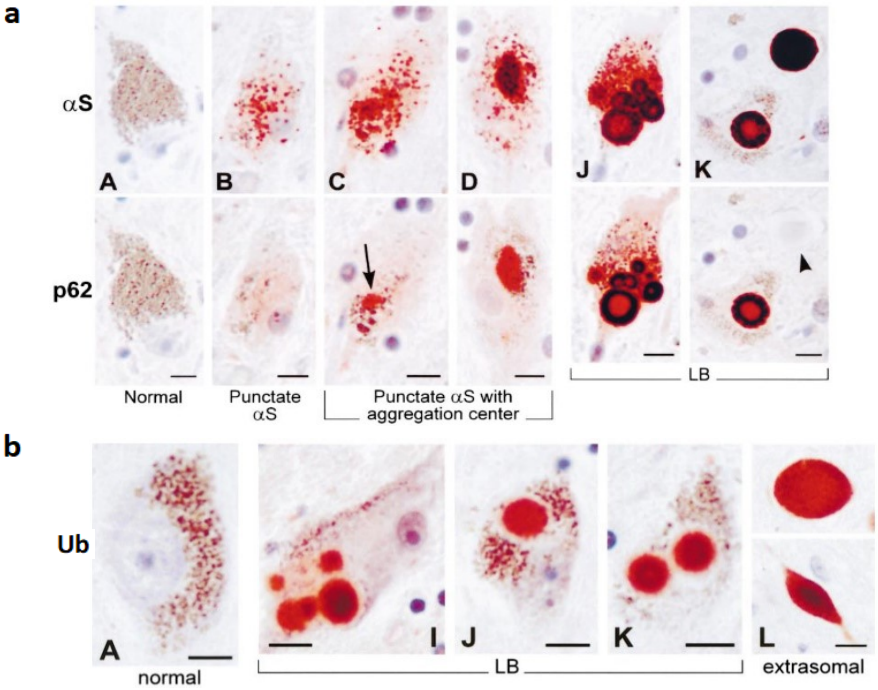

Figure 5.3 αSyn, ubiquitin and p62 immunoreactivity in LBs.
Adapted from *Kuusisto et al., 2003*.

p62 oligomerization has been demonstrated to occurs upon oxidation of p62 cysteines, as a sensor of the redox state of the cell (Carroll et al., 2018). p62 expression is under the regulation of the NF-E2-related factor 2 (Nrf2), which is activated in response to oxidative stress (Jain et al., 2010). Coherently, DOPAL-induced oxidative stress is well recognized, giving its intrinsic propensity to auto-oxidation and associated generation of ROS like other catechols. Of course, this could be fit within a positive feedback loop that includes mitochondrial dysfunction, the main source of ROS in PD (De Lazzari et al., 2017). Even though our focus was mainly aimed to the study of neuronal functional features like synapses, observing the EM images we collected on primary neurons in our CLEM experiments, we noticed several compromised mitochondria (fragmented, swollen and without clearly defined cristae) in the DOPAL-treated samples. This confirmed a more general impact of DOPAL in the cellular homeostasis, which includes all the main pathways considered relevant in PD-pathology. Interestingly, a very recently published paper highlighted complex I inhibition and mitochondrial dyshomeostasis in the presence of DOPAL-αSyn oligomers (Sarafian et al., 2019). This is extremely relevant as it underlines an additional link among the most important players in the neurodegeneration of dopaminergic SNpc neurons according to the *Catecholaldehyde hypothesis*.

αSyn has been appointed as the preferential target for DOPAL modification mainly because of its abundance at synapses and the presence of numerous lysines in its sequence. However, many other proteins can be targeted by DOPAL, leading to protein cross-linking (Plotegher and Bubacco, 2016). In this frame, both the observed ubiquitin and p62 accumulation and aggregation might result from a direct DOPAL modification of their several lysines and cysteines in their sequence.

So far, we analyzed the DOPAL-induced effects on neurons and stable cells in the presence of the endogenous and the overexpressed αSyn. Future experiments will aim to dissect the specific contribution of DOPAL and αSyn (for example, by modulating the αSyn and DOPAL levels in a αSyn-null background) in the considered neurotoxicity read-outs, in order to really address the intriguing question about the potential synergistic effect of αSyn and DOPAL in driving the degeneration of the nigrostriatal neurons in PD.

5.3 DOPAL as potential on site target for therapy.

As mentioned before, the therapeutic strategies currently available for PD are only symptomatic. Among them, MAO inhibitors have been used since the 1960s and many of them are currently FDA approved drugs, even though their long-term efficacy has been questioned. A potential drawbacks of MAO inhibition is the increased levels of cytosolic DA that might lead to decreased TH activity due to feedback inhibition. Conversely, if not properly stored in synaptic vesicles, DA undergoes auto-oxidation, resulting in oxidative stress (Goldstein et al., 2016). Anyway, if considered in the light of the *Catecholaldehyde Hypothesis*, the MAO inhibition approach sounds even more promising as it would block at least one source of DOPAL build-up (Masato et al., 2019). It follows that the potential of MAO inhibition as disease modifiers hinge on two aspects: the first is an accurate patient stratification as more prone to develop DOPAL build-up based on ALDHs dysfunction. The second is early action, being that the DOPAL build-up and the synaptic damage likely precede neuronal death and disease manifestation.

Here, we propose an alternative strategy to target DOPAL neurotoxicity by scavenging the reactive aldehydes with an excess of tolerable molecules with an amino moiety, which would react in place of the protein lysines. Specifically, we explored a beneficial role of aminoguanidine and metformin, which are already used in the treatment of diabetic pathologies against the accumulation of AGEs. Our *in vitro* experiments demonstrated the biguanidine protective role in preventing DOPAL modification of αSyn lysines and DOPAL-induced αSyn oligomerization, leaving αSyn in its physiological state, which is essential for the protein to exerts its function at the synapses. On the other hand, both molecules appeared to ameliorate DOPAL-dependent alterations of the UPS and ALP in preliminary experiments. Of note, targeting the proteolytic pathways in neurodegenerative diseases is now in the spotlight in the therapeutics design.

Of course, further investigations should address the pharmacology of biguanidines and the neuroprotective activity in PD, starting from *in vivo* models suitable to test the *Catecholaldehyde hypothesis* (Masato et al., 2019).

5.4 Conclusions.

Our work contributed in shedding light on the hypothesis that an altered DA metabolism is detrimental, leading to αSyn-associated impaired proteostasis and neurodegeneration in PD. The working hypothesis (**Fig. 5.4**) starts from previous evidence of the DOPAL-induced αSyn oligomerization and resulting synapse dysfunction. Here, we demonstrated that DOPAL affects αSyn trafficking among the different neuronal compartments and decreases αSyn clearance. We also observed a potential impairment of the protein degradations systems, with high accumulation of ubiquitinated proteins and p62. Hence, we speculate that the DOPAL-dependent altered neuronal proteostasis, a fact that would fit with further αSyn accumulation (and eventually fibrillation), as well as general aberrant protein burden, results in the formation of LB inclusions in dopaminergic SNpc neurons. Finally, the overload of αSyn in MVBs together with blocked autophagy suggests the exosomal pathway as mechanism of αSyn oligomers release and spreading.

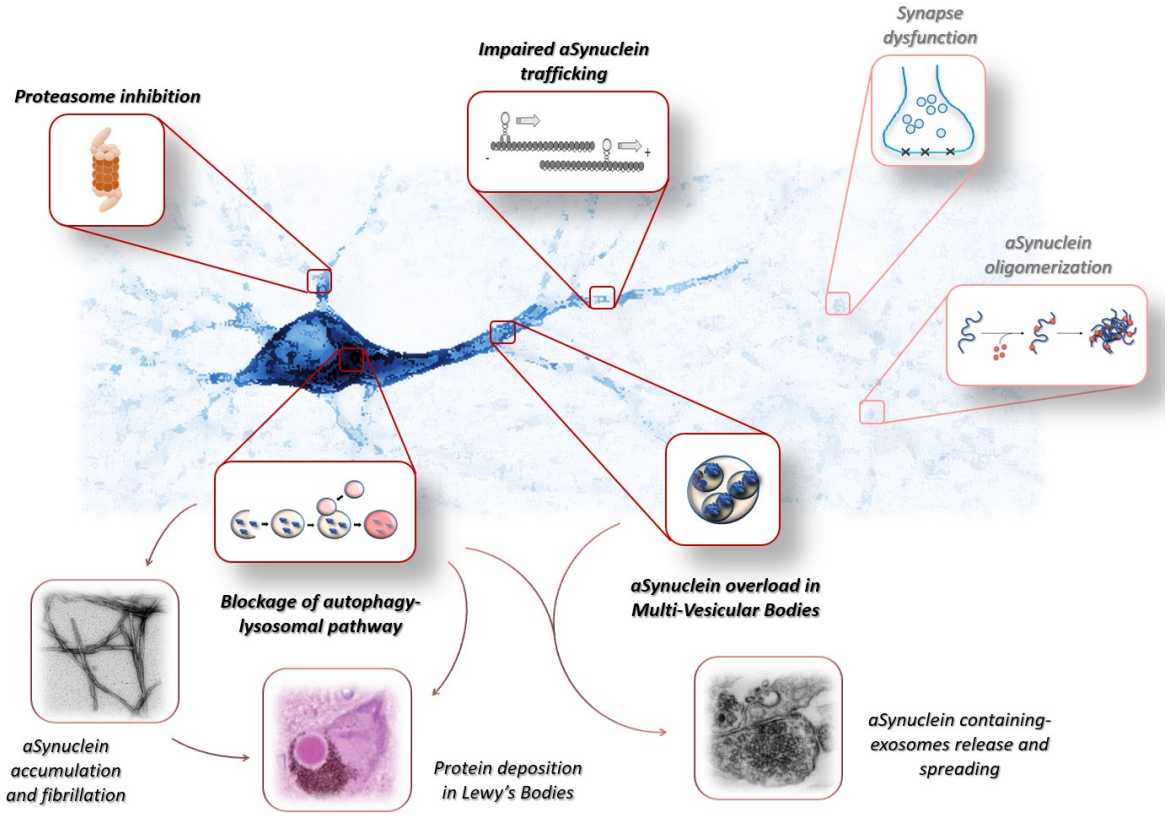

Figure 5.4 Working hypothesis.

In conclusions, we provided additional evidence of the role of DOPAL in the pathogenesis of PD and the higher vulnerability of dopaminergic SNpc neurons. Further investigations on both up-stream effectors as well as down-stream outcomes of DOPAL build-up are necessary. More likely, the combination of age, genetic predisposition and environmental factors are responsible for the dysregulation of several pathways, including DA metabolism, redox state homeostasis, αSyn and neuronal proteostasis (George and Brundin, 2017; Goldstein et al., 2014). Until the synergistic action of all these factors overcome the threshold and lead to the neurodegeneration in PD. Hence, in a therapeutic perspective, this is now translated into the idea of targeting multiple processes at the same time to increase the chances to develop a disease-modifying strategy. Since DOPAL appears as a crucial hub in all the affected pathways in PD, we suggest DOPAL itself as on-site target for therapy.

6. APPENDIX.

6.1 DOPAL-αSynuclein containing exosomes affect synapse architecture in recipient neurons.

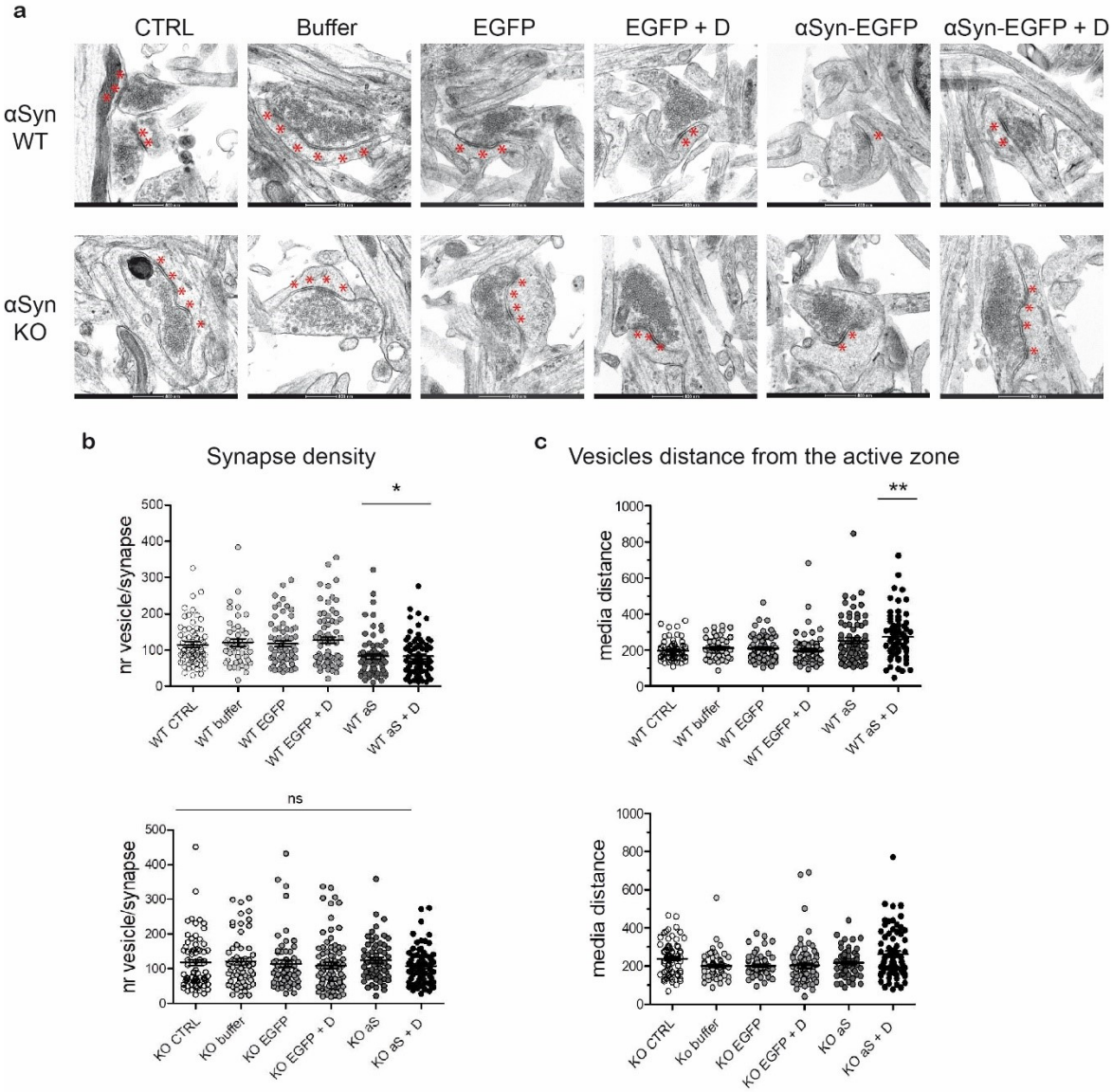

Figure S1. αSyn-containing exosomes affect synaptic vesicles pools in recipient neurons. Primary cortical neurons from wild-type and αSyn knock-out (C57BL/6JOlaHsd) mice were incubated with αSyn-EGFP-containing exosomes (and relative controls). Exosomes were previously purified by ultracentrifugation from αSyn-EGFP or EGFP overexpressing HEK293T cells, after an overnight 100 μM DOPAL treatment. In each condition, pre-synaptic terminals were imaged by TEM (scale bar: 500 nm) and analyzed by LoClust tool. The active zones were identified as electron-dense areas (red stars in the figures) and the synaptic vesicles were manually annotated. Incubation with αSyn-EGFP-containing exosomes (but not the controls) leads to a decreased vesicles per synapse and an increased distance from the active zone, especially with DOPAL. Of note, the effect is detected only in WT neurons, suggesting a relevant contribution of endogenous αSyn in worsening αSyn-induced alterations on synapse functionality. *Berti et al., unpublished data.*

6.2 Strategy set-up to generate αSynuclein-derived DOPAL-modified peptides as epitope of an anti- DOPAL-modified αSynuclein antibody.

a

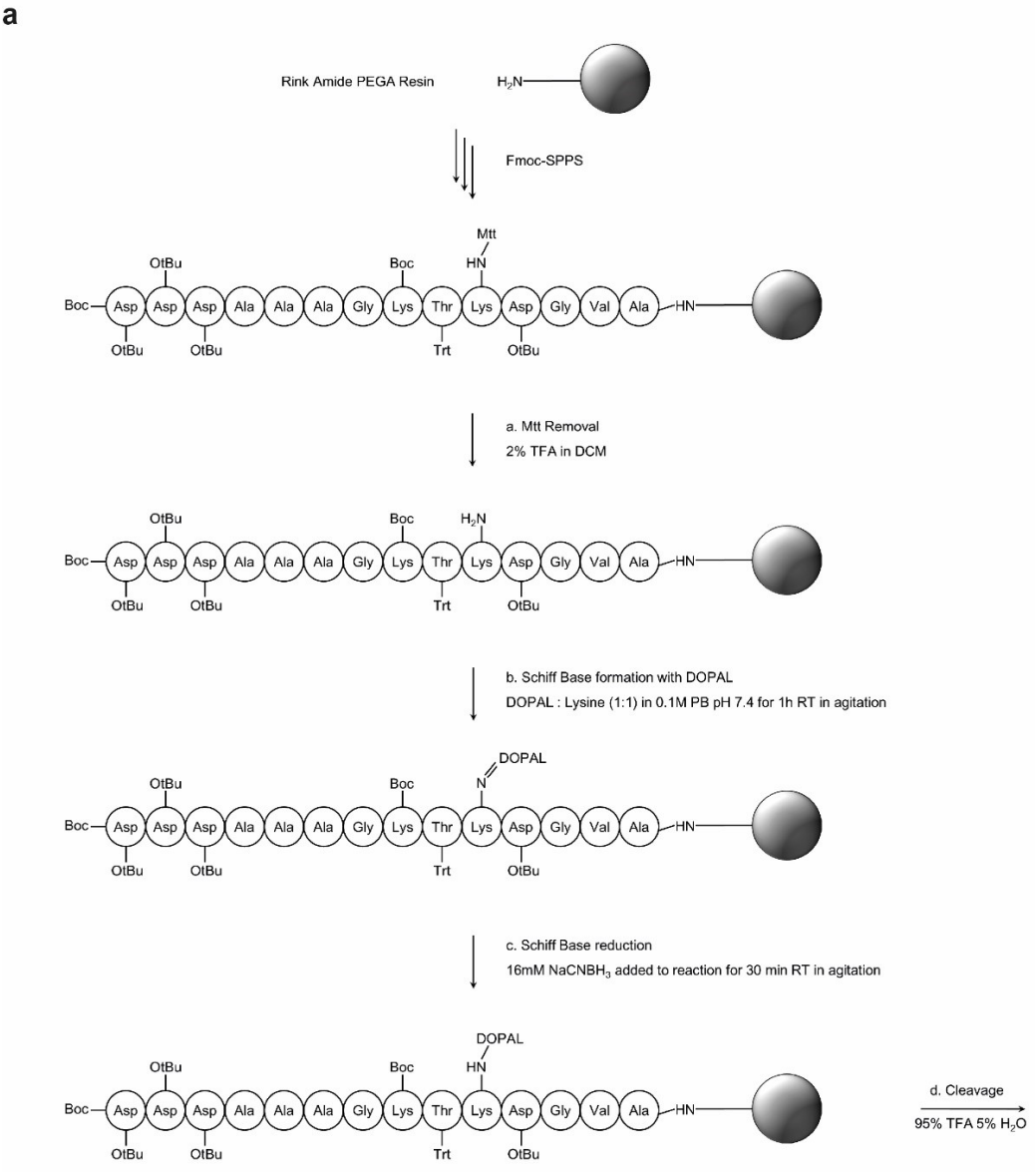

b

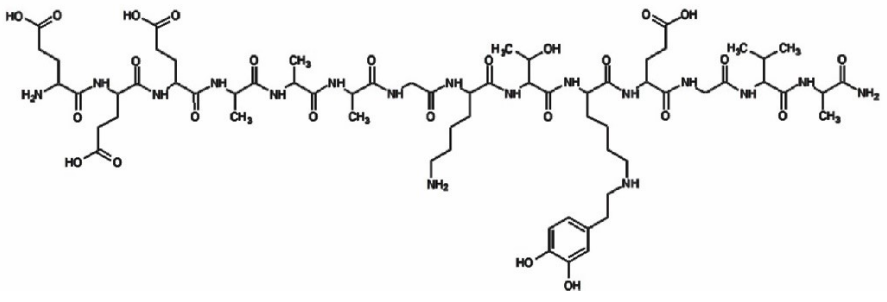

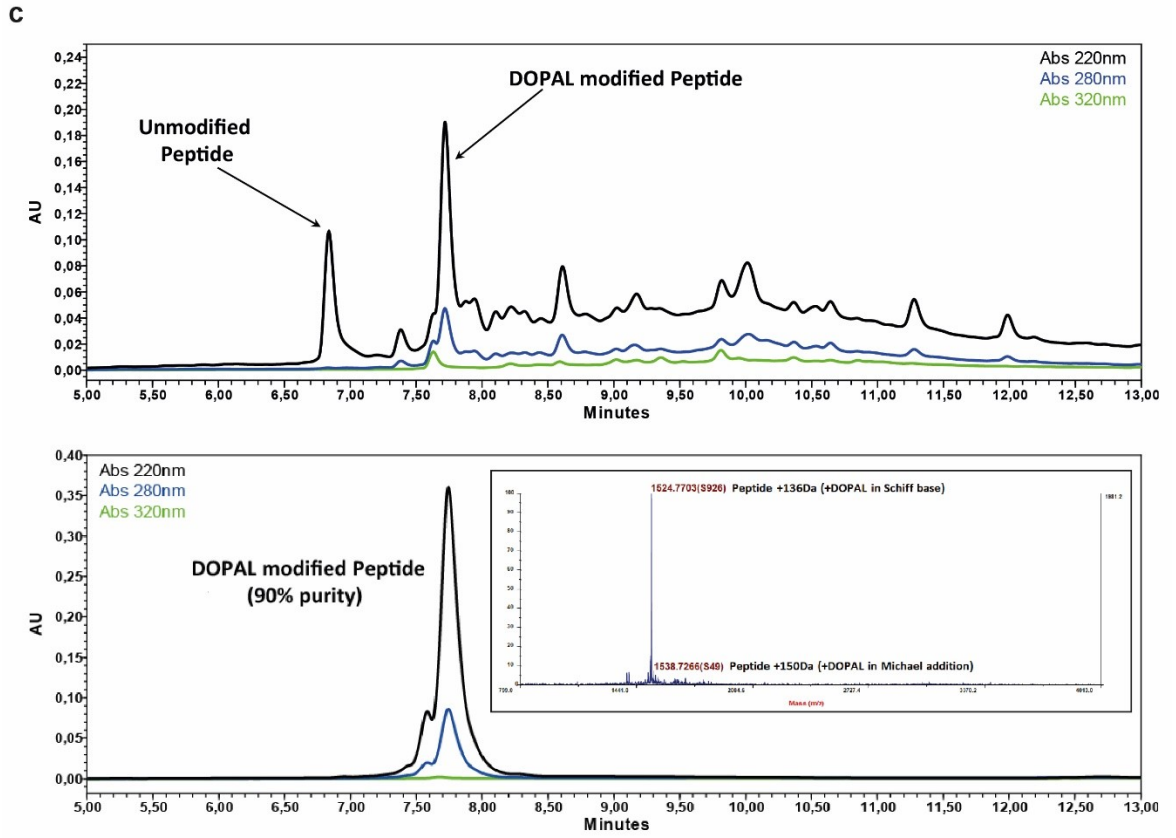

Figure S2. αSyn-derived peptide site specific modification by DOPAL obtained in solid-phase peptide synthesis. (a) Reaction scheme of the DOPAL-modified peptide synthesis on Rink Amide PEGA resin. The *Mtt* protecting group on one lysine within the KTKEGV sequence, allows the site specific modification by DOPAL on the other one. Instead, the *BOC* group protects the N-terminal amine in peptidyl resin during the Schiff base formation. The reduction with $NaCNBH_3$ stabilizes the covalent reaction between DOPAL aldehyde and lysine amine. **(b)** Molecular structure of the expected peptide with a lysine-specific modification by DOPAL, with a predicted molecular weight of 1524 Da. **(c)** RP-HPLC on Phenomenex Jupiter column (300 Å/5 µm, 250 mm × 4.6 mm) using linear gradients of eluent B in eluent A (A: 0.1% TFA in H2O, B: 0.08% TFA in ACN) of the crude reaction and the purified DOPAL-modified peptide. The predicted molecular weight was confirmed by mass spectrometry with MALDI TOF/TOF analysis. *In collaboration with Michele Sandre and Peptide Facility – CRIBI of the University of Padova.*

References.

Alafuzoff;, E.K.S., Salminen, A., and Alafuzoff, I. (2001). Ubiquitin-binding protein p62 is present in neuronal and glial inclusions in human tauopathies and synucleinopathies. Neuroreport *12*, 2085–2090.

Alam, P., Bousset, L., Melki, R., and Otzen, D.E. (2019). α-synuclein oligomers and fibrils: a spectrum of species, a spectrum of toxicities. J. Neurochem. *150*, 522–534.

Alexopoulou, Z., Lang, J., Perrett, R.M., Elschami, M., Hurry, M.E.D., Kim, H.T., Mazaraki, D., Szabo, A., Kessler, B.M., Goldberg, A.L., et al. (2016). Deubiquitinase Usp8 regulates α-synuclein clearance and modifies its toxicity in Lewy body disease. Proc. Natl. Acad. Sci. U. S. A. *113*, E4688-97.

Almandoz-Gil, L., Welander, H., Ihse, E., Khoonsari, P.E., Musunuri, S., Lendel, C., Sigvardson, J., Karlsson, M., Ingelsson, M., Kultima, K., et al. (2017). Low molar excess of 4-oxo-2-nonenal and 4-hydroxy-2-nonenal promote oligomerization of alpha-synuclein through different pathways. Free Radic. Biol. Med. *110*, 421–431.

Alvarez-Erviti, L., Seow, Y., Schapira, A.H., Gardiner, C., Sargent, I.L., Wood, M.J.A., and Cooper, J.M. (2011). Lysosomal dysfunction increases exosome-mediated alpha-synuclein release and transmission. Neurobiol. Dis. *42*, 360–367.

Ambroziak, W., and Pietruszko, R. (1987). Human aldehyde dehydrogenase: metabolism of putrescine and histamine. Alcohol. Clin. Exp. Res. *11*, 528–532.

Ambroziak, W., and Pietruszko, R. (1991). Human aldehyde dehydrogenase. Activity with aldehyde metabolites of monoamines, diamines, and polyamines. J. Biol. Chem. *266*, 13011–13018.

Anderson, D.G., Mariappan, S.V.S., Buettner, G.R., and Doorn, J.A. (2011). Oxidation of 3,4-Dihydroxyphenylacetaldehyde, a Toxic Dopaminergic Metabolite, to a Semiquinone Radical and an ortho -Quinone. J. Biol. Chem. *286*, 26978–26986.

Anderson, D.G., Florang, V.R., Schamp, J.H., Buettner, G.R., and Doorn, J.A. (2016). Antioxidant-Mediated Modulation of Protein Reactivity for 3,4-Dihydroxyphenylacetaldehyde, a Toxic Dopamine Metabolite. Chem. Res. Toxicol. *29*, 1098–1107.

Anwar, S., Peters, O., Millership, S., Ninkina, N., Doig, N., Connor-Robson, N., Threlfell, S., Kooner, G., Deacon, R.M., Bannerman, D.M., et al. (2011). Functional Alterations to the Nigrostriatal System in Mice Lacking All Three Members of the Synuclein Family. J. Neurosci. *31*, 7264–7274.

Bai, X., Wey, M.C.-Y., Martinez, P.A., Shi, C., Fernandez, E., and Strong, R. (2017). Neurochemical and motor changes in mice with combined mutations linked to Parkinson's disease. Pathobiol. Aging Age Relat. Dis. *7*, 1267855.

Bellucci, A., Navarria, L., Falarti, E., Zaltieri, M., Bono, F., Collo, G., Grazia, M., Missale, C., Spano, P., and Spano, P. (2011). Redistribution of DAT/α-Synuclein Complexes Visualized by "In Situ" Proximity Ligation Assay in Transgenic Mice Modelling Early Parkinson's Disease. PLoS One *6*, e27959.

Biosa, A., Outeiro, T.F., Bubacco, L., and Bisaglia, M. (2018). Diabetes Mellitus as a Risk Factor for Parkinson's Disease: a Molecular Point of View. Mol. Neurobiol. 8754–8763.

Bisaglia, M., Soriano, M.E., Arduini, I., Mammi, S., and Bubacco, L. (2010). Molecular characterization of dopamine-derived quinones reactivity toward NADH and glutathione: implications for mitochondrial dysfunction in Parkinson disease. Biochim. Biophys. Acta *1802*, 699–706.

Bisaglia, M., Greggio, E., Beltramini, M., and Bubacco, L. (2013). Dysfunction of dopamine homeostasis: clues in the hunt for novel Parkinson's disease therapies. FASEB J. *27*, 2101–2110.

Bisaglia, M., Filograna, R., Beltramini, M., and Bubacco, L. (2014). Are dopamine derivatives implicated in the pathogenesis of Parkinson's disease? Ageing Res. Rev. *13*, 107–114.

Blumenstock, S., Rodrigues, E.F., Peters, F., Blazquez-Llorca, L., Schmidt, F., Giese, A., and Herms, J. (2017). Seeding and transgenic overexpression of alpha-synuclein triggers dendritic spine pathology in the neocortex. EMBO Mol. Med. *9*, 716–731.

Boassa, D., Berlanga, M.L., Yang, M.A., Terada, M., Hu, J., Bushong, E.A., Hwang, M., Masliah, E., George, J.M., and Ellisman, M.H. (2013). Mapping the Subcellular Distribution of -Synuclein in Neurons using Genetically Encoded Probes for Correlated Light and Electron Microscopy: Implications for Parkinson's Disease Pathogenesis. J. Neurosci. *33*, 2605–2615.

Boassa, D., Lemieux, S.P., Lev-Ram, V., Hu, J., Xiong, Q., Phan, S., Mackey, M., Ramachandra, R., Peace, R.E., Adams, S.R., et al. (2019). Split-miniSOG for Spatially Detecting Intracellular Protein-Protein Interactions by Correlated Light and Electron Microscopy. Cell Chem. Biol.

Bousset, L., Pieri, L., Ruiz-Arlandis, G., Gath, J., Jensen, P.H., Habenstein, B., Madiona, K., Olieric, V., Böckmann, A., Meier, B.H., et al. (2013). Structural and functional characterization of two alpha-synuclein strains. Nat. Commun. *4*, 2575.

Braak, H., Del Tredici, K., Rüb, U., de Vos, R.A.I., Jansen Steur, E.N.H., and Braak, E. (2003). Staging of brain pathology related to sporadic Parkinson's disease. Neurobiol. Aging *24*, 197–211.

Breydo, L., Wu, J.W., and Uversky, V.N. (2012). α-Synuclein misfolding and Parkinson's disease. Biochim. Biophys. Acta - Mol. Basis Dis. *1822*, 261–285.

Brichta, L., and Greengard, P. (2014). Molecular determinants of selective dopaminergic vulnerability in Parkinson's disease: an update. Front. Neuroanat. *8*, 152.

Brighina, L., Riva, C., Bertola, F., Saracchi, E., Fermi, S., Goldwurm, S., and Ferrarese, C. (2013). Analysis of vesicular monoamine transporter 2 polymorphisms in Parkinson's disease. Neurobiol. Aging *34*, 1712.e9-13.

Burbulla, L.F., Song, P., Mazzulli, J.R., Zampese, E., Wong, Y.C., Jeon, S., Santos, D.P., Blanz, J., Obermaier, C.D., Strojny, C., et al. (2017). Dopamine oxidation mediates mitochondrial and lysosomal dysfunction in Parkinson's disease. Science (80-.). *351*, 1255–1261.

Burke, W.J., Li, S.W., Williams, E.A., Nonneman, R., and Zahm, D.S. (2003). 3,4-Dihydroxyphenylacetaldehyde is the toxic dopamine metabolite in vivo: implications for Parkinson's disease pathogenesis. Brain Res. *989*, 205–213.

Burke, W.J., Kumar, V.B., Pandey, N., Panneton, W.M., Gan, Q., Franko, M.W., O'Dell, M., Li, S.W., Pan, Y., Chung, H.D., et al. (2008). Aggregation of alpha-synuclein by DOPAL, the monoamine oxidase metabolite of dopamine. Acta Neuropathol. *115*, 193–203.

Burre, J., Sharma, M., Tsetsenis, T., Buchman, V., Etherton, M.R., and Sudhof, T.C. (2010). -Synuclein Promotes SNARE-Complex Assembly in Vivo and in Vitro. Science (80-.). *329*, 1663–1667.

Burré, J. (2015). The Synaptic Function of α-Synuclein. J. Parkinsons. Dis. *5*, 699–713.

Burré, J., Sharma, M., and Südhof, T.C. (2014). α-Synuclein assembles into higher-order multimers upon membrane binding to promote SNARE complex formation. Proc. Natl. Acad. Sci. U. S. A. *111*, E4274-83.

Cai, H., Liu, G., Sun, L., and Ding, J. (2014). Aldehyde Dehydrogenase 1 making molecular inroads into the differential vulnerability of nigrostriatal dopaminergic neuron subtypes in Parkinson's disease. Transl. Neurodegener. *3*, 27.

Camell, C.D., Sander, J., Spadaro, O., Lee, A., Nguyen, K.Y., Wing, A., Goldberg, E.L., Youm, Y.-H., Brown, C.W., Elsworth, J., et al. (2017). Inflammasome-driven catecholamine catabolism in macrophages blunts lipolysis during ageing. Nature *550*, 119.

Carroll, B., Otten, E.G., Manni, D., Stefanatos, R., Menzies, F.M., Smith, G.R., Jurk, D., Kenneth, N., Wilkinson, S., Passos, J.F., et al. (2018). Oxidation of SQSTM1/p62 mediates the link between redox state and protein homeostasis. Nat. Commun. *9*, 256.

Carvey, P.M., Punati, A., and Newman, M.B. (2006). Progressive dopamine neuron loss in Parkinson's disease: the multiple hit hypothesis. Cell Transplant. *15*, 239–250.

Casida, J.E., Ford, B., Jinsmaa, Y., Sullivan, P., Cooney, A., and Goldstein, D.S. (2014). Benomyl, aldehyde dehydrogenase, DOPAL, and the catecholaldehyde hypothesis for the pathogenesis of Parkinson's disease. Chem. Res. Toxicol. *27*, 1359–1361.

Caudle, W.M., Richardson, J.R., Wang, M.Z., Taylor, T.N., Guillot, T.S., McCormack, A.L., Colebrooke, R.E., Di Monte, D.A., Emson, P.C., and Miller, G.W. (2007). Reduced vesicular storage of dopamine causes progressive nigrostriatal neurodegeneration. J. Neurosci. *27*, 8138–8148.

Chamoli, M., Chinta, S.J., and Andersen, J.K. (2018). An inducible MAO-B mouse model of Parkinson's disease: a tool towards better understanding basic disease mechanisms and developing novel therapeutics. J. Neural Transm. *125*, 1651–1658.

Chen, Z.J., and Sun, L.J. (2009). Nonproteolytic Functions of Ubiquitin in Cell Signaling. Mol. Cell *33*, 275–286.

Chen, L., Ding, Y., Cagniard, B., Van Laar, A.D., Mortimer, A., Chi, W., Hastings, T.G., Kang, U.J., and Zhuang, X. (2008). Unregulated cytosolic dopamine causes neurodegeneration associated with oxidative stress in mice. J. Neurosci. *28*, 425–433.

Ciechanover, A., and Kwon, Y.T. (2015). Degradation of misfolded proteins in neurodegenerative diseases: therapeutic targets and strategies. Exp. Mol. Med. *47*, e147–e147.

Conway, K.A., Rochet, J.C., Bieganski, R.M., and Lansbury, P.T. (2001). Kinetic stabilization of the alpha-synuclein protofibril by a dopamine-alpha-synuclein adduct. Science *294*, 1346–1349.

Corrigan, F.M., Murray, L., Wyatt, C.L., and Shore, R.F. (1998). Diorthosubstituted Polychlorinated Biphenyls in Caudate Nucleus in Parkinson's Disease. Exp. Neurol. *150*, 339–342.

Cuervo, A.M., Stefanis, L., Fredenburg, R., Lansbury, P.T., and Sulzer, D. (2004). Impaired Degradation of Mutant α-Synuclein by Chaperone-Mediated Autophagy. Science (80-.). *305*.

Dahmene, M., Bérard, M., and Oueslati, A. (2017). Dissecting the Molecular Pathway Involved in PLK2 Kinase-mediated α-Synuclein-selective Autophagic Degradation. J. Biol. Chem. *292*, 3919–3928.

Damier, P., Kastner, A., Agid, Y., and Hirsch, E.C. (1996). Does monoamine oxidase type B play a role in dopaminergic nerve cell death in Parkinson's disease? Neurology *46*, 1262–1269.

Danzer, K.M., Kranich, L.R., Ruf, W.P., Cagsal-Getkin, O., Winslow, A.R., Zhu, L., Vanderburg, C.R., and McLean, P.J. (2012). Exosomal cell-to-cell transmission of alpha synuclein oligomers. Mol. Neurodegener. *7*, 42.

Dawson, T.M., and Dawson, V.L. (2002). Neuroprotective and neurorestorative strategies for Parkinson's disease. Nat. Neurosci. *5*, 1058–1061.

Dettmer, U. (2018). Rationally Designed Variants of α-Synuclein Illuminate Its in vivo Structural Properties in Health and Disease. Front. Neurosci. *12*, 623.

Dexter, D.T., Wells, F.R., Lees, A.J., Agid, F., Agid, Y., Jenner, P., and Marsden, C.D. (1989). Increased nigral iron content and alterations in other metal ions occurring in brain in Parkinson's disease. J. Neurochem. *52*, 1830–1836.

Doorn, J.A., Florang, V.R., Schamp, J.H., and Vanle, B.C. (2014). Aldehyde dehydrogenase inhibition generates a reactive dopamine metabolite autotoxic to dopamine neurons. Parkinsonism Relat. Disord. *20 Suppl 1*, S73-5.

Dorsey, E.R., Constantinescu, R., Thompson, J.P., Biglan, K.M., Holloway, R.G., Kieburtz, K., Marshall, F.J., Ravina, B.M., Schifitto, G., Siderowf, A., et al. (2007). Projected number of people with Parkinson disease in the most populous nations, 2005 through 2030. Neurology *68*, 384–386.

Ebrahimi-Fakhari, D., Cantuti-Castelvetri, I., Fan, Z., Rockenstein, E., Masliah, E., Hyman, B.T., McLean, P.J., and Unni, V.K. (2011). Distinct Roles In Vivo for the Ubiquitin–Proteasome System and the Autophagy–Lysosomal Pathway in the Degradation of α-Synuclein. J. Neurosci. *31*, 14508–14520.

Farzam, A., Chohan, K., Strmiskova, M., Hewitt, S.J., Park, D.S., Pezacki, J.P., and Özcelik, D. (2019). A functionalized hydroxydopamine quinone links thiol modification to neuronal cell death. Redox Biol. 101377.

Fauvet, B., Mbefo, M.K., Fares, M.-B., Desobry, C., Michael, S., Ardah, M.T., Tsika, E., Coune, P., Prudent, M., Lion, N., et al. (2012). α-Synuclein in central nervous system and from erythrocytes, mammalian cells, and Escherichia coli exists predominantly as disordered monomer. J. Biol. Chem. *287*, 15345–15364.

Feldman, D.E., and Frydman, J. (2000). Protein folding in vivo: the importance of molecular chaperones. Curr. Opin. Struct. Biol. *10*, 26–33.

Fellman, J.H. (1958). The rearrangement of epinephrine. Nature *182*, 311–312.

Fernandez, E., Koek, W., Ran, Q., Gerhardt, G.A., France, C.P., and Strong, R. (2006). Monoamine metabolism and behavioral responses to ethanol in mitochondrial aldehyde dehydrogenase knockout mice. Alcohol. Clin. Exp. Res. *30*, 1650–1658.

Filograna, R., Civiero, L., Ferrari, V., Codolo, G., Greggio, E., Bubacco, L., Beltramini, M., and Bisaglia, M. (2015). Analysis of the Catecholaminergic Phenotype in Human SH-SY5Y and BE(2)-M17 Neuroblastoma Cell Lines upon Differentiation. PLoS One *10*, e0136769.

Fitzmaurice, A.G., Rhodes, S.L., Lulla, A., Murphy, N.P., Lam, H.A., O'Donnell, K.C., Barnhill, L., Casida, J.E., Cockburn, M., Sagasti, A., et al. (2013). Aldehyde dehydrogenase inhibition as a pathogenic mechanism in Parkinson disease. Proc. Natl. Acad. Sci. U. S. A. *110*, 636–641.

Fitzmaurice, A.G., Rhodes, S.L., Cockburn, M., Ritz, B., and Bronstein, J.M. (2014). Aldehyde dehydrogenase variation enhances effect of pesticides associated with Parkinson disease. Neurology *82*, 419–426.

Florang, V.R., Rees, J.N., Brogden, N.K., Anderson, D.G., Hurley, T.D., and Doorn, J.A. (2007). Inhibition of the oxidative metabolism of 3,4-dihydroxyphenylacetaldehyde, a reactive intermediate of dopamine metabolism, by 4-hydroxy-2-nonenal. Neurotoxicology *28*, 76–82.

Follmer, C., Coelho-Cerqueira, E., Yatabe-Franco, D.Y., Araujo, G.D.T., Pinheiro, A.S., Domont, G.B., and Eliezer, D. (2015). Oligomerization and Membrane-binding Properties of Covalent Adducts Formed by the Interaction of a-Synuclein with the Toxic Dopamine Metabolite 3,4-Dihydroxyphenylacetaldehyde (DOPAL). J. Biol. Chem. *290*, 27660–27679.

Fonseca, T.L. da, Villar-Piqué, A., and Outeiro, T.F. (2015). The Interplay between Alpha-Synuclein Clearance and Spreading. Biomolecules *5*, 435.

Fusco, G., Sanz-Hernandez, M., and De Simone, A. (2018). Order and disorder in the physiological membrane binding of α-synuclein. Curr. Opin. Struct. Biol. *48*, 49–57.

Galter, D., Buervenich, S., Carmine, A., Anvret, M., and Olson, L. (2003). ALDH1 mRNA: presence in human dopamine neurons and decreases in substantia nigra in Parkinson's disease and in the ventral tegmental area in schizophrenia. Neurobiol. Dis. *14*, 637–647.

George, S., and Brundin, P. (2017). Solving the conundrum of insoluble protein aggregates. Lancet Neurol. *16*, 258–259.

Goldstein, D.S., Sullivan, P., Holmes, C., Kopin, I.J., Basile, M.J., and Mash, D.C. (2011). Catechols in post-mortem brain of patients with Parkinson disease. Eur. J. Neurol. *18*, 703–710.

Goldstein, D.S., Sullivan, P., Cooney, A., Jinsmaa, Y., Sullivan, R., Gross, D.J., Holmes, C., Kopin, I.J., and Sharabi, Y. (2012). Vesicular uptake blockade generates the toxic dopamine metabolite 3,4-dihydroxyphenylacetaldehyde in PC12 cells: relevance to the pathogenesis of Parkinson's disease. J. Neurochem. *123*, 932–943.

Goldstein, D.S., Sullivan, P., Holmes, C., Miller, G.W., Alter, S., Strong, R., Mash, D.C., Kopin, I.J., and Sharabi, Y. (2013). Determinants of buildup of the toxic dopamine metabolite DOPAL in Parkinson's disease. J. Neurochem. *126*, 591–603.

Goldstein, D.S., Kopin, I.J., and Sharabi, Y. (2014). Catecholamine autotoxicity. Implications for pharmacology and therapeutics of Parkinson disease and related disorders. Pharmacol. Ther. *144*, 268–282.

Goldstein, D.S., Jinsmaa, Y., Sullivan, P., Holmes, C., Kopin, I.J., and Sharabi, Y. (2016). Comparison of Monoamine Oxidase Inhibitors in Decreasing Production of the Autotoxic Dopamine Metabolite 3,4-Dihydroxyphenylacetaldehyde in PC12 Cells. J. Pharmacol. Exp. Ther. *356*, 483–492.

Grünblatt, E., and Riederer, P. (2016). Aldehyde dehydrogenase (ALDH) in Alzheimer's and Parkinson's disease. J. Neural Transm. *123*, 83–90.

Hallengren, J., Chen, P.-C., and Wilson, S.M. (2013). Neuronal Ubiquitin Homeostasis. Cell Biochem. Biophys. *67*, 67–73.

Hollenbeck, P.J. (1993). Products of endocytosis and autophagy are retrieved from axons by regulated retrograde organelle transport. J. Cell Biol. *121*, 305–315.

Hornykiewicz, O. (1998). Biochemical aspects of Parkinson's disease. Neurology *51*, S2-9.

Iwai, A., Masliah, E., Yoshimoto, M., Ge, N., Flanagan, L., de Silva, H.A., Kittel, A., and Saitoh, T. (1995). The precursor protein of non-A beta component of Alzheimer's disease amyloid is a presynaptic protein of the central nervous system. Neuron *14*, 467–475.

Jain, A., Lamark, T., Sjøttem, E., Larsen, K.B., Awuh, J.A., Øvervatn, A., McMahon, M., Hayes, J.D., and Johansen, T. (2010). p62/SQSTM1 is a target gene for transcription factor NRF2 and creates a positive feedback loop by inducing antioxidant response element-driven gene transcription. J. Biol. Chem. *285*, 22576–22591.

Janezic, S., Threlfell, S., Dodson, P.D., Dowie, M.J., Taylor, T.N., Potgieter, D., Parkkinen, L., Senior, S.L., Anwar, S., Ryan, B., et al. (2013). Deficits in dopaminergic transmission precede neuron loss and dysfunction in a new Parkinson model. Proc. Natl. Acad. Sci. *110*, E4016–E4025.

Jensen, P.H., Li, J.-Y., Dahlström, A., and Dotti, C.G. (1999). Axonal transport of synucleins is mediated by all rate components. Eur. J. Neurosci. *11*, 3369–3376.

Ji, C.H., and Kwon, and Y.T. (2017). Crosstalk and Interplay between the Ubiquitin-Proteasome System and Autophagy. Mol. Cells *40*, 441–449.

Jinsmaa, Y., Florang, V.R., Rees, J.N., Anderson, D.G., Strack, S., and Doorn, J.A. (2009). Products of Oxidative Stress Inhibit Aldehyde Oxidation and Reduction Pathways in Dopamine Catabolism Yielding Elevated Levels of a Reactive Intermediate. Chem. Res. Toxicol. *22*, 835–841.

Jinsmaa, Y., Sullivan, P., Gross, D., Cooney, A., Sharabi, Y., and Goldstein, D.S. (2014). Divalent metal ions enhance DOPAL-induced oligomerization of alpha-synuclein. Neurosci. Lett. *569*, 27–32.

Jinsmaa, Y., Sharabi, Y., Sullivan, P., Isonaka, R., and Goldstein, D.S. (2018). 3,4-Dihydroxyphenylacetaldehyde-Induced Protein Modifications and Their Mitigation by N-Acetylcysteine. J. Pharmacol. Exp. Ther. *366*, 113–124.

Jinsmaa, Y., Isonaka, R., Sharabi, Y., and Goldstein, D. (2019). 3,4-Dihydroxyphenylacetaldehyde is more efficient than dopamine in oligomerizing and quinonizing alpha-synuclein. J. Pharmacol. Exp. Ther. jpet.119.262246.

Kalia, L. V, and Lang, A.E. (2015). Parkinson's disease. Lancet (London, England) *386*, 896–912.

Kang, S.S., Ahn, E.H., Zhang, Z., Liu, X., Manfredsson, F.P., Sandoval, I.M., Dhakal, S., Iuvone, P.M., Cao, X., and Ye, K. (2018). α-Synuclein stimulation of monoamine oxidase-B and legumain protease mediates the pathology of Parkinson's disease. EMBO J. e201798878.

Katayama, H., Yamamoto, A., Mizushima, N., Yoshimori, T., and Miyawaki, A. (2008). GFP-like Proteins Stably Accumulate in Lysosomes. Cell Struct. Funct. *33*, 1–12.

Katayama, H., Kogure, T., Mizushima, N., Yoshimori, T., and Miyawaki, A. (2011). A Sensitive and Quantitative Technique for Detecting Autophagic Events Based on Lysosomal Delivery. Chem. Biol. *18*, 1042–1052.

Katila, N., Bhurtel, S., Shadfar, S., Srivastav, S., Neupane, S., Ojha, U., Jeong, G.-S., and Choi, D.-Y. (2017). Metformin lowers α-synuclein phosphorylation and upregulates neurotrophic factor in the MPTP mouse model of Parkinson's disease. Neuropharmacology *125*, 396–407.

Kaushik, S., and Cuervo, A.M. (2015). Proteostasis and aging. Nat. Med. *21*, 1406–1415.

Khanna, M., Chen, C.-H., Kimble-Hill, A., Parajuli, B., Perez-Miller, S., Baskaran, S., Kim, J., Dria, K., Vasiliou, V., Mochly-Rosen, D., et al. (2011). Discovery of a novel class of covalent inhibitor for aldehyde dehydrogenases. J. Biol. Chem. *286*, 43486–43494.

King, G., and Holmes, R. (1997). Human corneal and lens aldehyde dehydrogenases. Purification and properties of human lens ALDH1 and differential expression as major soluble proteins in human lens (ALDH1) and cornea (ALDH3). Adv. Exp. Med. Biol. *414*, 19–27.

Klyosov, A.A., Rashkovetsky, L.G., Tahir, M.K., and Keung, W.M. (1996). Possible role of liver cytosolic and mitochondrial aldehyde dehydrogenases in acetaldehyde metabolism. Biochemistry *35*, 4445–4456.

Koppaka, V., Thompson, D.C., Chen, Y., Ellermann, M., Nicolaou, K.C., Juvonen, R.O., Petersen, D., Deitrich, R.A., Hurley, T.D., and Vasiliou, V. (2012). Aldehyde Dehydrogenase Inhibitors: a Comprehensive Review of the Pharmacology, Mechanism of Action, Substrate Specificity, and Clinical Application. Pharmacol. Rev. *64*, 520–539.

Kunadt, M., Eckermann, K., Stuendl, A., Gong, J., Russo, B., Strauss, K., Rai, S., Kügler, S., Falomir Lockhart, L., Schwalbe, M., et al. (2015). Extracellular vesicle sorting of α-Synuclein is regulated by sumoylation. Acta Neuropathol. *129*, 695–713.

Kurth, J.H., Kurth, M.C., Poduslo, S.E., and Schwankhaus, J.D. (1993). Association of a monoamine oxidase B allele with Parkinson's disease. Ann. Neurol. *33*, 368–372.

Kuusisto, E., Parkkinen, L., and Alafuzoff, I. (2003). Morphogenesis of Lewy Bodies: Dissimilar Incorporation of α-Synuclein, Ubiquitin, and p62. J. Neuropathol. Exp. Neurol. *62*, 1241–1253.

Van Laar, V.S., Mishizen, A.J., Cascio, M., and Hastings, T.G. (2009). Proteomic identification of dopamine-conjugated proteins from isolated rat brain mitochondria and SH-SY5Y cells. Neurobiol. Dis. *34*, 487–500.

Lamensdorf, I., Eisenhofer, G., Harvey-White, J., Nechustan, A., Kirk, K., and Kopin, I.J. (2000). 3,4-Dihydroxyphenylacetaldehyde potentiates the toxic effects of metabolic stress in PC12 cells. Brain Res. *868*, 191–201.

Larsen, K.E., and Sulzer, D. (2002). Autophagy in neurons: a review. Histol. Histopathol. *17*, 897–908.

Lashuel, H.A., Overk, C.R., Oueslati, A., and Masliah, E. (2013). The many faces of α-synuclein: from structure and toxicity to therapeutic target. Nat. Rev. Neurosci. *14*, 38–48.

LaVoie, M.J., Ostaszewski, B.L., Weihofen, A., Schlossmacher, M.G., and Selkoe, D.J. (2005). Dopamine covalently modifies and functionally inactivates parkin. Nat. Med. *11*, 1214–1221.

De Lazzari, F., Bubacco, L., Whitworth, A.J., and Bisaglia, M. (2017). Superoxide Radical Dismutation as New Therapeutic Strategy in Parkinson's Disease. Aging Dis. *9*, 716–728.

Leão, A.H.F.F., Sarmento-Silva, A.J., Santos, J.R., Ribeiro, A.M., and Silva, R.H. (2015). Molecular, Neurochemical, and Behavioral Hallmarks of Reserpine as a Model for Parkinson's Disease: New Perspectives to a Long-Standing Model. Brain Pathol. *25*, 377–390.

Lee, M.J., Lee, J.H., and Rubinsztein, D.C. (2013). Tau degradation: The ubiquitin–proteasome system versus the autophagy-lysosome system. Prog. Neurobiol. *105*, 49–59.

Legros, H., Dingeval, M.-G., Janin, F., Costentin, J., and Bonnet, J.-J. (2004). Toxicity of a Treatment Associating Dopamine and Disulfiram for Catecholaminergic Neuroblastoma SH-SY5Y Cells: Relationships with 3,4-Dihydroxyphenylacetaldehyde Formation. Neurotoxicology *25*, 365–375.

Li, S.W., Lin, T.S., Minteer, S., and Burke, W.J. (2001). 3,4-Dihydroxyphenylacetaldehyde and hydrogen peroxide generate a hydroxyl radical: possible role in Parkinson's disease pathogenesis. Brain Res. Mol. Brain Res. *93*, 1–7.

Liang, C.-L., Wang, T.T., Luby-Phelps, K., and German, D.C. (2007). Mitochondria mass is low in mouse substantia nigra dopamine neurons: Implications for Parkinson's disease. Exp. Neurol. *203*, 370–380.

Lima, V. de A., do Nascimento, L.A., Eliezer, D., and Follmer, C. (2018). Role of Parkinson's Disease-linked Mutations and N-Terminal Acetylation on the Oligomerization of α-Synuclein Induced by DOPAL. ACS Chem. Neurosci. acschemneuro.8b00498.

Lin, M.Z., Glenn, J.S., and Tsien, R.Y. (2008). A drug-controllable tag for visualizing newly synthesized proteins in cells and whole animals. Proc. Natl. Acad. Sci. U. S. A. *105*, 7744–7749.

Lin, X., Parisiadou, L., Sgobio, C., Liu, G., Yu, J., Sun, L., Shim, H., Gu, X.-L., Luo, J., Long, C.-X., et al. (2012). Conditional Expression of Parkinson's Disease-Related Mutant -Synuclein in the Midbrain Dopaminergic Neurons Causes Progressive Neurodegeneration and Degradation of Transcription Factor Nuclear Receptor Related 1. J. Neurosci. *32*, 9248–9264.

Liu, G., Yu, J., Ding, J., Xie, C., Sun, L., Rudenko, I., Zheng, W., Sastry, N., Luo, J., Rudow, G., et al. (2014). Aldehyde dehydrogenase 1 defines and protects a nigrostriatal dopaminergic neuron subpopulation. J. Clin. Invest. *124*, 3032–3046.

Liu, G., Sgobio, C., Gu, X., Sun, L., Lin, X., Yu, J., Parisiadou, L., Xie, C., Sastry, N., Ding, J., et al. (2015). Selective expression of Parkinson's disease-related Leucine-rich repeat kinase 2 G2019S missense mutation in midbrain dopaminergic neurons impairs dopamine release and dopaminergic gene expression. Hum. Mol. Genet. *24*, 5299–5312.

Logan, T., Bendor, J., Toupin, C., Thorn, K., and Edwards, R.H. (2017). α-Synuclein promotes dilation of the exocytotic fusion pore. Nat. Neurosci. *20*, 681–689.

Los, G. V., Encell, L.P., McDougall, M.G., Hartzell, D.D., Karassina, N., Zimprich, C., Wood, M.G., Learish, R., Ohana, R.F., Urh, M., et al. (2008). HaloTag: A Novel Protein Labeling Technology for Cell Imaging and Protein Analysis. ACS Chem. Biol. *3*, 373–382.

Lotharius, J., and Brundin, P. (2002). Pathogenesis of parkinson's disease: dopamine, vesicles and α-synuclein. Nat. Rev. Neurosci. *3*, 932–942.

Lulla, A., Barnhill, L., Bitan, G., Ivanova, M.I., Nguyen, B., O'Donnell, K., Stahl, M.C., Yamashiro, C., Klärner, F.-G., Schrader, T., et al. (2016). Neurotoxicity of the Parkinson Disease-Associated Pesticide Ziram Is Synuclein-Dependent in Zebrafish Embryos. Environ. Health Perspect. *124*, 1766–1775.

Machiya, Y., Hara, S., Arawaka, S., Fukushima, S., Sato, H., Sakamoto, M., Koyama, S., and Kato, T. (2010). Phosphorylated alpha-synuclein at Ser-129 is targeted to the proteasome pathway in a ubiquitin-independent manner. J. Biol. Chem. *285*, 40732–40744.

MacKerell, A.D., and Pietruszko, R. (1987). Chemical modification of human aldehyde dehydrogenase by physiological substrate. Biochim. Biophys. Acta *911*, 306–317.

MacKerell, A.D., Blatter, E.E., and Pietruszko, R. (1986). Human aldehyde dehydrogenase: kinetic identification of the isozyme for which biogenic aldehydes and acetaldehyde compete. Alcohol. Clin. Exp. Res. *10*, 266–270.

Mallajosyula, J.K., Kaur, D., Chinta, S.J., Rajagopalan, S., Rane, A., Nicholls, D.G., Di Monte, D.A., Macarthur, H., and Andersen, J.K. (2008). MAO-B Elevation in Mouse Brain Astrocytes Results in Parkinson's Pathology. PLoS One *3*, e1616.

Mandel, S.A., Fishman, T., and Youdim, M.B.H. (2007). Gene and protein signatures in sporadic Parkinson's disease and a novel genetic model of PD. Parkinsonism Relat. Disord. *13*, S242–S247.

Manzer, R., Qamar, L., Estey, T., Pappa, A., Petersen, D.R., and Vasiliou, V. (2003). Molecular cloning and baculovirus expression of the rabbit corneal aldehyde dehydrogenase (ALDH1A1) cDNA. DNA Cell Biol. *22*, 329–338.

Marchitti, S.A., Deitrich, R.A., and Vasiliou, V. (2007). Neurotoxicity and metabolism of the catecholamine-derived 3,4-dihydroxyphenylacetaldehyde and 3,4-dihydroxyphenylglycolaldehyde: the role of aldehyde dehydrogenase. Pharmacol. Rev. *59*, 125–150.

Marchitti, S.A., Brocker, C., Stagos, D., and Vasiliou, V. (2008). Non-P450 aldehyde oxidizing enzymes: the aldehyde dehydrogenase superfamily. Expert Opin. Drug Metab. Toxicol. *4*, 697–720.

Maroteaux, L., Campanelli, J.T., and Scheller, R.H. (1988). Synuclein: a neuron-specific protein localized to the nucleus and presynaptic nerve terminal. J. Neurosci. *8*, 2804–2815.

Masato, A., Plotegher, N., Boassa, D., and Bubacco, L. (2019). Impaired dopamine metabolism in Parkinson's disease pathogenesis. Mol. Neurodegener. 2019 141 *14*, 1–21.

Mattammal, M.B., Haring, J.H., Chung, H.D., Raghu, G., and Strong, R. (1995). An endogenous dopaminergic neurotoxin: implication for Parkinson's disease. Neurodegeneration *4*, 271–281.

Mazzulli, J.R., Mishizen, A.J., Giasson, B.I., Lynch, D.R., Thomas, S.A., Nakashima, A., Nagatsu, T., Ota, A., and Ischiropoulos, H. (2006). Cytosolic Catechols Inhibit -Synuclein Aggregation and Facilitate the Formation of Intracellular Soluble Oligomeric Intermediates. J. Neurosci. *26*, 10068–10078.

Mazzulli, J.R., Burbulla, L.F., Krainc, D., and Ischiropoulos, H. (2016). Detection of Free and Protein-Bound *ortho* -Quinones by Near-Infrared Fluorescence. Anal. Chem. *88*, 2399–2405.

McCaffery, P., and Dräger, U.C. (1994). High levels of a retinoic acid-generating dehydrogenase in the meso-telencephalic dopamine system. Proc. Natl. Acad. Sci. U. S. A. *91*, 7772–7776.

McGlinchey, R.P., and Lee, J.C. (2015). Cysteine cathepsins are essential in lysosomal degradation of α-synuclein. Proc. Natl. Acad. Sci. U. S. A. *112*, 9322–9327.

Meerbrey, K.L., Hu, G., Kessler, J.D., Roarty, K., Li, M.Z., Fang, J.E., Herschkowitz, J.I., Burrows, A.E., Ciccia, A., Sun, T., et al. (2011). The pINDUCER lentiviral toolkit for inducible RNA interference in vitro and in vivo. Proc. Natl. Acad. Sci. *108*, 3665–3670.

Meiser, J., Weindl, D., and Hiller, K. (2013). Complexity of dopamine metabolism. Cell Commun. Signal. *11*, 34.

Mexas, L.M., Florang, V.R., and Doorn, J.A. (2011). Inhibition and covalent modification of tyrosine hydroxylase by 3,4-dihydroxyphenylacetaldehyde, a toxic dopamine metabolite. Neurotoxicology *32*, 471–477.

Michell, A.W., Tofaris, G.K., Gossage, H., Tyers, P., Spillantini, M.G., and Barker, R.A. (2007). The Effect of Truncated Human α-Synuclein (1–120) on Dopaminergic Cells in a Transgenic Mouse Model of Parkinson's Disease. Cell Transplant. *16*, 461–474.

Middleton, E.R., and Rhoades, E. (2010). Effects of Curvature and Composition on α-Synuclein Binding to Lipid Vesicles. Biophys. J. *99*, 2279–2288.

Mitchell, D.Y., and Petersen, D.R. (1987). The oxidation of alpha-beta unsaturated aldehydic products of lipid peroxidation by rat liver aldehyde dehydrogenases. Toxicol. Appl. Pharmacol. *87*, 403–410.

Mor, D.E., Tsika, E., Mazzulli, J.R., Gould, N.S., Kim, H., Daniels, M.J., Doshi, S., Gupta, P., Grossman, J.L., Tan, V.X., et al. (2017). Dopamine induces soluble α-synuclein oligomers and nigrostriatal degeneration. Nat. Neurosci. *20*, 1560–1568.

Morgan, C.A., Parajuli, B., Buchman, C.D., Dria, K., and Hurley, T.D. (2015). N,N-diethylaminobenzaldehyde (DEAB) as a substrate and mechanism-based inhibitor for human ALDH isoenzymes. Chem. Biol. Interact. *234*, 18–28.

Myeku, N., Metcalfe, M.J., Huang, Q., and Figueiredo-Pereira, M. (2011). Assessment of Proteasome Impairment and Accumulation/Aggregation of Ubiquitinated Proteins in Neuronal Cultures. (Humana Press, Totowa, NJ), pp. 273–296.

Nalls, M.A., Blauwendraat, C., Vallerga, C.L., Heilbron, K., Bandres-Ciga, S., Chang, D., Tan, M., Kia, D.A., Noyce, A.J., Xue, A., et al. (2019). Expanding Parkinson's disease genetics: novel risk loci, genomic context, causal insights and heritable risk. BioRxiv 388165.

Nemani, V.M., Lu, W., Berge, V., Nakamura, K., Onoa, B., Lee, M.K., Chaudhry, F.A., Nicoll, R.A., and Edwards, R.H. (2010). Increased Expression of α-Synuclein Reduces Neurotransmitter Release by Inhibiting Synaptic Vesicle Reclustering after Endocytosis. Neuron *65*, 66–79.

Nguyen, M., and Krainc, D. (2018). LRRK2 phosphorylation of auxilin mediates synaptic defects in dopaminergic neurons from patients with Parkinson's disease. Proc. Natl. Acad. Sci. U. S. A. *115*, 5576–5581.

Nicotra, A., Pierucci, F., Parvez, H., and Senatori, O. (2004). Monoamine Oxidase Expression during Development and Aging. Neurotoxicology 155–165.

Norris, E.H., Giasson, B.I., Hodara, R., Xu, S., Trojanowski, J.Q., Ischiropoulos, H., and Lee, V.M.-Y. (2005). Reversible inhibition of alpha-synuclein fibrillization by dopaminochrome-mediated conformational alterations. J. Biol. Chem. *280*, 21212–21219.

Oueslati, A. (2016). Implication of Alpha-Synuclein Phosphorylation at S129 in Synucleinopathies: What Have We Learned in the Last Decade? J. Parkinsons. Dis. *6*, 39–51.

Oueslati, A., Schneider, B.L., Aebischer, P., and Lashuel, H.A. (2013). Polo-like kinase 2 regulates selective autophagic α-synuclein clearance and suppresses its toxicity in vivo. Proc. Natl. Acad. Sci. U. S. A. *110*, E3945-54.

Panneton, W.M., Kumar, V.B., Gan, Q., Burke, W.J., and Galvin, J.E. (2010). The Neurotoxicity of DOPAL: Behavioral and Stereological Evidence for Its Role in Parkinson Disease Pathogenesis. PLoS One *5*, e15251.

Peelaerts, W., Bousset, L., Baekelandt, V., and Melki, R. (2018). α-Synuclein strains and seeding in Parkinson's disease, incidental Lewy body disease, dementia with Lewy bodies and multiple system atrophy: similarities and differences. Cell Tissue Res. *373*, 195–212.

Pérez-Revuelta, B.I., Hettich, M.M., Ciociaro, A., Rotermund, C., Kahle, P.J., Krauss, S., and Di Monte, D.A. (2014). Metformin lowers Ser-129 phosphorylated α-synuclein levels via mTOR-dependent protein phosphatase 2A activation. Cell Death Dis. *5*, e1209–e1209.

Perez, R.G., Waymire, J.C., Lin, E., Liu, J.J., Guo, F., and Zigmond, M.J. (2002). A role for alpha-synuclein in the regulation of dopamine biosynthesis. J. Neurosci. *22*, 3090–3099.

Pifl, C., Rajput, A., Reither, H., Blesa, J., Cavada, C., Obeso, J.A., Rajput, A.H., and Hornykiewicz, O. (2014). Is Parkinson's Disease a Vesicular Dopamine Storage Disorder? Evidence from a Study in Isolated Synaptic Vesicles of Human and Nonhuman Primate Striatum. J. Neurosci. *34*, 8210–8218.

Plotegher, N., and Bubacco, L. (2016). Lysines, Achilles' heel in alpha-synuclein conversion to a deadly neuronal endotoxin. Ageing Res. Rev. *26*, 62–71.

Plotegher, N., Berti, G., Ferrari, E., Tessari, I., Zanetti, M., Lunelli, L., Greggio, E., Bisaglia, M., Veronesi, M., Girotto, S., et al. (2017). DOPAL derived alpha-synuclein oligomers impair synaptic vesicles physiological function. Sci. Rep. *7*, 40699.

Polymeropoulos, M.H., Lavedan, C., Leroy, E., Ide, S.E., Dehejia, A., Dutra, A., Pike, B., Root, H., Rubenstein, J., Boyer, R., et al. (1997). Mutation in the -Synuclein Gene Identified in Families with Parkinson's Disease. Science (80-.). *276*, 2045–2047.

Prots, I., Grosch, J., Brazdis, R.-M., Simmnacher, K., Veber, V., Havlicek, S., Hannappel, C., Krach, F., Krumbiegel, M., Schütz, O., et al. (2018). α-Synuclein oligomers induce early axonal dysfunction in human iPSC-based models of synucleinopathies. Proc. Natl. Acad. Sci. U. S. A. *115*, 7813–7818.

Rajalingam, K., and Dikic, I. (2016). Expanding the Ubiquitin Code. Cell *164*, 1074-1074.e1.

Raposo, G., and Stoorvogel, W. (2013). Extracellular vesicles: exosomes, microvesicles, and friends. J. Cell Biol. *200*, 373–383.

Rathinasamy, K., and Panda, D. (2006). Suppression of microtubule dynamics by benomyl decreases tension across kinetochore pairs and induces apoptosis in cancer cells. FEBS J. *273*, 4114–4128.

Rees, J.N., Florang, V.R., Anderson, D.G., and Doorn, J.A. (2007). Lipid Peroxidation Products Inhibit Dopamine Catabolism Yielding Aberrant Levels of a Reactive Intermediate. Chem. Res. Toxicol. *20*, 1536–1542.

Rees, J.N., Florang, V.R., Eckert, L.L., and Doorn, J.A. (2009). Protein Reactivity of 3,4-Dihydroxyphenylacetaldehyde, a Toxic Dopamine Metabolite, Is Dependent on Both the Aldehyde and the Catechol. Chem. Res. Toxicol. *22*, 1256–1263.

Reichard, J.F., Vasiliou, V., and Petersen, D.R. (2000). Characterization of 4-hydroxy-2-nonenal metabolism in stellate cell lines derived from normal and cirrhotic rat liver. Biochim. Biophys. Acta *1487*, 222–232.

Rooke, N., Li, D.J., Li, J., and Keung, W.M. (2000). The mitochondrial monoamine oxidase-aldehyde dehydrogenase pathway: a potential site of action of daidzin. J. Med. Chem. *43*, 4169–4179.

Ross, C.A., and Poirier, M.A. (2004). Protein aggregation and neurodegenerative disease. Nat. Med. *10*, S10–S17.

Rotermund, C., Machetanz, G., and Fitzgerald, J.C. (2018). The therapeutic potential of metformin in neurodegenerative diseases. Front. Endocrinol. (Lausanne).

Rott, R., Szargel, R., Shani, V., Hamza, H., Savyon, M., Abd Elghani, F., Bandopadhyay, R., and Engelender, S. (2017). SUMOylation and ubiquitination reciprocally regulate α-synuclein degradation and pathological aggregation. Proc. Natl. Acad. Sci. U. S. A. *114*, 13176–13181.

Roy, S. (2017). Synuclein and dopamine: the Bonnie and Clyde of Parkinson's disease. Nat. Neurosci. *20*, 1514–1515.

Sampaio, T.F., dos Santos, E.U.D., de Lima, G.D.C., dos Anjos, R.S.G., da Silva, R.C., Asano, A.G.C., Asano, N.M.J., Crovella, S., and de Souza, P.R.E. (2018). MAO-B and COMT Genetic Variations Associated With Levodopa Treatment Response in Patients With Parkinson's Disease. J. Clin. Pharmacol. *58*, 920–926.

Santos, J.R., Cunha, J.A.S., Dierschnabel, A.L., Campêlo, C.L.C., Leão, A.H.F.F., Silva, A.F., Engelberth, R.C.G.J., Izídio, G.S., Cavalcante, J.S., Abílio, V.C., et al. (2013). Cognitive, motor and tyrosine hydroxylase temporal impairment in a model of parkinsonism induced by reserpine. Behav. Brain Res. *253*, 68–77.

Sarafian, T.A., Yacoub, A., Kunz, A., Aranki, B., Serobyan, G., Cohn, W., Whitelegge, J.P., and Watson, J.B. (2019). Enhanced mitochondrial inhibition by 3,4-dihydroxyphenyl-acetaldehyde (DOPAL)-oligomerized α-synuclein. J. Neurosci. Res. jnr.24513.

Schneider, S.A., and Alcalay, R.N. (2017). Neuropathology of genetic synucleinopathies with parkinsonism: Review of the literature. Mov. Disord. *32*, 1504–1523.

Senior, S.L., Ninkina, N., Deacon, R., Bannerman, D., Buchman, V.L., Cragg, S.J., and Wade-Martins, R. (2008). Increased striatal dopamine release and hyperdopaminergic-like behaviour in mice lacking both alpha-synuclein and gamma-synuclein. Eur. J. Neurosci. *27*, 947–957.

Shahmoradian, S.H., Lewis, A.J., Genoud, C., Hench, J., Moors, T.E., Navarro, P.P., Castaño-Díez, D., Schweighauser, G., Graff-Meyer, A., Goldie, K.N., et al. (2019). Lewy pathology in Parkinson's disease consists of crowded organelles and lipid membranes. Nat. Neurosci. *22*, 1099–1109.

Shibasaki, Y., Baillie, D.A.M., St. Clair, D., and Brookes, A.J. (1995). High-resolution mapping of SNCA encoding α-synuclein, the non-Aβ component of Alzheimer’s disease amyloid precursor, to human chromosome 4q21.3→q22 by fluorescence in situ hybridization. Cytogenet. Genome Res. *71*, 54–55.

Shu, X., Lev-Ram, V., Deerinck, T.J., Qi, Y., Ramko, E.B., Davidson, M.W., Jin, Y., Ellisman, M.H., and Tsien, R.Y. (2011). A Genetically Encoded Tag for Correlated Light and Electron Microscopy of Intact Cells, Tissues, and Organisms. PLoS Biol. *9*, e1001041.

Sotiropoulos, I., Galas, M.-C., Silva, J.M., Skoulakis, E., Wegmann, S., Maina, M.B., Blum, D., Sayas, C.L., Mandelkow, E.-M., Mandelkow, E., et al. (2017). Atypical, non-standard functions of the microtubule associated Tau protein. Acta Neuropathol. Commun. *5*, 91.

Spillantini, M.G., Schmidt, M.L., Lee, V.M.-Y., Trojanowski, J.Q., Jakes, R., and Goedert, M. (1997). Alpha-synuclein in Lewy bodies. Nature *388*, 839–840.

Spillantini, M.G., Crowther, R.A., Jakes, R., Hasegawa, M., and Goedert, M. (1998). alpha-Synuclein in filamentous inclusions of Lewy bodies from Parkinson's disease and dementia with lewy bodies. Proc. Natl. Acad. Sci. U. S. A. *95*, 6469–6473.

Stefanis, L., Emmanouilidou, E., Pantazopoulou, M., Kirik, D., Vekrellis, K., and Tofaris, G.K. (2019). How is alpha-synuclein cleared from the cell? J. Neurochem. *150*, jnc.14704.

Sulzer, D. (2007). Multiple hit hypotheses for dopamine neuron loss in Parkinson's disease. Trends Neurosci. *30*, 244–250.

Sulzer, D., and Surmeier, D.J. (2013). Neuronal vulnerability, pathogenesis, and Parkinson's disease. Mov. Disord. *28*, 41–50.

Sun, Y.-X., Wang, X.-H., Xu, A.-H., and Zhao, J.-H. (2014). Functional polymorphisms of the MAO gene with Parkinson disease susceptibility: A meta-analysis. J. Neurol. Sci. *345*, 97–105.

Surmeier, D.J., Obeso, J.A., and Halliday, G.M. (2017a). Selective neuronal vulnerability in Parkinson disease. Nat. Rev. Neurosci. *18*, 101–113.

Surmeier, D.J., Obeso, J.A., and Halliday, G.M. (2017b). Parkinson's Disease Is Not Simply a Prion Disorder. J. Neurosci. *37*, 9799–9807.

Tehranian, R., Montoya, S.E., Van Laar, A.D., Hastings, T.G., and Perez, R.G. (2006). Alpha-synuclein inhibits aromatic amino acid decarboxylase activity in dopaminergic cells. J. Neurochem. *99*, 1188–1196.

Teravskis, P.J., Covelo, A., Miller, E.C., Singh, B., Martell-Martínez, H.A., Benneyworth, M.A., Gallardo, C., Oxnard, B.R., Araque, A., Lee, M.K., et al. (2018). A53T Mutant Alpha-Synuclein Induces Tau-Dependent Postsynaptic Impairment Independently of Neurodegenerative Changes. J. Neurosci. *38*, 9754–9767.

Tessari, I., Bisaglia, M., Valle, F., Samorì, B., Bergantino, E., Mammi, S., and Bubacco, L. (2008). The Reaction of α-Synuclein with Tyrosinase. J. Biol. Chem. *283*, 16808–16817.

Thornalley, P.J. (2003). Use of aminoguanidine (Pimagedine) to prevent the formation of advanced glycation endproducts. Arch. Biochem. Biophys. *419*, 31–40.

Tofaris, G.K., Kim, H.T., Hourez, R., Jung, J.-W., Kim, K.P., and Goldberg, A.L. (2011). Ubiquitin ligase Nedd4 promotes alpha-synuclein degradation by the endosomal-lysosomal pathway. Proc. Natl. Acad. Sci. U. S. A. *108*, 17004–17009.

Tysnes, O.B., and Storstein, A. (2017). Epidemiology of Parkinson's disease. J. Neural Transm. *124*, 901–905.

Um, J.-H., Kim, Y.Y., Finkel, T., and Yun, J. (2018). Sensitive Measurement of Mitophagy by Flow Cytometry Using the pH-dependent Fluorescent Reporter mt-Keima. J. Vis. Exp. e58099.

Utton, M.A., Noble, W.J., Hill, J.E., Anderton, B.H., and Hanger, D.P. (2005). Molecular motors implicated in the axonal transport of tau and α-synuclein. J. Cell Sci. *118*, 4645–4654.

Vargas, K.J., Schrod, N., Davis, T., Laugks, U., Lucic, V., Chandra, S.S., Fernandez-Busnadiego, R., and Taguchi, Y. V (2017). Synucleins Have Multiple Effects on Presynaptic Architecture. Cell Rep. *18*, 161–173.

Vasiliou, V., Pappa, A., and Estey, T. (2004). Role of human aldehyde dehydrogenases in endobiotic and xenobiotic metabolism. Drug Metab. Rev. *36*, 279–299.

Vicente Miranda, H., Szegő, É.M., Oliveira, L.M.A., Breda, C., Darendelioglu, E., de Oliveira, R.M., Ferreira, D.G., Gomes, M.A., Rott, R., Oliveira, M., et al. (2017). Glycation potentiates α-synuclein-associated neurodegeneration in synucleinopathies. Brain *140*, 1399–1419.

Vijayan, V., and Verstreken, P. (2017). Autophagy in the presynaptic compartment in health and disease. J. Cell Biol. *216*, 1895–1906.

Volpicelli-Daley, L.A. (2017a). Effects of α-synuclein on axonal transport. Neurobiol. Dis. *105*, 321–327.

Volpicelli-Daley, L.A. (2017b). Effects of α-synuclein on axonal transport. Neurobiol. Dis. *105*.

Wakabayashi, K., Tanji, K., Odagiri, S., Miki, Y., Mori, F., and Takahashi, H. (2013). The Lewy Body in Parkinson's Disease and Related Neurodegenerative Disorders. Mol. Neurobiol. *47*, 495–508.

Wang, L., Xie, C., Greggio, E., Parisiadou, L., Shim, H., Sun, L., Chandran, J., Lin, X., Lai, C., Yang, W.-J., et al. (2008). The chaperone activity of heat shock protein 90 is critical for maintaining the stability of leucine-rich repeat kinase 2. J. Neurosci. *28*, 3384–3391.

Wang, L., Das, U., Scott, D.A., Tang, Y., McLean, P.J., and Roy, S. (2014). α-synuclein multimers cluster synaptic vesicles and attenuate recycling. Curr. Biol. *24*, 2319–2326.

Wang, Y.-C., Lauwers, E., and Verstreken, P. (2017). Presynaptic protein homeostasis and neuronal function. Curr. Opin. Genet. Dev. *44*, 38–46.

Wegrzynowicz, M., Bar-On, D., Calo', L., Anichtchik, O., Iovino, M., Xia, J., Ryazanov, S., Leonov, A., Giese, A., Dalley, J.W., et al. (2019). Depopulation of dense α-synuclein aggregates is associated with rescue of dopamine neuron dysfunction and death in a new Parkinson's disease model. Acta Neuropathol. 1–21.

Werner, C.J., Heyny-von Haussen, R., Mall, G., and Wolf, S. (2008). Proteome analysis of human substantia nigra in Parkinson's disease. Proteome Sci. *6*, 8.

Wey, M.C.-Y., Fernandez, E., Martinez, P.A., Sullivan, P., Goldstein, D.S., and Strong, R. (2012). Neurodegeneration and motor dysfunction in mice lacking cytosolic and mitochondrial aldehyde dehydrogenases: implications for Parkinson's disease. PLoS One *7*, e31522.

Wilhelm, B.G., Mandad, S., Truckenbrodt, S., Krohnert, K., Schafer, C., Rammner, B., Koo, S.J., Classen, G.A., Krauss, M., Haucke, V., et al. (2014). Composition of isolated synaptic boutons reveals the amounts of vesicle trafficking proteins. Science (80-.). *344*, 1023–1028.

Wong, Y.C., and Krainc, D. (2017). α-synuclein toxicity in neurodegeneration: mechanism and therapeutic strategies. Nat. Med. *23*, 1–13.

Xiao, T., Shoeb, M., Siddiqui, M.S., Zhang, M., Ramana, K. V, Srivastava, S.K., Vasiliou, V., and Ansari, N.H. (2009). Molecular cloning and oxidative modification of human lens ALDH1A1: implication in impaired detoxification of lipid aldehydes. J. Toxicol. Environ. Health. A *72*, 577–584.

Xilouri, M., Brekk, O.R., and Stefanis, L. (2013). Alpha-synuclein and Protein Degradation Systems: a Reciprocal Relationship. Mol. Neurobiol. *47*, 537–551.

Yoshida, A., Hsu, L.C., and Davé, V. (1992). Retinal oxidation activity and biological role of human cytosolic aldehyde dehydrogenase. Enzyme *46*, 239–244.

Zarow, C., Lyness, S.A., Mortimer, J.A., Chui, H.C., W, B., and DD, W. (2003). Neuronal Loss Is Greater in the Locus Coeruleus Than Nucleus Basalis and Substantia Nigra in Alzheimer and Parkinson Diseases. Arch. Neurol. *60*, 337–341.

Zhang, X., Ye, Y.-L., Wang, Y.-N., Liu, F.-F., Liu, X.-X., Hu, B.-L., Zou, M., and Zhu, J.-H. (2015). Aldehyde dehydrogenase 2 genetic variations may increase susceptibility to Parkinson's disease in Han Chinese population. Neurobiol. Aging *36*, 2660.e9-13.

Zhang, Z., Su Kang, S., Liu, X., Hee Ahn, E., Zhang, Z., He, L., Michael Iuvone, P., Duong, D.M., Seyfried, N.T., Benskey, M.J., et al. (2017). Asparagine endopeptidase cleaves α-synuclein and mediates pathologic activities in Parkinson's disease. Nat. Struct. Mol. Biol. *24*, 632–642.

Zhao, C.C., Cai, H.B., Wang, H., and Pan, S.Y. (2016). Role of ADH2 and ALDH2 gene polymorphisms in the development of Parkinson's disease in a Chinese population. Genet. Mol. Res. *15*.